Atomic Layer Deposition of
Metal Oxide Thin Films for
Si Heterojunction Solar Cells

STW
Nieuwe technologie
mogelijk maken

TU/e

Bart Macco

Atomic Layer Deposition
of Metal Oxide Thin Films
for Si Heterojunction Solar Cells

PROEFSCHRIFT

ter verkrijging van de graad van doctor aan de Technische Universiteit Eindhoven, op gezag van de rector magnificus prof.dr.ir. F.P.T. Baaijens, voor een commissie aangewezen door het College voor Promoties, in het openbaar te verdedigen op woensdag 5 oktober 2016 om 16:00 uur

door

Bart Macco

geboren te Sittard

Dit proefschrift is goedgekeurd door de promotoren en de samenstelling van de promotiecommissie is als volgt:

voorzitter:	prof.dr.ir. G.M.W. Kroesen
1e promotor:	prof.dr.ir. W.M.M. Kessels
2e promotor:	prof.dr. R.E.I. Schropp
leden:	Prof.Dr. B. Rech (TU Berlin)
	prof.dr. A. Polman (UvA)
	prof.dr. A.P.H.J. Schenning
	prof.dr. M. Karppinen (Aalto University)
	dr. M. Creatore

Het onderzoek dat in dit proefschrift wordt beschreven is uitgevoerd in overeenstemming met de TU/e Gedragscode Wetenschapsbeoefening.

Funding information

Contents

Avant donc que d'écrire, apprenez à penser.
Selon que notre idée est plus ou moins obscure,
L'expression la suit, ou moins nette, ou plus pure.
Ce que l'on conçoit bien s'énonce clairement,
Et les mots pour le dire arrivent aisément.

Hâtez-vous lentement, et sans perdre courage,
Vingt fois sur le métier remettez votre ouvrage,
Polissez-le sans cesse, et le repolissez,
Ajoutez quelquefois, et souvent effacez.

Nicolas Boileau, *L'Art Poétique* (1674)

1

General Introduction

"Atomic Layer Deposition of Metal Oxide Thin Films for Si Heterojunction Solar Cells" - A dissertation title bearing a lot of concepts, the meaning of which might not be immediately evident to every reader. Therefore, this introductory chapter serves (1) to give a global overview of the current status of and developments in the field of Si heterojunction photovoltaics and (2) to show how the line of research taken within this project fits into this picture.

This overview chapter is followed by a more in-depth chapter entitled "Atomic Layer Deposition for High Efficiency Crystalline Silicon Solar Cells". This chapter was written within this project for the publisher Wiley, and is to be included in the book "Atomic Layer Deposition in Energy Conversion Applications", edited by J. Bachmann. This chapter explains the main high-efficiency Si photovoltaic technologies, the role of functional thin films as passivation layer, transparent conductive oxides (TCOs) and passivating contacts in these technologies, as well as the use of atomic layer deposition (ALD) for the preparation of these films. Together, these two chapters should serve as an excellent basis for understanding and appreciating the research chapters that follow in this dissertation.

1.1   Crystalline Si photovoltaics: Current status and developments

From a consumer point of view, the most prominent change seen in the field of photovoltaics (PV) is probably the major decrease in price of a rooftop system over the last decades. This decrease in price is displayed in Figure 1, where the average price for a PV

rooftop system with a size of 10 - 100 kWp in Germany has been plotted. For comparison: The cost of a rooftop system in 1990 was around 14 €/Wp and is currently close to 1 €/Wp. Thanks to this major drop in price, the levelized cost of electricity (LCOE) of PV has in many countries already dropped below the commercial kWh price, i.e. *grid parity* has been achieved.*

One might think that great technological innovations in the design of the solar cells stand at the basis of such a dramatic decrease in price. However, by far most of the present production volume is based on the conventional, relatively low-tech Al-BSF cell (Aluminum back-surface field cell, a schematic of which is shown in Figure 2). Higher efficiency technologies such as the PERC (Passivated Emitter Rear Cell) and the silicon heterojunction (SHJ) technologies, which will be discussed later, are only recently starting to gain ground in high volume manufacturing, despite having existed for at least a decade in research environments. It is mostly the large increase in production volume that have brought the prices down.

The role of the production volume in reducing the price is known as either the price experience curve, the learning curve or Swanson's law. It states that the price of photovoltaic modules drops by twenty percent for each doubling of cumulative shipped volume. This empirical effect is shown in Figure 3. As can be seen, the module cost accurately follows this trend, with deviations in the early 2000s and around 2010 being due to a polysilicon shortage and overproduction, respectively.

To the author's opinion, the learning curve precisely demonstrates why stable subsidy programmes have been the key to bringing the cost of PV to the low level we witness today. It is a common misnomer that the primary aim of subsidies is to make PV affordable today. It is rather the establishment of a stable market through a stable subsidy programme which increases production volume and thereby leads to the associated reduction in product costs in the future. As a primary example, the feed-in tariff introduced in Germany by law compensates producers of renewable electricity for a period of 20 years. The 20 year-period guarantee created a very stable market for companies to invest in, which led to an increase in production volume and thereby contributed to the low PV prices we have today.

Nonetheless, even though prices have decreased such that grid parity has been achieved in many countries, further reductions in photovoltaic electricity costs are still desired: Firstly, although the price has decreased below household prices in many countries, it has only decreased to levels below the industry prices in select countries. Additionally,

---

*Often the price per Wp is used to express the price of PV energy. To the author's opinion, the LCOE is a much better figure of merit. Even though it is a number which is harder to assess, it encompasses all aspects that determine the final price per kWh produced. The price per Wp does not take into account the fact that different technologies can have different average output per Wp. For example, in general heterojunction cells produce more kWh/kWp than homojunction cells since they have a better temperature coefficient and perform better under low-illumination conditions.
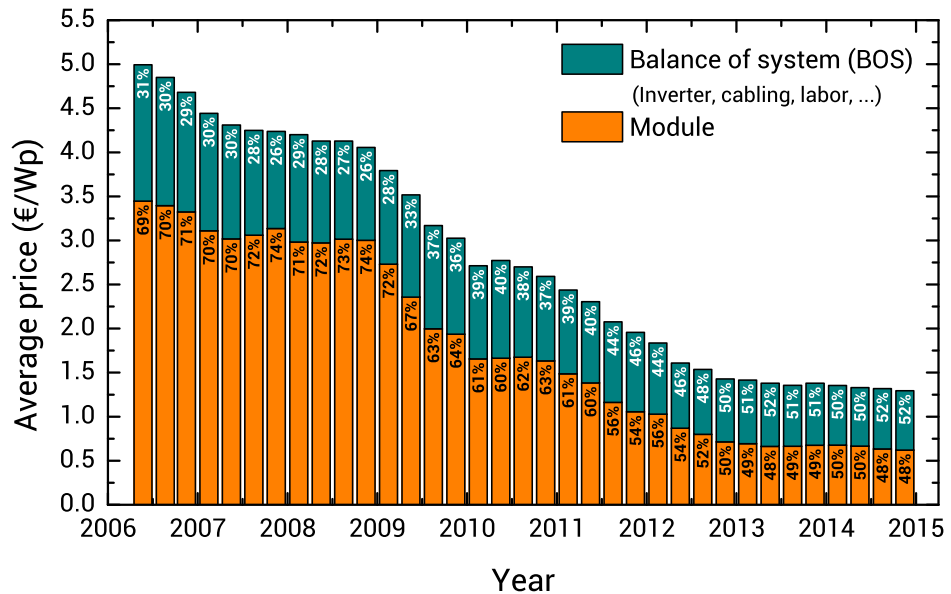
Figure 1: Development of the average price of a PV rooftop system with a size of 10 - 100 kWp in Germany over the last decade. The price is divided into the module price and the balance of system, which encompasses all the other aspects such as inverter, cabling, installation material and labor costs. Data was taken from the 2016 Fraunhofer photovoltaics report. [1]

the intermittent character of most renewables necessitates the use of energy storage and smart-grid solutions in order to guarantee a continuous power supply, which adds to the cost. Another important but often overlooked challenge is that the value of PV electricity decreases as its market share increases. This can be understood from the fact that electricity prices fluctuate during the day, depending on the current supply and demand. Since most solar power is produced concurrently, solar power mainly becomes its own competitor within the market. This effect, also known as "value deflation", is nicely discussed in a recent Nature Energy publication by Sivaram and Kann, where they propose a cost target of US$0.25 per Wp for the mid of the century in order for photovoltaics to remain competitive and to sustain its increasing market share. [2]

According to the learning curve, the module cost can be expected to decrease further in the coming years due to a further increase in cumulative shipped volume. Then why devote a PhD thesis to the development of new materials for high-efficiency photovoltaics, if we have come so far with the low-tech Al-BSF cells? At this point, it is important to realize that costs other than the module are becoming more and more dominant in determining the total LCOE of PV electricity. Such other costs include the inverter, cabling and installation materials, labor, etcetera, and are referred to as the balance of system (BOS). The increasing share of the BOS in the total cost of PV can
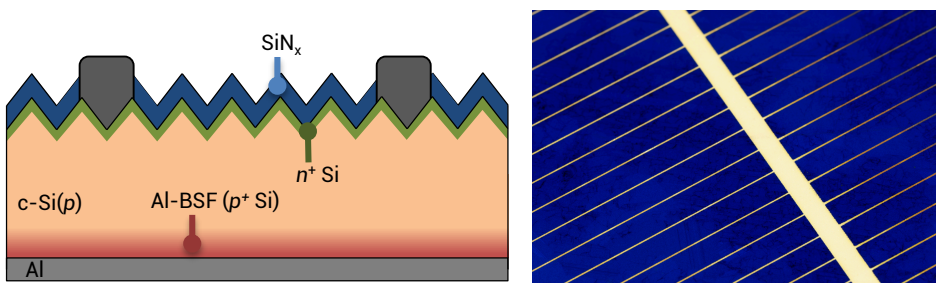
Figure 2: (Left) Schematic of the <u>Al</u>uminum <u>b</u>ack-<u>s</u>urface <u>f</u>ield cell. A highly-doped n^+ region makes the front side of the *p*-type wafer electron-selective and serves for lateral conduction of electrons. A silicon nitride (SiN$_x$) film serves both for antireflection and passivation of the surface (and bulk in the case of multicrystalline silicon). A eutectic formed at the rear between Al and Si creates a p^+-region, also known as the back surface field (BSF). The BSF makes the rear selective for holes. (Right) Picture of the front side of an Al-BSF cell. The SiN$_x$ anti-reflection coating gives the cell its blue appearance.

be seen in Figure 1, which shows that currently the BOS accounts for more than half of the cost. Therefore, in the hypothetical case that modules would become available for free, this would only cut the system price in half. This is exactly the reason why for a sustained decrease of the cost of PV electricity on the long term increases in module *efficiency* rather than decreases in module *cost* are becoming increasingly important, as an increased power output also decreases the relative share of the BOS.

1.2 Thin film technology for high efficiency c-Si photovoltaics

As the previous discussion showed, increases in cell (or module) efficiency are becoming increasingly important for further cost reduction. Fortunately, many concepts other than the Al-BSF cell exist which can (potentially) attain higher efficiency values, and the current world record efficiency stands at 25.6%.[3] In Figure 4 the evolution of the cell efficiency of various c-Si solar cell concepts is displayed. Readers unfamiliar with the cell concepts of Figure 4 are referred to schematics of such cells which can be found on page 24. The cell concepts have been divided into *homojunctions* and *heterojunctions*. Homojunctions refer to cell concepts where a (heavily) doped region within the c-Si itself is used to selectively extract either holes or electrons at one of the metal electrodes, such as the Al-BSF cell. This contrasts to silicon heterojunctions (SHJ) concepts, in which thin films are deposited on the silicon surface in order to selectively extract either charge carrier.

In both homojunctions and heterojunction concepts functional thin films are playing an ever increasing role for attaining higher efficiencies. For homojunctions, *passivation* layers are employed to suppress surface recombination and thereby achieve higher V_{oc} values. In heterojunctions, thin films provide almost all the critical functions for pho-
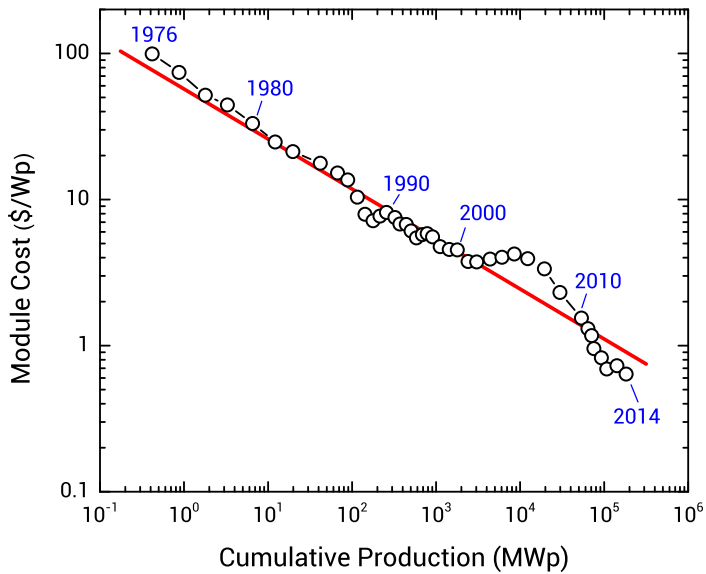
Figure 3: The learning curve of Si photovoltaics. The curve shows that by good approximation, the price of a photovoltaic module decreases by 20% for each doubling of the cumulative production. [1]

tovoltaic operation, i.e. surface passivation, carrier selectivity and lateral charge transport. The developments in the field of homojunctions will be discussed further in the next chapter. For the purpose of this introduction, let's for now focus on the developments of the heterojunction cells, which are the topic of this dissertation.

Si heterojunction (SHJ) cells were already investigated by Sanyo (now Panasonic) in the 1980's. [26] A schematic of their archetypical SHJ cell is shown in Figure 5, along with a brief explanation of the working principle. One of the major breakthroughs for this concept was the insertion of the intrinsic *a*-Si:H layers in between the c-Si base and the doped *a*-Si:H layers. [27] This resulted in excellent surface passivation over the whole Si surface and enables the extremely high open-circuit voltage (V_{oc}) values that can be obtained of up to 750 mV. [28] This contrasts to homojunction cells for which the V_{oc} is typically well below 700 mV. This low voltage stems from (mostly) Auger recombination in the highly doped regions (HDRs) in the c-Si base and surface recombination at the highly recombination active Si-metal contacts. Because of the leading role of the *a*-Si:H(*i*) passivation layer, Sanyo coined their technology HIT (<u>H</u>eterojunction with <u>I</u>ntrinsic <u>T</u>hin layer). [27] Sanyo has since then succesfully commercialized this technology. Figure 4 clearly shows that HIT technology belongs to the cell types having the highest efficiencies and has seen a steady increase over the last decade. Together with the expiration of Sanyo's most important HIT patents in 2010, this has led to strong interest in this technology both from industry and research.
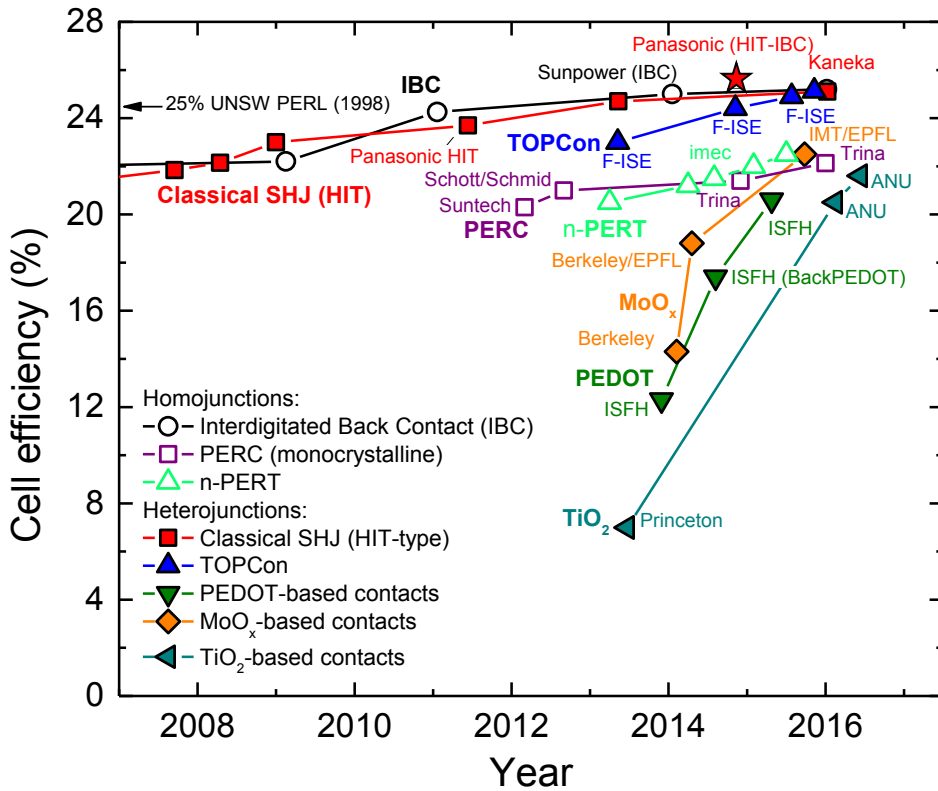
Figure 4: Chart of the evolution of the record efficiencies of a selection of c-Si photovoltaic technologies. The technologies have been sorted by their type of carrier-selective contact, and institute names have been added to the efficiency values. Values for the IBC [4], PERC [5,6], n-PERT [7,8], HIT [9,10,11,12,3], TOPCon [13,14,15,16], PEDOT-based [17,18,19], MoO$_x$-based [20,21,22] and TiO$_2$-based [23,24,25] cells have been added.

Starting from the classical SHJ cell configuration in Figure 5, many developments have taken place over the last few years. New materials to replace the conventional *a*-Si:H and TCO layers in the SHJ cell have emerged, such as MoO$_x$ and *high-mobility* TCOs. In addition, totally new heterojunction concepts, often referred to as *passivating contacts*[†] have appeared. In order to demonstrate the interplay between these developments in the field and the course of research presented in this dissertation, the next section will discuss a timeline of these developments and relate them to the research chapters in this thesis.

[†]Currently there is no real consensus yet on the use of these terms in literature. For example, passivating contacts, passivated contacs, and carrier-selective contacts are all in use. In this disseration, heterojunctions refer to all non-homojunction cells, SHJ cells to the HIT-type heterojunction, and passivating contacts to the novel types of heterojunctions.
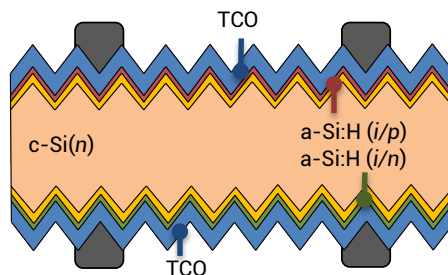
Figure 5: Schematic of a bifacial HIT-type SHJ cell. A c-Si wafer is used as the light-absorbing semiconductor. The wafer is typically *n*-type because of its high bulk lifetime, and is textured to enhance light absorption in the wafer. Intrinsic *a*-Si:H films effectively passivate the full front and rear surface, whereas *p*- and *n*-doped *a*-Si:H layers make the front and rear side hole- and electron-selective, respectively. Transparent conductive oxides (TCOs), typically Sn-doped indium oxide (ITO), at the front and rear side act as antireflection coating and provide lateral conduction of charge carriers to the metal grid. The metal contacts are typically made by screenprinting.

1.3 Framework of this thesis and the relation to developments for SHJ cells

The work presented in this dissertation is part of the FLASH (Fundamentals and Application of Silicon Heterojunction solar cells) programme, funded by Stichting Technologie en Wetenschap (STW). The FLASH consortium consists of a mix of academic and industrial entities, and aims to strengthen the position of (mostly) Dutch research institutes and industry in the field of SHJ solar cells. On September 1st 2012, about one year after the kick-off of the FLASH programme itself in August 2011, the author enrolled into the project entitled "Amorphous Silicon Growth Kinetics and Interface Engineering for Si Heterojunction Solar Cells". Looking at the title of this thesis, the reader might be surprised to see that no mention of amorphous silicon is made at all. In fact, not a single chapter in this thesis is specifically devoted to amorphous silicon passivation layers, although amorphous silicon does play a pervasive role in this work as passivation layer.[‡] Instead, it was chosen quite early on in the project to focus on various functional metal oxide thin films for SHJ solar cells. This change of focus was mainly motivated by the rapid changes the field of silicon heterojunctions has been seeing in recent years and the opportunities we saw to align our research to these developments.

Around mid 2012 - early 2013 there appeared a few key publications involving the interaction between the transparent conductive oxide (TCO) layer and the *a*-Si:H layers, which in hindsight triggered us to look at the *a*-Si:H-TCO system as a whole. Demaurex *et al.* showed that the exposure of the *a*-Si:H layers to harsh plasma conditions during sputter deposition of the TCO layer damages the *a*-Si:H layers and thus strongly reduces

---

[‡]At the start of the project a new low-temperature approach to make highly passivating *a*-Si:H layers from an inductively coupled plasma was developed. A manuscript is currently near completion, but not included in this dissertation.

the passivation.[29] Although (much of) the initial passivation quality can be recovered by a post-deposition anneal, the microstructure of the *a*-Si:H layers is irreversibly altered. Therefore a natural question arose: Could we make better cells if we could prevent this plasma damage altogether? From this, the idea emerged to use the deposition technique of atomic layer deposition (ALD) to prepare the TCO for SHJ cells instead of sputtering. In a thermal ALD process no plasma is used, so sputter damage can be avoided. It was at that point that ALD came into this thesis work.

Our research group already had a strong background both in ALD itself as well as in applying such layers in various photovoltaic devices, including c-Si, copper indium gallium selenide (CIGS), and dye-sensitized solar cells (DSSCs).[30,31] For c-Si devices, it is the surface passivation of (mostly) the p^+-region in homojunction devices by Al_2O_3 where our group has made a great contribution both in terms of research and towards commercialization.[31] Having access to both this expertise and a wide range of materials that can be made by ALD in our laboratories, why not see if we can apply ALD thin films in the field of heterojunction cells as well?

Having realized this, it was a natural choice to use ALD to prepare TCOs of Al-doped zinc oxide (ZnO:Al) instead of using sputtered ITO. Various ALD processes to prepare doped ZnO had already been developed in our group for other projects.[32,33,34] Therefore, we set out to study the effect of depositing ALD ZnO:Al on the *a*-Si:H-based surface passivation, the results of which are outlined in **Chapter 3** and which have been published in *Semiconductor Science & Technology*.[35] Indeed, it was found that during ALD no damage is induced to the *a*-Si:H layers in contrast to sputtering. Inspired by this promising result, a collaboration was set up with EPFL to test our ALD ZnO:Al in devices. It was found that the use of ALD can indeed lead to higher internal voltages, although the formation of an oxide interlayer between the TCO and *a*-Si:H layers forms a challenge that needs further research. These results were published in IEEE Journal of Photovoltaics, but are not included in this thesis.[36]

However, the absence of plasma-induced damage when using ALD was not the full story. Both in our own experiments as well as in the collaboration with EPFL, we observed that the application of the TCO resulted in a decrease of the minority carrier lifetime at low injection levels.[36] Such an effect lowers the (implied) fill factor (*FF*) of the cell, and around the same time (mid 2013) this was also reported on by Rößler *et al*.[37] They attributed this phenomenon to a too low work function of the ZnO:Al TCO. This gave us the idea to vary the work function of the ALD TCO by varying doping level in order to see how this affected the minority carrier lifetime at low injection levels. The key merit of ALD in this experiment is the freedom to accurately control the doping level of the TCO, as opposed to sputtered TCOs for which the doping level is more or less fixed by the doping ratio of the sputter target. Indeed, it was observed that increasing the

doping of the ZnO TCO (i.e. decreasing the work function) results in stronger reductions of the low-injection level minority carrier lifetime. Therefore our results, which are also included in **Chapter 3**, show that variation of the doping level is another way to optimize the band structure of the HIT cell.

Looking at the table of contents, one can see that the remaining chapters are about ALD of two metal oxides that have so far gone unmentioned: Hydrogen-doped indium oxide (In_2O_3:H) and molybdenum oxide (MoO_x). How did these materials get into the project and why are we interested in them? To illustrate this, let's go back to the HIT structure for a moment. As mentioned before, the classical HIT-structure shown in Figure 5 can achieve extremely high V_{oc} values up to 750 mV. Also excellent *FF* values exceeding 80% are not uncommon. It is however the short-circuit current density J_{sc} values that have historically been lower than that of the homojunctions concepts. This can be understood from the fact that the homojunction technologies feature only highly transparent thin films at the front side such as SiN_x, Al_2O_3 and SiO_2, whereas the *a*-Si:H and the TCO layers found in HIT cells can induce quite significant optical losses. Fortunately, more transparent alternative hole-selective and TCO materials have been found over the last few years. Although it is not always disclosed which materials are used in the record cells, it can be expected that these new materials have played a large role in enabling the steady increase of the J_{sc} to values from well below 40 mA/cm^2 to values close to 41 mA/cm^2 in recent years. For instance, the record HIT-type cell of Kaneka with an efficiency of 25.1% has a J_{sc} of 40.8 mA/cm^2, which is very close to the maximum of ∼44 mA/cm^2 if all the photons present in the solar spectrum with a photon energy above the bandgap of c-Si contribute to the photocurrent.[12]

High-mobility transparent conductive oxides

The first development enabling higher J_{sc} values is the emergence of so-called *high-mobility* TCO materials, most notably the aforementioned In_2O_3:H. In Figure 6 the absorption coefficients of ITO and In_2O_3:H are shown. For the ITO layer, optical losses at low photon energies mainly originate from the relatively high carrier density (∼3-5 × 10^{20} cm^{-3}). The free carriers reduce the refractive index *n* and increase the extinction coefficient *k* at low photon energies, leading to increased reflection and absorption of IR photons, respectively. Typical J_{sc} losses over 2 mA/cm^2 are not uncommon.[38] In_2O_3:H is such a high-mobility TCO which features a much higher mobility of >100 cm^2/Vs compared to ITO (∼40 cm^2/Vs). The high mobility allows for a strong reduction of the carrier density towards the low 10^{20} cm^{-3} level without compromising its electrical conductivity. As can be seen from Figure 6, this leads to negligible absorptive losses at low photon energies. In_2O_3:H was originally prepared by sputtering[39] and early 2013 EPFL

published a paper showing the implementation of this high-mobility TCO in a HIT cell, demonstrating a substantial $\sim$2 mA/cm^2 gain in J_{sc} and a cell efficiency of 22.1%.[40]
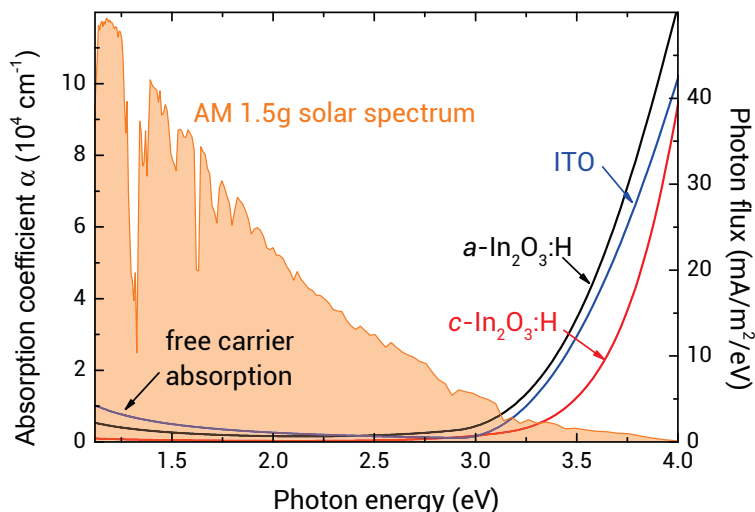
Figure 6: Absorption coefficients of ITO and both amorphous and polycrystalline In$_2$O$_3$:H. The AM1.5g solar spectrum has been added for reference.

Given the developments regarding In$_2$O$_3$:H, one might think that the development of In$_2$O$_3$:H by ALD was deliberately pursued within this project. This would have been a logical choice, since it could potentially combine the soft deposition of ALD with the excellent material properties of In$_2$O$_3$:H. This is actually not exactly how it went, there was a bit more serendipity at play: After the experiments with ALD ZnO:Al, it was realized that the use of ZnO:Al as the front TCO severely limited the efficiency: The commonly-employed ITO layer is generally speaking more transparent and conductive than ZnO:Al. Moreover, indium oxide has a higher work function of $\sim$5 eV compared to ZnO ($\sim$4.4 eV), which makes it more suited for contacting the hole-collecting side. Therefore, it was decided to pursue the development of an ALD process to prepare ITO. In order to be able to prepare Sn-doped In$_2$O$_3$, first an ALD process for the preparation of undoped In$_2$O$_3$ had to be developed. From the literature, the In$_2$O$_3$ ALD process developed at Argonne National Lab using the indium cyclopentadienyl (InCp) precursor and a combination of H$_2$O and O$_2$ as oxidant was selected and quite quickly adapted to our own ALD system.[41]

It was just before attempting to dope our ALD In$_2$O$_3$ by Sn that the author became familiar with the aforementioned work on sputtered H-doped In$_2$O$_3$ and its implementation in SHJ cells. Also for the ALD In$_2$O$_3$ we found that amorphous material could be made by depositing at low processing temperatures (100 ^{o}C) on Al$_2$O$_3$ substrates. Moreover, by analyzing the elemental composition of the film it was found that the films contained

substantial amounts of atomic hydrogen ($\sim$4 at. %). Apparently, the ALD In_2O_3 film was unintentionally being doped with H during the ALD process, i.e. we had inadvertently grown In_2O_3:H by ALD. Therefore the idea came to mind to also try to post-crystallize such an amorphous In_2O_3:H (*a*-In_2O_3:H) layer in order to see if similar improvements upon post-crystallization could be obtained for the ALD In_2O_3:H material. Indeed, this turned out to work wonderfully: After only annealing the *a*-In_2O_3:H for ten minutes at 200 °C record-high mobility values of 138 cm^2/Vs and a low resistivity of 0.27 mΩcm were obtained. Moreover, transmission electron microscopy (TEM) imaging revealed a large grain size of a few hundred nm and excellent in-grain quality. These promising initial results were quickly communicated in *Rapid Research Letters*[42], and they form **Chapter 4** of this dissertation.

At that point, it became clear that the ALD In_2O_3:H material had a lot of potential. Therefore, the material was studied in great detail. Firstly, the doping mechanism and electron scattering in ALD In_2O_3:H has been studied in order to understand the origin of the high mobility. It has been shown that the only relevant electron scattering mechanisms in the material are unavoidable mechanisms, i.e. phonon and ionized impurity scattering, and that scattering due to material imperfections is negligible. This means that the ALD films feature the highest possible carrier mobility at that carrier density. Furthermore, H has been identified as an excellent dopant, as it can both passivate defects at the grain boundaries, while at the same time it does not lead to scattering when it is not an active dopant. These findings were published in *ACS Applied Materials & Interfaces*[43] which has become **Chapter 5** of this dissertation. In **Chapter 6** an electron microscopy study of the post-crystallization step, which is key to attaining the excellent material properties, is presented. The study revealed the crystallization mechanism and kinetics of ALD In_2O_3:H, and clearly demonstrates why the In_2O_3:H films should be prepared at the lowest possible temperature prior to post-crystallization.The resulting manuscript in **Chapter 6** has been accepted for publication in *Journal of Applied Physics*.

Passivating contacts

As mentioned before, also parasitic absorption in the *a*-Si:H layers on the front side of the HIT cell limits the J_{sc} of the cell. As can be seen in Figure 8, *a*-Si:H mostly absorbs at higher photon energies. Holman *et al*. have quantified the losses induced by the *a*-Si:H layers: To a first order approximation, each nanometer of intrinsic and p-type *a*-Si:H result in a J_{sc} loss of 0.1 and 0.16 mA/cm^2, respectively. Typical thicknesses of the intrinsic and p-type *a*-Si:H layers are 5 and 10 nm, resulting in about 2.1 mA/cm^2 loss of photocurrent.[44] Similar as for ITO, also more transparent materials have emerged to replace the doped *a*-Si:H layer. Examples of such new materials include wider band

gap *p*-doped silicon oxides and carbides, sometimes combined with a microcrystalline structure to both improve the doping efficiency and the transparency due to the indirect bandgap. [45,46,47] However, from a physics point of view these materials are not that different from *a*-Si:H(*p*), since they also rely on *p*-type doping for achieving carrier-selectivity.

Figure 4 shows more fundamentally different heterojunction concepts that have appeared since the start of this project. Examples include heterojunctions based on metal oxides (MoO$_x$ and TiO$_2$), polymers (PEDOT) and the Tunnel Oxide Passivated Contact (TOPCon) cell.[§] These concepts are often referred to as *passivating contacts*, and as can be seen, these cell concepts have already made it (close) to the very high-efficiency segment within a few years' time.

Interestingly, these new heterojunctions all emerged around the same time. Although the reason for this is hard to pinpoint, to the author's feeling the acceptance of a new way of thinking about solar cells in the last few years has played a large role in this. Historically, Si solar cells were mostly described by semiconductor physics terms such as built-in voltage and space charge region. Although these have been successful in describing homojunction cells, they more or less lose their meaning when it comes to heterojunctions. Another way of thinking that facilitates talking about heterojunction contacts (as well as homojunctions) was advocated by Peter Würfel and is described in his book "Physics of Solar Cells". The author was lucky enough to meet him and attend his lectures at the Quantsol summer school in 2013. Although a full treatise of his approach is beyond the scope of this introductory chapter, the most important elements have been summarized in Figure 7. For the full picture, the reader is encouraged to read the book itself, along with more recent publications by Uli Würfel (Peter's son) and Andres Cuevas [48], Koswatta *et al.* [49], and an overview paper from our own group. [50] Moreover, the thesis of Sjoerd Smit (a colleague from the FLASH project) provides a mathematical treatment of the various types of selective membranes. [51]

[§]These structures will be treated in more detail in the next chapter. Again, the curious reader can find schematics of such cells on page 24.
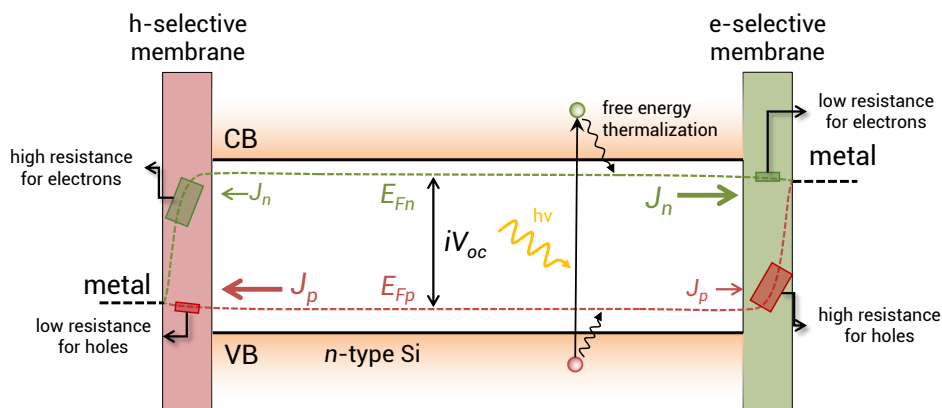
Figure 7: Schematic of the "Würfellian" picture of the physics of solar cells. The absorption of light leads to a non-equilibrium carrier distribution which necessitates the use of separate Fermi levels for electrons (E_{Fn}) and holes (E_{Fp}), as opposed to the single Fermi level E_F as used for a semiconductor in equilibrium. After excitation, the free energy of the carriers quickly thermalizes towards their quasi Fermi levels (as opposed to thermalization of electrostatic energy to the band edges in the classical view). The difference in free energy between the two Fermi levels is known as the implied V_{oc} ($_iV_{oc}$) and it is the gradients of these quasi-Fermi levels that are the thermodynamic driving force for both the electron (J_n) and hole currents (J_p). At either side of the solar cell, selective membranes are present that have a high asymetry in their conductivity for electrons and holes. In homojunctions and the HIT concept, this asymetry in conductivity is achieved by having highly doped Si. More novel concepts use asymetries in band offsets or differences in work function in order to achieve asymetric conduction towards the metal contact. Because of the difference in conductivities in the membrane, a voltage builds up between both metal contacts that can be used to extract work.

Among these new concepts, it was mostly MoO$_x$ that caught our attention early 2014: Battaglia *et al*. demonstrated that thermally evaporated MoO$_x$ can be used as an effective hole-selective material on c-Si in a c-Si/MoO$_x$/ITO stack.[20] MoO$_x$ relies on its high work function of $\sim$6.6 eV in order to fabricate a hole-selective contact. Although MoO$_x$ is much more transparent than *a*-Si:H(*p*) (see Figure 8), the initial cell reported only had an efficiency of 14.3% since its V_{oc} (580 mV) was mostly limited by the absence of a dedicated surface passivation layer.[¶] As can be seen in Figure 4, the efficiency of MoO$_x$-based heterojunctions has since then rapidly increased. Only three months after the initial report of Battaglia *et al*., the efficiency increased to 18.8%.[21] The key step was the insertion of a 10 nm *a*-Si:H(*i*) passivation layer in between the c-Si base and the evaporated MoO$_x$, which increased the V_{oc} to well above 700 mV. The next improvement to 22.5% was achieved by switching from screenprinted metal contacts which require thermal curing to room-temperature electro-deposited copper:[22] It was found that during the sputtering of the In$_2$O$_3$:H layer an intermixed MoO$_x$/In$_2$O$_3$:H layer forms. This mixing layer increases in thickness at temperatures >130°C, and is thought to be the

---

[¶]Or potentially, the contact was not *selective* enough, i.e. the MoO$_x$ did not induce a strong enough asymetry in the conductances for both charge carriers.

main cause for the observed *FF* degradation.
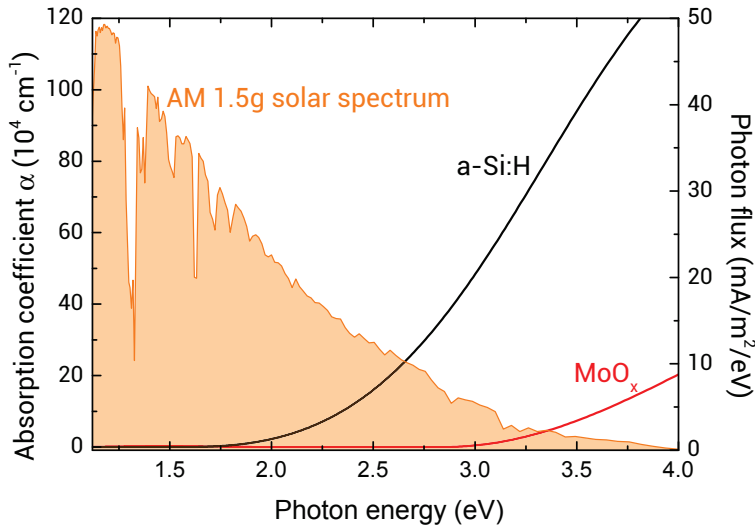
Figure 8: Absorption coefficients of *a*-Si:H and MoO$_x$. The AM1.5g solar spectrum has been added for reference.

Motivated by these promising results, we started to pursue the development of an ALD process for MoO$_x$. Since the MoO$_x$ layer is only a few nanometers thick and its performance is highly dependent on its thickness[21], it was thought that ALD would be highly suited for this application given its excellent thickness control. Since no good low-temperature (≤ 200 °C) thermal ALD processes were available, it was decided to develop a new O$_2$ plasma-based process using (N^{t}Bu)$_2$(NMe$_2$)$_2$Mo as molybdenum precursor. The ALD process itself as well as the material properties have been characterized in-depth. The ALD MoO$_x$ films were found to be amorphous from the lowest attempted deposition temperature of 50°C up to deposition temperatures of ∼250 °C. At higher temperatures, a transition from amorphous to polycrystalline growth was observed, which was accompanied by a strong increase in growth per cycle (GPC). The films were found to be slightly substoichiometric with a O/Mo ratio of ∼2.9 and the films were found to be free of impurities, besides for a hydrogen content of up to 11 at. %. These results were published in *Journal of Vacuum Science and Technology: A*[52] and can be found as **Chapter 7** in this dissertation.

After the development of the process, a front stack consisting of *a*-Si:H and ALD MoO$_x$ and ALD In$_2$O$_3$:H was made in order to assess the potential of the ALD materials for SHJ solar cells. Promisingly, a high level of passivation was achieved, as witnessed by the high $_iV_{oc}$ of 717 mV, and optical simulations of this stack showed a very promising J_{sc} of 41.7 mA/cm^2. In addition, TEM analysis showed a very sharp interface

between the ALD MoO_x and the ALD In_2O_3:H layer. The absence of layer intermixing between MoO_x and In_2O_3:H is potentially a strong point of the ALD approach over sputtering. These results have been published in *Rapid Research Letters*[53] and are included in **Chapter 8** in this dissertation.

In **Chapter 9**, the current status of the implementation of both the developed ALD In_2O_3:H and MoO_x films into actual solar cell devices will be discussed. A collaboration with ECN has been set up to implement ALD In_2O_3:H in their baseline silicon heterojunction cell, whereas a collaboration with Fraunhofer ISE has been set up to evaluate the potential of the ALD MoO_x layer as hole-selective contact. The current progress of the implementation as well as remaining challenges and possible pathways to resolve those challenges will be outlined. **Chapter 10** serves as a concluding chapter. A summary of the main outcomes of this project is given and follow-up research activities will be highlighted.

References

[1] Fraunhofer, ©Fraunhofer ISE: Photovoltaics Report (2016).

[2] V. Sivaram and S. Kann, Nature Energy **1**, 16036 (2016).

[3] K. Masuko, M. Shigematsu, T. Hashiguchi, D. Fujishima, M. Kai, N. Yoshimura, T. Yamaguchi, Y. Ichihashi, T. Mishima, N. Matsubara, T. Yamanishi, T. Takahama, M. Taguchi, E. Maruyama, and S. Okamoto, IEEE Journal of Photovoltaics **4**, 1433 (2014).

[4] C. Battaglia, A. Cuevas, and S. De Wolf, Energy Environ. Sci. (2016), 10.1039/C5EE03380B.

[5] Z. Wang, P. Han, H. Lu, H. Qian, L. Chen, Q. Meng, N. Tang, F. Gao, Y. Jiang, J. Wu, W. Wu, H. Zhu, J. Ji, Z. Shi, A. Sugianto, L. Mai, B. Hallam, and S. Wenham, Progress in Photovoltaics: Research and Applications **20**, 260 (2012).

[6] M. A. Green, Solar Energy Materials and Solar Cells **143**, 190 (2015).

[7] J. John, L. Tous, F. Duerinckx, and N. Posthuma, Presented at the 2013 nPV workshop (2014).

[8] F. Duerinckx, M. Aleman, P. Choulat, L. Tous, M. Recaman, A. Uruena, R. Russell, I. Kuzma-Filipek, M. Haslinger, J. John, E. Cornagliotti, T. Bearda, S. Granata, J. Szlufcik, B. Hallam, J. Chen, S. Martin de Nicolas, S. De Wolf, and C. Ballif, Presented at the 2014 nPV workshop (2014).

[9] M. Taguchi, Y. Tsunomura, H. Innoue, T. Taira, T. Nakashima, T. Baba, H. Sakata, and E. Maruyama, Proceedings of the 24th European PVSEC, Hamburg , 1690 (2009).

[10] T. Kinoshita, D. Fujishima, A. Yano, S. Ogane, S. Tohoda, K. Matsuyama, Y. Nakamura, N. Tokuoka, H. Kanno, H. Sakata, M. Taguchi, and E. Maruyama, Proceedings of the 26th European Photovoltaic Solar Energy Conference, Hamburg , 871 (2011).

[11] M. Taguchi, A. Yano, S. Tohoda, K. Matsuyama, Y. Nakamura, T. Nishiwaki, K. Fujita, and E. Maruyama, IEEE Journal of Photovoltaics **4**, 96 (2014).

[12] D. Adachi, J. L. Hernández, and K. Yamamoto, Applied Physics Letters **107**, 233506 (2015).

[13] F. Feldmann, M. Bivour, C. Reichel, M. Hermle, and S. W. Glunz, Solar Energy Materials and Solar Cells **120**, 270 (2014).

[14] F. Feldmann, M. Bivour, C. Reichel, H. Steinkemper, M. Hermle, and S. W. Glunz, Solar Energy Materials and Solar Cells **131**, 46 (2014).

[15] A. Moldovan, F. Feldmann, M. Zimmer, J. Rentsch, J. Benick, and M. Hermle, Solar Energy Materials and Solar Cells , 1 (2015).

[16] S. W. Glunz, F. Feldmann, A. Richter, M. Bivour, C. Reichel, H. Steinkemper, J. Benick, and M. Hermle, Presented at the 31st European Photovoltaic Solar Energy Conference and Exhibition (2015).

[17] J. Schmidt, V. Titova, and D. Zielke, Applied Physics Letters **103**, 183901 (2013).

[18] D. Zielke, A. Pazidis, F. Werner, and J. Schmidt, Solar Energy Materials and Solar Cells **131**, 110 (2014).

[19] D. Zielke, C. Niehaves, W. Lövenich, A. Elschner, M. Hörteis, and J. Schmidt, Energy Procedia **77**, 331 (2015).

[20] C. Battaglia, X. Yin, M. Zheng, I. D. Sharp, T. Chen, S. McDonnell, A. Azcatl, C. Carraro, B. Ma, R. Maboudian, R. M. Wallace, and A. Javey, Nano letters **14**, 967 (2014).

[21] C. Battaglia, S. M. de Nicolás, S. De Wolf, X. Yin, M. Zheng, C. Ballif, and A. Javey, Applied Physics Letters **104**, 113902 (2014).

[22] J. Geissbühler, J. Werner, S. Martin de Nicolas, L. Barraud, A. Hessler-Wyser, M. Despeisse, S. Nicolay, A. Tomasi, B. Niesen, S. De Wolf, and C. Ballif, Applied Physics Letters **107**, 081601 (2015).

[23] S. Avasthi, W. E. McClain, G. Man, A. Kahn, J. Schwartz, and J. C. Sturm, Applied Physics Letters **102**, 203901 (2013).

[24] X. Yang, P. Zheng, Q. Bi, and K. Weber, Solar Energy Materials and Solar Cells **150**, 32 (2016).

[25] X. Yang, Q. Bi, H. Ali, K. Davis, W. V. Schoenfeld, and K. Weber, Advanced Materials **28**, 5891 (2016).

[26] S. De Wolf, A. Descoeudres, Z. C. Holman, and C. Ballif, Green **2**, 7 (2012).

[27] M. Tanaka, M. Taguchi, T. Matsuyama, T. Sawada, S. Tsuda, S. Nakano, H. Hanafusa, and Y. Kuwano, Japanese Journal of Applied Physics **31**, 3518 (1992).

[28] S. Y. Herasimenka, W. J. Dauksher, and S. G. Bowden, Applied Physics Letters **103**, 053511 (2013).

[29] B. Demaurex, S. De Wolf, A. Descoeudres, Z. C. Holman, and C. Ballif, Applied Physics Letters **101**, 171604 (2012).

[30] J. A. van Delft, D. Garcia-Alonso, and W. M. M. Kessels, Semiconductor Science and Technology **27**, 074002 (2012).

[31] G. Dingemans and W. M. M. Kessels, Journal of Vacuum Science & Technology A: Vacuum, Surfaces, and Films **30**, 040802 (2012).

[32] Y. Wu, P. M. Hermkens, B. W. H. van de Loo, H. C. M. Knoops, S. E. Potts, M. A. Verheijen, F. Roozeboom, and W. M. M. Kessels, Journal of Applied Physics **114**, 024308 (2013).

[33] Y. Wu, S. E. Potts, P. M. Hermkens, H. C. M. Knoops, F. Roozeboom, and W. M. M. Kessels, Chemistry of Materials **25**, 4619 (2013).

[34] D. Garcia-Alonso, S. E. Potts, C. A. A. van Helvoirt, M. A. Verheijen, and W. M. M. Kessels, J. Mater. Chem. C **3**, 3095 (2015).

[35] B. Macco, D. Deligiannis, S. Smit, R. A. C. M. M. van Swaaij, M. Zeman, and W. M. M. Kessels, Semiconductor Science and Technology **29**, 122001 (2014).

[36] B. Demaurex, J. P. Seif, S. Smit, B. Macco, W. M. M. Kessels, J. Geissbuhler, S. De Wolf, and C. Ballif, IEEE Journal of Photovoltaics **4**, 1387 (2014).

[37] R. Rößler, C. Leendertz, L. Korte, N. Mingirulli, and B. Rech, Journal of Applied Physics **113**, 144513 (2013).

[38] Z. C. Holman, M. Filipič, A. Descoeudres, S. De Wolf, F. Smole, M. Topič, and C. Ballif, Journal of Applied Physics **113**, 013107 (2013).

[39] T. Koida, M. Kondo, K. Tsutsumi, A. Sakaguchi, M. Suzuki, and H. Fujiwara, Journal of Applied Physics **107**, 033514 (2010).

[40] L. Barraud, Z. C. Holman, N. Badel, P. Reiss, A. Descoeudres, C. Battaglia, S. De Wolf, and C. Ballif, Solar Energy Materials and Solar Cells **115**, 151 (2013).

[41] J. A. Libera, J. N. Hryn, and J. W. Elam, Chemistry of Materials **23**, 2150 (2011).

[42] B. Macco, Y. Wu, D. Vanhemel, and W. M. M. Kessels, physica status solidi (RRL) - Rapid Research Letters **8**, 987 (2014).

[43] B. Macco, H. C. M. Knoops, and W. M. M. Kessels, ACS Applied Materials & Interfaces **7**, 16723 (2015).

[44] Z. C. Holman, A. Descoeudres, L. Barraud, F. Z. Fernandez, J. P. Seif, S. De Wolf, and C. Ballif, IEEE Journal of Photovoltaics **2**, 7 (2012).

[45] J. Peter Seif, A. Descoeudres, M. Filipič, F. Smole, M. Topič, Z. Charles Holman, S. De Wolf, and C. Ballif, Journal of Applied Physics **115**, 024502 (2014).

[46] T. Mueller, S. Schwertheim, M. Scherff, and W. R. Fahrner, Applied Physics Letters **92**, 033504 (2008).

[47] T. Mueller, S. Schwertheim, K. Meusinger, B. Wdowiak, R. Klimkeit, W. R. Fahrner, E. D. Lgbe, and H. Str, in *2009 34th IEEE Photovoltaic Specialists Conference (PVSC)* (IEEE, 2009) pp. 002378–002382.

[48] U. Wurfel, A. Cuevas, and P. Wurfel, IEEE Journal of Photovoltaics **5**, 461 (2015).

[49] P. Koswatta, M. Boccard, and Z. Holman, 2015 IEEE 42nd Photovoltaic Specialist Conference (PVSC) , 1 (2015).

[50] J. Melskens, B. W. H. van de Loo, B. Macco, M. F. J. Vos, J. Palmans, S. Smit, and W. M. M. Kessels, in *2015 IEEE 42nd Photovoltaic Specialist Conference (PVSC)*, June (IEEE, 2015) pp. 1–6.

[51] S. Smit, *Passivating selective contacts for silicon photovoltaics: Solar cells designed by physics*, Ph.D. thesis (2016).

[52] M. F. J. Vos, B. Macco, N. F. W. Thissen, A. A. Bol, and W. M. M. Kessels, Journal of Vacuum Science & Technology A: Vacuum, Surfaces, and Films **34**, 01A103 (2016).

[53] B. Macco, M. F. J. Vos, N. F. W. Thissen, A. A. Bol, and W. M. M. Kessels, physica status solidi (RRL) – Rapid Research Letters **9**, 393 (2015)

2

Atomic Layer Deposition for High Efficiency Crystalline Silicon Solar Cells

2.1 Introduction to high-efficiency crystalline silicon solar cells

At present, crystalline silicon (Si) solar cells are being mass-produced at a typical rate of 43 GWp/year, and they dominate the photovoltaic (PV) market with a share of >90%.[1] The success of Si solar cells over other solar cell technologies lies in their ever improving cost-effectiveness. In fact, the Si solar cells themselves are not even the main contributor to the total cost of solar electricity anymore.[1] Because of this, higher conversion efficiencies have become the main driver for a further cost reduction of solar electricity. As is the case for most semiconductor devices, also for Si solar cells a precise engineering of interfaces has proven to be key in achieving optimal device performance and consequently higher conversion efficiencies. For instance, by reducing the interface defect density of Si by a thin passivation layer of Al_2O_3, the efficiency of Si solar cells could significantly be enhanced. It was for this particular application that the potential of atomic layer deposition (ALD) for Si solar cells was for the first time revealed in 2004.[2] Due to the development of novel high-throughput ALD reactors, ALD of Al_2O_3 has

since then even found its way to the high-volume manufacturing (HVM) of Si solar cells. Today, Al_2O_3 nanolayers prepared by ALD can account for a $\sim$1% absolute increase in conversion efficiency of commercial solar cells and they are incorporated in solar cells with record efficiencies of >25% on a lab scale.[3] In a broader context, the success of ALD Al_2O_3 also triggered the exploration of ALD for the preparation of other functional layers for a variety of commercial solar cells. For example ALD is used for the deposition of transparent conductive oxides (TCOs). TCOs should be simultaneously transparent and conductive, and therefore should have a high electron mobility. It turns out that ALD is well suited for the deposition of such films, as is for instance evident from ALD TCOs with record-high electron mobilities of 138 cm^2/Vs.[4] This chapter will illustrate that ALD is in fact an enabler of novel high-efficiency Si solar cells, owing to its (unique) merits such as a high material quality, precise thickness control and the ability to prepare film stacks in a well-controlled way. In the remainder of this section, a brief overview of the field of Si solar cells is given, where for each concept the present and potential role of ALD is discussed.

In short, a solar cell can deliver power when excess electrons and holes, created by the absorption of light in the semiconductor, are extracted separately by electrodes. To enable this, the two types of electrodes should be made selective for the extraction of only electrons or holes. Commonly, Si solar cells are classified by the type of junction which is formed in the creation of such carrier selective contacts. Based on such classification, in Figure 1, a concise overview of the most common Si solar cell concepts is given. Note that each individual concept will be discussed in more detail below. The first class of solar cells (which is industrially by far the most used) is based on homojunctions, which are formed by doping separate regions of the Si, making them strongly n or p-type (also referred to as n^+ or p^+ Si). In this way, the metal electrode which contacts the n^+ or p^+ Si is made selective for the extraction of either electrons or holes, respectively. Heterojunctions, which are junctions between Si and other materials, are also used to achieve such charge-carrier selectivity. Interestingly, for all these types of cells, i.e., whether involving homojunctions, heterojunctions, or a combination of both, record conversion efficiencies over 25% have been demonstrated on a lab scale.[3,5,6,7,8] Although such efficiencies are already close to the predicted fundamental limit of 29.4% for Si solar cells,[9] research efforts are still ongoing to attain more cost-effective approaches for the high-volume manufacturing of such cells in industry.

2.1.1   ALD for Si homojunction solar cells

The current workhorse of the PV industry is the aluminium back-surface field (Al-BSF) solar cell which is based on p-type Si (see Figure 1). It typically yields moderate conver-

sion efficiencies of 19-20% and can be manufactured very cost-effectively. On the front side, an n^+ Si region is present (conventionally termed an 'emitter'), which makes the front contacts selective for the extraction of electrons. Moreover, the n^+ Si also serves as lateral conduction pathway for electrons to the front contact grid. In between the metal contacts, hydrogenated amorphous silicon nitride, a-SiN$_x$:H (also referred to as SiN$_x$) is typically present as anti-reflection coating (ARC). Additionally, the SiN$_x$ reduces electron-hole recombination at the Si surface, which is referred to as surface passivation. The latter is vital to achieve a high open-circuit voltage, V_{oc}, and hence a high solar cell efficiency. At the full back side of the Al-BSF solar cell, Al is screen-printed and subsequently (partially) alloyed with the Si by a high temperature "firing" step at 800 °C. In this way, Al contacts Al-doped (p^+-type) Si, and a hole-selective contact is formed. In the Al-BSF concept, generally no layers are prepared by ALD.

A more advanced concept, which is still industrial but allows for higher conversion efficiencies, is the so-called passivated emitter rear contact (PERC) solar cell. Instead of using Al over the full area (as is the case for the Al-BSF cell), it uses local Al contacts at the rear side. In this way, the Si surface in between the contacts can be passivated by a thin film, which reduces charge carrier recombination and in this way enhances the conversion efficiency. In the last decade, ALD of Al$_2$O$_3$ has been proven to be very successful for the passivation of this lowly-doped p-type Si back surface, and this application even paved the way for ALD for implementation in solar cell manufacturing.

Besides reducing charge-carrier recombination at the Si back surface, the recombination via defects in the Si bulk should also be minimized to attain high conversion efficiencies. For instance, rather than the low-cost multicrystalline Si, which has defects at its grain boundaries, more expensive monocrystalline Si wafers can be used. Also n-type Si wafers can be used instead of the conventionally used p-type Si wafers, as they generally have a higher bulk material quality due to e.g., the absence of boron-oxygen defects. Therefore, n-type cell concepts compete with (p-type) PERC concepts for a spot in the high efficiency segment. Most solar cells based on n-type Si require p-type doping of the full Si front surface (such a cell is not shown in Figure 1). For a long time, this approach was considered to be challenging, in part due to a lack of a suitable passivation scheme for p^+ Si. Also for the passivation of these p^+ Si surfaces, Al$_2$O$_3$ prepared by ALD resulted in a breakthrough, yielding solar cell conversion efficiencies of up to 23.2% at that time.[10]

Finally, even higher efficiencies can in principle be obtained by using interdigitated back-contact (IBC) cell concepts,[6] albeit at the price of requiring more processing steps. In IBC concepts, the electron- as well as the hole-selective contacts are localized at the back side to avoid parasitic absorption and reflection by front metallization. Also for IBC solar cells, ALD layers are being investigated, for instance to passivate defects at

Homojunction-based c-Si solar cells

SiN$_x$

c-Si(p)

n^+ Si

Al-BSF

Al

Al-BSF cell
- Mass-produced
- No ALD
- Cell efficiency ~16-20%

High efficiency homojunctions cells:
- ALD for surface passivation (Al$_2$O$_3$, SiO$_2$)

SiN$_x$

c-Si(p)

Al$_2$O$_3$/SiN$_x$

n^+ Si

Local BSF

Al

PERC/PERL
23.9%

SiN$_x$

SiO$_2$/SiN$_x$

n^+ Si

p^+ n^+ n^+ p^+

Interdigitated back contact (IBC)
25%

Silicon heterojunction cells:
- ALD for TCOs

Heterojunction-based c-Si solar cells

TCOs: **In$_2$O$_3$:H, IZO**

c-Si(n)

a-Si:H (i/p)
a-Si:H (i/n)

TCOs: **doped ZnO**

Panasonic HIT
24.7%

SiN$_x$

c-Si(n)

a-Si:H(n)

a-Si:H(p)

Passivation
layer

IBC-SHJ
25.6%

Novel heterojunctions/passivating contacts
- ALD for TCOs, tunnel oxides and carrier-selective oxides

Al$_2$O$_3$/SiN$_x$

c-Si(n)

SiO$_2$ tunnel oxide

p^+ Si

n^+ poly-Si

Al

TOPCon
25.1 %

TCOs: **In$_2$O$_3$:H, IZO**

Passivating
tunnel oxides
SiO$_2$, Al$_2$O$_3$, HfO$_2$

h-selective oxides
MoO$_x$, WO$_x$, VO$_x$

c-Si(n)

e-selective oxides: **TiO$_2$**, ...

Al

Metal-oxide based
passivating contact cell (MoO$_x$: 22.5%)

Figure 1: Various silicon solar cell concepts and their current record efficiencies (January 2016). Note that these efficiencies might be several percent absolute lower when produced industrially. The first class of cells is based on homojunctions, the second class on heterojunctions. The functional thin films which could be prepared by ALD are indicated in bold.

the n^+ or p^+ Si surfaces at the back side of the solar cell simultaneously. [11]

2.1.2 ALD for Si heterojunction solar cells

A radically different solar cell design, which has successfully been developed by Panasonic (formerly Sanyo), is the heterojunction with intrinsic thin layer (HIT^{TM}), [12] generally referred to as the silicon heterojunction (SHJ) concept. Here, intrinsic and doped hydrogenated amorphous Si (*a*-Si:H) layers are used for the passivation of the Si surfaces and to achieve selectivity for the extraction of charge carriers, respectively. For conventional Si homojunction solar cells, the lateral conduction of excess charge carriers towards the metal grid takes place via the highly-doped regions. However, in SHJ cells, such regions are absent, which is why TCOs are used on both sides of the SHJ cell. In fact, TCOs prepared by ALD can fulfil the stringent requirements set by the SHJ cells in terms of processing (e.g., a low deposition temperature <200 °C, and soft deposition) as well as in material quality (e.g., high conductivity and transparency and a suitable workfunction). Despite its high potential, ALD is not yet implemented in HVM for this application. Nonetheless, the deposition of TCOs in industrial ALD reactors has already been achieved. [13]

The discrepancy between the maximal efficiency for conventional SHJ cells (25.1% [14]) and the fundamental limit of Si solar cells (i.e., 29.4% [9]) is partially attributed to the parasitic absorption or reflection by the front *a*-Si:H layers and the TCO. This can be overcome in several ways. For instance, by using an IBC SHJ concept, no front TCO is required and the *a*-Si:H layers are only used at the back side. In this way, the current world record efficiency for silicon solar cells of 25.6% has been achieved by Panasonic. [7] It is not disclosed at this moment whether ALD is used in this concept.

2.1.3 Novel passivating contacts and ALD

Due to the limit in processing temperature which can be a challenge for HVM and due to parasitic absorption of *a*-Si:H based heterojunction cells, research efforts are also targeting other types of materials that make the electrodes carrier-selective. These are generally referred to as passivating contacts. For example, a novel passivating contact approach is the tunnel oxide passivated contact (TOPCon). It has excellent thermal stability and so far has reached an conversion efficiency of 25.1%. [3] TOPCon is in fact a hybrid cell design, as on the front a classical homojunction is formed, which is passivated by Al_2O_3, whereas at the full back side a highly-doped (partially) crystalline Si passivating contact forms a heterojunction. The contact is made selective to extract either electrons or holes by the choice of dopant. Moreover, a very thin, passivating tunnel oxide at the interface between Si and the partially crystalline Si is key in achieving

the high conversion efficiencies.[15] Conceivably, the precise thickness control offered by ALD can play a key role in studying and optimizing the often encountered trade-off between surface passivation and contact resistance in passivating contacts.

Interestingly, there is also increasing interest in novel heterojunctions based on metal-oxides as passivating contacts. Preferably, they are fully transparent, in contrast to partially crystalline Si and *a*-Si:H. If such a passivating contact can be used on the full area of the solar cell, they could yield a significant process simplification. Metal oxides of interest include for example MoO_x[16], WO_x[17], NiO_x[18], and TiO_2[19], for which ALD processes readily exist and are also being explored.[20] Also well-defined stacks of metal oxides or other materials can be used, which provide surface passivation, carrier selectivity as well as lateral conduction.[21,22] Potentially, such stacks could find their way into novel silicon solar cell concepts, allowing for very high conversion efficiencies in combination with cost-effective manufacturing.

2.1.4   Outline of this chapter

The chapter is organized as follows. In section 2.2, the role of ALD in preparing passivation layers for homojunction Si solar cells is discussed. Special attention is given to the physics of surface passivation, the surface passivation by ALD Al_2O_3, ALD as a high-throughput deposition technique in the PV industry and recent developments in the field of passivation layers prepared by ALD. Section 2.3 focuses on TCOs prepared by ALD for use in heterojunction Si solar cells, such as doped ZnO and In_2O_3 films. Therefore, the physics of TCOs and the specific requirements of TCOs for SHJ cells are briefly discussed first. Finally, in section 2.4, novel passivating contacts based on metal oxides are considered. Various unique aspects of ALD, such as the ability to prepare precisely tailored stacks play an important role here.

2.2 Nanolayers for surface passivation of Si homojunction solar cells

In this section, the status-quo and opportunities for ALD passivation layers for Si homo-junction solar cells are discussed. First, the physical mechanisms of surface recombi-nation and the basics of surface passivation are treated. Next, an overview of ALD Al_2O_3, which is widely used for the passivation of p and p^+-type surfaces, is given. Moreover, also the requirements for deposition techniques in the high-volume manufacturing of silicon solar cells in industry are discussed together with novel high-throughput ALD reactors. In the last section, further opportunities and recent developments in the field of ALD for the passivation of Si are outlined. Examples include ALD layers for the pas-sivation of n^+ Si, the passivation of surfaces with demanding topologies and recent developments of novel, alternative passivation layers prepared by ALD.

2.2.1 Basics of surface passivation

The physics of surface recombination

By the absorption of light in Si, excess electrons and holes are created (see Figure 2), with densities Δn and Δp, respectively, which increases their respective densities n and p from their equilibrium values n_0 and p_0 to $n = n_0 + \Delta n$ and $p = p_0 + \Delta p$. After generation, the excess charge carriers thermalize very rapidly (i.e., in $\sim 10^{-12}$ s) to the temperature of the Si lattice, T. Rather than by a single Fermi energy level, E_F, which is used to describe semiconductors in the dark, under illumination the distributions of electrons and holes can be described by their own quasi-Fermi energies, E_{Fn} and E_{Fp}. Also here, the carrier densities are still given by the energetic distance of the quasi Fermi level to the conduction and valence band, respectively. For Boltzmann statistics, the pn product is given by;

$$pn = (p_0 + \Delta p)(n_0 + \Delta n) = n_i^2 \exp\left(\frac{E_{Fn} - E_{Fp}}{kT}\right) \tag{2.1}$$

With n_i the intrinsic carrier density and k the Boltzmann constant. The free energy per electron hole pair is E_{Fn} - E_{Fp} , and corresponds to the implied voltage $_iV_{oc}$ in the cell, i.e., $E_{Fn} - E_{Fp} = q_iV_{oc}$ with q the elementary charge. The quasi-Fermi level splitting in-duced by the generation of charge carriers is also the driver of processes which tend to restore thermodynamic equilibrium. In such processes excess charge carriers recom-bine and their associated free energy is lost. To a certain extent this recombination is unavoidable, because of intrinsic channels, which are direct (radiative) and Auger re-combination. In these processes, the energy is transferred to a photon and/or phonons

or a third carrier, respectively. Also recombination via extrinsic lattice defects or impurities which form states in the band gap of Si can take place, a pathway which is named after Shockley, Read, and Hall (SRH) who formulated the theory describing this kind of recombination. In particular at the surface, as the silicon lattice terminates, a high density of Si dangling bonds is natively present, which form defect levels (e.g., P_{b0} defects) and therefore induce strong SRH recombination.
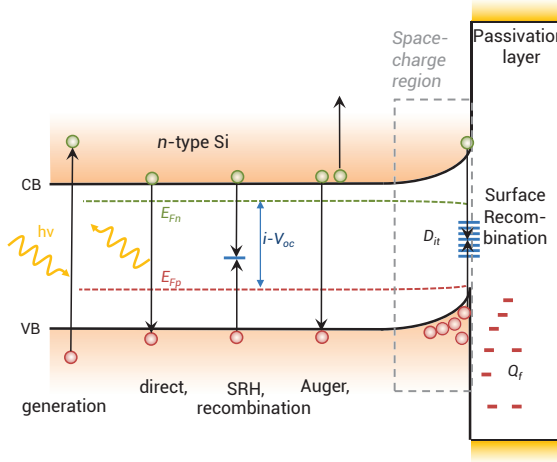
Figure 2: Schematic band diagram of the passivated silicon surface, indicating the generation of excess carriers by the absorption of light and the recombination thereof, which can take place either directly, via a third carrier (in the Auger process) or via interface defect states (SRH recombination). At the surface, a high density of interface (defect) states D_{it} exists. A passivation layer reduces the D_{it}, and (in this example) reduces the electron concentration at the surface via a negative fixed charge density Q_f, which induces a space-charge region and upwards band-bending.

The recombination rate of charge carriers at the surface U_s (with units $\mathrm{cm^{-2}s^{-1}}$) can be described via the extended SRH formalism, which considers a continuum of defects throughout the band gap of Si, with energy-dependent density, $D_{it}(E)$;

$$U_s = (p_s n_s - n_{i,eff,s}^2) \int_{E_g} \frac{dE}{\frac{n_s + n_1(E)}{S_{p0}(E)} + \frac{p_s + p_1(E)}{S_{n0}(E)}} \tag{2.2}$$

with $S_{n0} = v_t D_{it}(E)\sigma_n(E)$ and $S_{p0} = v_t D_{it}(E)\sigma_p(E)$. In these expressions, v_t is the thermal velocity, $n_{i,eff,s}$ the *effective* intrinsic carrier concentration at the surface (taking into account band gap narrowing and Fermi-Dirac statistics), n_s and p_s the electron and hole concentrations at the surface, $\sigma_n(E)$ and $\sigma_p(E)$ the (energy-dependent) hole or electron capture cross sections respectively, which are directly related to the physical processes of carrier capture by the defect states. The SRH densities n_1 and p_1, given by

$n_1 = N_c\exp\left(-\frac{E_C-E_t}{kT}\right)$, $p_1 = N_v\exp\left(\frac{E_V-E_t}{kT}\right)$, determine the effectiveness of the defects as recombination sites, where E_t the energy level of the defect and N_C and N_V the effective density of states of the conduction and valence band, respectively. In particular defects near the center of the band gap of Si are most effective as recombination sites. Also when the capture rate of electrons by a defect equals the capture rate of holes, i.e., when the following condition is satisfied:

$$\sigma_p \times p_s \approx \sigma_n \times n_s \qquad (2.3)$$

the defect is most effective as a recombination site.

Even though U_s is the main physical parameter which should be minimized, it is experimentally not directly accessible. For this reason, other figures of merit are usually used to assess the surface recombination (see Table 1), such as the effective minority carrier lifetime τ_{eff} or the implied open circuit voltage $_iV_{oc}$, which are both ideally as high as possible. However, both these parameters also include the influence of other recombination processes, such as those in the bulk of Si. To quantify only the surface recombination, the effective surface recombination velocity S_{eff} or surface saturation current density J_{0s} can be evaluated.[23,24] The latter parameter J_{0s} (with units Acm^{-2}) offers the advantage that it (for flat quasi-Fermi levels) directly translates to the open-circuit voltage V_{oc} of the solar cell via:

$$V_{oc} = \frac{nkT}{q}\ln\left(\frac{J_{sc}}{J_{0s} + J_{0,others}} + 1\right) \qquad (2.4)$$

with n the ideality factor, J_{sc} the short-circuit current density and $J_{0,others}$ a parameter accounting for other recombination pathways, such as in the Si bulk. Due to the large surface-to-volume ratio in Si solar cells, the surface can be the dominant recombination source. With current trends toward thinner or higher quality Si wafers, bulk recombination is further reduced, making surface recombination even more important.

Surface passivation

To minimize surface recombination, several strategies can be used. First of all, the D_{it} which is natively present can be reduced by orders of magnitude by several approaches, which is referred to as chemical passivation. Chemical passivation can be obtained by depositing a thin film on the silicon surface, which binds to the Si dangling bonds. Moreover, (atomic) hydrogen released from the passivation scheme or forming gas in

Table 1: A selection of commonly used parameters to assess surface passivation quality. Some parameters not only account for recombination at the surface, but also encompass recombination in the highly-doped region (HDR), in the Si bulk or in the space-charge region (SCR) induced in the Si by the passivation scheme. The parameters are evaluated with respect to their average carrier densities in the Si bulk (n, p), the densities at the surface (n_s, p_s), the edge of the SCR (n_d, p_d), or the base side of the HDR (n_w, p_w). They can be assessed by photoconductance (PC), photoluminescence (PL), current-voltage (J-V) or Suns-V_{oc} measurements.

Parameter	Symbol	Encompasses recombination in or at the Si	Assessed by	Definition
Effective minority carrier lifetime	τ_{eff}	Bulk, HDR, SCR, surface	PC, PL	$\tau_{eff} \equiv \dfrac{\Delta n}{U_{(total)}}$
Surface recombination velocity (SRV)	S	Surface	*Inaccessible (in most cases)*	$S \equiv \dfrac{U_s}{\Delta n_s}$
Effective surface recombination velocity	S_{eff}	Surface, SCR	PC, PL	$S_{eff} \equiv \dfrac{U_s}{\Delta n_d}$
Implied open-circuit voltage	i-V_{oc}	Bulk, HDR, SCR, surface	PC, PL	$i\text{-}V_{OC} \equiv \dfrac{kT}{q}\ln\left(\dfrac{np}{n_i^2}\right)$
Surface saturation current density	J_{0s}	Surface	PC, PL	$J_{0s} \equiv qU_s\left(\dfrac{p_s n_s}{n_{i,eff,s}^2} - 1\right)^{-1}$
("Emitter") Saturation current density	J_{0e}, J_0	HDR, SCR, surface	PC, PL, J-V, Suns-V_{oc}	$J_{0e} \equiv qU_{HDR-surface}\left(\dfrac{p_w n_w}{n_{i,eff,w}^2} - 1\right)^{-1}$

a post deposition anneal (PDA) can subsequently passivate remaining defects. The most prominent examples of materials used for surface passivation of solar cells include thermally grown SiO_2 [25], plasma-enhanced chemical vapor deposited (PECVD) SiN_x [26], PECVD *a*-Si:H and ALD Al_2O_3. [27,28] Naturally, to achieve chemical passivation, the passivation layers should also exhibit few states at energy levels which are relevant for charge carrier-recombination in Si. For this reason, materials with a wide band gap and low impurity content are most successful. Metals on the contrary have a large and continuous distribution of states and therefore act as catalyst for carrier recombination when brought in contact with Si.
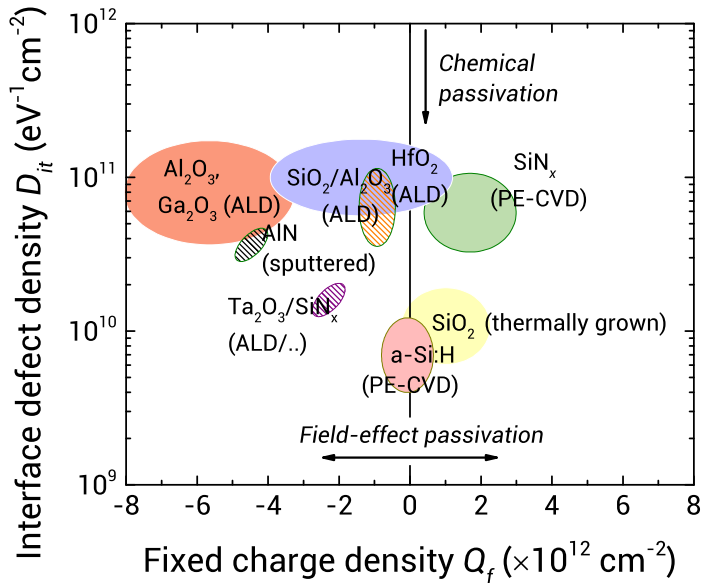
Figure 3: Schematic overview of typical interface defect densities and fixed charge densities of passivation schemes, adapted from Cuevas *et al*. [29] Note that the actual interface properties might strongly depend on the processing conditions of the passivation layer.

Another strategy to reduce surface recombination is the suppression of either the electron or hole concentration at the surface (see equation 2.2). Such suppression can be achieved via band bending in the Si, for instance by a fixed charge density Q_f in the passivation layer, and is commonly known as field-effect passivation. Thermally-grown SiO_2 natively possesses a slight positive $Q_f \sim 10^{11}$ cm^{-2}, SiN_x a strong positive Q_f (typically $\sim 3 \times 10^{12}$ cm^{-2}) whereas ALD Al_2O_3 films typically exhibit a strong negative Q_f ($\sim 10^{12}$–10^{13} cm^{-2}). [30] In Figure 3, a schematic overview of interface properties of various passivation schemes is given.

Naturally, the carrier densities at the Si surface are, besides band bending, also largely

dictated by the (local) doping level of the silicon N_s. The polarity of the fixed charge density in the dielectric is of importance when passivating doped surfaces, as the Q_f can either further reduce or increase the minority carrier density, and in this way has a strong influence on the surface recombination. For instance for heavily p-type doped surfaces (p^+ Si), electrons are the minority carriers. The passivation scheme for such surface therefore ideally has a negative Q_f to reduce the electron concentration even further. For n^+ Si surfaces on the other hand, electrons are the majority carriers and their density is not reduced significantly by a negative Q_f. Even worse, the negative Q_f increases the minority carrier density which increases surface recombination.

To further illustrate the effect of the doping level and fixed charge density on the surface recombination, in Figure 4 the SRH equation is evaluated for a fixed level of chemical passivation. Interestingly, for very high doping levels (i.e., $N_s > 10^{20}$ cm^{-3}), the density and polarity of fixed charges in the range evaluated here have virtually no influence on the surface recombination, which is low in all cases. For lower N_s (i.e., in the range of $\sim 10^{20}$ cm^{-3} or lower) the condition where the SRH recombination is the strongest (equation 2.3) is met, but only when a passivation layer with the 'wrong' charge polarity is used. Explicitly put, a high J_{0s} arises for a negative Q_f on n^+ -type Si or for positive Q_f on p^+ Si surfaces. Finally, for lower N_s (i.e., $N_s < 10^{18}$ cm^{-3}), the passivation quality is excellent, even in case of a 'wrong' charge polarity. In that case, the band bending induced by the fixed charge density brings the Si surface into inversion. Even though in that case the surface can be very well passivated, inversion layers are still undesirable in most solar cells. It is shown that they can form parasitic shunt pathways and possibly induce SRH recombination in the depletion region which is formed near the surface, having an adverse impact on the efficiency of solar cells.[31,32] In summary, it can be stated that for passivation schemes a low D_{it} is always preferred, whereas in general the ideal Q_f depends on the surface doping concentration of the Si. Methods to control the Q_f of ALD passivation schemes will be discussed in section 2.2.4.

Finally, it should be noted that in case of very strong surface recombination, such as for poorly passivated surfaces or when metal is contacting Si, the surface recombination rate becomes limited by the transport of excess charge carriers towards the surface. In this case, the presence of a highly-doped (p^+ or n^+ Si) region can significantly reduce the transport of excess carriers towards the surface and in this way reduce recombination. Well-known examples are the p^+ Si and n^+ Si regions of Si homojunction solar cells (see Figure 1), which 'shield' the metal contacts and make them selective for the extraction of only one charge carrier type. For well-passivated surfaces on the other hand, the transport of minority carriers through the highly-doped region is generally not limiting or affecting the surface recombination rate. Then, the highly-doped region is called *transparent*.
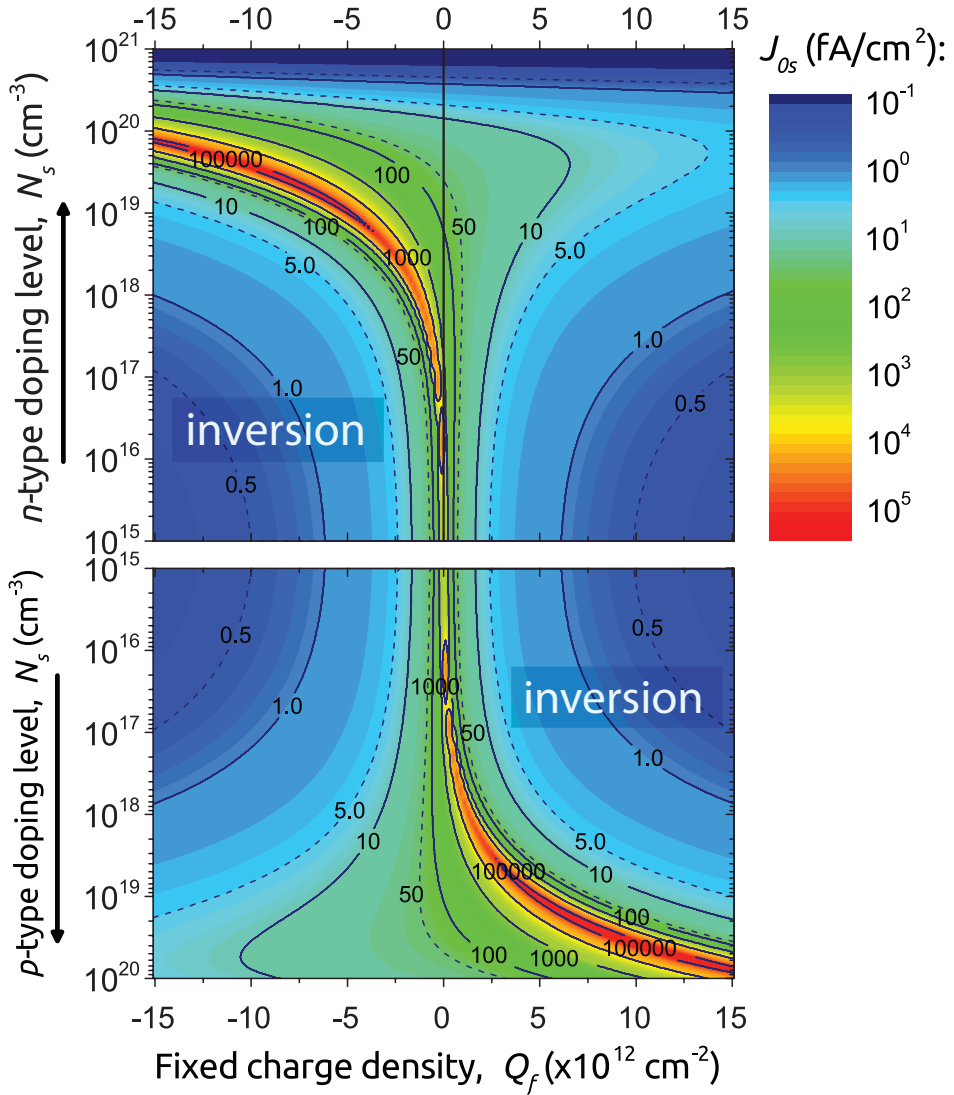
Figure 4: The effects of the fixed charge density Q_f and the surface doping concentration N_s on the surface saturation current density J_{0s} for a fixed level of chemical passivation. The results are evaluated using equation 2.2 for $S_{n0} = S_{p0} = 5000$ cm/s. The carrier densities are derived from the Girisch algorithm [33] using Fermi-Dirac statistics, $n_i = 9.65 \times 10^9$ cm^{-3}, [34] a base injection level of $\Delta n = 1 \times 10^{15}$ cm^{-3} and base doping level of $N_{base} = 1 \times 10^{15}$ cm^{-3}. For the band-gap narrowing of n- and p-type Si, the empirical models of Yan and Cuevas are used. [35,36]

Compatibility with Si homojunction solar cells

For implementation in Si solar cell manufacturing, passivation schemes should meet many requirements, both from a device and processing perspective. From an optical point of view, a high transparency to the solar spectrum is necessary when passivating the front or (for bifacial cells, which capture light from both sides) the rear surface. Moreover, a suitable refractive index n of $\sim$2 at 2 eV is preferred for anti-reflection purposes, although sometimes the passivation scheme can be combined with a separate ARC. In contrast, a low refractive index is preferred when acting as dielectric mirror on the back side of the solar cell.

As solar cells are designed to last for decades, also a long-term stability of the passivation scheme is necessary. Passivation schemes can in particular suffer from light- or potential-induced degradation (LID or PID, respectively). An ultrahigh temperature stability (i.e., up to 800 ^{o}C for some seconds) is required when screen- or stencil-printed metal fingers are "fired" through the passivation layer and ARC to contact the Si. In contrast, when the contacts are made at low temperatures by electro-plating, this requirement is redundant. However in the latter process, a pinhole-free thin film with a low leakage current is necessary to prevent undesired "ghost" plating of metal. Finally, the implementation in solar cells can also put (technological) requirements on the processing of passivation schemes. For instance a large area uniformity is desired, with solar cell dimensions 156x156 mm^2 being the industrial standard. Moreover, a low-temperature process for the preparation of the passivation layer is preferred, not only from a cost-perspective, but also because high temperatures (for instance used for thermal oxidation) can cause severe degradation of the Si bulk quality,[37] in particular for multicrystalline Si. In addition to passivation of its surface, for multicrystalline Si also the passivation of defects located at grain boundaries by hydrogen can be required.

2.2.2   Surface passivation by ALD Al$_2$O$_3$

The passivation of *p*-type Si and heavily doped *p$^+$*-type Si surfaces is very relevant for many high-efficiency solar cell concepts. Nonetheless, historically, before the introduction of ALD Al$_2$O$_3$, the passivation of such *p*-type Si surfaces was challenging. Thermal oxidation of Si yields excellent levels of chemical passivation with a very low positive Q_f, but its passivation of boron-doped surfaces is not stable over time.[38] Besides, thermal oxidation depletes the boron-doping near the surface, and its high temperature processing can have an adverse impact on the bulk lifetime.[37,39] SiN$_x$ on the other hand, although very well suited as passivation layer for *n$^+$* Si and as ARC, is undesirable for the passivation of *p*-type Si surfaces due to its positive Q_f.

The first results on Si surface passivation for solar cells by Al$_2$O$_3$ were reported in

the 1980s by Hezel and Jaeger.[40,41] In this case the Al_2O_3 was prepared by CVD (pyrolysis). Nonetheless, the broad recognition of Al_2O_3 as an outstanding surface passivation layer was yet to come. It was not until 2006, before this was realized. This time, it was reported by Agostinelli *et al.*[27] and Hoex *et al.*[42] that Al_2O_3 provides excellent passivation on *p*-type Si surfaces. In these cases, the Al_2O_3 was prepared by ALD using trimethylaluminum (TMA) and H_2O or O_2 plasma as precursors. The excellent levels of surface passivation offered by the Al_2O_3 films were attributed to a combination of excellent chemical and field-effect passivation.

In particular, ALD Al_2O_3 provides a very low D_{it} of $<10^{11}$ cm^{-2}, while it distinctively exhibits a large negative Q_f of 10^{12}–10^{13} cm^{-2}.[30] Such interface properties were already reported in the first ALD Al_2O_3 experiments using TMA and H_2O in 1989.[43] Due to its negative Q_f, Al_2O_3 is the ideal match for the passivation of *p*- and *p*$^+$ Si surfaces.[28] Shortly after its (re-)discovery, the first solar cells with ALD Al_2O_3 demonstrated high efficiencies, for instance PERC and PERL cells of 20.6%,[44] and 23.2%[45] efficiency, respectively. Due to these advantages, ALD of Al_2O_3 has now found its way into solar cell manufacturing, as will be extensively discussed in section 2.2.3. Moreover, the full potential of Al_2O_3 has likely not yet been reached, as is evident from e.g., recent results where Si solar cells with Al_2O_3 passivation layers demonstrated conversion efficiencies over 25%.[3] For an extensive overview on the topic of surface passivation by Al_2O_3, the reader is referred to Dingemans and Kessels.[30] Here, some key aspects related to surface passivation by ALD Al_2O_3 will be outlined.

ALD of Al_2O_3 for passivation

The most commonly applied and widely-studied ALD process for Al_2O_3 is based on TMA as metal-organic precursor with either H_2O, O_3 or O_2 plasma as coreactant. The first half-cycle can be described by the following reaction at the surface (*) for n =1,2[46]:

$$\text{TMA:} \quad nOH^* + Al(CH_3)_3 \rightarrow O_nAl(CH3)^*_{3-n} + nCH_4 \qquad (2.5)$$
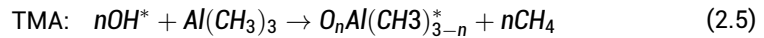
After a purge step, the second ALD half-cycle takes place, which in the case of thermal ALD can be described by the following ligand-exchange reaction:

$$\text{H}_2\text{O:} \quad Al(CH_3)^* + H_2O \rightarrow AlOH^* + CH_4 \qquad (2.6)$$
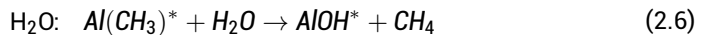
As a sufficient thermal budget is required for the latter to take place, alternatively highly-reactive species are often used in so-called energy-enhanced ALD processes,

such as O_3 or O_2 plasma when working at lower temperatures. Possible combustion-like reaction pathways are:

$$O_2 \text{ plasma:} \quad Al(CH_3)^* + 4O \rightarrow AlOH^* + CO_2 + H_2O$$
$$O_3: \quad Al(CH_3)^* + 4/3O_3 \rightarrow AlOH^* + CO_2 + H_2O$$

$$(2.7)$$

The resulting Al_2O_3 films are amorphous, with a high optical band gap of $\sim$6.4 eV. The latter makes Al_2O_3 films very suitable for application at the front surface of solar cells. Depending on the synthesis method, Al_2O_3 has a refractive index of $\sim$1.55-1.65 at 2 eV which is too low for application as an ARC, for which reason it is often capped by SiN_x.
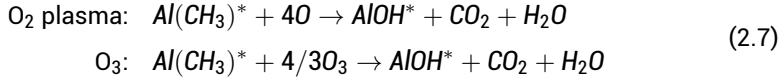
In the as-deposited state, the passivation quality provided by Al_2O_3 strongly depends on the oxidant chosen during the ALD process (see Figure 5). When using water or ozone as oxidant, the passivation can be reasonable in the as-deposited state. However, for plasma-assisted ALD, the passivation is initially very poor. In fact, the surface is de-passivated as a result of plasma damage, in particular due to vacuum ultraviolet radiation which is emitted in the plasma step.[47,48] The D_{it} of as-deposited ALD Al_2O_3 films can be strongly reduced by a short PDA at temperatures between 400-450°C, with comparable results for an anneal in forming gas (N_2/H_2) or N_2 ambient.[49] In actual Si solar cell processing, a dedicated PDA is often redundant because of the high temperatures used in the subsequent processing steps, such as the deposition of SiN_x or contact firing steps.

Hydrogenation of interface defects

Before the deposition of Al_2O_3, commonly the SiO_2 which is natively present at the Si surface, is removed by dipping the Si in diluted hydrofluoric acid (HF). Nevertheless, after ALD the Si/Al_2O_3 interface is in fact an $Si/SiO_2/Al_2O_3$ interface, as is commonly observed by e.g., transmission electron microscopy (TEM) (see Figure 6).[42,50]

The remaining defects at the Si/SiO_2 interface are effectively passivated by hydrogen which is released from the Al_2O_3 during subsequent PDA. Evidence for this hydrogenation was found experimentally by the deposition of deuterated Al_2O_3, where deuterium present in the Al_2O_3 film diffused during PDA to the Si/SiO_2 interface.[51] The activation energy for the interface hydrogenation does not depend on the amount of hydrogen which is incorporated in the Al_2O_3 films, but the rate of hydrogenation does.[52] Therefore, the hydrogenation of interface defects is to some extend dependent on the amount of hydrogen present in the Al_2O_3 film and on its microstructure.[53] The best passivation properties are found for dense and hydrogen-containing Al_2O_3 films, such as for ALD
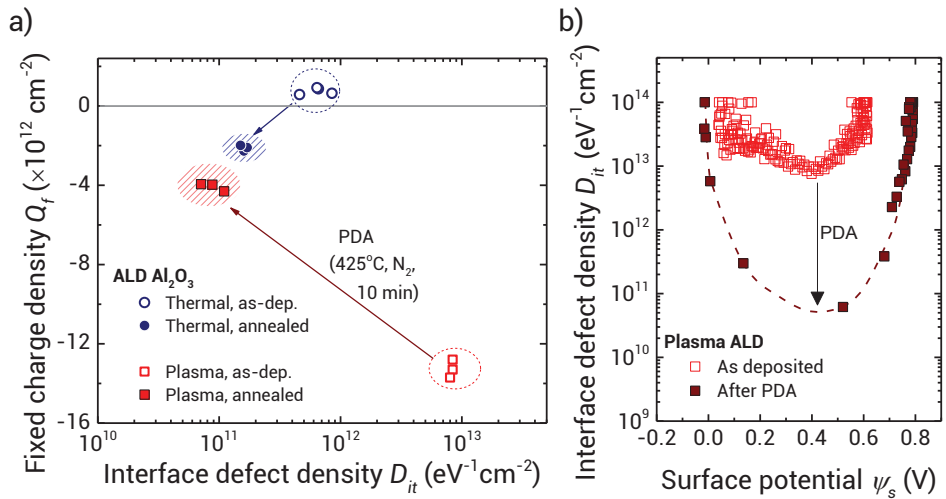
Figure 5: Interface properties as determined by corona oxide characterization of semiconductors (COCOS) of n-type Si (100) passivated by Al_2O_3 films which are prepared by plasma (i.e., using O_2 plasma) or thermal ALD (i.e., using H_2O) in as-deposited state and after post-deposition anneal at 425 °C in N_2 ambient. (a) After annealing, the D_{it} reduces significantly for both deposition methods. (b) The D_{it} of the Si/Al_2O_3 interface is particularly reduced at mid gap. N. Nandakumar of National University of Singapore is acknowledged for the COCOS measurements.

Al_2O_3 films deposited at $\sim$200 °C.

Interestingly, Al_2O_3 can also be used to passivate defects when it is not deposited directly onto the Si surface. For instance, the passivation of Si by materials such as HfO_2, TiO_2, or deposited SiO_2 layers, could be strongly improved after capping by Al_2O_3 and a subsequent PDA. [25,51,54,55] In fact, for SiO_2, it has even been shown that the Al_2O_3 capping layer can even be removed after PDA, without compromising the improved passivation properties. [30,55] Nonetheless, capping by Al_2O_3 not only ensures the hydrogenation of interface defects during a PDA, but can also improve the long-term and high-temperature stability of the surface passivation stack. [56,51]

Finally, it has to be noted that although that the hydrogenation provided by the Al_2O_3 is preferred for passivation, the hydrogen can also lead to some adverse effects in solar cell manufacturing. For instance, a rapid increase in temperature (such as when contacts are "fired" through the dielectric) can induce blistering of the Al_2O_3 film (see Figure 7). [58] Most likely hydrogen released from the Al_2O_3 at higher temperatures builds up under the Al_2O_3 film, which acts as a diffusion barrier, eventually causing a local delamination. [58,59] In actual solar cell processing, the formation of blisters can be avoided by slowly releasing hydrogen using a more gradual increase in temperature during subsequent process steps. Furthermore, the formation of blisters can be avoided by using thin Al_2O_3 films (i.e., less than 10 nm in thickness). [59] Interestingly, solar cell concepts
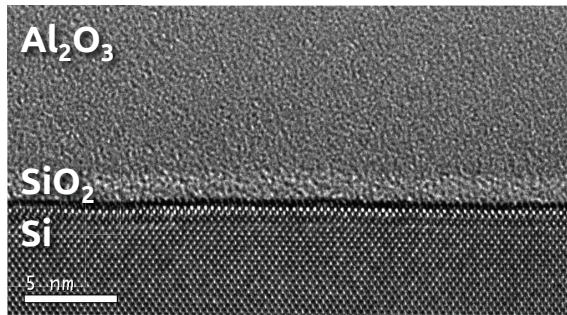
Figure 6: High-resolution TEM image of the annealed Al_2O_3 layer prepared by plasma ALD on Si, showing the amorphous character of the Al_2O_3 layer. The SiO_2 interface layer has a thickness of 1.5 nm.
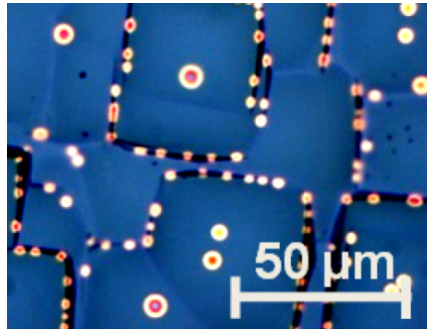
Figure 7: Optical microscopy image of blisters formed in an Al_2O_3/SiN_x film after firing at 850 °C. The film stack passivates a Si surface with a random pyramid texture. Adapted from Bordihn et al.[57]

exist where the blisters in the Al_2O_3 film are used to advantage, to form local point contacts to the Si.[60]

Interface engineering by Al_2O_3

From a scientific as well as from a processing perspective, it is interesting to see the effect of Al_2O_3 thickness on the surface passivation quality. The best passivation results are found for Al_2O_3 thicknesses >5 nm for plasma ALD,[61] and >10 nm for thermal ALD.[30] For very thin Al_2O_3 layers, the level of chemical passivation achieved after PDA starts to deteriorate, which likely can be attributed to a lack of interface hydrogenation during PDA.[61] Interestingly, it has been demonstrated that the fixed charge density of Al_2O_3 however is located in very close vicinity of the Si-Al_2O_3 interface, i.e., within the first 2 nm of the Al_2O_3.[61]

The latter is very relevant for Si solar cell processing. SiN_x is conventionally used as an ARC due to its suitable refractive index (tuneable between 1.9-2.7), but when deposited directly on Si it is not an ideal match for p-type or p^+-type Si due to its positive

Q_f. By using Al_2O_3 as thin interlayer in Al_2O_3/SiN_x stacks, the total Q_f of the stacks becomes negative.[62] Therefore, Al_2O_3/SiN_x stacks are an ideal match for the passivation of the front p^+-type surfaces. The fact that very thin Al_2O_3 layers can be used, makes ALD a viable technique for high-volume manufacturing (HVM), as will be further discussed in section 2.2.3. It has to be stressed however, that for ultra-thin Al_2O_3 layers (i.e., <10 nm) in Al_2O_3/SiN_x stacks, the interface properties such as Q_f and D_{it} are strongly dependent on the thickness of the Al_2O_3 film, the process conditions during film growth and subsequent firing or annealing conditions.[62]

Influence of the surface conditions on the passivation properties

It is common that the interface properties of passivation schemes are significantly dependent on the Si surface conditions, such as the doping level, crystallographic termination and the surface topology.[63,64] Such aspects have also been investigated for ALD Al_2O_3.

For highly-doped p^+ Si surfaces with a wide range of surface doping concentrations, very low J_0 values are reported regardless of the oxidant used during ALD.[28,65,66,67] In fact, Al_2O_3 passivates the p^+ Si surface so effectively, that Auger recombination within the highly-doped region is often the dominant recombination mechanism and the principal contributor to the measured J_0.[65,66,68] Recently, it has even been shown by Black *et al.* that the interface parameters Q_f and S_{n0} for boron-doped Si surfaces passivated by Al_2O_3 prepared by thermal ALD are in fact independent of the surface doping concentration, at least up to $N_s \leq 3 \times 10^{19}$ cm^{-3}.[67] Nonetheless, care must still be taken when passivating p^+ Si, as in some cases a boron-rich layer (which is a boron-Si compound) can be formed on the Si surface during boron-diffusion, which can inhibit the surface passivation by ALD Al_2O_3 and other passivation layers.[65,69] Overall, as stated before, ALD Al_2O_3 is very effective for the passivation of p- and p^+-Si surfaces, virtually independent of the surface doping concentration.

For highly-doped n^+ Si surfaces, the level of passivation provided by ALD Al_2O_3 is in many cases found to be compromised due to its negative Q_f,[70,71,72] as could be expected on the basis of Figure 4. This holds in particular for surface doping levels in the range of 10^{18}-10^{20} cm^{-3}. Although on lowly-doped n-type Si surfaces excellent passivation results by Al_2O_3 are achieved, here the negative Q_f leads to inversion, which is undesired in solar cells. Therefore, also (novel) ALD-based schemes are successfully being explored for the passivation of n and n^+-type Si surfaces, as will be discussed further in section 2.2.4.

Besides the doping level, the passivation of Si surfaces can strongly depend on other surface conditions, such as the crystallographic orientation. For ALD Al_2O_3 however,

Table 2: Comparison of typical film and equipment requirements by the integrated-circuit (IC) and photovoltaic (PV) industries. Adapted from Granneman *et al*.[74]

	IC industry	PV industry
# process steps per device	*200-400*	*15-20*
Film uniformity (%)	*>99*	*>96*
Particle generation	*Important*	*Irrelevant*
Metal (Fe) contamination (cm^{-2})	*<10^{10}*	*<10^{12}*
Cost-of-ownership ($/wafer)	*3-10*	*0.03-0.05*
Equipment Cost (M$)	*2-5*	*0.5-2.5*
Equipment Throughput (wafers/hr)	*10-50*	*1000-3000*
Equipment Uptime	*>95%*	*>95%*
Wafer breakage	*1:50,000*	*1:1000*

dedicated studies so far revealed marginal differences in the passivation of Si (100) and (111) surfaces.[68] On the other hand, the surface cleaning influences to the final passivation properties of Al$_2$O$_3$ and should therefore be considered.[73]

2.2.3 ALD in solar cell manufacturing

Requirements for manufacturing in the PV industry

The success of ALD Al$_2$O$_3$ as a passivation layer on a lab-scale was the incentive for the development of high-throughput ALD reactors, specifically designed for the photovoltaic industry. Even though high-throughput ALD reactors were readily used for manufacturing in the integrated-circuit (IC) industry, the demands set by the IC and PV industry are markedly different (see Table 2). Whereas the requirements in terms of e.g., particle generation and film uniformity are relaxed for the PV industry compared to the IC industry, the former is rigorously more demanding in terms of throughput and costs. The production lines for crystalline Si solar cells are typically designed for a throughput of up to 1 wafer/s, whereas the costs for e.g., the deposition of Al$_2$O$_3$ are (depending on cell design) only allowed to be 0.03-0.05 $/wafer in order to remain cost-effective.

For the deposition of thin films, ALD is competing with physical vapour deposition (PVD), plasma-enhanced (PE) and atmospheric pressure (AP) chemical vapour deposition (CVD) and spray pyrolysis. In general, to compete with the abovementioned deposition techniques, ALD processes should offer additional advantages. For instance, they should be low-cost and preferably provide benefits in terms of spatial uniformity and solar cell efficiency. Furthermore, a high yield of the ALD process, efficient precursor usage and low-temperature processing would aid in attaining a low cost-of-ownership. Apart

from an optimized reactor design, another way to ensure an efficient precursor usage and optimized throughput is to minimize precursor dosing until the ALD half-reactions are at the onset of saturation. As long as the quality and homogeneity of the deposited films are still acceptable, this might be a valid approach. In addition, also "solar grade" precursors can be used. These precursors are less pure and hence are lower cost.[75,76] When ALD films can be used on both sides of the solar cells (see e.g., section 2.2.3), or when stringent requirements are set on the composition, uniformity and thickness of the films or film stacks, such as for passivating contacts, ALD in particular might become the deposition method of choice.

High-throughput ALD reactors

Two distinct ALD methods are being used for high-volume manufacturing in the PV industry, i.e., temporal and spatial ALD, which differ in the way the precursors are delivered to the solar cells (see Figure 8).
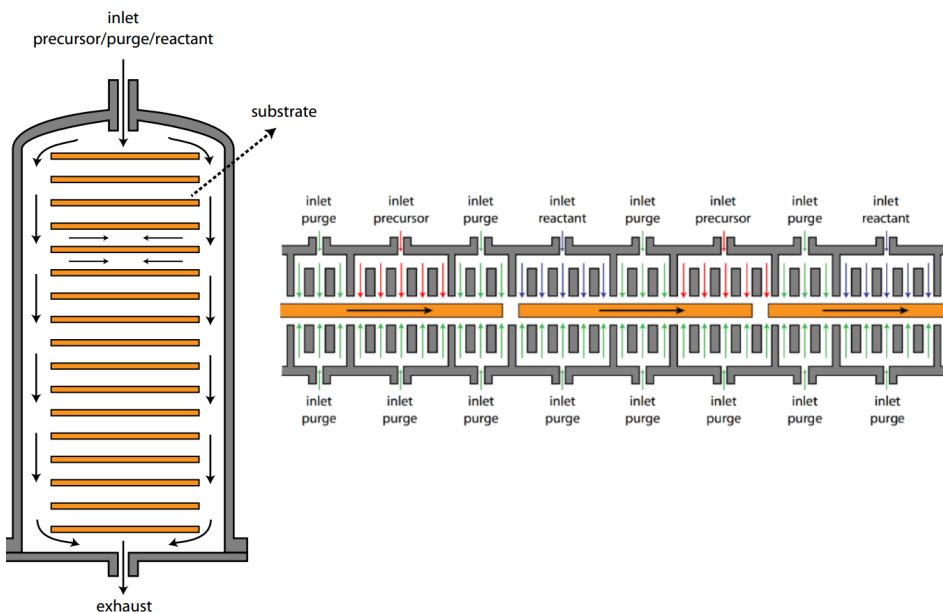
Figure 8: Schematic representation of batch ALD (left) and spatial ALD (right), adapted from van Delft *et al*.[77]

With *temporal* ALD, the precursor and co-reactant dosing are separated in *time* by purge or pump steps. Using temporal ALD, which is the most common form of ALD in research and development, a sufficiently high throughput for the PV industry can be achieved by placing many wafers (typically 500-1000 wafers) simultaneously in a batch

Table 3: Comparison of industrial aspects for temporal and spatial ALD.

	Temporal ALD	Spatial ALD
Processing:	Batch	In-line
Pressure:	~1 Torr	Atmospheric or lower
Single side deposition by:	back-to-back wafer stacking	Precursor injection from one side of the wafer
Double side deposition	Viable (no back-to-back stacking, half the throughput)	Viable (when precursor injection from both sides of the wafer)
Companies for Si PV:	ASM, Beneq	Levitech, SoLayTec
Deposition on walls:	Yes	No
Limit on throughput:	Purge and dose times	Surface reaction kinetics
Deposition of stacks:	Flexible	Possible
Turn-around-time for ~nm films:	Long (~0.5-1 hour)	Short (<1 min)

reactor. As the wafers are placed back-to-back, parasitic deposition on the other side of the wafers (*wrap-around*) is ideally avoided. As ALD uniquely is a surface limited deposition method, homogeneous films can in principle be obtained on all wafers. Generally, in batch reactors the purge, precursor and reactant dosing times must be longer compared to singlewafer ALD tools, due to the very large surface areas which are exposed. Therefore, in batch ALD it is often preferred to use O_3 rather than H_2O as coreactant due to its higher reactivity and because it allows for shorter purge times.

In *spatial* ALD (S-ALD), the precursor and co-reactant dosing steps are separated not in *time*, as is the case for temporal ALD, but in *space*. The wafers can float on N_2 bearings through S-ALD reactors, and move through separated precursor and co-reactant zones (see Figure 8), which are separated from each other by nitrogen gas bearings at (sub-) atmospheric pressures. In this way, the lengthy purge times which are otherwise required to separate the precursor and reactant gases are avoided. As only the wafers encounter the spatially separated precursors, the ALD half-reactions take only place at the surface of the wafer, and (ideally) not on the reactor walls. The spatial ALD concept is particularly interesting for in-line processing and can, because of the absence of purge steps, operate at atmospheric pressure. Moreover, in principle no pumps or fast switching valves are required. In Table 3, a selection of industrial aspects of temporal and spatial ALD are compared.

ALD Al_2O_3 in PV industry

Besides ALD, also other synthesis methods of Al_2O_3 are suitable for the passivation of Si surfaces, such as PECVD or AP-CVD and sputtering.[41,67,78,79,80] In the PV indus-

try, PECVD is in particular competing with ALD as a deposition method for Al_2O_3, as PECVD reactors are already installed in most production lines for the deposition of SiN_x, whereas ALD is a relatively new technique in the field of PV manufacturing. Nonetheless, as was discussed in the section 2.2.3, even very thin, homogeneous, films of Al_2O_3 of less than 2 nm in thickness could be sufficient for solar cells to benefit from its negative Q_f when combined with a SiN_x ARC or a SiO_2 dielectric mirror. The fact that very thin Al_2O_3 layers can be used, makes ALD in particular interesting for HVM. Moreover, in direct comparisons, the best passivation properties of Al_2O_3 are so far often achieved when it is prepared by ALD. [67,81]

For instance, Schmidt *et al.*[81] compared in 2010 the Si surface passivation provided by single layers of Al_2O_3 prepared by sputtering, PECVD, spatial ALD and temporal ALD. In Figure 9, a selection of results is given. ALD, with plasma ALD in particular, yielded the highest passivation performance before as well as after a high-temperature firing step. Importantly, the found differences in surface passivation quality translated well to differences in conversion efficiency of PERC solar cells, ranging from 20.1% for solar cells where the Al_2O_3 was prepared by sputtering, to 21.4% for solar cells where it was deposited by ALD and subsequently was capped by PECVD SiO_2.[81] Note that research activities on the passivation by Al_2O_3 by various passivation methods are still ongoing. For Al_2O_3 films prepared by sputtering for instance, the absence of hydrogen or the presence of sputter damage affected the surface passivation.[30] Indeed, the preparation of Al_2O_3 films by sputtering has since 2010 been significantly improvement when using a hydrogen-containing ambient.[82]

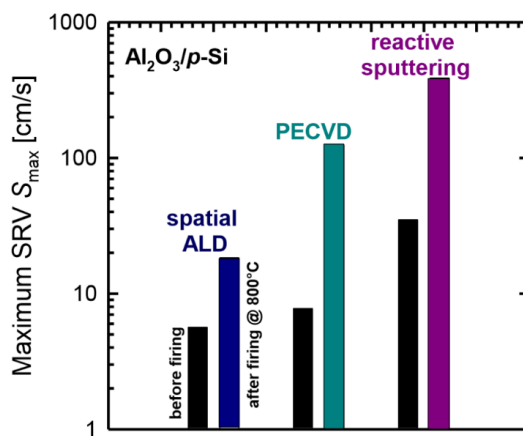**Figure 9:** Comparison between the passivation quality in terms of upper limit of S_{eff} or *SRV* (where a low S_{eff} is preferred) of Al_2O_3 passivation layers prepared by spatial ALD, PECVD and sputtering. Adapted from Schmidt *et al.*[81]

Currently, both spatial and temporal ALD systems are being piloted in the PV industry for the HVM of thin Al_2O_3 layers. Due to the excellent passivation of thermal ALD Al_2O_3 films, to date no high-throughput reactors capable of plasma ALD have been developed for the Si PV industry yet. Very similar results in passivation are reported on lowly-doped Si surfaces for spatial as well as temporal ALD of Al_2O_3 when combined with SiN_x capping layers,[30,74] even in direct comparison.[81] Also, no significant differences in passivation quality by both deposition methods are found for either n^+ or p^+ Si surfaces, which is indicative of the robustness of ALD as a deposition method.[83] However, as will become clear in the following sections, the different reactor designs each have their own distinct advantages in terms of the preparation of doped films and stacks, and in terms of processing complexity. In the end, cost-of-ownership and yield considerations are expected to play a decisive role in the final choice of reactor type or deposition method for the HVM in the PV industry.

2.2.4   New developments for ALD passivation schemes

With the passivation of *p*-type and p^+ Si surfaces by ALD being fully established, research incentives are currently also targeting the passivation of n^+ Si surfaces by ALD. Moreover, ALD passivation layers are being explored to enable novel light trapping schemes that otherwise suffer from a high surface recombination, such as "black Si" texturing. Finally, other new passivation materials prepared by ALD are also being explored, and ALD-based passivation schemes are being further tuned using doping or the fabrication of stacks. In this section, these recent developments in the field of surface passivation by ALD are outlined.

ALD stacks for the passivation of n^+ Si and p^+ Si surfaces

The passivation of n^+ Si surfaces is very relevant for many high-efficiency solar cell designs (see Figure 1). Unfortunately, as was mentioned in the previous sections, the negative Q_f makes Al_2O_3 less than ideal for this application. Additionally, for e.g., IBC solar cells, n^+ and p^+ Si regions are adjacent and preferably passivated simultaneously. By using passivation schemes without a significant Q_f, but with a high level of chemical passivation (i.e., a low D_{it}), effects associated with a 'wrong' charge polarity, such as depletion region recombination or parasitic shunting can ideally be avoided on both surface types. In such a "zero-charge" approach, rather than relying on field-effect passivation by a fixed charge, the high doping levels at the n^+ and p^+ Si surfaces could ensure the local reduction of the minority charge carrier density.[11] Finally, the simultaneous passivation of n^+ and p^+ Si surfaces by ALD could also be of interest from an (industrial) perspective, as it could allow for the simultaneous passivation of both sides

of solar cells in a single ALD run. Fortunately, the negative Q_f of Al_2O_3-based layers can be tuned in several ways.

First, the Q_f of Al_2O_3 single layers is reduced by using higher deposition temperatures (i.e., ~300-500°C), although this approach comes at the expense of reduced chemical passivation.[84,85] Furthermore, the fixed charge density of Al_2O_3 was found to be reduced by capping it with (PECVD) SiN_x in combination with a subsequent high-temperature (>800°C) firing step.[71] Richter *et al.* demonstrated that such a Al_2O_3/SiN_x stack is well capable of passivating n^+ surfaces with a wide range of surface doping concentrations (~10^{18}–2×10^{20} cm^{-3}).[71] Nonetheless, in this stack, a negative Q_f of ~1.9×10^{12} cm^{-2} is still present,[62] which is not ideal for implementation in solar cells due to inversion or depletion region effects.

Alternatively, ALD SiO_2/Al_2O_3 or HfO_2/Al_2O_3 stacks prepared at 200 °C (e.g., using $Hf(NMeEt)_4$ and H_2O for HfO_2, and $SiH_2(NEt_2)_2$ and O_2 plasma for SiO_2) can be used as passivation schemes with tunable Q_f.[54,56] The Al_2O_3 capping layer in these stacks ensures the hydrogenation of the Si-SiO_2 or Si-HfO_2 interface during annealing, resulting in excellent levels of chemical passivation, with D_{it} values <10^{11} cm^{-2}.[54,56] The very thin (i.e., 2-4 nm) SiO_2 or HfO_2 interlayer in its turn prevents the formation of a negative Q_f in the Al_2O_3.[54,56,86] For thicker SiO_2 interlayers (>4 nm), the overall charge polarity of SiO_2/Al_2O_3 stacks even becomes positive, (depending on the preparation method of SiO_2) as the SiO_2 layer contains a very low positive Q_f in the bulk.[56,86,87] Overall, the 'digital' thickness control and the excellent homogeneity of the interlayers provided by ALD enables a precise control of Q_f in SiO_2/Al_2O_3 and HfO_2/Al_2O_3 stacks.[11,54,56] Recently, it was demonstrated that ALD SiO_2/Al_2O_3 stacks outperform the passivation of n^+ Si surfaces provided by single layers of Al_2O_3 or by fired Al_2O_3/SiN_x stacks.[11]

As mentioned, the possibility to passivate n^+ Si with an ALD-based passivation scheme opens up new opportunities for ALD reactors in HVM. For S-ALD, Al_2O_3 can be deposited on p^+ Si, whereas simultaneously SiO_2/Al_2O_3 stacks could be deposited on the n^+ Si side of the solar cell using the bottom side of the spatial ALD reactor. For batch ALD, both sides of solar cells could be passivated in a single deposition run. In fact, SiO_2/Al_2O_3 stacks have already successfully been scaled up in industrial batch ALD reactors.[11]

ALD for the passivation of surfaces with demanding topologies

Most high-efficiency solar cells have, at least at the front surface, a random-pyramid (RP) texture (created by wet-chemical etching) in combination with an ARC, to ensure good light trapping and correspondingly a high short-circuit current density (see Figure 11a). The random-pyramid texture typically results in an increase of roughly ~1.7 in
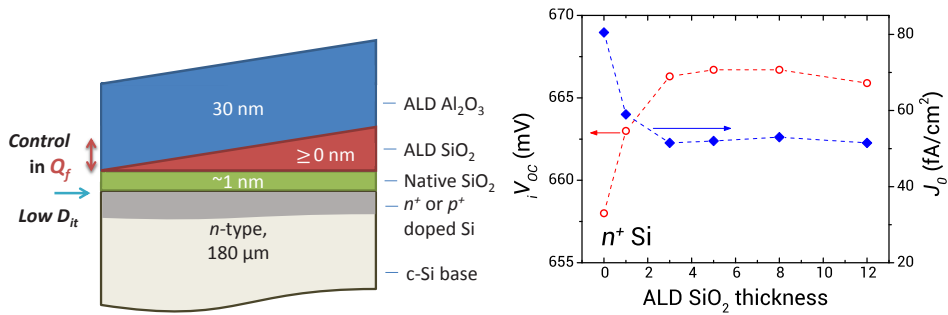
Figure 10: Schematic display of the SiO_2/Al_2O_3 passivation scheme (left). Passivation results obtained using SiO_2/Al_2O_3 stacks on an n^+ Si surface (having $N_s = 2\times10^{20}$ cm^{-3}) on a symmetrical lifetime sample (right), adapted from van de Loo *et al.*[11]

surface recombination for Al_2O_3-based passivation schemes compared to planar surfaces,[88] which can be attributed to the increase in surface area. Alternatively, the front surface can be etched by reactive ions, which creates a very rough surface topology, referred to as "black silicon" (see Figure 11b). Black Si exhibits excellent light trapping properties, even without ARC.[89,90] Compared to RP-textured Si, black Si shows particularly a high absorption in the short-wavelength range. Moreover, its absorption is less dependent on the angle of incidence compared to RP-textured Si.[90]
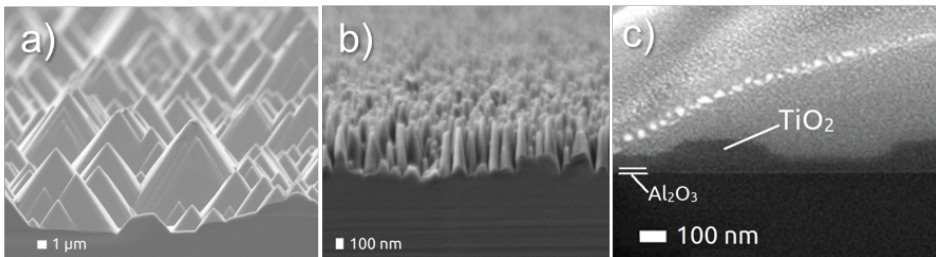
Figure 11: SEM images of different approaches which are used to enhance the light absorption in Si solar cells. In (a) the current industrial standard method is used, where random-pyramids (RP) are created on the Si surface by a wet-chemical etch. On the RP-textured surface, the passivation layer and ARC are deposited afterwards. In (b) black Si texture is shown which is made by reactive ion etching and subsequently is passivated by a 30 nm Al_2O_3 film prepared by plasma ALD. In (c) a cross-sectional image of samples with a nano-patterned TiO_2 layer is shown, which is adapted from Spinelli *et al.*[91] The TiO_2 is deposited by electron beam evaporation on a 30 nm Al_2O_3 film prepared by plasma ALD, which provides the surface passivation.

Despite of these benefits, the surface area of the black Si surface is significantly increased compared to planar substrates, typically by a factor in the range of 7- 14.[92,93] This strong increase in surface area puts stringent requirements on the passivation quality of the black Si surface. For a long time, solar cells with black Si texture only

achieved efficiencies <18.2%. Only recently, it has been reported on IBC cells comprising black Si with an conversion efficiency of 22.1%.[90] In this case, the black Si surface was passivated by Al_2O_3 deposited by thermal ALD.[90] Conceivably, a full coverage of Al_2O_3 films over the pillars of the black-Si (see e.g., the TEM results in Figure 12), is crucial for the surface passivation, making ALD an ideal candidate. Moreover, it is commonly observed that the recombination rate of charge carriers at the black Si surfaces is much lower than what would be expected on the basis of the large surface area.[92,93,94,95] An important reason for this observation is that the field-effect passivation is markedly more effective for black Si textures than for planar or random pyramid-textured surfaces.[92,95] More specifically, the fixed charge density in the passivation layer can bring the needles of the black Si texture almost completely into inversion or accumulation, and in this way effectively suppresses the surface recombination. Finally, for application in solar cells, more heavily-doped black Si surfaces textures are also relevant. Whereas first results for Al_2O_3 on p^+ doped black Si are promising,[96] for n^+ doped black-Si surfaces, the SiO_2/Al_2O_3 or HfO_2/Al_2O_3 ALD stacks discussed in the previous section could be interesting candidates.

Besides black Si, ALD Al_2O_3 films also have been used for the surface passivation of other textures with an even more demanding surface topology, such as Si-nanowires or hierarchical textures.[89,97] For such topologies, multiple precursor dosing steps are even used during ALD to ensure a good conformality of the film over the nanostructure.[89] Interestingly, light-trapping approaches have also been developed in which flat Si surfaces could be used.[91] In this approach, the flat surface was passivated by ALD Al_2O_3. On top of the passivation layer, nano-sized TiO_2 resonators are deposited, which enhance the light trapping in the Si (see Figure 11).[91] This approach not only makes the texturing of the surface and the use of an ARC redundant, they moreover do not adversely affect the surface passivation provided by the ALD Al_2O_3 films and are therefore very promising for application in solar cells.

Novel ALD-based passivation schemes

After the tremendous success of ALD Al_2O_3, the surface passivation properties of various other materials prepared by ALD has also been explored, including TiO_2, Ta_2O_5, and Ga_2O_3. A selection of passivation results and corresponding interface properties for these materials is given in Table 4. Recently, Cuevas and co-workers identified Ga_2O_3[98] and Ta_2O_5[99] prepared by ALD (the latter in combination with PECVD SiN_x capping layer) as materials which provide excellent surface passivation. Although outstanding surface passivation results have been demonstrated, these materials do not yet offer apparent benefits in terms of processing complexity, cost or passivation quality compared to e.g.,
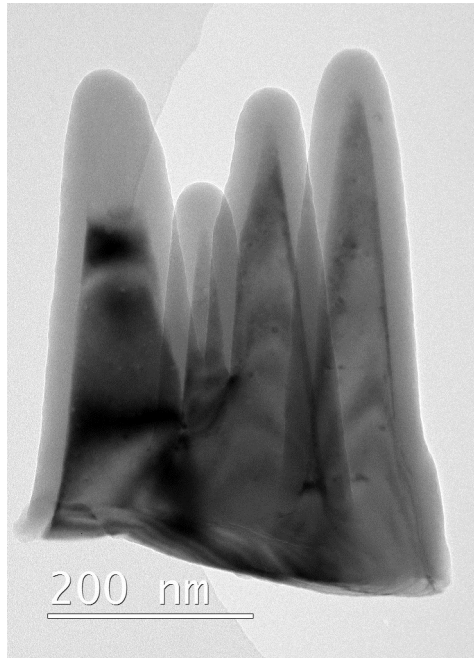
Figure 12: Bright-Field TEM image of black-Si pillars of Figure 11b . A conformal layer Al_2O_3 of 30 nm thickness is deposited by plasma ALD.

Al_2O_3 films or SiO_2/Al_2O_3 stacks. Nonetheless, these novel materials might become very useful in the emerging field of passivating contacts, as will be discussed in section 2.4.

Other passivation materials can be interesting because of their refractive index of $\sim$2 at 2 eV, which makes them also suitable as ARCs. TiO_2 was for instance traditionally used before SiN_x as ARC in Si solar cells, although it was gradually being replaced by SiN_x due to the poor passivation quality of the former. However, Liao *et al*. recently demonstrated excellent surface passivation by TiO_2 using thermal ALD using $TiCl_4$ and H_2O as precursors.[100] The passivation of TiO_2 could be achieved after a PDA in combination with a subsequent lightsoaking step.[100] Interestingly, TiO_2 is also potentially suitable as a part of a passivating contact.

Besides the deposition of single layers, ALD is also well-suited to prepare stacks or doped films in a well-controlled way. This ability can potentially be used to carefully tune the electrical or optical properties of the passivation layer or scheme. For instance, using materials with different refractive indices, it is possible to make double-layered or graded ARCs, or Bragg mirrors to enhance light trapping in solar cells. A passivation scheme prepared by ALD which is also suitable as ARC could be a stack of Al_2O_3/ZnO, where even improvements in passivation properties were found after capping the Al_2O_3 by ZnO.[22] The interface properties such as D_{it} and Q_f of ALD Al_2O_3 or SiO_2 layers could

also be improved by using doping.[101,102] For instance, it was found that Al_2O_3 doped with TiO_2 has a slightly more negative Q_f compared to single layers of Al_2O_3.[101]

Finally, ALD also offers the possibility to make nanolaminates or alloys, which potentially also could be used to improve the passivation properties and can even add new functionalities to it. For example, it has been reported that ALD TiO_2-Al_2O_3 nanolaminates have an increased conductivity compared to a single layer of Al_2O_3, albeit at the price of a reduced passivation quality.[102] Moreover, Al_2O_3-TiO_2 nanolaminates are successfully used to enhance the damp-heat stability of the surface passivation scheme, as they act as a moisture barrier layer.[103] Al_2O_3-TiO_2 'alloys' also have been explored (deposited using an Al_2O_3:TiO_2 ALD cycle ratio of 1:1), resulting in a slight improvement in surface passivation.[104] Overall, it has been demonstrated that the precise control in film growth and film composition offered by ALD opens up numerous possibilities to further develop ALD-based passivation schemes.

Table 4: Selection of optimal surface passivation conditions provided by several materials prepared by ALD. The SiN_x layers which are sometimes used as capping layer are prepared by PECVD. Note that S_{eff} depends on the doping level of the bulk. Therefore, only S_{eff} data based on polished, float-zone, n-type Si wafers with a base resistivity of 1-5 Ωcm are included here. For each process, the substrate temperature T_{dep} and growth-per-cycle (GPC) are indicated.

Material or stack	Metal precursor	Reactant	T_{dep} (°C)	GPC (Å)	PDA (°C, gas)	D_{it} ($\times 10^{11}$ eV^{-1}cm^{-2})	Q_f ($\times 10^{12}$ cm^{-2})	S_{eff} (cm s^{-1})	Ref
Al_2O_3	AlMe$_3$	O$_2$ plasma	200	1.1	450, N$_2$	0.8	-5.6	2.8	47
	AlMe$_3$	O$_3$	200	0.9	400, N$_2$	1.0	-3.4	6.0	47
	AlMe$_3$	H$_2$O	200	1.1	350, N$_2$	0.4	-1.3	4.0	47
SiO_2	SiH$_2$(NEt$_2$)$_2$	O$_2$ plasma	200	1.2	400, N$_2$	10	0.6 - 0.8	25*	55
SiO_2/Al_2O_3	SiH$_2$(NEt$_2$)$_2$	O$_2$ plasma	200	1.2	400, N$_2$	1	-5.8 - 0.6	3	55
HfO_2/Al_2O_3	Hf(NMeEt)$_4$	H$_2$O	150	1.1	350, N$_2$/H$_2$	<1	-(4-1)	<1	87
Ta_2O_5	Ta$_2$(OEt)$_{10}$	H$_2$O	250	0.3	no	n.a.	-1.8	467	99
Ta_2O_5/SiN_x	Ta$_2$(OEt)$_{10}$	H$_2$O	250	0.3	no	n.a.	-1.0	3.2	99
TiO_2	TiCl$_4$	H$_2$O	100	0.6	200-250, N$_2$, light soaking	n.a.	n.a.	2.8	100
Ga_2O_3	GaMe$_3$	O$_3$	250	0.2	350, H$_2$/Ar	n.a.	n.a.	6.5	98

2.3 Transparent conductive oxides for Si heterojunction solar cells

In this section, the role of ALD in preparing both ZnO- and In_2O_3-based TCOs for SHJ solar cells is reviewed. First, the basics of TCOs and important aspects with respect to implementation in SHJ solar cells will be reviewed. From this it follows that the upcoming high-mobility In_2O_3-based TCOs are especially promising for use on the front side of the solar cell due to their excellent conductivity and transparency. Consequently, these TCOs have played a key role in achieving the recent record efficiencies for SHJ cells. ZnO-based TCOs are mostly promising as a low-cost alternative at the rear side of the solar cell, since the optoelectronic requirements at the rear side are less stringent whereas the work function of ZnO is also more suited for the electron-collecting side.

ALD processes of both ZnO- and In_2O_3-based TCOs will be discussed. In the subsection on ALD of doped ZnO-based films (ZnO:X, X=Al, B, Ga, …), the high control over the doping level offered by the use of dopant supercycles is discussed.[105,106] The challenge of dopant clustering which is inherent to the supercycle approach is addressed, together with several strategies to mitigate this clustering. For (doped) In_2O_3, an overview of existing ALD processes is given, with special attention to the ALD process of high-mobility H-doped In_2O_3, given the very promising properties it can provide.[4,107] Finally, recent developments in the HVM of ALD TCOs, with a focus on (doped) ZnO, is briefly touched upon.

2.3.1 Basics of TCOs in SHJ solar cells

Lateral conductivity

The first requirement of a TCO is that it should have a low resistivity in order to prevent excessive Ohmic losses during lateral charge transport to the metal grid. The resistivity ρ is determined by the carrier density N_e and the mobility μ_e of the charge carriers by $\rho = (N_e \mu_e e)^{-1}$, in which e is the elementary charge. A typical sheet resistance for the front TCO with a thickness of 75 nm is ~40 $\Omega/\square$, which translates to a resistivity of 0.3 mΩcm.[108] Note that the TCO should preferably also serve as an antireflection coating to maximize the incoupling of light, which more or less fixes the thickness to 75 nm given that TCOs typically have a refractive index of around 2. In Figure 13, the dashed isolines of constant resistivity show the typical N_e (>1×10^{20} cm^{-3}) and μ_e values that are needed to achieve such resistivity values.

TCOs typically have a high band gap of ~3 eV and therefore a very low intrinsic carrier density N_e. Nonetheless, thin films of In_2O_3 and ZnO are often unintentionally n-type doped by the presence of doubly charged oxygen vacancies (V_o^{2+}) and singly charged H$^+$, which leads to a typical N_e up to a level of ~10^{19} cm^{-3} or higher. In order to achieve

a sufficiently low resistivity, TCOs are often intentionally further n-type doped by other elements such as Sn for In_2O_3 and Al, Ga and B for ZnO to increase N_e to the order of 10^{20}-10^{21} cm^{-3}.

The carrier mobility μ_e is limited by the scattering of charge carriers. An intrinsic, unavoidable scattering process is phonon scattering. Depending on the quality of the (typically) polycrystalline TCO, also extrinsic scattering processes can be significant, for example on crystallographic defects such as grain boundaries and other impurities. Nonetheless, typically the dominant scattering process for carrier density values in the range of interest (>1×10^{20} cm^{-3}) is the Coulombic scattering that arises from the introduction of ionized dopants, known as ionized impurity scattering (IIS). For homogeneously dispersed ionized dopants, the mobility limit due to IIS, μ_{ii}, can be calculated by:[109]

$$\mu_{ii} = \frac{3(\varepsilon_r\varepsilon_0)^2 h^3}{Z^2 m^{*2} e^3} \frac{N_e}{N_i} \frac{1}{F_{ii}^{np}(\zeta_0)} \qquad (2.8)$$

In this equation, h is Planck's constant, ε_0 and ε_r are the vacuum and relative permittivity, respectively, and m^* the effective electron mass. Z is the charge state of the ionized impurity and N_i the concentration of ionized impurities. $F_{ii}^{np}(\zeta_0)$ is the screening function for IIS in a degenerate semiconductor which depends on the carrier density through the factor $\zeta_0 = (3\pi^2)^{1/3}\varepsilon_r\varepsilon_0 h^2 N_e^{1/3}/m^* e^2$.[109] For N_e values >1×10^{20} cm^{-3}, IIS limits the mobility of ZnO to approximately <50 cm^2/Vs and that of In_2O_3 to <150 cm^2/Vs.[110,111] In this respect, In_2O_3 is at a clear advantage, which is mostly caused by a lower effective mass of the electrons of ~0.2-0.3 m_e as compared to ~0.4-0.5 m_e for ZnO. The limits of the carrier mobility as a function of carrier density in ZnO- and In_2O_3-based TCOs, which for high carrier densities is mainly caused by IIS, are shown in Figure 13 by the blue solid lines.

Transparency

Besides having a low resistivity, TCOs should provide excellent transparency for the photon energy range of interest for solar cells (~1.12 − 3.5 eV). Due to their high band gap (E_g>3 eV), ZnO and In_2O_3 are in principle very transparent up to that photon energy, as can be seen by the spectral absorption coefficient of nominally-undoped ZnO in Figure 14(a). Above the band gap of ~3 eV, a strong increase in optical absorption in the ZnO is observed as expected. For higher doping, the onset of absorption shifts to higher photon energies, which corresponds to an increase in optical band gap. This effect is known as the Burstein-Moss (BM) shift: As can be seen in Figure 14(b), the Fermi level
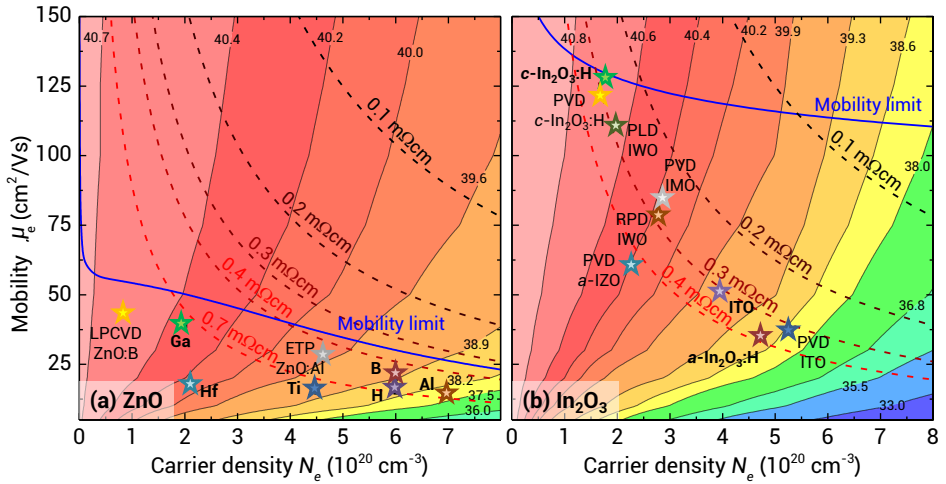
Figure 13: Contour plots of the simulated J_{sc} (in mA/cm^2) of SHJ solar cells featuring a ZnO-based (a) or In$_2$O$_3$-based (b) TCO as a function of carrier density and mobility. Dashed lines are isolines of constant resistivity. The simulated cell structure consists of a textured wafer with 5 nm of intrinsic a-Si:H, 10 nm of p-type a-Si:H and 75 nm of TCO on the front side of the solar cell. Photon currents were simulated using OPAL2 [112] and the optical constants of In$_2$O$_3$ and ZnO were taken from ellipsometry measurements. [106,107] In order to calculate the effect of free-carrier absorption for varying carrier density and mobility, the contribution of the Drude oscillator ε_{Drude} to the modeled dielectric function was varied accordingly. The interband absorption was assumed to remain constant, together with a constant m^* of 0.23m_e for In$_2$O$_3$ and 0.4m_e for ZnO, respectively. The thick solid line is the mobility limit as a function of the carrier density. For ZnO, this was calculated using the Masetti model [113] with the most recent parameters of Ellmer *et al.* [114] The mobility limit for In$_2$O$_3$ was calculated using the mobility limits due to both phonon and ionized impurity scattering. [109,107] For ZnO, literature values (found in Table 5) of ALD films with various dopant atoms are displayed, as well as ZnO:B made by low-pressure CVD and ZnO:Al by expanding thermal plasma CVD. [115] For In$_2$O$_3$, values for amorphous (a-In$_2$O$_3$:H) and crystallized indium oxide (c-In$_2$O$_3$:H) (prepared by ALD) [107], ITO [106], IMO [106] and amorphous IZO [116] (prepared by sputtering) and IWO (prepared by reactive plasma deposition (RPD) [117] and pulsed laser deposition (PLD) [118]) are shown. ALD processes are denoted in bold. [119]

E_F of ZnO is close to the conduction band since it is (almost) degenerate by the unintentional doping. By increased doping of the TCO, the Fermi level is raised further into the conduction band. This leads to an increase of the optical band gap, since the occupied states in the bottom of the conduction band are unavailable for optical transitions from the top of the valence band. In this respect, high doping of the TCO is beneficial since the transparency is extended to higher photon energies. This advantage is however relatively small, since very few photons are present in the solar spectrum at these high photon energies, as can be seen in Figure 14(a).

The free carriers generated by doping lead to increased free carrier absorption (FCA) at low photon energies due to an increase in Drude absorption, as can be seen in Figure 14(a). This is a very detrimental effect, since the solar spectrum contains the most photons at low photon energy. Additionally, this increased Drude contribution reduces
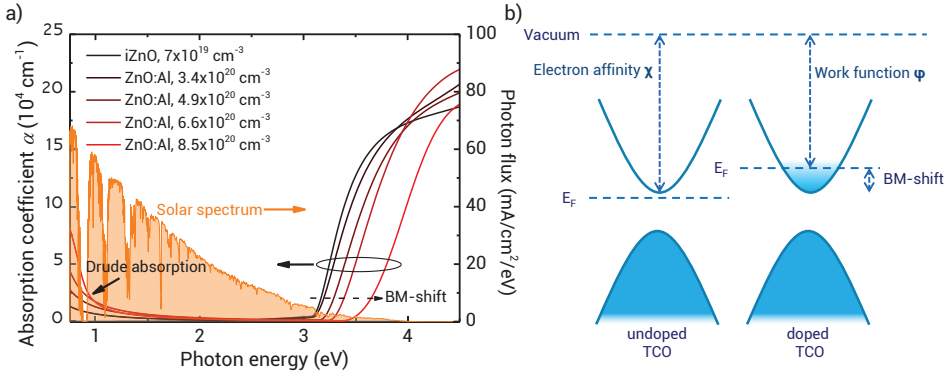
Figure 14: (a) Absorption coefficient of Al-doped ZnO layers of varying carrier density prepared by thermal ALD at 200 °C using DEZ and DMAI as Zn and Al source, respectively. The increasing Drude contribution and Burstein-Moss (BM) shift with doping level are indicated. (b) Schematic band diagram of an unintentionally doped TCO (left) and an intentionally doped TCO (right). The electron affinity χ denotes the energetic distance from the conduction band edge to the vacuum level, whereas the work function φ is the distance from the Fermi level E_F to the vacuum.

the refractive index n at low photon energies, leading to enhanced free carrier reflection (FCR) due to a refractive index mismatch. The Drude contribution to the complex dielectric function ε_{Drude} is determined by the plasma frequency ω_p and the scatter frequency ω_τ :[120]

$$\varepsilon_{Drude}(\omega) = -\frac{\omega_p^2}{\omega^2 + i\omega\omega_\tau}$$
$$\omega_p = \sqrt{\frac{e^2 N_e}{\varepsilon_0 m^*}} \qquad (2.9)$$
$$\omega_\tau = \frac{e}{m^* \mu_e}$$

where ω_p denotes the onset frequency of the Drude contribution, whereas the damping term ω_τ determines the broadening around the onset frequency. From these equations, it can be seen that a high mobility is advantageous in two ways. First, it reduces the required N_e for a low resistivity and thereby it reduces ω_p. At the same time a high mobility (or low ω_τ) reduces the Drude contribution above the plasma frequency because of a reduced broadening.

The effect of the Drude contribution on the J_{sc} of a SHJ solar cell due to FCA and FCR is shown for both ZnO and In$_2$O$_3$-based TCOs in the simulated contour plots of Figure 13. The figure shows that a high μ_e and low N_e are key to achieving a high J_{sc}. On the other hand, both a high μ_e and N_e are desirable for a low resistivity. In this respect, the

higher mobility limit of In_2O_3 compared to ZnO allows for higher J_{sc} as well as lower resistivity values. Nonetheless, the contour plot shows a lower sensitivity of the J_{sc} for N_e and μ_e in the case of ZnO in comparison to In_2O_3. This is mostly due to the higher effective electron mass in ZnO, which leads to a lower ω_p and ω_τ for a given N_e and μ_e, respectively.

For comparison, a selection of carrier density and mobility values taken from literature reports (which will be discussed in the next section) are shown in Figure 13, in which the bold-faced labels denote ALD processes. The ZnO-based processes show mobility values well below the mobility limit, which indicates that scattering processes related to material quality (e.g., grain boundary and neutral impurity scattering) play an important role. Nonetheless, ALD is at least on par with other deposition methods, especially since the reported films deposited by expanding thermal plasma (ETP) and low pressure CVD (LPCVD) were much thicker (>500 nm).

For the In_2O_3-based processes, it can be seen that various high-mobility TCOs have appeared that greatly outperform sputtered ITO. In particular, crystallized In_2O_3:H (*c*-In_2O_3:H) is very promising because of the low resistivity (<0.3 mΩcm) and very high J_{sc} due to a μ_e which is very close to the mobility limit. This material was initially developed by sputtering[121], but recently also an ALD process has been developed as will be discussed later.[4,107] Nonetheless, it has proven to be difficult to make a good metal-TCO contact for this material and the H-doped material is less stable at operating conditions, which however can be remedied by the use of bilayers.[122,123] Recently also sputtered amorphous Zn-doped indium oxide (IZO) has gained interest, as it combines a relatively high μ_e (~60 cm²/Vs) with good metal-TCO contact properties and stability.[116,123] Also Mo-doped In_2O_3 (IMO) and W-doped In_2O_3 (IWO) are high-mobility TCOs, and SHJ solar cells based on the latter TCO in combination with copper metallization have reached efficiencies exceeding 22%.[117]
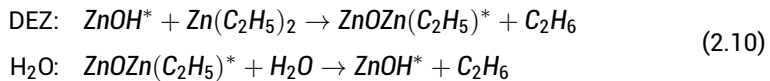
Compatibility with SHJ solar cells

It is required that the produced TCO and the processing thereof is compatible with the SHJ solar cell design and processing. The restrictions in terms of TCO processing are mostly dictated by the ultrathin intrinsic and doped *a*-Si:H layers. Especially the *p*-type doped a-Si:H layer is very temperature sensitive, and this puts an upper limit on the processing temperature of 200 °C.[108] Additionally, these ultrathin layers are prone to plasma-induced damage. For example, sputter deposition of TCOs leads to plasma-induced damage of the underlying *a*-Si:H films, thereby reducing the level of surface passivation.[106,124]Although post-deposition annealing can (partially) recover this damage, the microstructure of the *a*-Si:H layers is irreversibly altered.[124]

In addition to the considerations above, also the work function φ of the TCO is of importance. The front TCO contacting the a-Si:H(p) layer preferably has a φ equal or exceeding the φ of the a-Si:H(p) layer ($\sim$5.3 eV), whereas the rear TCO contacting the a-Si:H(n) layer preferably has a φ equal or below the φ of the aSi:H(n) layer ($\sim$4.2 eV).[125] A mismatch in φ leads to a Schottky contact between the doped a-Si:H/TCO layer, and the associated depletion region can extend into the Si wafer and reduce the band bending, thereby seriously affecting the fill factor and even the open circuit voltage.[126,127] Although this effect can be mitigated by increasing the thickness and doping level of a-Si:H layers, this comes at the expense of enhanced parasitic light absorption and defect density in especially the a-Si:H(p) layer.[125,128] As can be seen in the schematic of Figure 14(b), the φ of a degenerate TCO is determined by the electron affinity χ and the doping level through the Burstein-Moss shift $\chi - \Delta E_{BM} = \varphi$ (ignoring band gap narrowing).[129] Therefore, control over the work function of the TCO through its doping level is of importance for the optimization of the doped a-Si:H/TCO contact.[106,125,128] Since the electron affinity χ of ZnO ($\sim$4.4 eV) is lower than that of In$_2$O$_3$ (5.0 eV), ZnO seems more suited to contact the a-Si:H(n) layer whereas lowly-doped In$_2$O$_3$ is more suited for the front a-Si:H(p) layer.[129] Together with the less stringent requirements on transparency at the rear side of the cell, ZnO-based TCOs are therefore more likely to be an effective low-cost alternative for indium-based TCOs at this side of the cell.[130] In fact, it has been recently shown that doped ZnO can replace the rear ITO without conversion efficiency loss.[130]

2.3.2 ALD of transparent conductive oxides

ALD of doped ZnO

The by far most studied ALD process for ZnO is the process based on diethyl zinc (DEZ, ZnEt$_2$) and water, which yields high growth rates (typically >1.5 Å/cycle) at temperatures <200 °C.[131] The process can be described by the following reaction:[132]

$$
\begin{aligned}
\text{DEZ:} \quad & ZnOH^* + Zn(C_2H_5)_2 \rightarrow ZnOZn(C_2H_5)^* + C_2H_6 \\
\text{H}_2\text{O:} \quad & ZnOZn(C_2H_5)^* + H_2O \rightarrow ZnOH^* + C_2H_6
\end{aligned}
\tag{2.10}
$$

Unintentionally doped ZnO made by ALD can have an electron density up to $\sim 10^{19}$ cm^{-3} due to the presence of oxygen vacancies and/or H dopants. Nonetheless, the resistivity of ZnO is typically in the high 10^{-3} Ωcm regime, which necessitates cationic doping in order to reach the (low) 10^{-4} Ωcm regime required for SHJ solar cell applications.

The most prevalent approach for doping of ZnO is by Al using TMA, although other dopant precursors and atoms such as B, Ga, Ti, Hf and even H have gained significant interest over the last years. An overview of low temperature ALD processes of doped ZnO can be found in Table 5.

The introduction of dopants in the ZnO matrix is most commonly achieved using so-called ALD supercycles. The principle of an ALD supercycle is shown in Figure 15. In such an ALD supercycle, an integer number n of ZnO cycles is followed by one dopant cycle. By repeating such supercycles, a structure as is shown in Figure 16(a) is obtained, in which the dopants lie in distinct planes. This is distinctly different from CVD and PVD methods in which the dopants are randomly incorporated into the lattice. The vertical spacing of dopants can be accurately controlled by the number of ZnO cycles between the dopant (e.g., Al_2O_3) steps, i.e., the cycle ratio *n*. Therefore, using such a supercycle approach, the carrier density can be controlled with great accuracy by the cycle ratio *n*, as shown in Figure 16(b).
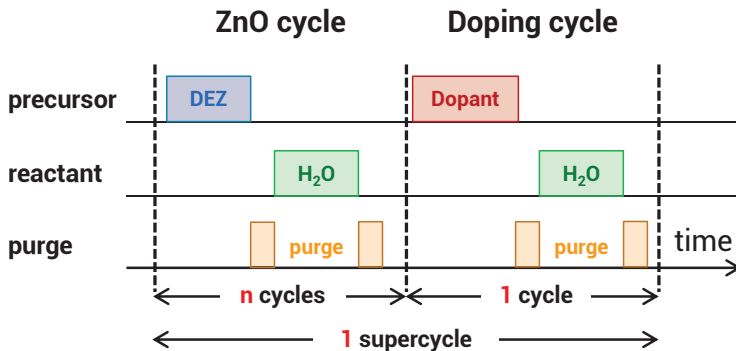

Figure 15: Schematic representation of the ALD supercycle principle. In ALD supercycles used for doping of ZnO, *n* cycles of the ZnO ALD process are followed by 1 cycle of a process containing a dopant element (Al, B, Ga, ...). This supercycle is repeated until the desired film thickness is reached. Adapted from Knoops *et al.*[46]

For a proper control of the vertical spacing of the dopants, it is important to be aware of deviations from steady-state ALD behavior that can occur when switching ALD processes in the supercycle approach. For example, a reduction in growth rate has been observed for ZnO after either a doping step using TMA or a DMAI, which only recovers after 4 ZnO cycles.[136,144] This reduction has been attributed to the coexistence of AlOH* and ZnOH* surface species after the Al_2O_3 step, which leads to proton transfer from the AlOH* group to the relatively basic ZnOH* group, resulting in a reduced density of surface OH groups.[136] Additionally, for the case of TMA it has been observed that ZnO can be etched during the TMA exposure step by the following reaction:

Table 5: Selection of reported low-temperature ALD processes of doped ZnO using DEZ as the Zn source.

Dopant	Doping precursor	T_{dep} (°C)	Doping level (at. %)	N_e (10^{20} cm^{-3})	μ_e (cm²/Vs)	ρ (mΩcm)	Ref
Al	AlMe$_3$	200	1.9	1.4	14	3.1	133
	AlMe$_3$*	170	-	4.3	7	2.1	134
	AlMe$_3$†	200	7	8	-	-	135
	AlMe$_2$(O^{i}Pr)	250	4.6	10	6	1.1	136
	AlMe$_2$(O^{i}Pr)	200	-	0.7-7	13-16	0.7-6.7	106
B	B(O^{i}Pr)$_3$	150-240	1.6	<3	<12	2.2-3.5	137
	B$_2$H$_6$	150	-	~6	~20	0.64	138
Ti	Ti(OCHMe$_2$)$_4$	200	1.6	2.9	20	1.05	139
			-	~4.5	~15	0.9	140
Ga	GaMe$_3$	210	-	~2	25-40	0.8	141
Hf	Hf(NMeEt)$_4$	220	1.7	2.1	17	1.6	142
H	H$_2$ plasma	200	-	6	15	0.7	143

* This process uses dehydroxylation to decrease the amount of TMA deposited.
† This process uses functionalization by alkyl alcohols to decrease the amount of TMA deposited.

$$ZnOH^* + Al(CH_3)_3 \rightarrow Al(CH_3)OH^* + Zn(CH_3)_2 \tag{2.11}$$
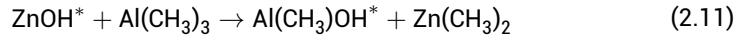
Such effects show that the growth per super cycle (GPSC) can vary from what would be expected from linear addition of the growth rates of the comprising ALD cycles.
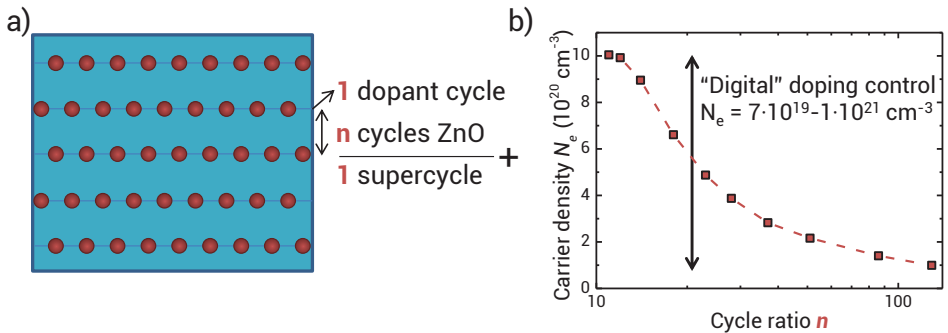

Figure 16: (a) Schematic representation of the superstructure obtained when using ALD supercycles. The cycle ratio *n* controls the vertical spacing of the dopants. (b) Demonstration of the accurate control over the carrier density in ZnO that is possible using the supercycle approach. The used process employs DMAI as dopant precursor and DEZ as Zn precursor, at a deposition temperature of 200 °C.

The supercycle approach presented inherently results in planes of high dopant density in the superstructure, which potentially leads to clustering of dopants. Such clustering can have several detrimental effects. First, clustering leads to a reduced doping efficiency, which enhances neutral impurity scattering by inactive dopants and limits the maximum achievable doping level. Secondly, the dopant cycle can interrupt the grain growth of the ZnO, thereby enhancing grain boundary scattering.[105] Finally, for a given dopant density, ionized impurity scattering is minimized when the dopants are isotropically distributed. Therefore, besides control over the vertical spacing, also control over the lateral spacing of dopants is highly desired for optimization of doped ZnO layers.

Several approaches have been proposed in literature to reduce this dopant clustering by reducing the number of dopant atoms deposited per cycle. Wu *et al*. have shown that by replacing TMA as dopant precursor by a bulkier precursor, such as DMAI, the lateral distance between Al atoms can be increased due to enhanced steric hindrance, as is schematically shown in 17.[136] Because of the decrease in Al atoms deposited per dopant cycle from ∼1.1 at/nm^2 to ∼0.3 at/nm^2, the percentage of Al atoms in the film that are active as dopant, i.e., the doping efficiency, increases from ∼10% to almost 60%.[136] Due to this, a maximum carrier density level up to 10^{21} cm^{-3} could be achieved, as opposed to a maximum of ∼4×10^{20} cm^{-3} for TMA.

Besides the use of steric hindrance, the amount of Al deposited in the dopant step can

Clustered dopants
Low doping efficiency

Low steric hindrance
High # Al atoms nm^{-2} $cycle^{-1}$

Dispersed dopants
Enhanced doping efficiency

Enhanced steric hindrance
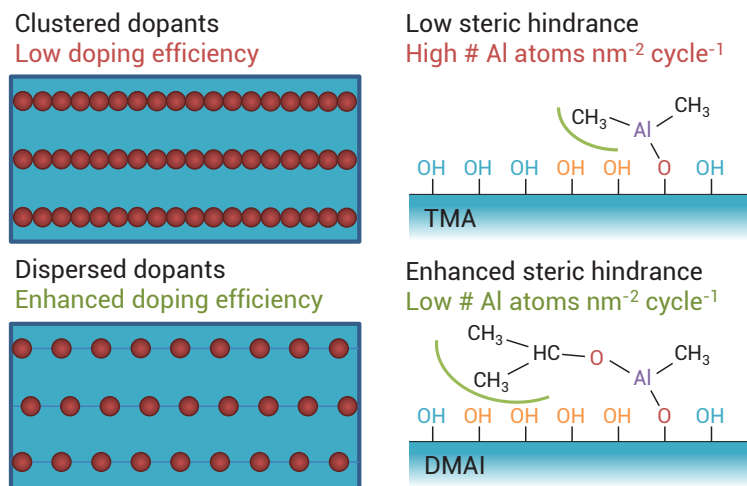**Low # Al atoms nm^{-2} $cycle^{-1}$**

Figure 17: Schematic of the correlation between dopant clustering and doping efficiency. One approach for reduced dopant clustering is the use of dopant precursors with bulky ligands that lead to steric hindrance, as is shown for TMA and DMAI in the figure.

also be reduced by reducing the amount of hydroxyl sites available for TMA chemisorption. A rather simple approach was used by Park *et al*., who prolonged the purge time after the water dose in order to reduce the amount of hydroxyl groups via dehydroxylation reactions.[134] Another approach is to dose the TMA immediately after the last DEZ dose, i.e., to omit the H_2O dose. Since less hydroxyl sites are available for TMA chemisorption, the Al incorporation is reduced and the doping efficiency is enhanced.[144] Finally, functionalization of the surface by exposure to alkyl alcohols prior to TMA exposure can be used to reduce the amount of sites available for chemisorption of TMA. The alkoxide or alkoxylate surface groups that are formed are subsequently removed during the oxidant step.[135]

Beyond Al doping: Doping by B, Ti, Ga, Hf and H

Although Al doping has been the by far most studied dopant for ZnO, other dopant atoms such as B, Ti, Ga, Hf and even H have gained significant interest as well. Boron-doping of ZnO, well known in the field of low-pressure CVD, has been demonstrated using both B_2H_6 and triisopropyl borate ($B(O^iPr)_3$, or TIB) as B-precursors. Using B_2H_6, Sang *et al*. reported on ZnO:B with a promisingly low resistivity of 0.64 mΩcm obtained at a low deposition temperature of 150 °C (See Table 5).[138] Also the carrier mobility, 20 cm^2/Vs, was quite respectable. Despite these promising results, few further reports on the use of B_2H_6 as ALD dopant can be found in literature. This could very well be due to the high

toxicity of B_2H_6 in conjunction with its extremely high vapor pressure, which renders controlled dosing difficult. [137] Recently, $B(O^iPr)_3$ has emerged as a promising alternative B-precursor. At a deposition temperature of 200 °C a low resistivity of 0.9 mΩcm could be achieved. Like in the case of DMAI, the $B(O^iPr)_3$ precursor benefits from its bulky ligands in reducing the amount of B dopants deposited per cycle. [137]

As can be seen from Table 5, also the use of Ti and Ga as dopant has been shown to enable resistivity values <1 mΩcm. Interestingly, Thomas *et al*. have demonstrated that it is also possible to dope ZnO with H by interleaving ZnO cycles by H_2 plasma treatments. [143] In this way, a resistivity of 0.7 mΩcm was achieved at a reasonably high mobility of 15 cm^2/Vs. To conclude this section on doped ZnO, several groups have shown that resistivity values well below 1 mΩcm can be achieved at low temperatures (<200 °C). Key to achieving efficient doping is reduction of dopant clustering through the use of clever approaches to reduce the number of dopant atoms deposited per cycle. Even though values typical for conventional sputtered ITO ($\sim$0.4 mΩcm) cannot be reached, considerations regarding cost and material availability could make doped ZnO an effective alternative to ITO, especially at the rear side of a SHJ solar cell.

ALD of In_2O_3

Although historically Sn-doped In_2O_3 (ITO) has been the most widely used TCO for SHJ solar cells, relatively less literature on ALD of In_2O_3-based TCOs seems to be available compared to ZnO. In Table 6, a brief overview of ALD processes of (doped) In_2O_3 is shown. In 1995 Asikainen *et al*. demonstrated ALD of both In_2O_3 and ITO using a halide $InCl_3$ precursor, and achieved a very low resistivity of 0.25 mΩcm by Sn-doping. [145] However, the process featured a low GPC of 0.2 Å and required a high deposition temperature of 500 °C. At lower temperatures, the use of $In(acac)_3$, $In[(^iPrN)_2CN(CH_2Me)]_3$, $InMe_3$, DMLDMIn, $In(TMHD)_3$ and InCp have been reported. $In(acac)_3$ and $In[(^iPrN)_2CN(CH_2Me)]_3$ have a somewhat higher GPC, but the optoelectronic properties have so far not been reported. $InMe_3$ and H_2O can yield a reasonable resistivity ($\sim$3 mΩcm) at an intermediate temperature (200-250 °C) and a GPC of 0.39 Å. In 2006, Elam *et al*. demonstrated an ALD process for In_2O_3 based on cyclopentadienyl indium (InCp) and ozone at temperatures 200-450 °C. [151] Promisingly, a high GPC of 1.3-2.0 Å was achieved and a very low resistivity of 0.3 mΩcm was reached at 275 °C by Sn-doping using TDMASn and H_2O_2. A few years later, Libera *et al*. showed that although H_2O and O_2 by themselves do not yield growth in combination with InCp, a combination of H_2O and O_2 as oxidants yields a high GPC (1.0-1.6 Å) at very low deposition temperatures (100-250 °C). [153] They proposed that both oxidants are needed for growth since they serve different roles, i.e., H_2O eliminates the Cp ligand and O_2 oxidizes the surface In from oxidation state +1 to +3.

Table 6: Selection of reported ALD processes for (doped) In_2O_3.

Dopant	Precursors	T_{dep} (°C)	N_e (10^{20} cm^{-3})	μ_e (cm²/Vs)	ρ (mΩcm)	GPC (Å)	Ref
-	InCl₃, H₂O	500	0.25	72	3	0.2	145
Sn	InCl₃, SnCl₂, H₂O	500	5.2	47	0.25	0.2	145
-	In(acac)₃, H₂O	160-255	-	-	30-6×10⁴	0.15-0.25	146
-	In[(iPrN)₂CN(CH₂Me)]₃, H₂O	230-300	-	-	-	0.45	147
-	InMe₃, H₂O	200-250	0.27	84	2.8	~0.39	148
-	DMLDMIn, H₂O	300	0.75	28.7	1.6	0.6	149
-	In(TMHD)₃, O₂ plasma	100-400	-	-	2.5-18	0.14	150
-	InCp, O₃	200-450	-	-	16	1.3-2.0	151
Sn	InCp, O₃, TDMASn, H₂O₂	275	4	50	0.3	1.1-1.7	152
H?	InCp, H₂O+O₂	100-250	0.8-4.5	38-111	0.34-2.5	1.0-1.6	153
H‡	InCp, H₂O+O₂	100	1.8	138	0.27	1.2	4,107

‡ The films were post-crystallized at 150-200 °C

Moreover, a low resistivity of 0.34 mΩcm was achieved for an amorphous film at 100 °C. The highest mobility value of 111 cm^2/Vs was achieved at 140 °C, which is around the amorphous polycrystalline growth transition temperature.

Macco *et al.* have demonstrated that the ALD process of Libera *et al.* using InCp and a combination of O_2 and H_2O actually unintentionally yields H-doped In_2O_3 (In_2O_3:H), where an amorphous film deposited at 100 °C has a H content of 4.2 at. %.[107] By low temperature post-deposition annealing at 150-200 °C, solid phase crystallization of the film occurs, which yields a low resistivity of 0.27 mΩcm at a record-high electron mobility of 138 cm^2/Vs and a relatively low carrier density of 1.8×10^{20} cm^{-3}. This combination leads to negligible free carrier absorption in the photon energy range relevant for SHJ solar cells.[4] In fact, the quality of crystallized layers is such that only phonon and ionized impurity scattering processes play a role, meaning that the mobility is at its fundamental limit, as can also be seen in Figure 13(b).[107] The excellent optoelectronic properties in combination with the low temperature processing and high growth rate make this process very interesting for SHJ solar cell applications. To the authors' knowledge, there are currently no ALD processes reported for IZO, IMO and IWO, which is a clear opportunity for further development.

2.3.3 High volume manufacturing of ALD TCOs

Although ALD is not yet used in industry for the preparation of TCOs for SHJ solar cells, the ALD approach can potentially offer some key benefits over the most-commonly used sputtering method. First, due to the absence of harsh plasma conditions during ALD, plasma damage (e.g., during sputtering) to the substrate is avoided. Therefore, recent studies have focused on the use of ALD as a "soft deposition" method to deposit TCOs in SHJ solar cells and have demonstrated improved passivation.[106,154] Additionally, as shown in the section on ALD of doped ZnO, ALD allows for a high level of control over the doping level of the TCO and thereby its work function. This greatly facilitates the optimization of the doped *a*-Si:H/TCO contact by varying the doping level and potentially even the doping profile.[106,125,128] Moreover, after the recent introduction of high-throughput ALD reactors for HVM of Al_2O_3 in the PV industry, also the deposition of (doped) ZnO by such reactors, most notably spatial ALD (S-ALD), is being explored.[155,156,77,157,158] As can be seen in Table 7, S-ALD processes have been reported that combine high deposition rates exceeding 1 nm/s with rather good material properties. In particular, Ellinger *et al.* showed that a very low resistivity (<0.5 mΩcm) can be obtained at high growth rates (1.5 nm/s), on par with typical growth rates obtained with sputtering, at an intermediate deposition temperature (250 °C).

A key difference between temporal and spatial ALD of doped TCOs is that in spatial

Table 7: Selection of reported S-ALD results of both intrinsic and doped ZnO using DEZ as the Zn source.

Doping precursor	Growth rate (nm/s)	T_{dep} (°C)	N_e (10^{20} cm^{-3})	μ_e (cm^2/Vs)	ρ (mΩcm)	Ref
-	0.6	200	-	-	$1\text{-}2\times10^5$	159, 160
-	~1	75-250	0.2-0.7	14-30	4-150	158
$AlMe_3$	0.2	200	5	6	2	161
$AlMe_2(O^iPr)$	~1.5	250	-	-	0.46	162
$InMe_3$	0.1	200	6	3	3	157
$GaMe_3$	0.4	250	-	-	2	163

ALD the dopants can, apart from using the supercycle approach, also be introduced by premixing or by co-injection with the other precursor, due to a homogeneous delivery of the precursor to the substrate. In such approaches, both precursors compete for reactive surface sites. As a result, the amount of dopant incorporation depends for example on the partial pressures of both precursors and can even depend on exposure times. [161] One might thus say that some level of control which is typical for the supercycle approach is lost when switching to premixed or co-injected precursors. Nonetheless, the good material properties that have been reported and the ability to even successfully deposit other multicomponent oxides such as InGaZnO demonstrate that this is not necessarily a drawback for the industrial application of precursor mixing or co-injection in S-ALD. [158]

2.4 Prospects for ALD in passivating contacts

In this section, the upcoming field of passivating contacts and the possible role of ALD therein will be discussed. First, the basic principles and requirements of passivating contacts and some of its concepts will be outlined. Subsequently, examples of passivating tunnel and carrier-selective oxides and the use of ALD for preparing such oxides will be reviewed.

2.4.1 Basics of passivating contacts

A passivating contact is typically a stack of thin films on the Si absorber, which passivates the Si surface and simultaneously acts as a selective membrane for either holes or electrons. Examples include the traditional silicon heterojunction cell and the TOPCon concept, as discussed in the introduction.

How to make a passivating contact

To briefly illustrate the working principle and the merits of passivating contacts, schematic band diagrams of example strategies to produce carrier-selective contacts are shown in Figure 18. All diagrams consider the Si under illumination, which leads to excess charge carriers. Since in a metal (or TCO) there can be no quasi-Fermi level splitting, the two quasi-Fermi levels must converge at the contact. Since a gradient in a Fermi level represents a force, this leads to a current of both electrons (J_n) and holes (J_p) towards the metal:

$$J_n = en\mu_n\nabla E_{Fn}, J_p = ep\mu_p\nabla E_{Fp} \qquad (2.12)$$

In these equations, μ_n and μ_p are the electron and hole mobility. Also note that all these quantities in principle depend on the spatial coordinate x. In order for a contact to be selective, the region or film(s) in between the Si and metal contact must, besides providing passivation, induce a strong asymmetry in the electron and hole currents to the metal contact. In order to understand how this asymmetry can be achieved, one should realize that equation 2.12 is basically Ohm's law for electrons and holes.[164] If the conductivity for a charge carrier is high (i.e., a high product of mobility and carrier concentration), there will be a low gradient in quasi-Fermi level towards the contact for a given current (i.e., little voltage drop). Therefore, in the case of a passivating contact, the quasi-Fermi level of the carrier that is to be extracted should be as flat as possible (i.e., low resistance), whereas the other quasi-Fermi level should show a high degree of bending (i.e., high resistance). This is markedly different from an ideal passivation layer on Si where both quasi-Fermi levels are flat (high resistance to both carriers), and

a Si/metal contact, in which case in principle both quasi-Fermi levels will bend (low resistance to both carriers).

In Figure 18(a), the conventional method for making an electron-selective contact ($J_n \gg J_p$) is shown, i.e., by heavily doping the Si. The selectivity for electrons arises from the high resistance for holes in the heavily doped n^+ Si region. Note that the holes actually experience a strong force towards the metal, as seen by the strong gradient of the Fermi level, E_{Fp}. Nevertheless, the hole current J_p in this region is very low since the large energetic distance between the valence band and E_{Fp} ensures a low density of holes p and hence a high resistivity for holes. Although contacts based on such homojunctions can be very selective, the V_{oc} of such devices is typically limited by Auger recombination occurring in the highly-doped region. This drawback is avoided by using passivating contacts, examples of which are depicted in Figure 18(b-d).

In Figure 18(b) the TOPCon concept is shown. Here, the n^+ doping of the (partially) crystalline Si layer provides selectivity to extract electrons in a fashion quite similar to the doped region of Figure 18(a). A very thin SiO_2 tunnel oxide of $\sim$1.4 Å, typically prepared by a nitric acid oxidation step (NAOS), provides chemical passivation and acts as a diffusion barrier for dopants. Note that the typical thickness of the doped Si layer (few tens of nanometers) is much less than a typical doped region ($\sim$0.5 μm) and thus leads to much less Auger recombination.

In Figure 18(c), an electron-selective contact is formed by band-alignment: A wide band gap material is deposited on Si, with little (or ideally no) conduction band offset. In this way, the hole current J_p is greatly reduced by the large valence band offset. Again, the strong gradient in E_{Fp} shows that the holes experience a strong force towards the metal, but the large energetic distance between the valence band and E_{Fp} ensures a low density of holes p in the metal oxide film and thereby a low hole current J_p. Note that for simplicity it is here assumed here that no band bending occurs (i.e., no fixed charge and equal work functions of the n-type Si and the metal oxide film are assumed).

In Figure 18(d), a hole-selective contact is formed by induced band-bending: In this example, the high work function ($>\sim$5.5 eV) of a metal oxide (such as MoO_x, WO_x or VO_x), induces a strong upward bend bending at the n-type Si surface leading to inversion. Whereas the band bending reduces the electron concentration at the surface, the band bending facilitates a high hole current J_p to the metal.

In Figure 19 an overview is given of the band offsets with Si of (a selection of) oxides that are of interest for the formation of a passivating contact. It should be noted that these values can vary considerably depending on the exact processing conditions, and the values are therefore indicative. Ta_2O_5, TiO_2 and strontium titanate (STO) are of interest as electron-selective contact due to their small conduction band offset. Likewise, NiO is of interest as a hole-selective contact due to its small conduction band
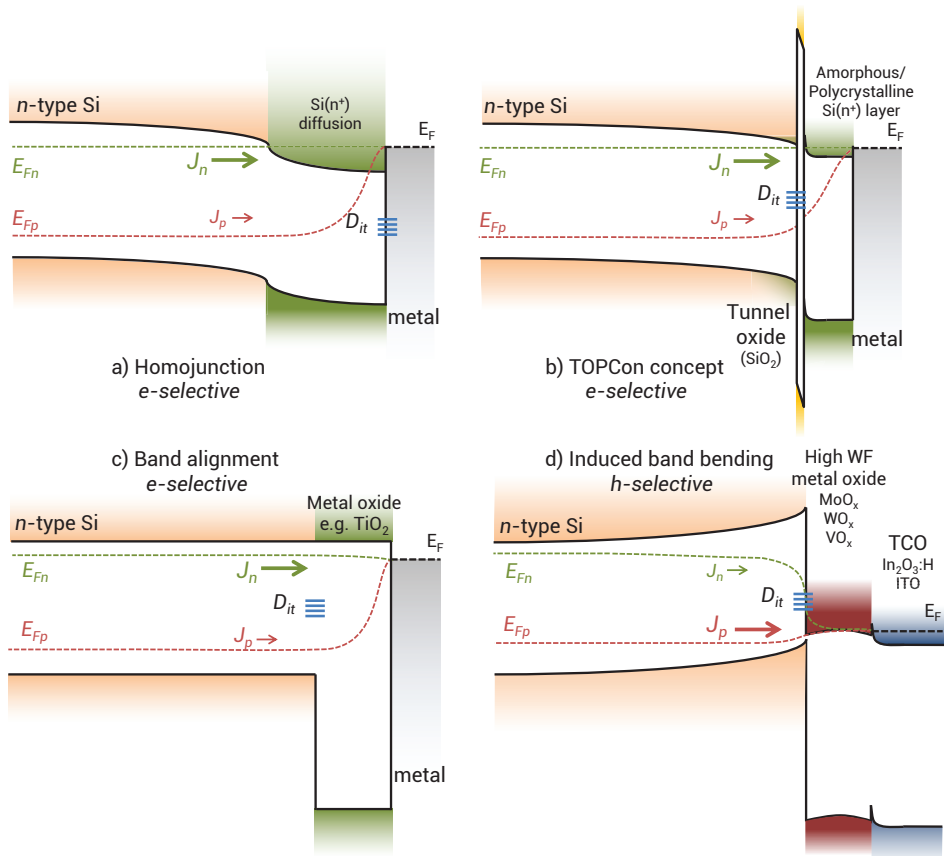
Figure 18: Schematic band diagrams of various approaches for making carrier selective contacts. All band diagrams refer to the situation under illumination and are not drawn to scale. (a) A conventional electron-selective contact made by n^+-type doping. (b) An electron-selective contact made by the TOPCon concept, consisting of a tunnel oxide and a thin (partially) crystalline n^+-Si film. (c) An electron-selective contact which is realized through *band-alignment* of the Si with a metal oxide film. (d) A hole-selective contact which is realized through *induced band-bending* by a high work function metal oxide film. Often concepts (c) and (d) also employ separate ultra-thin passivation layers, but these were not drawn for simplicity.

offset,[18,165] whereas MoO_3 and WO_3 form hole-selective contacts by induced band-bending.[166,17]

For simplicity, separate passivation layers were not shown in the band diagrams in Figure 18. Nonetheless, since the oxides used for selectivity generally do not offer (excellent) passivation, many passivating contact schemes employ a-Si:H or ultrathin (<2 nm) tunnel oxide layers such as Al_2O_3 and SiO_2 in the between the Si and the carrier-selective layer for interface passivation.§
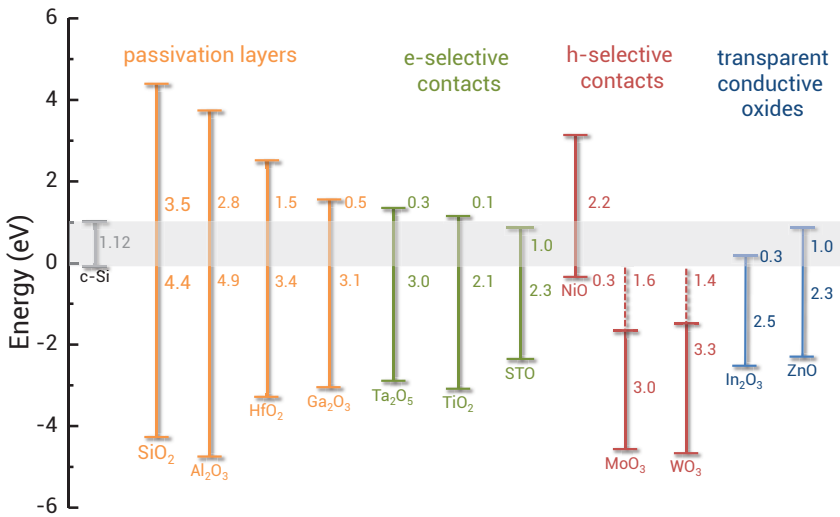
Figure 19: Schematic of the band offsets of a selection of oxides with Si. Offsets are denoted in eV. Adapted from references 167 and 168.

In Figure 19, also typically used oxide passivation layers are shown. As discussed in section 2.2, such oxides should have a low interface defect density D_{it}, whereas the presence of a fixed charge density Q_f can be either beneficial or detrimental to the passivation quality depending on the doping of the wafer. When applied to passivating contacts, additional requirements for such layers come into play. Since the oxides should allow for tunneling, the D_{it} should be low even for ultrathin (<2 nm) layers. The presence of fixed charge is also of importance, as the band bending induced by fixed charge can affect the selectivity, analogous to the case of Figure 18(d). For example, the high negative fixed charge of Al_2O_3 makes Al_2O_3 more suited for hole-selective contacts rather than electron-selective contacts. Finally, the band offsets with Si play a role as well since tunnel probabilities are inversely and exponentially proportional to the band off-

§Besides providing interface passivation, these layers are also thought to aid in selectivity: If for example a-Si:H is added in between the Si and high ψ metal oxide of Figure 18(d), most of the drop in E_{Fn} will occur in the a-Si:H instead of in the Si. Since the mobility in a-Si:H is orders of magnitudes lower than in Si, this will lead to a reduced J_n towards the metal contact, according to equation 2.

sets. For example, for SiO_2 the asymmetry in the valence band (4.4 eV) and conduction band (3.5 eV) offset makes it such that electrons tunnel much easier than holes.[169] Therefore, asymmetry in the band offsets can also aid in selectivity.

Requirements of a passivating contact

To assess the potential of various passivating contact schemes, it is instructive to discuss the two main figures of merit of a passivating contact:

- The contact resistance ρ_c for the charge carrier type the contact should be selective to.

- The recombination current of the other charge carrier type to the metal contact, which can be characterized by J_0.

To a first order approximation, the contact resistance influences the *FF*, whereas the recombination current limits the V_{oc}. In Figure 20, a contour plot of the maximum Si solar cell efficiency is displayed as a function of the ρ_c and J_0 values of the rear contact. This calculation assumes a full area rear contact with no other loss mechanisms (no optical losses, no other recombination anywhere in the cell and no other resistive losses), and thus represents the upper bound of the solar cell efficiency set by the rear contact.

As can be seen from Figure 20, high efficiency (>25 %) devices require both low ρ_c (<1 Ωcm^2) and J_0 (<100 fA/cm^2) values, a region which can be defined as a criterion for being a passivating contact. For comparison, a typical Si/metal contact in a *p*-type Al-BSF concept has a very low contact resistivity ($\sim$5 mΩcm^2), but the high J_0 (>500 fA/cm^2) severely limits the cell efficiency. On the other hand, an Al_2O_3 passivation layer can yield a very low J_0 (<10 fA/cm^2), but is insulating. For this reason, many solar cell designs (e.g., PERC and PERL) employ a local metal contacting scheme: By making local metal contacts to the silicon, a trade-off is made between passivated regions of low J_0 ($J_{0,pass}$) with contacting regions that have a high J_0 ($J_{0,cont}$) but a low ρ_c. The effective J_0 and ρ_c of a locally contacted rear are determined by the contact area fraction *f* by the relations $J_{0,eff} = fJ_{0,cont} + (1 - f)J_{0,pass}$ and $\rho_{c,eff} = \rho_c/f$. However, local contacting might add to processing complexity and additionally induces resistive *FF* losses in the bulk of Si due to the required lateral transport of carriers therein, as shown in Figure 21.[3]

Figure 20 also shows literature values for various passivating contact concepts, as well as for various rear sides of cells using partial metallization. The classical SHJ concept based on (doped) *a*-Si:H layers is probably the best-known example of a passivating contact. The rear contact of the current record solar cell of Kaneka (25.1% efficiency) combines a very low J_0 value of 12 fA/cm^2 with a low contact resistivity of 30
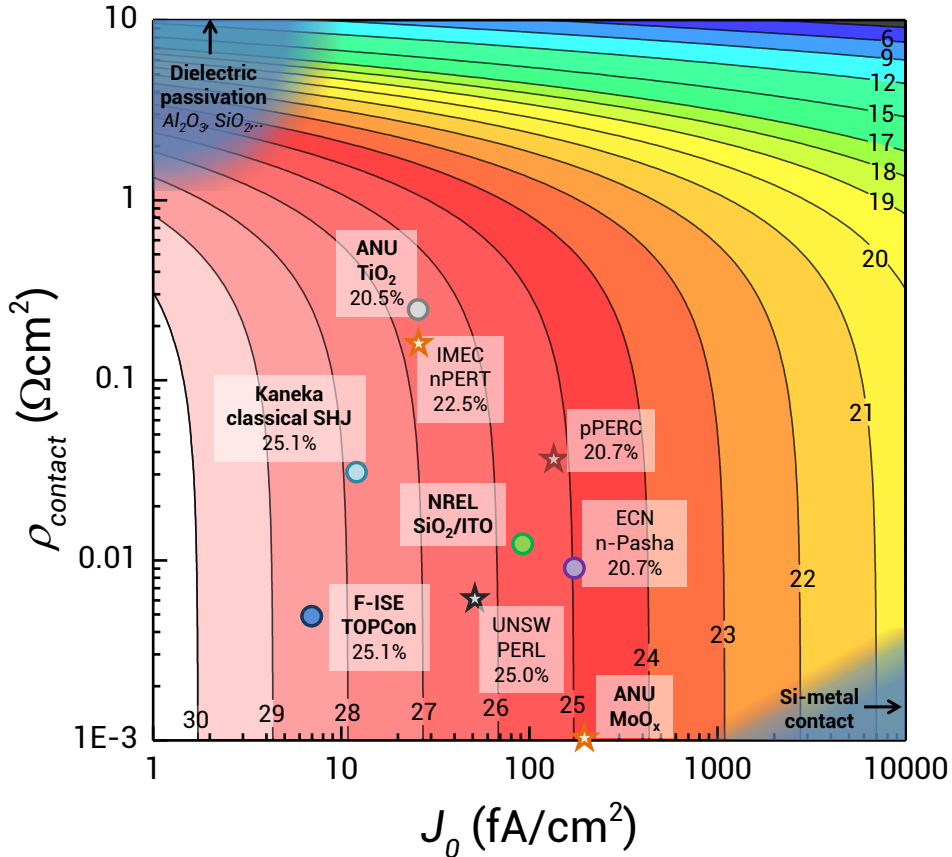
Figure 20: Contour plot of the calculated upper limit of efficiency of a solar cell featuring a full area passivating contact, as a function of J_0 and ρ_c. The calculation is done similarly as in references [170] and [171] and assumes no other recombination channels (surface nor bulk), no shunting and no optical losses (i.e., a J_{sc} of 44 mA/cm^2). For comparison, data points for various reported structures/cells are shown, along with the efficiencies of the full devices. These include a SHJ cell of Kaneka [14,172], the TOPCon concept of F-ISE [3,173], the SiO$_2$/ITO stack of NREL [170], the TiO$_2$ cell of ANU [174], the UNSW PERL cell [175], a *p*-type PERC cell [175], the IMEC nPERT cell [176], the ECN nPasha cell [175,172] and a *p*-type Si/MoO$_x$ contact [177]. Hole-selective contacts are denoted by star-shaped symbols, whereas electron-selective contacts are denoted by circular symbols. Concepts employing a full area rear contact are noted in bold. For the PERL cell, the J_0 was estimated using the reported surface recombination velocity in reference [175] and case 3 in reference [24]. For cell concepts that use a partial rear contact, the J_0 and ρ_c values have been corrected for the contact area fraction *f*.
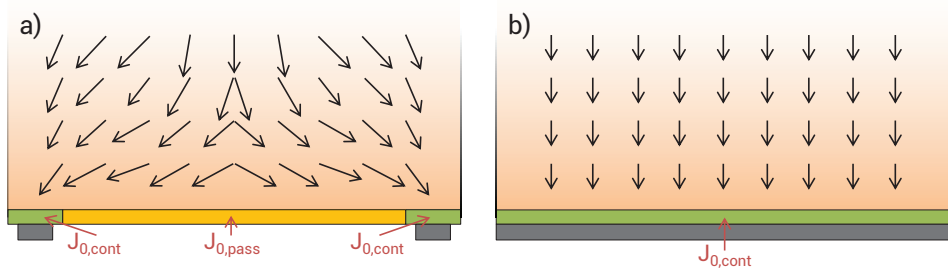
Figure 21: Schematic showing the current flow pattern in (a) a locally contacted cell and (b) a solar cell with a full-area rear contact. Adapted from Glunz *et al.*[3]

$m\Omega cm^2$.[14] The TOPCon concept and the SiO_2/ITO stack of Young *et al.*[170] (as will be discussed below) are both electron-selective contacts that use a tunnel oxide. As can be seen, both concepts have a very low ρ_c, demonstrating that efficient transport can occur through such oxides. Moreover, the TOPCon concept shows that very low J_0 values can be achieved with tunnel oxides. Due to the excellent properties of such passivating contacts, full area contacts can be employed while still having a low J_0. This has the benefit of having one-dimensional charge transport in the solar cell, thereby reducing resistive losses due to lateral transport, as well as being very straightforward from a processing point of view. As can be seen, the solar cell concepts employing partial rear metallization are also capable of reaching low ρ_c values, but the local metal contacts inevitably lead to higher J_0 values. As will be discussed below, other metal oxide films are promising for passivating contact formation as well, such as TiO_2 for electron-selective contacts and MoO_x, WO_x and VO_x for hole-selective contacts. Evaporated MoO_x directly on p-type Si has been reported to have a very low contact resistivity (1 $m\Omega cm^2$) and an intermediate J_0 of $\sim$200 fA/cm^2, as can be seen in Figure 20.[177] Because of the low ρ_c and intermediate J_0, such contacts are best used in a partial rear contacting scheme, as shown by a reported 20.4% efficient solar cell using a 5% rear contact area fraction.[178] Moreover, MoO_x has been used as a replacement of the a-Si:H(p) layer in a conventional SHJ solar cell. Due to the passivating properties of the a-Si:H layer, an impressive 22.5% efficiency has been reported for a full area front contact.[179] The J_0 and ρ_c values of the a-Si:H/MoO_x/TCO contact were not reported for this solar cell.

2.4.2 ALD for passivating contacts

As was discussed in the previous section, (stacks of) various thin films are of interest to serve as passivating contact, which in principle can be prepared by ALD. Moreover, the use of ALD may offer distinct advantages, e.g., in terms of processing/doping control and the easy manufacturing of stacks. Nonetheless, this new field has yet to be fully

explored. Therefore, in this section the possible role of ALD in preparing tunneling oxides and carrier-selective oxides is discussed, addressing both the few examples of ALD already shown in this field as well as the future prospects.

ALD for tunneling oxides

For tunnel oxides, the contact resistivity (i.e., ρ_c) and level of surface passivation (i.e., J_0) are extremely dependent on the thickness of the oxide. Therefore, it is expected that the submonolayer thickness control over a large surface area offered by ALD can be a key enabler in this respect. It is worth mentioning that ultrathin ALD Al_2O_3 has also been used in between the metal contacts and the highly-doped region of the Si wafer in PERC cells. Although this is strictly spoken not a passivating contact, it has been shown that only 2 cycles of Al_2O_3 enhances the passivation (12 mV increase in V_{oc}) without a significant increase in contact resistivity.[180]

A tunneling ALD Al_2O_3 film has been successfully used in a Al_2O_3/ZnO(:Al) stack to make a hole-selective contact, fully prepared by ALD.[22,21] Such a stack achieves selectivity towards holes by the negative fixed charge in the Al_2O_3 which leads to accumulation of holes at the Si surface, which is analogous to the use of a high work function metal oxide as in Figure 18(d). The holes subsequently recombine with the electrons in the conduction band of the ZnO(:Al). Interestingly, such a stack takes advantage of the fact that the fixed charge in Al_2O_3 has been observed to be interfacial, i.e., it resides at the Si-Al_2O_3 interface, and is thus persistent even for ultrathin films.[181] Additionally, the position of the Fermi level in the TCO, which is readily tuned in ALD by control of the doping level, was found to be crucial for the working of such a contact. Nonetheless, although this work nicely demonstrates a proof-of-concept, the high reported J_0 (>10^4 fA/cm^2) and intermediate ρ_c (>1Ωcm^2) values hinder a high efficiency.

Besides Al_2O_3, many passivating contacts employ SiO_2 as tunnel oxide. Young *et al*. have shown that a stack of thin SiO_2 and sputtered ITO can also make an electron-selective contact through energetic lineup of the Fermi levels of the Si and the heavily degenerate ITO.[170] Promisingly, a low J_0 of 92.5 fA/cm^2 and a contact resistivity ρ_c of only 11.5 mΩcm^2 were achieved, as indicated in Figure 20. Remarkably, the optimal SiO_2 thickness prior to ITO sputtering was found to be 4.5 nm, much more than would be expected on the basis of a tunneling process. This has been attributed to intermixing of the SiO_2/ITO layer by the energetic ions coming from the plasma.[170] In this respect, atomic layer deposition of TCOs (In_2O_3:H, ZnO)[106] could be a much better controlled process due to the absence of plasma-related damage.[124]

Finally it is worth noting that the use of ultrathin ALD metal oxides as tunneling layers has already been explored in the field of organic PV.[182,183] Specifically, ALD layers of

Ga_2O_3 and Ta_2O_5 have been used successfully in such cells. These two materials have recently been shown to provide excellent Si surface passivation, making also these materials highly interesting for passivating contact formation for Si solar cells. [98,99]

ALD for electron-selective contacts

An electron-selective contact has been prepared by an ultrathin (1-4 nm) layer of TiO_2 by Avasthi *et al*. [19] The selectivity of this film is achieved through band alignment as shown in Figure 18(c). Although the work of Avasthi *et al*. demonstrates the electron selectivity of TiO_2, the rather simple device structure and lack of passivation severely limited the performance of the device. Promisingly, as discussed earlier, Liao *et al*. have demonstrated that it is possible to achieve excellent surface passivation using a thermal ALD process using $TiCl_4$ and H_2O at 100 °C to deposit TiO_2, which suggests that this concept could be optimized further. [100] In other work also a very low surface recombination velocity of 16 cm/s was observed for a carefully prepared TiO_2/Si heterojunction, showing that this interface can be highly passivating. [184] Yang *et al*. have subsequently demonstrated that 4.5 nm of TiO_2 prepared by ALD (using $Ti(O^iPr)_4$ and H_2O at 230 °C) can also yield a relatively low contact resistivity of $\sim$0.25 Ωcm^2 and a J_0 of 25 fA/cm^2. [174] When combining this ALD TiO_2 with a 1.5 nm SiO_2 interlayer, they demonstrated an impressive 20.5% efficiency for their champion cell.

As can be seen from Figure 19, also Ta_2O_5 and STO have the proper band alignment to serve as an electron-selective contact. As already pointed out in section 2.2.4, ALD Ta_2O_5 can provide excellent surface passivation when capped with SiN_x. [99] Therefore, the use of a dedicated passivation layer in between the Si and Ta_2O_5 can potentially be avoided. Nonetheless, the observed negative fixed charge of $\sim$10^{12} cm^{-3} observed might hinder the working as a selective electron contact.

STO is mostly known in the semiconductor industry for its very high dielectric constant. It has been shown experimentally that the conduction band off-set of STO on both *n*- and *p*-type Si is negligible ($\sim$0.1 eV) and does not change significantly if a very thin SiO_2 interlayer is applied (<1.2 nm). [185] More importantly, DFT calculations predict that the conduction band offset is highly dependent on the initial layer of the STO thin film: The desired negligible conduction band offset (0.1-0.2 eV) occurs when the initial layer of the STO film consists of SrO, whereas a higher offset of 1.2-1.3 eV has been predicted when the initial layer consists of TiO_2. [186] Since both the interfacial and bulk composition can be controlled accurately by ALD by choosing the appropriate initial cycle (TiO_2 or SrO) and cycle ratio, [187] respectively, it can be expected that ALD is very well suited for the preparation of such oxides.

¶The reported GPC is the growth per supercycle for a [SrO]/[TiO$_2$] cycle ratio of 1:3
#The reported GPC is the growth per supercycle for a [SrO]/[TiO$_2$] cycle ratio of 1:1

Table 8: Selection of ALD processes reported in literature of potential carrier-selective oxides.

Metal Oxide	Metal Precursor	Reactant	T_{dep} (^{0}C)	GPC (Å)	Ref
Electron-selective oxides					
TiO_2	$Ti(O^iPr)_4$	H_2O	150-300	0.2-0.3	188
	$TiCl_4$	H_2O	100	0.6	100
	$Ti(Cp^*)(OMe)_3$	O_2 plasma	50-300	0.5	189
	$Ti(NMe_2)_4$	H_2O	25-325	0.5-1.4	190
Ta_2O_5	$Ta_2(OEt)_{10}$	H_2O	250	0.3	99
	$Ta(NMe_2)_5$	O_2 plasma	100-250	0.8-0.9	189
	$Ta(NMe_2)_5$	H_2O/O_3	200-300	0.9/1.1	191
STO	$Cp(Me)_5Ti(OMe)_3$ + $Sr(^iPr_3Cp)_2DME$	O_2 plasma	150-350	2.3-2.6¶	187
	$Ti(O^iPr)_4$ + $Sr(thd)_2$	H_2O plasma	250	0.6#	192
Hole-selective oxides					
MoO_x	$(N^tBu)_2(NMe_2)_2Mo$	O_3	100-300	0.3-2.4	193
	$(N^tBu)_2(NMe_2)_2Mo$	O_2 plasma	50-350	0.8-1.9	20, 194
	$Mo(CO)_6$	O_3	152-172	0.8	195
WO_x	$(N^tBu)_2(NMe_2)_2W$	H_2O	300-350	0.4-1.0	196
	$W(CO)_6$	O_3	195-205	0.2	197
	$WH_2(^iPrCp)_2$	O_2 plasma	300	0.9	198
VO_x	$V(NEtMe)_4$	H_2O	125-200	0.8	199
	$VO(OPr)_3$	H_2O	170-190	1.0	200
	$VO(OPr)_3$	O_2/H_2O plasma	50-200	0.7	201
NiO_x	$Ni(Et_2Cp)_2$	O_3	150-300	0.4-0.9	202
	$Ni(thd)_2$	H_2O	260	0.4	203
	$Ni(Cp)_2$	H_2O	165	-	204
	$Ni(dmamp)_2$	H_2O	120	0.8	205

ALD for hole-selective contacts

Molybdenum oxide (MoO_x) is well-known in the organic PV literature as a hole transport material. However, it has only very recently been demonstrated that evaporated MoO_x can replace the hole-selective a-Si:H(p) layer at the front of a standard SHJ solar cell.[16,177,206] The working principle of such a selective hole contact is thought to be based on the high work function of MoO_x ($\sim$6.6 eV), as shown in Figure 18(d). Promisingly, the reduced optical losses enable a substantial enhancement in photocurrent of 1.9 mA/cm^2. Currently, the highest reported efficiency for a MoO_x-based SHJ is already 22.5%, which is very promising given the novelty of this approach.[179]

Recently, it has also been shown that MoO_x can be deposited by plasma-enhanced ALD using $(N^tBu)_2(NMe_2)_2Mo$ and O_2 plasma at temperatures down to 50 °C.[194] Additionally, this ALD MoO_x layer was implemented in an a-Si:H/MoO_x/ALD In_2O_3:H stack (Figure 22), and a high level of passivation in combination with a high optical transparency was demonstrated.[20] In other work, initial solar cell results based on ALD MoO_x have been reported, although the efficiency (11%) is not yet on par with its evaporated counterpart.[207]
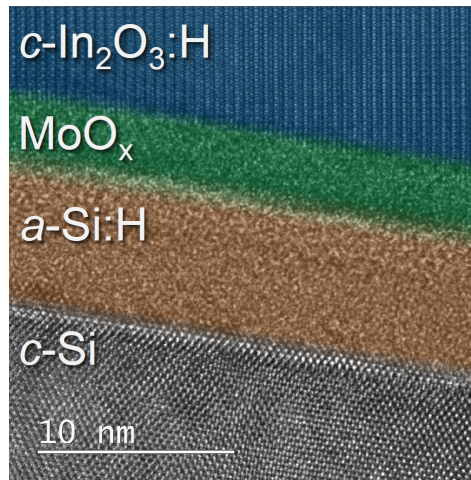
Figure 22: False-colored cross-sectional TEM image of a stack of amorphous silicon, ALD MoO_x and crystallized ALD hydrogen-doped indium oxide (c-In_2O_3:H). Adapted from Macco $et\ al.$[20]

For the other aforementioned hole-selective materials of WO_x, VO_x and NiO_x, there have been no reports yet on the use of ALD to make carrier-selective contacts with these materials. Since all these materials can be made by ALD, it is likely that this will be explored in the near future. The assessment of the passivation quality, possibly in combination with an a-Si:H layer or a tunnel oxide, and the carrier-selectivity should be the main focus when screening ALD approaches for the fabrication of passivating

contacts.

2.5   Conclusions and outlook

In the field of Si photovoltaics, ALD of Al_2O_3 resulted in a break-through in the passivation of p-type Si surfaces. As a result, it is currently incorporated in solar cells with high efficiencies over 25% and it enables challenging concepts, such as solar cells with black Si surface textures. Due to these successes, in the last few years high-throughput reactors based on temporal and spatial ALD have successfully been developed. These reactors can meet the stringent demands of high-volume manufacturing in photovoltaic industries in terms of throughput and cost, and ALD is competitive with other techniques for the deposition of Al_2O_3. Also other materials prepared by ALD have successfully been explored for the passivation of Si. Examples include HfO_2, SiO_2, Ga_2O_3, Ta_2O_5 and TiO_2, which altogether can passivate a variety of doped surfaces. The passivation by SiO_2/Al_2O_3 stacks has recently even been successfully scaled up using batch ALD.

Apart from surface passivation, also the potential of ALD to prepare transparent conductive oxides, such as doped ZnO and In_2O_3 films, has been recognized. Key advantages of ALD as deposition method of TCOs include a very precise control in film properties, in particular when using extrinsic dopants, such as for doped ZnO. Moreover, its soft nature does not induce damage on sensitive a-Si:H passivation layers. For In_2O_3 TCOs prepared by ALD, the electron mobility is record high and reaches even the fundamental limit. The latter allows for the best possible trade-off between conductivity and transparency. Altogether, these merits make ALD very promising as deposition method for TCOs in Si solar cell manufacturing, although its potential is yet to be demonstrated on a solar cell level. Moreover, also the industrial viability of ALD to prepare TCOs in solar cell manufacturing remains to be determined, although the deposition of doped ZnO films by high-throughput spatial ALD reactors has recently been achieved.

Finally, an interesting, emerging field of research governs passivating contacts. In this field, very thin films or stacks of metal oxides (i.e., a thickness of 1-80 nm) should meet many requirements in terms of surface passivation, carrier selectivity to Si, a low contact resistance, etc. Fortunately, ALD is ideally suited to deposit such stacks in a precisely controlled way. Moreover, the knowledge gained from ALD of TCOs and passivating films can be combined in this field. For instance, stacks of Al_2O_3/ZnO are pioneered as a hole-selective contact to Si, whereas SiO_2/In_2O_3 stacks are promising as an electron-selective passivating contact. With high-throughput ALD reactors available, it is likely that if such passivating contact schemes have come to full development, they can be prepared in a single deposition run, even on both sides of the solar cells at once. This could yield a significant process simplification in Si solar cell manufacturing and

would underline the potential of ALD in the field of photovoltaics.

References

[1] Fraunhofer, ©Fraunhofer ISE: Photovoltaics Report (2016).

[2] G. Agostinelli, P. Vitanov, Z. Alexieva, A. Harizanova, H. F. W. Dekkers, S. De Wolf, and G. Beaucarne, Proceedings of the 19th European PVSEC, WIP, Paris (2004).

[3] S. W. Glunz, F. Feldmann, A. Richter, M. Bivour, C. Reichel, H. Steinkemper, J. Benick, and M. Hermle, Presented at the 31st European Photovoltaic Solar Energy Conference and Exhibition (2015).

[4] B. Macco, Y. Wu, D. Vanhemel, and W. M. M. Kessels, physica status solidi (RRL) - Rapid Research Letters **8**, 987 (2014).

[5] M. A. Green, K. Emery, Y. Hishikawa, W. Warta, and E. D. Dunlop, Progress in Photovoltaics: Research and Applications **22**, 701 (2014).

[6] P. J. Cousins, D. D. Smith, H.-C. Luan, J. Manning, T. D. Dennis, A. Waldhauer, K. E. Wilson, G. Harley, and W. P. Mulligan, in *2010 35th IEEE Photovoltaic Specialists Conference* (IEEE, 2010) pp. 275–278.

[7] K. Masuko, M. Shigematsu, T. Hashiguchi, D. Fujishima, M. Kai, N. Yoshimura, T. Yamaguchi, Y. Ichihashi, T. Mishima, N. Matsubara, T. Yamanishi, T. Takahama, M. Taguchi, E. Maruyama, and S. Okamoto, IEEE Journal of Photovoltaics **4**, 1433 (2014).

[8] D. Smith, P. Cousins, S. Westerberg, R. De Jesus-Tabajonda, G. Aniero, and Y.-C. Shen, IEEE Journal of Photovoltaics **4**, 1465 (2014).

[9] A. Richter, M. Hermle, and S. W. Glunz, IEEE Journal of Photovoltaics **3**, 1184 (2013).

[10] J. Benick, B. Hoex, M. C. M. van de Sanden, W. M. M. Kessels, O. Schultz, and S. W. Glunz, Applied Physics Letters **92**, 253504 (2008).

[11] B. W. H. van de Loo, H. C. M. Knoops, G. Dingemans, G. J. M. Janssen, M. W. P. E. Lamers, I. G. Romijn, A. W. Weeber, and W. M. M. Kessels, Solar Energy Materials and Solar Cells **143**, 450 (2015).

[12] M. Taguchi, A. Yano, S. Tohoda, K. Matsuyama, Y. Nakamura, T. Nishiwaki, K. Fujita, and E. Maruyama, IEEE Journal of Photovoltaics **4**, 96 (2014).

[13] N. Nandakumar, B. Dielissen, D. Garcia-alonso, Z. Liu, and W. M. M. Kessels, in *Technical proceedings of the 6th WCPEC conference* (2014) pp. 577–578.

[14] D. Adachi, J. L. Hernández, and K. Yamamoto, Applied Physics Letters **107**, 233506 (2015).

[15] A. Moldovan, F. Feldmann, M. Zimmer, J. Rentsch, J. Benick, and M. Hermle, Solar Energy Materials and Solar Cells , 1 (2015).

[16] C. Battaglia, S. M. de Nicolás, S. De Wolf, X. Yin, M. Zheng, C. Ballif, and A. Javey, Applied Physics Letters **104**, 113902 (2014).

[17] L. G. Gerling, S. Mahato, A. Morales-Vilches, G. Masmitja, P. Ortega, C. Voz, R. Alcubilla, and J. Puigdollers, Solar Energy Materials and Solar Cells , 1 (2015).

[18] R. Islam and K. C. Saraswat, in *2014 IEEE 40th Photovoltaic Specialist Conference (PVSC)* (IEEE, 2014) pp. 0285–0289.

[19] S. Avasthi, W. E. McClain, G. Man, A. Kahn, J. Schwartz, and J. C. Sturm, Applied Physics Letters **102**, 203901 (2013).

[20] B. Macco, M. F. J. Vos, N. F. W. Thissen, A. A. Bol, and W. M. M. Kessels, physica status solidi (RRL) – Rapid Research Letters **9**, 393 (2015).

[21] S. Smit, D. Garcia-Alonso, S. Bordihn, M. S. Hanssen, and W. M. M. Kessels, Solar Energy Materials and Solar Cells **120**, 376 (2014).

[22] D. Garcia-Alonso, S. Smit, S. Bordihn, and W. M. M. Kessels, Semiconductor Science and Technology **28**, 082002 (2013).

[23] J. A. del Alamo and R. Swanson, IEEE Transactions on Electron Devices **31**, 1878 (1984).

[24] K. R. McIntosh and L. E. Black, Journal of Applied Physics **116**, 014503 (2014).

[25] G. Dingemans, M. C. M. van de Sanden, and W. M. M. Kessels, physica status solidi (RRL) - Rapid Research Letters **5**, 22 (2011).

[26] B. Hoex, F. J. J. Peeters, A. J. M. Erven, M. D. Bijker, W. M. M. Kessels, and M. C. M. van de Sanden, in *2006 IEEE 4th World Conference on Photovoltaic Energy Conference*, Vol. 1 (IEEE, 2006) pp. 1036–1039.

[27] G. Agostinelli, A. Delabie, P. Vitanov, Z. Alexieva, H. Dekkers, S. De Wolf, and G. Beaucarne, Solar Energy Materials and Solar Cells **90**, 3438 (2006).

[28] B. Hoex, J. Schmidt, R. Bock, P. P. Altermatt, M. C. M. Van De Sanden, and W. M. M. Kessels, Applied Physics Letters **91**, 112107 (2007).

[29] A. Cuevas, T. Allen, J. Bullock, Yimao Wan, Di, and Xinyu Zhang, in *2015 IEEE 42nd Photovoltaic Specialist Conference (PVSC)*, 1 (IEEE, 2015) pp. 1–6.

[30] G. Dingemans and W. M. M. Kessels, Journal of Vacuum Science & Technology A: Vacuum, Surfaces, and Films **30**, 040802 (2012).

[31] S. Dauwe, L. Mittelstadt, A. Metz, and R. Hezel, Progress in Photovoltaics: Research and Applications **10**, 271 (2002).

[32] I. Dirnstorfer, D. K. Simon, P. M. Jordan, and T. Mikolajick, Journal of Applied Physics **116**, 044112 (2014).

[33] R. B. M. Girisch, R. P. Mertens, and R. F. De Keersmaecker, IEEE Transactions on Electron Devices **35**, 203 (1988).

[34] P. P. Altermatt, A. Schenk, F. Geelhaar, and G. Heiser, Journal of Applied Physics **93**, 1598 (2003).

[35] D. Yan and A. Cuevas, Journal of Applied Physics **114**, 044508 (2013).

[36] D. Yan and A. Cuevas, Journal of Applied Physics **116**, 194505 (2014).

[37] P. J. Cousins and J. E. Cotter, Solar Energy Materials and Solar Cells **90**, 228 (2006).

[38] A. F. Thomson and K. R. McIntosh, Applied Physics Letters **95**, 052101 (2009).

[39] A. S. Grove, O. Leistiko, and C. T. Sah, Journal of Applied Physics **35**, 2695 (1964).

[40] K. Jäger and R. Hezel, Proceedings of the 18th IEEE PVSC, Las Vegas , 1752 (1985).

[41] R. Hezel and K. Jaeger, Journal of The Electrochemical Society **136**, 518 (1989).

[42] B. Hoex, S. B. S. Heil, E. Langereis, M. C. M. Van De Sanden, and W. M. M. Kessels, Applied Physics Letters **89**, 042112 (2006).

[43] G. S. Higashi and C. G. Fleming, Applied Physics Letters **55**, 1963 (1989).

[44] J. Schmidt, A. Merkle, R. Brendel, B. Hoex, M. C. M. van de Sanden, and W. M. M. Kessels, Progress in Photovoltaics: Research and Applications **16**, 461 (2008).

[45] J. Benick, B. Hoex, M. C. M. van de Sanden, W. M. M. Kessels, O. Schultz, and S. W. Glunz, Applied Physics Letters **92**, 253504 (2008).

[46] H. C. M. Knoops, S. E. Potts, A. A. Bol, and W. M. M. Kessels, *Handbook of Crystal Growth*, second edition ed. (Elsevier B.V., 2015) pp. 1101–1134.

[47] G. Dingemans, N. M. Terlinden, D. Pierreux, H. B. Profijt, M. C. M. van de Sanden, and W. M. M. Kessels, Electrochemical and Solid-State Letters **14**, H1 (2011).

[48] H. B. Profijt, P. Kudlacek, M. C. M. van de Sanden, and W. M. M. Kessels, Journal of The Electrochemical Society **158**, G88 (2011).

[49] G. Dingemans, R. Seguin, P. Engelhart, M. C. M. V. D. Sanden, and W. M. M. Kessels, physica status solidi (RRL) - Rapid Research Letters **4**, 10 (2010).

[50] B. Hoex, M. Bosman, N. Nandakumar, and W. M. M. Kessels, physica status solidi (RRL) - Rapid Research Letters **7**, 937 (2013).

[51] G. Dingemans, W. Beyer, M. C. M. van de Sanden, and W. M. M. Kessels, Applied Physics Letters **97**, 152106 (2010).

[52] A. Richter, J. Benick, M. Hermle, and S. W. Glunz, Applied Physics Letters **104**, 061606 (2014).

[53] G. Dingemans, F. Einsele, W. Beyer, M. C. M. van de Sanden, and W. M. M. Kessels, Journal of Applied Physics **111**, 093713 (2012).

[54] D. K. Simon, P. M. Jordan, I. Dirnstorfer, F. Benner, C. Richter, and T. Mikolajick, Solar Energy Materials and Solar Cells **131**, 72 (2014).

[55] G. Dingemans, C. A. A. van Helvoirt, D. Pierreux, W. Keuning, and W. M. M. Kessels, Journal of the Electrochemical Society **159**, H277 (2012).

[56] G. Dingemans, N. M. Terlinden, M. A. Verheijen, M. C. M. van de Sanden, and W. M. M. Kessels, Journal of Applied Physics **110**, 093715 (2011).

[57] S. Bordihn, V. Mertens, J. W. Müller, and W. M. M. Kessels, Journal of Vacuum Science & Technology A: Vacuum, Surfaces, and Films **32**, 01A128 (2014).

[58] S. G. A. Richter, S. Henneck, J. Benick, M. Hörteis, M. Hermle, in *Proceedings of the 25th EU-PVSEC, Valencia, Spain* (2010) pp. 1453 – 1459.

[59] L. Hennen, E. H. A. Granneman, and W. M. M. Kessels, in *2012 38th IEEE Photovoltaic Specialists Conference*, August (IEEE, 2012) pp. 1049−1054.

[60] B. Vermang, H. Goverde, A. Uruena, A. Lorenz, E. Cornagliotti, A. Rothschild, J. John, J. Poortmans, and R. Mertens, Solar Energy Materials and Solar Cells **101**, 204 (2012).

[61] N. M. Terlinden, G. Dingemans, W. M. M. Kessels, and M. C. M. van de Sanden, Applied Physics Letters **96**, 112101 (2010).

[62] D. Schuldis, A. Richter, J. Benick, P. Saint-Cast, M. Hermle, and S. W. Glunz, Applied Physics Letters **105**, 231601 (2014).

[63] P. P. Altermatt, J. O. Schumacher, A. Cuevas, M. J. Kerr, S. W. Glunz, R. R. King, G. Heiser, and A. Schenk, Journal of Applied Physics **92**, 3187 (2002).

[64] S. C. Baker-Finch and K. R. McIntosh, IEEE Journal of Photovoltaics **1**, 59 (2011).

[65] K. R. C. Mok, B. W. H. van de Loo, A. H. G. Vlooswijk, W. M. M. Kessels, and L. K. Nanver, IEEE Journal of Photovoltaics **5**, 1310 (2015).

[66] B. Liao, R. Stangl, F. Ma, T. Mueller, F. Lin, A. G. Aberle, C. S. Bhatia, and B. Hoex, Journal of Physics D: Applied Physics **46**, 385102 (2013).

[67] L. E. Black, T. G. Allen, K. R. McIntosh, and A. Cuevas, Journal of Applied Physics **115**, 093707 (2014).

[68] W. Liang, K. J. Weber, D. Suh, S. P. Phang, J. Yu, A. K. McAuley, and B. R. Legg, IEEE Journal of Photovoltaics **3**, 678 (2013).

[69] S. P. Phang, W. Liang, B. Wolpensinger, M. A. Kessler, and D. MacDonald, IEEE Journal of Photovoltaics **3**, 261 (2013).

[70] B. Hoex, M. C. M. van de Sanden, J. Schmidt, R. Brendel, and W. M. M. Kessels, physica status solidi (RRL) - Rapid Research Letters **6**, 4 (2012).

[71] A. Richter, J. Benick, A. Kimmerle, M. Hermle, and S. W. Glunz, Journal of Applied Physics **116**, 243501 (2014).

[72] S. Bordihn, G. Dingemans, V. Mertens, J. W. Muller, and W. M. M. Kessels, IEEE Journal of Photovoltaics **3**, 925 (2013).

[73] S. Bordihn, P. Engelhart, V. Mertens, G. Kesser, D. Köhn, G. Dingemans, M. M. Mandoc, J. W. Müller, and W. M. M. Kessels, Energy Procedia **8**, 654 (2011).

[74] E. H. A. Granneman, V. I. Kuznetsov, and P. Vermont, ECS Transactions **61**, 3 (2014).

[75] G. Dingemans and W. M. M. Kessels, Proceedings of the 25th European Photovoltaic Solar Energy Conference , 1083 (2010).

[76] N. Nandakumar, F. Lin, B. Dielissen, F. Souren, X. Gay, R. Gortzen, S. Duttagupta, A. G. Aberle, and B. Hoex, in *28th European Photovoltaic Solar Energy Conference and Exhibition* (2013) pp. 1105–1107.

[77] J. A. van Delft, D. Garcia-Alonso, and W. M. M. Kessels, Semiconductor Science and Technology **27**, 074002 (2012).

[78] M. K. S. Miyajima, J. Irikawa, A. Yamada, in *Proceedings of the 23rd EU-PVSEC, Valencia, Spain*, September (2008) pp. 1029–1032.

[79] L. E. Black, T. G. Allen, A. Cuevas, K. R. McIntosh, B. Veith, and J. Schmidt, Solar Energy Materials and Solar Cells **120**, 339 (2014).

[80] T.-T. Li and A. Cuevas, physica status solidi (RRL) - Rapid Research Letters **3**, 160 (2009).

[81] J. Schmidt, F. Werner, and B. Veith, Photovoltaics International **10**, 2 (2010).

[82] X. Zhang and A. Cuevas, physica status solidi (RRL) – Rapid Research Letters **7**, 619 (2013).

[83] D. S. Saynova, I. G. Romijn, I. Cesar, M. W. P. E. Lamers, A. Gutjahr, G. Dingemans, H. C. M. Knoops, B. W. H. van de Loo, W. M. M. Kessels, O. Siarheyeva, E. H. A. Granneman, L. Gautero, D. M. Borsa, P. R. Venema, and V. A. H. G., in *28th European Photovoltaic Solar Energy Conference and Exhibition* (2013) pp. 1188 – 1193.

[84] G. Dingemans and W. M. M. Kessels, in *ECS Transactions*, Vol. 41 (2011) pp. 293–301.

[85] S. Duttagupta, F.-J. Ma, S. F. Lin, T. Mueller, A. G. Aberle, and B. Hoex, IEEE Journal of Photovoltaics **3**, 1163 (2013).

[86] N. M. Terlinden, G. Dingemans, V. Vandalon, R. H. E. C. Bosch, and W. M. M. Kessels, Journal of Applied Physics **115**, 033708 (2014).

[87] D. K. Simon, P. M. Jordan, I. Dirnstorfer, F. Benner, C. Richter, and T. Mikolajick, Solar Energy Materials and Solar Cells **131**, 72 (2014).

[88] A. Richter, J. Benick, and M. Hermle, IEEE Journal of Photovoltaics **3**, 236 (2013).

[89] W.-C. Wang, C.-W. Lin, H.-J. Chen, C.-W. Chang, J.-J. Huang, M.-J. Yang, B. Tjahjono, J.-J. Huang, W.-C. Hsu, and M.-J. Chen, ACS applied materials & interfaces **5**, 9752 (2013).

[90] H. Savin, P. Repo, G. von Gastrow, P. Ortega, E. Calle, M. Garín, and R. Alcubilla, Nature Nanotechnology **10**, 624 (2015).

[91] P. Spinelli, B. Macco, M. A. Verschuuren, W. M. M. Kessels, and A. Polman, Applied Physics Letters **102**, 233902 (2013).

[92] G. von Gastrow, R. Alcubilla, P. Ortega, M. Yli-Koski, S. Conesa-Boj, A. Fontcuberta i Morral, and H. Savin, Solar Energy Materials and Solar Cells **142**, 29 (2015).

[93] T. G. Allen, J. Bullock, A. Cuevas, S. Baker-Finch, and F. Karouta, in *2014 IEEE 40th Photovoltaic Specialist Conference (PVSC)* (IEEE, 2014) pp. 562–566.

[94] M. Otto, M. Kroll, T. Käsebier, R. Salzer, A. Tünnermann, and R. B. Wehrspohn, Applied Physics Letters **100**, 1 (2012).

[95] P. Repo, A. Haarahiltunen, L. Sainiemi, M. Yli-Koski, H. Talvitie, M. C. Schubert, and H. Savin, IEEE Journal of Photovoltaics **3**, 90 (2013).

[96] P. Repo, J. Benick, G. V. Gastrow, V. Vähänissi, F. D. Heinz, J. Schön, M. C. Schubert, and H. Savin, Physica Status Solidi - Rapid Research Letters **7**, 950 (2013).

[97] Y. Liu, A. Das, Z. Lin, I. B. Cooper, A. Rohatgi, and C. P. Wong, Nano Energy **3**, 127 (2014).

[98] T. G. Allen and A. Cuevas, Applied Physics Letters **105**, 031601 (2014).

[99] Y. Wan, J. Bullock, and A. Cuevas, Applied Physics Letters **106**, 201601 (2015).

[100] B. Liao, B. Hoex, A. G. Aberle, D. Chi, and C. S. Bhatia, Applied Physics Letters **104**, 253903 (2014).

[101] F. Benner, P. M. Jordan, C. Richter, D. K. Simon, I. Dirnstorfer, M. Knaut, J. W. Bartha, and T. Mikolajick, Journal of Vacuum Science & Technology B: Microelectronics and Nanometer Structures **32**, 03D110 (2014).

[102] D. K. Simon, P. M. Jordan, M. Knaut, T. Chohan, T. Mikolajick, and I. Dirnstorfer, in *2015 IEEE 42nd Photovoltaic Specialist Conference (PVSC)* (IEEE, 2015) pp. 1–6.

[103] D. Suh, physica status solidi (RRL) - Rapid Research Letters **9**, 344 (2015).

[104] P. Repo, H. Talvitie, S. Li, J. Skarp, and H. Savin, Energy Procedia **8**, 681 (2011).

[105] Y. Wu, P. M. Hermkens, B. W. H. van de Loo, H. C. M. Knoops, S. E. Potts, M. A. Verheijen, F. Roozeboom, and W. M. M. Kessels, Journal of Applied Physics **114**, 024308 (2013).

[106] B. Macco, D. Deligiannis, S. Smit, R. A. C. M. M. van Swaaij, M. Zeman, and W. M. M. Kessels, Semiconductor Science and Technology **29**, 122001 (2014).

[107] B. Macco, H. C. M. Knoops, and W. M. M. Kessels, ACS Applied Materials & Interfaces **7**, 16723 (2015).

[108] S. De Wolf, A. Descoeudres, Z. C. Holman, and C. Ballif, Green **2**, 7 (2012).

[109] T. Pisarkiewicz, K. Zakrzewska, and E. Leja, Thin Solid Films **174**, 217 (1989).

[110] N. Preissler, O. Bierwagen, A. T. Ramu, and J. S. Speck, Physical Review B **88**, 085305 (2013).

[111] K. Ellmer, Nature Photonics **6**, 809 (2012).

[112] K. R. McIntosh and S. C. Baker-Finch, in *2012 38th IEEE Photovoltaic Specialists Conference* (IEEE, 2012) pp. 265–271.

[113] G. Masetti, M. Severi, and S. Solmi, Electron Devices, IEEE , 764 (1983).

[114] K. Ellmer and R. Mientus, Thin Solid Films **516**, 4620 (2008).

[115] K. Sharma, B. L. Williams, A. Mittal, H. C. M. Knoops, B. J. Kniknie, N. J. Bakker, W. M. M. Kessels, R. E. I. Schropp, and M. Creatore, International Journal of Photoenergy **2014**, 1 (2014).

[116] M. Morales-Masis, S. Martin De Nicolas, J. Holovsky, S. De Wolf, and C. Ballif, IEEE Journal of Photovoltaics **5**, 1340 (2015).

[117] J. Yu, J. Bian, W. Duan, Y. Liu, J. Shi, F. Meng, and Z. Liu, Solar Energy Materials and Solar Cells **144**, 359 (2016).

[118] P. F. Newhouse, C.-H. Park, D. A. Keszler, J. Tate, and P. S. Nyholm, Applied Physics Letters **87**, 112108 (2005).

[119] B. Macco, H. C. M. Knoops, M. F. J. Vos, Y. Kuang, M. A. Verheijen, and W. M. M. Kessels, Presented at the 31st European Photovoltaic Solar Energy Conference and Exhibition (2015).

[120] H. C. M. Knoops, B. W. H. van de Loo, S. Smit, M. V. Ponomarev, J.-W. Weber, K. Sharma, W. M. M. Kessels, and M. Creatore, Journal of Vacuum Science & Technology A: Vacuum, Surfaces, and Films **33**, 021509 (2015).

[121] T. Koida, H. Fujiwara, and M. Kondo, Japanese Journal of Applied Physics **46**, L685 (2007).

[122] L. Barraud, Z. C. Holman, N. Badel, P. Reiss, A. Descoeudres, C. Battaglia, S. De Wolf, and C. Ballif, Solar Energy Materials and Solar Cells **115**, 151 (2013).

[123] T. Tohsophon, A. Dabirian, S. De Wolf, M. Morales-Masis, and C. Ballif, APL Materials **3**, 116105 (2015).

[124] B. Demaurex, S. De Wolf, A. Descoeudres, Z. C. Holman, and C. Ballif, Applied Physics Letters **101**, 171604 (2012).

[125] K.-U. Ritzau, M. Bivour, S. Schröer, H. Steinkemper, P. Reinecke, F. Wagner, and M. Hermle, Solar Energy Materials and Solar Cells , 1 (2014).

[126] R. Rößler, C. Leendertz, L. Korte, N. Mingirulli, and B. Rech, Journal of Applied Physics **113**, 144513 (2013).

[127] M. Bivour, S. Schröer, and M. Hermle, Energy Procedia **38**, 658 (2013).

[128] A. Tomasi, F. Sahli, L. Fanni, J. P. Seif, S. M. D. Nicolas, N. Holm, J. Geissbühler, B. Paviet-salomon, P. Löper, S. Nicolay, S. D. Wolf, and C. Ballif, IEEE Journal of Photovoltaics **6**, 17 (2016).

[129] A. Klein, C. Körber, A. Wachau, F. Säuberlich, Y. Gassenbauer, S. P. Harvey, D. E. Proffit, and T. O. Mason, Materials **3**, 4892 (2010).

[130] G. R. P. Carroy, D. Muñoz, F. Ozanne, A. Valla, P. Mur, in *30th EU PVSEC* (2015) pp. 359 − 364.

[131] T. Tynell and M. Karppinen, Semiconductor Science and Technology **29**, 043001 (2014).

[132] J. W. Elam and S. M. George, Chemistry of Materials **15**, 1020 (2003).

[133] D.-J. Lee, H.-M. Kim, J.-Y. Kwon, H. Choi, S.-H. Kim, and K.-B. Kim, Advanced Functional Materials **21**, 448 (2011).

[134] H. K. Park and J. Heo, Applied Surface Science **309**, 133 (2014).

[135] A. Yanguas-Gil, K. E. Peterson, and J. W. Elam, Chemistry of Materials **23**, 4295 (2011).

[136] Y. Wu, S. E. Potts, P. M. Hermkens, H. C. M. Knoops, F. Roozeboom, and W. M. M. Kessels, Chemistry of Materials **25**, 4619 (2013).

[137] D. Garcia-Alonso, S. E. Potts, C. A. A. van Helvoirt, M. A. Verheijen, and W. M. M. Kessels, J. Mater. Chem. C **3**, 3095 (2015).

[138] B. Sang, A. Yamada, and M. Konagai, Solar Energy Materials and Solar Cells **49**, 19 (1997).

[139] D.-J. Lee, K.-J. Kim, S.-H. Kim, J.-Y. Kwon, J. Xu, and K.-B. Kim, Journal of Materials Chemistry C **1**, 4761 (2013).

[140] Z.-Y. Ye, H.-L. Lu, Y. Geng, Y.-Z. Gu, Z.-Y. Xie, Y. Zhang, Q.-Q. Sun, S.-J. Ding, and D. W. Zhang, Nanoscale research letters **8**, 108 (2013).

[141] A. W. Ott and R. P. H. Chang, Materials Chemistry and Physics **58**, 132 (1999).

[142] Y. Geng, Z.-Y. Xie, W. Yang, S.-S. Xu, Q.-Q. Sun, S.-J. Ding, H.-L. Lu, and D. W. Zhang, Surface and Coatings Technology **232**, 41 (2013).

[143] M. A. Thomas, J. C. Armstrong, and J. Cui, Journal of Vacuum Science & Technology A: Vacuum, Surfaces, and Films **31**, 01A130 (2013).

[144] J. S. Na, Q. Peng, G. Scarel, and G. N. Parsons, Chemistry of Materials **21**, 5585 (2009).

[145] T. Asikainen, Journal of The Electrochemical Society **142**, 3538 (1995).

[146] O. Nilsen, R. Balasundaraprabhu, E. V. Monakhov, N. Muthukumarasamy, H. Fjellvåg, and B. G. Svensson, Thin Solid Films **517**, 6320 (2009).

[147] M. Gebhard, M. Hellwig, H. Parala, K. Xu, M. Winter, and A. Devi, Dalton transactions **43**, 937 (2014).

[148] D.-J. Lee, J.-Y. Kwon, J. I. Lee, and K.-B. Kim, The Journal of Physical Chemistry C **115**, 15384 (2011).

[149] D. Kim, T. Nam, J. Park, J. Gatineau, and H. Kim, Thin Solid Films **587**, 1 (2015).

[150] R. K. Ramachandran, J. Dendooven, H. Poelman, and C. Detavernier, The Journal of Physical Chemistry C **119**, 11786 (2015).

[151] J. W. Elam, A. B. F. Martinson, M. J. Pellin, and J. T. Hupp, Chemistry of Materials **18**, 3571 (2006).

[152] J. W. Elam, D. A. Baker, A. B. F. Martinson, M. J. Pellin, and J. T. Hupp, Journal of Physical Chemistry C **112**, 1938 (2008).

[153] J. A. Libera, J. N. Hryn, and J. W. Elam, Chemistry of Materials **23**, 2150 (2011).

[154] B. Demaurex, J. P. Seif, S. Smit, B. Macco, W. M. M. Kessels, J. Geissbuhler, S. De Wolf, and C. Ballif, IEEE Journal of Photovoltaics **4**, 1387 (2014).

[155] R. L. Z. Hoye, D. Muñoz-Rojas, S. F. Nelson, A. Illiberi, P. Poodt, F. Roozeboom, and J. L. MacManus-Driscoll, APL Materials **3**, 040701 (2015).

[156] D. Munoz-Rojas and J. MacManus-Driscoll, Materials Horizons , 314 (2014).

[157] A. Illiberi, P. Poodt, P. J. Bolt, and F. Roozeboom, Chemical Vapor Deposition , 234 (2014).

[158] A. Illiberi, F. Roozeboom, and P. Poodt, ACS applied materials & interfaces **4**, 268 (2012).

[159] N. Nandakumar, B. Dielissen, D. Garcia-alonso, Z. Liu, and W. M. M. Kessels, in *Proceedings of the 6th World Conference on Photovoltaic Energy Conversion* (2014) pp. 2−3.

[160] N. Nandakumar, B. Dielissen, D. Garcia-Alonso, Z. Liu, R. Gortzen, W. M. M. Kessels, A. G. Aberle, and B. Hoex, IEEE Journal of Photovoltaics **5**, 1462 (2015).

[161] A. Illiberi, R. Scherpenborg, Y. Wu, F. Roozeboom, and P. Poodt, ACS Applied Materials and Interfaces **5**, 13124 (2013).

[162] C. R. Ellinger and S. F. Nelson, Chemistry of Materials **26**, 1514 (2014).

[163] N. Nandakumar, B. Hoex, B. Dielissen, D. Garcia-Alonso, R. Gortzen, W. M. M. Kessels, L. Fin, A. G. Aberle, and T. Mueller, Presented at the 25th Asia Photovoltaic Solar Energy Conference and Exhibition (2015).

[164] U. Wurfel, A. Cuevas, and P. Wurfel, IEEE Journal of Photovoltaics **5**, 461 (2015).

[165] R. Islam, G. Shine, and K. C. Saraswat, Applied Physics Letters **105**, 182103 (2014).

[166] M. Bivour, J. Temmler, H. Steinkemper, and M. Hermle, Solar Energy Materials and Solar Cells **142**, 34 (2015).

[167] P. Stradins, S. Essig, W. Nemeth, B. G. Lee, D. Young, A. Norman, Y. Liu, J.-w. Luo, E. Warren, A. Dameron, V. Lasalvia, M. Page, and Y. Ok, in *6th World Conference on Photovoltaic Energy Conversion*, December (2014).

[168] J. Robertson, Journal of Vacuum Science & Technology B: Microelectronics and Nanometer Structures **18**, 1785 (2000).

[169] K. K. Ng and H. C. Card, Journal of Applied Physics **51**, 2153 (1980).

[170] D. L. Young, W. Nemeth, S. Grover, A. Norman, B. G. Lee, and P. Stradins, in *2014 IEEE 40th Photovoltaic Specialist Conference (PVSC)* (IEEE, 2014) pp. 1−5.

[171] A. Khanna, T. Mueller, R. A. Stangl, B. Hoex, P. K. Basu, and A. G. Aberle, IEEE Journal of Photovoltaics **3**, 1170 (2013).

[172] Private communication (2015).

[173] F. Feldmann, M. Bivour, C. Reichel, M. Hermle, and S. W. Glunz, Solar Energy Materials and Solar Cells **120**, 270 (2014).

[174] X. Yang, P. Zheng, Q. Bi, and K. Weber, Solar Energy Materials and Solar Cells **150**, 32 (2016).

[175] A. Fell, K. R. McIntosh, P. P. Altermatt, G. J. M. Janssen, R. Stangl, A. Ho-Baillie, H. Steinkemper, J. Greulich, M. Muller, B. Min, K. C. Fong, M. Hermle, I. G. Romijn, and M. D. Abbott, IEEE Journal of Photovoltaics **5**, 1250 (2015).

[176] E. Cornagliotti, A. Uruena, M. Aleman, A. Sharma, L. Tous, R. Russell, P. Choulat, J. Chen, J. John, M. Haslinger, F. Duerinckx, B. Dielissen, R. Gortzen, L. E. Black, and J. Szlufcik, IEEE Journal of Photovoltaics **5**, 1366 (2015).

[177] J. Bullock, A. Cuevas, T. Allen, and C. Battaglia, Applied Physics Letters **105**, (2014).

[178] J. Bullock, C. Samundsett, A. Cuevas, D. Yan, Y. Wan, and T. Allen, in *2015 IEEE 42nd Photovoltaic Specialist Conference (PVSC)*, Vol. 5 (IEEE, 2015) pp. 1–4.

[179] J. Geissbühler, J. Werner, S. Martin de Nicolas, L. Barraud, A. Hessler-Wyser, M. Despeisse, S. Nicolay, A. Tomasi, B. Niesen, S. De Wolf, and C. Ballif, Applied Physics Letters **107**, 081601 (2015).

[180] D. Zielke, J. H. Petermann, F. Werner, B. Veith, R. Brendel, and J. Schmidt, physica status solidi (RRL) - Rapid Research Letters **5**, 298 (2011).

[181] F. Werner, B. Veith, D. Zielke, L. Kühnemund, C. Tegenkamp, M. Seibt, R. Brendel, and J. Schmidt, Journal of Applied Physics **109**, 2 (2011).

[182] A. K. Chandiran, M. K. Nazeeruddin, and M. Graetzel, Advanced Functional Materials **24**, 1615 (2014).

[183] A. K. Chandiran, N. Tetreault, R. Humphry-Baker, F. Kessler, E. Baranoff, C. Yi, M. K. Nazeeruddin, and M. Grätzel, Nano Letters **12**, 3941 (2012).

[184] G. Sahasrabudhe, S. M. Rupich, J. Jhaveri, A. H. Berg, K. A. Nagamatsu, G. Man, Y. J. Chabal, A. Kahn, S. Wagner, J. C. Sturm, and J. Schwartz, Journal of the American Chemical Society **137**, 14842 (2015).

[185] S. A. Chambers, Y. Liang, Z. Yu, R. Droopad, and J. Ramdani, Journal of Vacuum Science & Technology A: Vacuum, Surfaces, and Films **19**, 934 (2001).

[186] C. J. Först, C. R. Ashman, K. Schwarz, and P. E. Blöchl, Nature **427**, 53 (2004).

[187] V. Longo, N. Leick, F. Roozeboom, and W. M. M. Kessels, ECS Journal of Solid State Science and Technology **2**, N15 (2012).

[188] M. Ritala, M. Leskela, L. Niinisto, P. Haussalo, and L. Niinist, Chemistry of Materials **5**, 1174 (1993).

[189] S. E. Potts, W. Keuning, E. Langereis, G. Dingemans, M. C. M. van de Sanden, and W. M. M. Kessels, Journal of The Electrochemical Society **157**, P66 (2010).

[190] Q. Xie, Y.-L. Jiang, C. Detavernier, D. Deduytsche, R. L. Van Meirhaeghe, G.-P. Ru, B.-Z. Li, and X.-P. Qu, Journal of Applied Physics **102**, 083521 (2007).

[191] M. K. Kim, W. H. Kim, T. Lee, and H. Kim, Thin Solid Films **542**, 71 (2013).

[192] O. S. Kwon, S. K. Kim, M. Cho, C. S. Hwang, and J. Jeong, Journal of The Electrochemical Society **152**, C229 (2005).

[193] A. Bertuch, G. Sundaram, M. Saly, D. Moser, and R. Kanjolia, Journal of Vacuum Science & Technology A: Vacuum, Surfaces, and Films **32**, 01A119 (2014).

[194] M. F. J. Vos, B. Macco, N. F. W. Thissen, A. A. Bol, and W. M. M. Kessels, Journal of Vacuum Science & Technology A: Vacuum, Surfaces, and Films **34**, 01A103 (2016).

[195] M. Diskus, O. Nilsen, and H. Fjellvåg, Journal of Materials Chemistry **21**, 705 (2011).

[196] R. Liu, Y. Lin, L.-Y. Chou, S. W. Sheehan, W. He, F. Zhang, H. J. M. Hou, and D. Wang, Angewandte Chemie International Edition **50**, 499 (2011).

[197] J. Malm, T. Sajavaara, and M. Karppinen, Chemical Vapor Deposition **18**, 245 (2012).

[198] J.-g. Song, J. Park, W. Lee, T. Choi, H. Jung, C. W. Lee, S.-h. Hwang, J. M. Myoung, J.-h. Jung, S.-H. Kim, C. Lansalot-Matras, and H. Kim, ACS Nano **7**, 11333 (2013).

[199] T. Blanquart, J. Niinistö, M. Gavagnin, V. Longo, M. Heikkilä, E. Puukilainen, V. R. Pallem, C. Dussarrat, M. Ritala, and M. Leskelä, RSC Adv. **3**, 1179 (2013).

[200] S. Boukhalfa, K. Evanoff, and G. Yushin, Energy & Environmental Science **5**, 6872 (2012).

[201] J. Musschoot, D. Deduytsche, R. L. Van Meirhaeghe, and C. Detavernier, in *ECS Transactions*, Vol. 25 (ECS, 2009) pp. 29–37.

[202] H. Lu, G. Scarel, X. Li, and M. Fanciulli, Journal of Crystal Growth **310**, 5464 (2008).

[203] E. Lindahl, M. Ottosson, and J.-O. Carlsson, Chemical Vapor Deposition **15**, 186 (2009).

[204] J. Chae, H.-S. Park, and S.-w. Kang, Electrochemical and Solid-State Letters **5**, C64 (2002).

[205] T. S. Yang, W. Cho, M. Kim, K.-S. An, T.-M. Chung, C. G. Kim, and Y. Kim, Journal of Vacuum Science & Technology A: Vacuum, Surfaces, and Films **23**, 1238 (2005).

[206] C. Battaglia, X. Yin, M. Zheng, I. D. Sharp, T. Chen, S. McDonnell, A. Azcatl, C. Carraro, B. Ma, R. Maboudian, R. M. Wallace, and A. Javey, Nano letters **14**, 967 (2014).

[207] J. Ziegler, M. Mews, K. Kaufmann, T. Schneider, A. N. Sprafke, L. Korte, and R. B. Wehrspohn, Applied Physics A , 2 (2015)

3

Influence of Transparent Conductive Oxides on Passivation of *a*-Si:H/c-Si Heterojunctions as Studied by Atomic Layer Deposited Al-doped ZnO

Abstract: In silicon heterojunction solar cells, the main opportunities for efficiency gain lie in improvements of the front-contact layers. Therefore, the effect of transparent conductive oxides (TCOs) on the *a*-Si:H passivation performance has been investigated for Al-doped zinc oxide (ZnO:Al) layers made by atomic layer deposition (ALD). It is shown that the ALD process, as opposed to sputtering, does not impair the *chemical* passivation. However, the *field-effect* passivation is reduced by the ZnO:Al. The resulting decrease in low injection-level lifetime can be tuned by changing the ZnO:Al doping level (carrier density = $7 \times 10^{19} - 7 \times 10^{20}$ cm^3), which is explained by a change in the TCO workfunction. Additionally, it is shown that a $\sim$10-15 nm ALD ZnO:Al layer is sufficient to mitigate damage to the *a*-Si:H by subsequent sputtering, which is correlated to ALD film closure at this thickness.

3.1   Introduction

Silicon heterojunction (SHJ) solar cells have recently attracted much attention, as they have several distinct advantages over homojunction crystalline silicon (c-Si) solar cells. Examples include low-temperature processing (<200 °C), high conversion efficiencies and facile fabrication.[1] A typical SHJ solar cell consists of a c-Si wafer, symmetrically passivated by thin layers of intrinsic amorphous silicon (*a*-Si:H). Selective electron and hole contacts are formed by the deposition of *n*- and *p*-type *a*-Si:H films at the rear and front, respectively. A transparent conductive oxide (TCO) at the front, usually 75 nm of indium tin oxide (ITO), provides lateral conductivity and anti-reflection.

The key advantage of the SHJ concept over the homojunction c-Si solar cell in terms of performance is its superior minority carrier lifetime, resulting in record open-circuit voltages (V_{oc}) up to 750 mV.[2,3] This high carrier lifetime stems from a high bulk lifetime combined with an extremely well passivated wafer surface with *a*-Si:H, as opposed to the highly recombination-active diffused regions and metal contacts found in homojunction c-Si solar cells. However, parasitic light absorption in the front TCO and *a*-Si:H layers limits the SHJ solar cell short-circuit current J_{sc}.[4] Additionally, the deposition of the TCO using plasma-based deposition methods such as sputtering impairs the *chemical* passivation of *a*-Si:H through plasma damage (i.e. ion bombardment and plasma radiation), as shown by various authors.[5,6,7,8] In research, there has also been an increasing focus on the importance of a proper work function (WF) of the TCO, as a mismatched WF puts a lower bound on the thickness and doping level of the *a*-Si:H layers.[9,10,11,12,13] Consequently, improvements of both the front layer material properties and their deposition techniques are important drivers for the SHJ solar cell efficiency.[1]

In this work the influence of ZnO:Al TCOs, prepared by ALD, on the *chemical* and *field-effect* passivation of *a*-Si:H layers has systematically been investigated. It is shown that a ZnO:Al TCO deposited by ALD does not reduce the level of *chemical* passivation provided by *a*-Si:H passivation layers, which is a distinct advantage over the commonly-employed sputtering method. On the other hand, the presence of the TCO leads to a decrease in low injection-level lifetime. This has previously been attributed to a reduction in *field-effect* passivation due to a too low WF of the TCO[9,14]. Using the excellent doping control of the ALD process, it is shown that the change in *field-effect* passivation can be tuned by varying the doping level of the TCO, which is explained by a dependency of the WF of the TCO on its doping level. An initial comparison between a SHJ solar cell with a heavily doped ZnO:Al TCO prepared by ALD and a reference cell with sputtered ITO has shown an improvement of 10 mV in implied open-circuit voltage ($_iV_{oc}$) due to an improved *chemical* passivation. However, the fill-factor (*FF*) was found to be reduced, which is attributed to a too low WF of the TCO. Moreover, bilayers consisting of ALD

Table 1: Overview of the samples and corresponding ZnO:Al$_2$O$_3$ ratios, along with the resulting electrical properties for film thicknesses of 75 nm as determined by four-point-probe and modeling of spectroscopic ellipsometry data. [15] For the undoped ZnO film no Al$_2$O$_3$ cycles were used. Values for sputtered ITO are given for comparison.[*]

Sample name	ZnO:Al$_2$O$_3$ ratio	Carrier density N_e (10^{20} cm^{-3})	Mobility μ (cm^2/Vs)	Resistivity ρ (mΩcm)
Undoped (UD)	–	0.7	15.6	5.7
Low doping (LD)	128	1.0	14.9	4.2
Medium doping (MD)	28	3.0	14.8	1.4
High doping (HD)	10	7.0	13.4	0.7
ITO	–	5.3	35.8	0.4

ZnO:Al and sputtered ITO have been made to combine the softness of the ALD process with the lower resistivity of ITO. It is shown that this approach can greatly reduce the sputter damage at the expense of a small increase in TCO resistivity. The protective properties of the ALD layer have been correlated to the island growth during film nucleation.

3.2 Experimental details

Floatzone Si(100) wafers (*n*-type, 3 Ωcm) were used as substrates. After removal of the native oxide by a dip in 1% dilute HF, the wafers were symmetrically passivated with 10 nm of intrinsic *a*-Si:H deposited in an inductively coupled plasma reactor from Oxford instruments. Al-doped ZnO films were deposited in an Oxford instruments OpAL^{TM} ALD reactor at a substrate temperature of 200 °C. Zn(C$_2$H$_5$)$_2$ and deionized water vapor were used as precursors for the ZnO growth, whereas Al(CH$_3$)$_2$(O^{i}Pr) was used as the Al-precursor for doping. This ALD process for ZnO:Al has been described in detail elsewhere. [16] The doping level has been accurately controlled by changing the ZnO to Al$_2$O$_3$ cycle ratio, as summarized in Table 1. ITO sputtering took place in a Kurt J Lesker company radio frequency magnetron system at a deposition temperature of 110 °C, using a target composition In$_2$O$_3$:SnO$_2$ 90:10 wt%.

For the bilayers, the ZnO:Al and ITO layer thicknesses were varied, whilst maintaining a total bilayer thickness of 75 nm. Since the *a*-Si:H passivation is sensitive to thermal treatments, an equal thermal history was assured by keeping the samples equally long in the deposition chambers, irrespective of the required layer thickness. The *a*-Si:H surface passivation quality was evaluated from the injection-dependent minority carrier lifetime as determined using a Sinton WCT-100.

---

[*]For the ITO sample, the carrier density and mobility were obtained from Hall measurements.

3.3   Results and discussion

As can be seen in Table 1, decreasing the ZnO to Al_2O_3 cycle ratio results in a decrease in resistivity down to 0.7 mΩcm, close to the ITO reference value of 0.4 mΩcm. This decrease in resistivity mainly stems from an increase in carrier density by one order of magnitude due to the Al doping. The mobility is slightly impaired through increased ionized impurity scattering and disrupted grain growth caused by the Al doping. [17]
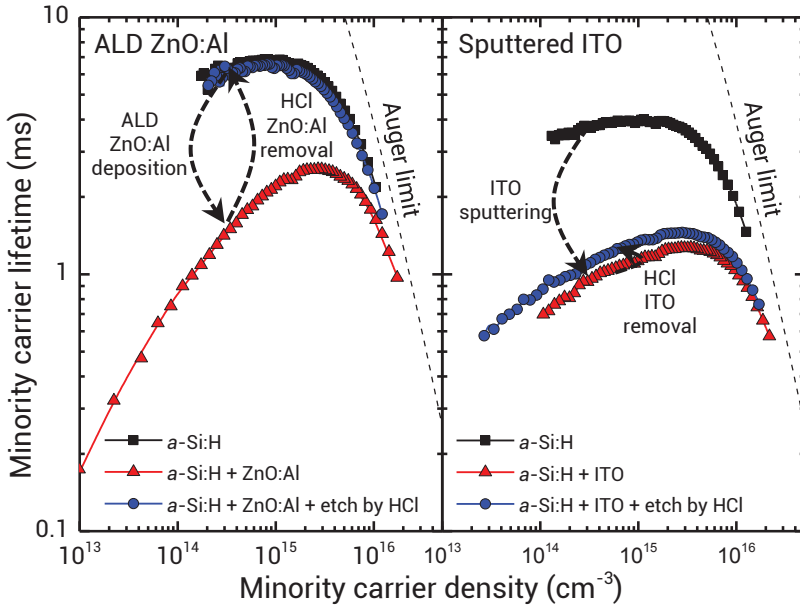

Figure 1: Comparison of the injection-dependent minority carrier lifetime after *a*-Si:H passivation, after deposition of the TCO (left ALD ZnO:Al (HD), right sputtered ITO) and after selective wet etch of the TCO with HCl. The Auger limit is shown for comparison, calculated using the parameterization reported by Richter *et al*. [18]

In order to assess whether the surface passivation provided by a 10 nm *a*-Si:H passivation layer is impaired by the ALD process, the effect of the deposition of the ZnO:Al on the injection-dependent minority carrier lifetime has been evaluated, as shown in Figure 1, left. Prior to the ZnO:Al deposition, an excellent level of surface passivation is provided by the *a*-Si:H film, as evidenced by a minority carrier lifetime of ∼7 ms at an injection level of 10^{15} cm^{-3}. After the deposition of 75 nm of highly-doped (HD) ZnO:Al, a strong decrease in minority carrier lifetime is observed, especially at lower injection levels. However, after a selective wet etch of the ZnO:Al film with HCl, a full recovery of the minority carrier lifetime to the initial state can be observed in Figure 1. From this reversibility it is concluded that the *chemical* passivation is not impaired by the ALD process, i.e. no damage is induced to the *a*-Si:H passivation layer. In a similar exper-
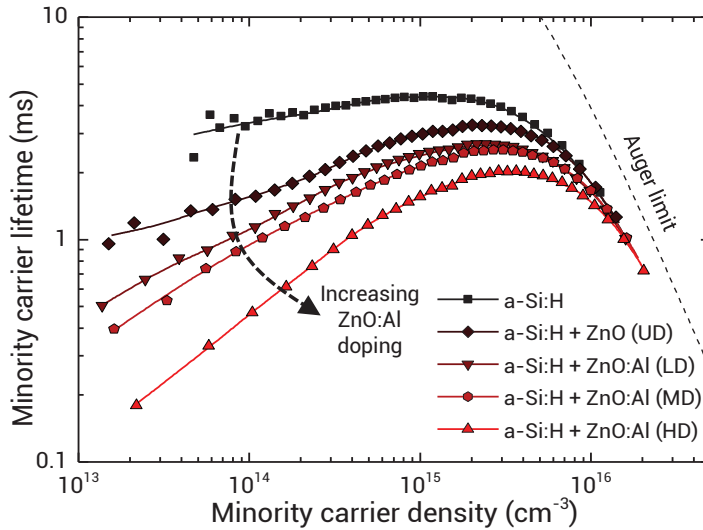
Figure 2: Effect of the ZnO:Al doping level on the *field-effect* passivation. The ZnO:Al doping levels have been labeled as in Table 1. The Auger limit is shown for comparison, calculated using the parameterization reported by Richter *et al*.[18]

iment using sputtered ITO as TCO (Figure 1, right) a decrease in passivation after the application of the TCO is seen as well. However, the only slight recovery after the HCl dip suggests that the sputtering process induces damage to the passivation layer which is retained even after the ITO removal.

The decrease in lifetime at low injection level after the application of a TCO has been observed before and translates to a reduced *FF* on the solar cell level.[9,10,19,20] As stated by Rößler *et al*., a too low WF of the TCO (<5.1 eV) in a TCO/*a*-Si:H(*p*/*i*)/c-Si(*n*) stack leads to a reduced c-Si band bending by extension of the depletion region of the TCO/a-Si:H Schottky-contact to the c-Si surface.[9] The resulting reduced *field-effect* passivation is dependent on the WF mismatch of the TCO and can be screened by increasing the *a*-Si:H doping level and thickness. Consequently, a mismatched TCO WF puts a lower bound on the *a*-Si:H thickness and doping level, severely limiting the freedom in SHJ design.[9,10]

The effect of the ZnO:Al WF on the *field-effect* passivation provided by 10 nm of intrinsic *a*-Si:H has been investigated by accurately changing the doping level of the TCO according to Table 1. Increased degenerate doping of the ZnO:Al shifts the Fermi level further above the conduction band (the electron affinity of ZnO:Al is ∼4.4 eV) through the Burstein−Moss effect, thereby reducing its WF.[21,22] As can be seen in Figure 2, the low injection-level lifetime decreases with increasing ZnO:Al doping. These results experimentally confirm the predicted effect of the TCO WF on the *field-effect* passivation

Table 2: Comparison of the solar cell parameters of 4 cm^2 SHJ solar cells featuring sputtered ITO and ALD ZnO:Al as a TCO. The cells were made at Delft University of Technology (except the ALD ZnO:Al films) using their baseline process and 285 μm planar float-zone *n*-type (3 Ωcm) wafers. The J_{sc} values refer to the active area of the solar cell.

TCO	$_iV_{oc}$ (mV)	V_{oc} (mV)	J_{sc} (mA/cm^2)	FF (%)	Efficiency (%)
ITO	712	708	34.3	75.4	18.3
ZnO:Al (HD)	722	711	33.6	70.4	16.8

and indicate that changing the doping level of the TCO rather than that of the *a*-Si:H(*p*) is a potential method to optimize the electrical contact. In this respect, graded doping of the TCO, readily achieved by ALD, could be a promising route to alleviate the constraints on the amorphous silicon layers, thereby allowing thinner and less doped *a*-Si:H layers to be used while maintaining a respectable sheet resistance.

An initial comparison has been made between SHJ solar cells featuring either sputtered ITO or ALD ZnO:Al (HD) as TCO. The highly doped ZnO:Al TCO with a sheet resistance of 90 Ω/$\square$ was chosen in order to minimize resistive losses and associated reductions in *FF*, which become significant for sheet resistances > 100 Ω/$\square$.[4] This way, differences in *FF* due to a mismatch in WF become more apparent. As can be seen in Table 2, the implied V_{oc} ($_iV_{oc}$) of a lifetime reference is 10 mV higher for the sample with an ALD TCO, which confirms that the non-damaging aspect of ALD can lead to an improved passivation of the solar cell precursor. The difference of 3 mV in V_{oc} on the device level is however smaller than expected on basis of the $_iV_{oc}$ of the solar cell precursors. Although speculative, it is very well possible that the V_{oc} on the device level is limited by edge recombination effects in the small solar cell structures or a reduction in the rear passivation after metallization. A difference in *FF* of 5% absolute is observed which is in accordance with the results in Figure 2: besides a slightly higher resistivity for the ZnO:Al layer, the reduced *FF* is attributed to the lower WF of the heavily doped ZnO:Al compared to the ITO in combination with an *a*-Si:H(*p*) doping level which is optimized for the ITO reference.[22]

Although the soft ALD process enables an improved passivation, these initial solar cells demonstrate that the *FF* is limited due to the higher resistivity and low WF of the heavily doped ZnO:Al layer. In view of this, the aforementioned approach of graded doping of the ZnO:Al layer seems logical to mitigate the *FF* losses related to the low WF of the TCO: a thin *i*-ZnO layer at the *a*-Si:H interface enhances the interfacial WF, expectedly without severely affecting the TCO resistivity. Also, the development of low resistivity, high WF (~5 eV) TCOs by ALD such as indium (tin) oxide is very promising in this respect.[23,24]
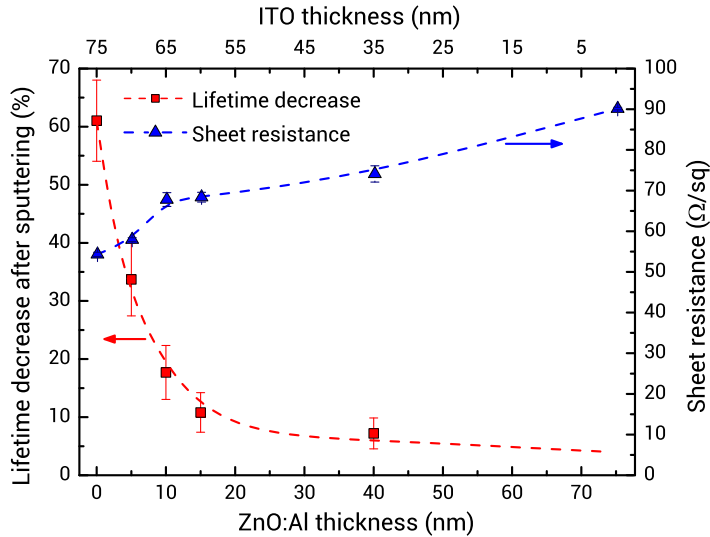
Figure 3: Relative decrease in minority carrier lifetime after ITO sputtering, evaluated at an injection level of 10^{15} cm^{-3}, and the sheet resistance of the bilayer for varying ZnO:Al and ITO thicknesses. Dashed lines are guides to the eye.

To further demonstrate the importance of the softness of the ALD technique, ALD ZnO:Al has been utilized in bilayers of ALD ZnO:Al (HD) and sputtered ITO to reduce damage to the *a*-Si:H passivation layers during ITO sputtering whilst maintaining a low TCO sheet resistance. In this experiment, the thickness of the ZnO:Al has been varied, while keeping the total thickness of the bilayer constant at 75 nm. The relative decrease in lifetime after ITO sputtering and the total sheet resistance of the bilayer is shown in Figure 3 for varying ZnO:Al/ITO thicknesses.

As seen from Figure 3, a decrease in lifetime of over 60% is observed when ITO is sputtered on a bare *a*-Si:H passivation layer. The reduction in lifetime decreases dramatically with increasing ZnO:Al thickness, showing that the ZnO:Al layers are effective in protecting the *a*-Si:H passivation layer from the sputtering process. The sheet resistance of the bilayer monotonically increases with the ZnO:Al thickness, as the resistivity of the ZnO:Al (0.7 mΩcm) is higher compared to that of ITO (0.4 mΩcm).

In order to gain further insight into the strong thickness dependence of the protective properties of the ALD layers, the initial growth of the ALD layer has been investigated by topview bright-field transmission electron microscopy (TEM) on SiO$_2$-coated TEM windows and *in-situ* spectroscopic ellipsometry measurements on *a*-Si:H layers.

As can be seen in Figures 3(a)-(c), the film with a nominal thickness of 5 nm is observed not to be closed, indicating so-called island growth, whereas the 15 nm film is closed. The presence of initial island growth on *a*-Si:H is corroborated qualitatively by
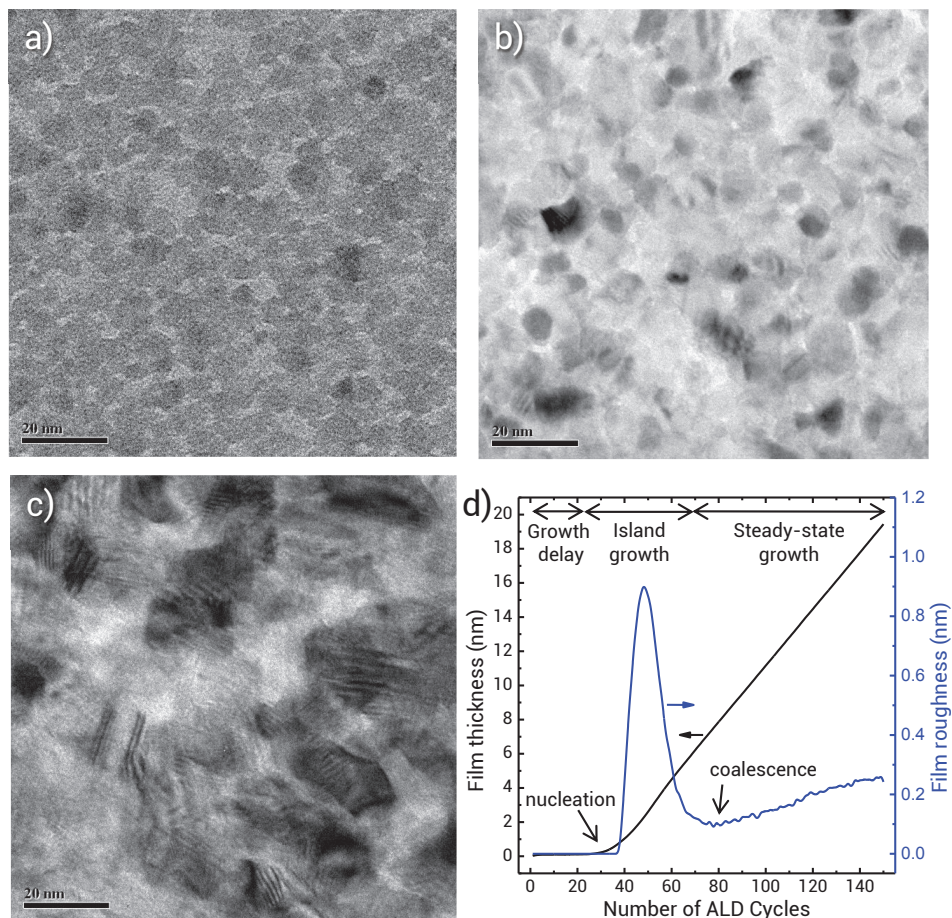
Figure 4: Bright-field top-view TEM images of ALD ZnO films on SiO$_2$-coated TEM windows with nominal film thicknesses of (a) 5 nm, (b) 15 nm and (c) 80 nm. (d) Effective film thickness and roughness as a function of the number of ALD cycles, as obtained by *in-situ* spectroscopic ellipsometry. The various stages of growth are indicated.

ellipsometry data (Figure 3(d)): after a growth delay island growth starts, manifested by an increased growth per cycle (GPC) and increased film roughness. After coalescence at an effective film thickness of $\sim$10 nm, the film roughness reduces and the film growth proceeds with a constant GPC of 1.6 Å. The observation of initial island growth up to an thickness of $\sim$10 nm is consistent with the lifetime trend in Figure 3, as the protective properties of the ALD layer improve sharply up to the point of film closure. These results suggest that the thickness of the ALD layer, but mostly its surface coverage is of importance for its protective properties. In this respect, surface pretreatments to improve the nucleation of the ALD process in order to achieve earlier film closure could be a successful approach to reduce the ALD film thickness required for protection of the surface.

3.4 Conclusions

In conclusion, it has been shown that ALD is an appealing deposition method for studying the role of TCO deposition in SHJ solar cells. The purely chemical ALD process is devoid of harmful plasma radiation and ion bombardment, typically encountered in plasma-based deposition processes such as sputtering. Therefore, the *chemical* passivation provided by *a*-Si:H does not degrade during the ALD process, resulting in an improved solar cell passivation. Note that the soft ALD process could possibly enable thinner front *a*-Si:H layers to reduce the parasitic absorption by the *a*-Si:H layers, as thinner *a*-Si:H layers exhibit a higher sensitivity to damage induced during deposition of the overlying TCO.[8] The soft nature and accurate doping control offered by ALD have also enabled the experimental verification of the correlation between the TCO doping level, or WF, and the low-injection level lifetime. Additionally, it has been shown that bilayers of ZnO:Al/sputtered ITO can lead to a drastic improvement of the final passivation level at a small expense of the sheet resistance due to a higher ZnO:Al resistivity. Fortunately, the higher resistivity and the lower WF of the ALD layer is not a fundamental problem, and the development of low resistivity, high WF TCOs by ALD such as indium (tin) oxide is very promising.

3.5 Acknowledgements

References

[1] S. De Wolf, A. Descoeudres, Z. C. Holman, and C. Ballif, Green **2**, 7 (2012).

[2] M. A. Green, K. Emery, Y. Hishikawa, W. Warta, and E. D. Dunlop, Progress in Photovoltaics: Research and Applications **21**, 827 (2013).

[3] M. Taguchi, A. Yano, S. Tohoda, K. Matsuyama, Y. Nakamura, T. Nishiwaki, K. Fujita, and E. Maruyama, IEEE Journal of Photovoltaics **4**, 96 (2014).

[4] Z. C. Holman, A. Descoeudres, L. Barraud, F. Z. Fernandez, J. P. Seif, S. De Wolf, and C. Ballif, IEEE Journal of Photovoltaics **2**, 7 (2012).

[5] B. Demaurex, S. De Wolf, A. Descoeudres, Z. C. Holman, and C. Ballif, Applied Physics Letters **101**, 171604 (2012).

[6] A. Illiberi, P. Kudlacek, A. H. M. Smets, M. Creatore, and M. C. M. van de Sanden, Applied Physics Letters **98**, 242115 (2011).

[7] D. Zhang, A. Tavakoliyaraki, Y. Wu, R. A. C. M. M. van Swaaij, and M. Zeman, Energy Procedia **8**, 207 (2011).

[8] D. Skorka, N. Brinkmann, and A. Gorgulla, Proceedings of the 28th European Photovoltaic Solar Energy Conference (2013) , 1162 (2013).

[9] R. Rößler, C. Leendertz, L. Korte, N. Mingirulli, and B. Rech, Journal of Applied Physics **113**, 144513 (2013).

[10] M. Bivour, S. Schröer, and M. Hermle, Energy Procedia **38**, 658 (2013).

[11] E. Centurioni and D. Iencinella, IEEE Electron Device Letters **24**, 177 (2003).

[12] L. Zhao, C. L. Zhou, H. L. Li, H. W. Diao, and W. J. Wang, Physica Status Solidi (a) **205**, 1215 (2008).

[13] R. Lachaume, W. Favre, P. Scheiblin, X. Garros, N. Nguyen, J. Coignus, D. Munoz, and G. Reimbold, Energy Procedia **38**, 770 (2013).

[14] C. Leendertz, N. Mingirulli, T. F. Schulze, J. P. Kleider, B. Rech, and L. Korte, Applied Physics Letters **98**, 202108 (2011).

[15] F. Ruske, A. Pflug, V. Sittinger, B. Szyszka, D. Greiner, and B. Rech, Thin Solid Films **518**, 1289 (2009).

[16] Y. Wu, S. E. Potts, P. M. Hermkens, H. C. M. Knoops, F. Roozeboom, and W. M. M. Kessels, Chemistry of Materials **25**, 4619 (2013).

[17] Y. Wu, P. M. Hermkens, B. W. H. van de Loo, H. C. M. Knoops, S. E. Potts, M. A. Verheijen, F. Roozeboom, and W. M. M. Kessels, Journal of Applied Physics **114**, 024308 (2013).

[18] A. Richter, S. W. Glunz, F. Werner, J. Schmidt, and A. Cuevas, Physical Review B **86**, 1 (2012).

[19] W. Favre, J. Coignus, N. Nguyen, R. Lachaume, R. Cabal, and D. Muñoz, Applied Physics Letters **102**, 181118 (2013).

[20] A. Descoeudres, Z. C. Holman, L. Barraud, S. Morel, S. De Wolf, and C. Ballif, IEEE Journal of Photovoltaics **3**, 83 (2013).

[21] E. Burstein, Physical Review **93**, 632 (1954).

[22] A. Klein, C. Körber, A. Wachau, F. Säuberlich, Y. Gassenbauer, S. P. Harvey, D. E. Proffit, and T. O. Mason, Materials **3**, 4892 (2010).

[23] B. Macco, Y. Wu, D. Vanhemel, and W. M. M. Kessels, physica status solidi (RRL) - Rapid Research Letters **8**, 987 (2014).

[24] J. A. Libera, J. N. Hryn, and J. W. Elam, Chemistry of Materials **23**, 2150 (2011)

4

High Mobility In$_2$O$_3$:H Transparent Conductive Oxides Prepared by Atomic Layer Deposition and Solid Phase Crystallization

Abstract: The preparation of high-quality In$_2$O$_3$:H, as transparent conductive oxide (TCO), is demonstrated at low temperatures. Amorphous In$_2$O$_3$:H films were deposited by atomic layer deposition at 100 °C, after which they underwent solid phase crystallization by a short anneal at 200 °C. TEM analysis has shown that this approach can yield films with a lateral grain size of a few hundred nm, resulting in electron mobility values as high as 138 cm^2/V s at a device-relevant carrier density of 1.8×10^{20} cm^{-3}. Due to the extremely high electron mobility, the crystallized films simultaneously exhibit a very low resistivity (0.27 mΩcm) and a negligible free carrier absorption. In conjunction with the low temperature processing, this renders these films ideal candidates for front TCO layers in for example silicon heterojunction solar cells and other sensitive optoelectronic applications.

4.1   Introduction

Transparent conductive oxides (TCOs) find their use in optoelectronic applications such as displays and solar cells. In general, these applications benefit from a simultaneous high conductivity and high transparency of the TCO. Since these applications are also often large-area and involve the use of temperature sensitive materials, both improvements in materials and the development of scalable and low temperature processes are important drivers for industry.

In recent years, atomic layer deposition (ALD) has attracted a lot of attention in the photovoltaics community for the uniform, large area deposition of thin films. The advent of high throughput ALD techniques such as batch and spatial ALD has made ALD industrially viable[1], as evidenced by the industrialization of ALD-based Al$_2$O$_3$ passivation layers for diffused-junction c-Si solar cells.[2] Various other photovoltaic concepts can also benefit from ALD, for example from other materials or from the excellent conformality of ALD in the case of nanostructured solar cells.[1] Moreover, energetic species during sputtering of TCOs can damage the substrate, as is well known for silicon heterojunction (SHJ) solar cells and OLEDs.[3,4,5,6] In the case of ALD, this damage does not occur.[7,8]

In the development of high-quality TCOs, the fundamental trade-off between conductivity and transparency due to free-carrier absorption (FCA) has to be considered. The conductivity σ is given by:

$$\sigma = \frac{1}{\rho} = N_e \mu e \tag{4.1}$$

in which ρ is the resistivity, N_e the carrier density, μ the carrier mobility and e the elementary charge. A low ρ can thus be achieved both by a high μ and a high N_e, which is usually achieved by doping of the TCO (e.g. In$_2$O$_3$:Sn, ZnO:Al). However, increased doping increases the plasma frequency ω_p of the film, given by:

$$\omega_p = \sqrt{\frac{e^2 N_e}{\varepsilon_0 \varepsilon_r m^*}} \tag{4.2}$$

with ε_0 and ε_r the vacuum and relative permittivity, respectively, and m^* the effective electron mass. The plasma frequency denotes the onset of FCA, thus increasing N_e reduces the transparency of the TCO at low photon energies. Therefore, a high μ is usually desired, as this allows for both a high conductivity and high transparency at low N_e. FCA is especially relevant for devices with a relatively low band gap E_g, such as c-Si based (E_g = 1.12 eV) SHJ solar cells. In these devices the TCO serves as a window layer providing lateral charge transport to the metal contacts, which puts stringent require-

ments on both the conductivity and transparency. For this reason, tin-doped indium oxide (In_2O_3:Sn or ITO), which typically has a higher μ with respect to other popular TCO materials such as ZnO and SnO, has historically been the TCO of choice for SHJ solar cells. In_2O_3:Sn films are usually made by sputtering and typical values for the μ reported in the literature lie in the range of 20-40 cm^2/Vs. [9,10]

In recent years, great progress has been made in improving the μ of thin-film In_2O_3. Mobility values over 100 cm^2/Vs have been reported with the use of alternative In_2O_3 dopants such as Mo, Ti, Zr and W. [11] Unfortunately, the required higher deposition temperatures (>300 °C) makes these approaches incompatible with for example polymeric substrates and SHJ solar cell processing. [12] In 2007, Koida *et al.* found that replacing the Sn doping with H doping can lead to good film properties at low processing temperatures. [13] By sputtering In_2O_3 at room temperature with the addition of H_2O vapor, hydrogenated amorphous In_2O_3:H films with small embedded crystallites were obtained. Upon a low temperature post-anneal (≤200 °C), solid phase crystallization (SPC) occured, resulting in a film with a Hall mobility as high as 140 cm^2/Vs and typical N_e values of $1-2\times10^{20}$ cm^{-3}. [13,14] The ρ of the resulting film is equal to that of a typical In_2O_3:Sn film, but the transmittance in the infrared is enhanced due to the lower N_e and higher μ.

The reduced FCA of In_2O_3:H compared to conventional In_2O_3:Sn makes In_2O_3:H a highly suitable TCO material for SHJ solar cells. Indeed, the application of sputtered In_2O_3:H in a SHJ solar cell can enhance the short circuit current density J_{sc} due to reduced FCA. [15,16,17,18] For example, Barraud *et al.* have demonstrated an increase in J_{sc} from 38.0 to 39.0 mA/cm^2 when replacing In_2O_3:Sn with In_2O_3:H, leading to a cell efficiency of 22.1%. [18] In 2011, Libera *et al.* demonstrated the growth of In_2O_3 films by ALD using cyclopentadienyl indium (InCp) and a combination of both H_2O and O_2 as reactants. [19] Their highest μ value (111 cm^2/Vs) was obtained using a simultaneous exposure of the film to O_2 and H_2O during the reactant step at a deposition temperature of 140 °C, which is just above the transition temperature from amorphous to polycrystalline growth. However, the influence of post-annealing on the In_2O_3 properties was not researched.

In this work a combined approach of the work of Koida *et al.* and Libera *et al.* was taken, i.e. amorphous In_2O_3:H films were deposited by ALD using InCp and a combination of both H_2O and O_2, followed by SPC by post-annealing. It will be shown that this ALD approach yields polycrystalline films with a lateral grain size of a few hundred nm, resulting in an excellent film quality in terms of μ and ρ. Also the potential of this approach to replace the front ITO layer in SHJ solar cells will be briefly addressed.
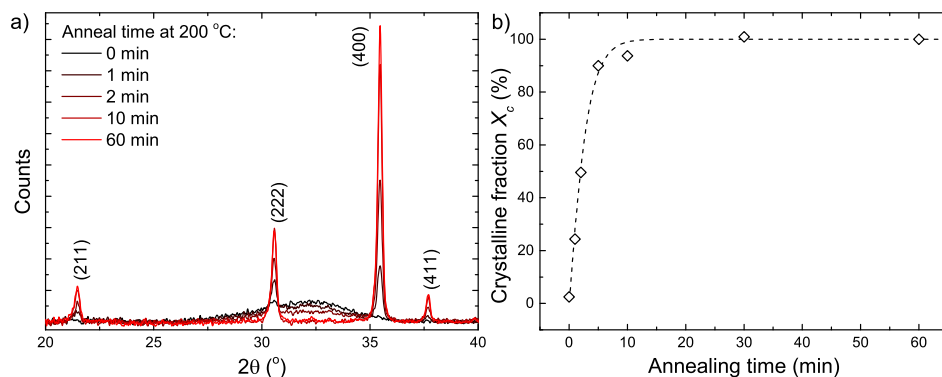
Figure 1: a) XRD 2θ scans for various annealing times at 200 °C. The Miller indices of the diffraction peaks of cubic In$_2$O$_3$ are indicated. b) Crystalline fraction as a function of annealing time at 200 °C, as determined by integration of the two main XRD peaks. The dashed line is a guide to the eye.

4.2   Experimental details

Si(100) wafers with a 430 nm thermal oxide, cut into 2x2 cm^2 samples, were used as substrates. Amorphous In$_2$O$_3$:H films of 75 nm thickness were deposited in an Oxford Instruments OpAL^{TM} ALD reactor at a substrate temperature of 100 °C. Cyclopentadienyl indium (InCp) and a combination of both H$_2$O and O$_2$ was used for ALD, leading to a growth of 0.12 nm per cycle. The used temperature is the lowest temperature that yields growth, i.e. the lower end of the ALD window. Prior to In$_2$O$_3$ deposition, a 2 nm Al$_2$O$_3$ layer was deposited by ALD using trimethylaluminum and H$_2$O as precursors. Post-deposition annealing took place in a Jipelec rapid thermal anneal (RTA) setup in an inert N$_2$ atmosphere at 200 °C. Growth at higher temperatures (>130 °C), which yields polycrystalline films, will not be discussed here as the films were of lower optoelectronic quality, also after post-annealing. Note that all samples were co-deposited in one run, and a good uniformity was observed.

4.3   Results and discussion

As determined by elastic recoil detection (ERD) analysis, the as-deposited samples have a H content of 4.2 at. %, which suggests that the In$_2$O$_3$ is unintentionally doped with H during the ALD process. X-ray diffraction (XRD) results shown in Figure 1(a) revealed that the as-deposited sample has a very broad feature around 32°, representing amorphous material and a very dim (222) peak, indicating the presence of a limited number of small crystals. Figure 1(a) also shows that various diffraction peaks belonging to the cubic In$_2$O$_3$ phase arise upon annealing at 200 °C, until the film is fully crystallized
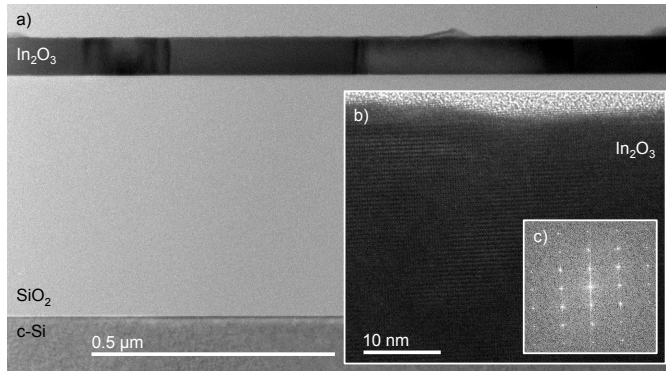
Figure 2: (a) Bright field cross-sectional TEM image of a crystallized In_2O_3:H. (b) High-resolution TEM and (c) the corresponding FFT pattern.

after 30 minutes. The crystallized films have a preferential <100> orientation, whereas polycrystalline films that are deposited at temperatures >130 °C exhibit a preferential <111> orientation (not shown).

Cross-sectional transmission electron microscopy (TEM) on a fully crystallized sample has revealed a large grain size and an excellent grain crystal quality. As shown in the Bright Field TEM image of Figure 2(a), the grains extend over the full film thickness and are a few hundred nanometer in lateral size. The BFTEM contrast is homogeneous over the crystals, indicating that the grains are virtually defect and stress free. The high-resolution TEM image in Figure 2(b) displays the defect-free nature of the crystals. The corresponding FFT pattern in Figure 2(c) displays a [011] zone axis pattern with the <100> direction being nearly parallel to the surface normal. Additionally, atomic force microscopy revealed a negligible RMS roughness of the films (< 0.6 nm), both before and after crystallization.

A measure for the film crystallinity X_c as a function of annealing time has been obtained from the XRD scans by comparing the sum of the peak areas I_{hkl} to the sum of the peak areas $I_{hkl,max}$ of a fully crystallized film:[20]

$$X_c = \frac{\Sigma_{hkl}I_{hkl}}{\Sigma_{hkl}I_{hkl_{max}}} \quad (4.3)$$

For this study, the two main diffraction peaks (i.e. (222) and (400)) have been used for the calculation of X_c. The calculated X_c as a function of annealing time is shown in Figure 1(b). The film shows rapid crystallization, and the process saturates after 10-30 minutes.

The evolution of the electronic properties as a function of film crystallinity, as obtained from Hall measurements, is shown in Figure 3. During crystallization, ρ decreases
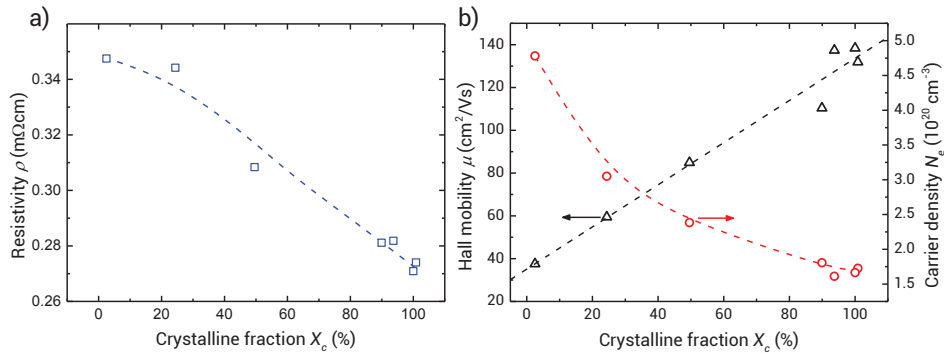
Figure 3: (a) Change in In$_2$O$_3$:H resistivity upon crystallization and (b) corresponding change in μ and N_e. Dashed lines are guides to the eye.

from 0.35 to 0.27 mΩcm. The value of μ (Figure 3(b)) increases linearly from 38 to as high as 138 cm^2/Vs after crystallization, similar to the value as obtained by Koida *et al.* To the authors' knowledge, these μ values are the highest reported to date for thin-film In$_2$O$_3$ at low processing temperatures (≤200 °C).[11,14] N_e decreases from 4.8×10^{20} cm^{-3} to 1.6×10^{20} cm^{-3}. The net decrease in ρ of the film upon crystallization thus stems from an increase in μ that outweighs the decrease in N_e.

In order to assess the optical absorption in the In$_2$O$_3$:H layers, the absorption coefficient has been extracted from spectroscopic ellipsometry (SE) data, as shown in Figure 4. The In$_2$O$_3$:H dielectric function was modelled by a combination of a Tauc-Lorentz (TL) oscillator to account for absorption across the direct optical bandgap and a Drude oscillator to account for FCA in the infrared part of the spectrum.[21] As can be seen, at low photon energy FCA decreases during crystallization. This stems both from the reduction in N_e, which reduces the plasma frequency of the film, and the increase in μ, which decreases the absorption above the plasma frequency. For the fully crystallized film, FCA above the band-gap of c-Si becomes negligible. The onset of absorption across the bandgap increases with crystallization, which can be both attributed to a change in optical bandgap and to a reduction in sub-gap defect states, as reflected by the fitted TL oscillator parameters: The Tauc optical gap E_T increases from 2.9 to 3.2 eV during crystallization, whereas the Tauc broadening parameter B_T decreases from 2.0 to 1.0 eV, indicating increased structural order in the film.[21] Overall, absorption in the optically relevant spectral range for solar cells, as reflected by the AM1.5g spectrum in Figure 4, is reduced by the crystallization process.

The presented approach to prepare In$_2$O$_3$:H seems especially promising to replace the front ITO layer in SHJ solar cells: Firstly, the negligible FCA can improve the red-response and consequently the J_{sc}. Secondly, the lower resistivity of In$_2$O$_3$:H reduces
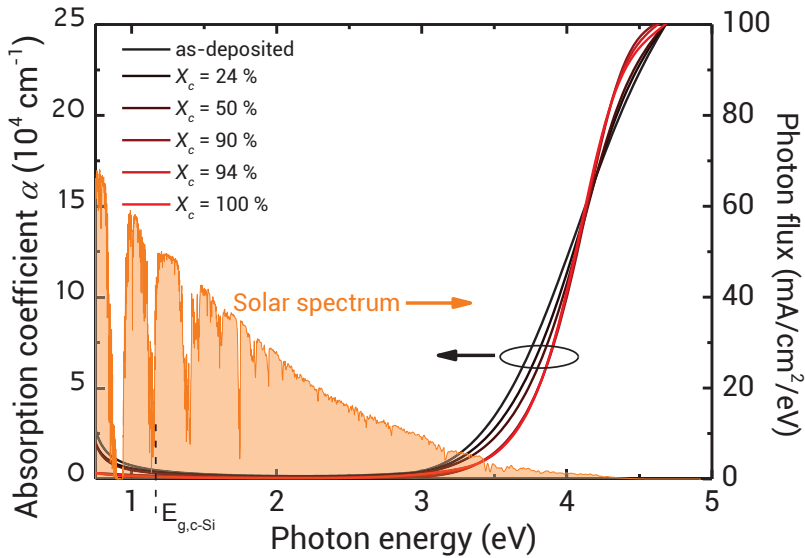
Figure 4: Absorption coefficient of In$_2$O$_3$:H films at various stages of crystallization. For reference, the bandgap of crystalline silicon and the AM1.5g solar irradiance spectrum are shown as well.

resistive losses and the required front metallization area. Thirdly, the soft nature of the ALD process is compatible with sensitive a-Si:H passivation layers. This has been corroborated by depositing In$_2$O$_3$:H on an n-type FZ wafer symmetrically passivated with 10 nm of a-Si:H, which leads to a low surface recombination velocity of 7 cm/s. Also note that the required post-anneal step is already standard in SHJ processing to cure the metal paste. [18]

4.4   Conclusions

It has been shown that In$_2$O$_3$:H films with both a very high μ and low ρ and low absorption can be prepared by the deposition of amorphous In$_2$O$_3$:H films by ALD at a temperature of 100 °C and by subsequent SPC for only 10 minutes at 200 °C. The combination of excellent material properties and the low temperature, damage-free processing makes this approach to prepare In$_2$O$_3$:H very promising for various sensitive optoelectronic applications, especially for TCO applications in SHJ solar cells.

Acknowledgements

References

[1] J. A. van Delft, D. Garcia-Alonso, and W. M. M. Kessels, Semiconductor Science and Technology **27**, 074002 (2012).

[2] G. Dingemans and W. M. M. Kessels, Journal of Vacuum Science & Technology A: Vacuum, Surfaces, and Films **30**, 040802 (2012).

[3] B. Demaurex, S. De Wolf, A. Descoeudres, Z. C. Holman, and C. Ballif, Applied Physics Letters **101**, 171604 (2012).

[4] A. Illiberi, P. Kudlacek, A. H. M. Smets, M. Creatore, and M. C. M. van de Sanden, Applied Physics Letters **98**, 242115 (2011).

[5] G. Gu, V. Bulović, P. E. Burrows, S. R. Forrest, and M. E. Thompson, Applied Physics Letters **68**, 2606 (1996).

[6] D. Vaufrey, M. B. Khalifa, J. Tardy, C. Ghica, M. G. Blanchin, C. Sandu, and J. A. Roger, Semiconductor Science and Technology **18**, 253 (2003).

[7] B. Demaurex, J. P. Seif, S. Smit, B. Macco, W. M. M. Kessels, J. Geissbuhler, S. De Wolf, and C. Ballif, IEEE Journal of Photovoltaics **4**, 1387 (2014).

[8] B. Macco, D. Deligiannis, S. Smit, R. A. C. M. M. van Swaaij, M. Zeman, and W. M. M. Kessels, Semiconductor Science and Technology **29**, 122001 (2014).

[9] K. Ellmer and R. Mientus, Thin Solid Films **516**, 4620 (2008).

[10] Z. C. Holman, A. Descoeudres, L. Barraud, F. Z. Fernandez, J. P. Seif, S. De Wolf, and C. Ballif, IEEE Journal of Photovoltaics **2**, 7 (2012).

[11] S. Calnan and A. Tiwari, Thin Solid Films **518**, 1839 (2010).

[12] S. De Wolf, A. Descoeudres, Z. C. Holman, and C. Ballif, Green **2**, 7 (2012).

[13] T. Koida, H. Fujiwara, and M. Kondo, Japanese Journal of Applied Physics **46**, L685 (2007).

[14] T. Koida, M. Kondo, K. Tsutsumi, A. Sakaguchi, M. Suzuki, and H. Fujiwara, Journal of Applied Physics **107**, 033514 (2010).

[15] T. Koida, H. Fujiwara, and M. Kondo, Applied Physics Express **1**, 041501 (2008).

[16] T. Koida, H. Fujiwara, and M. Kondo, Solar Energy Materials and Solar Cells **93**, 851 (2009).

[17] T. Koida, H. Sai, and M. Kondo, Energy Materials: Materials Science and Engineering for Energy Systems **7**, 102 (2012).

[18] L. Barraud, Z. C. Holman, N. Badel, P. Reiss, A. Descoeudres, C. Battaglia, S. De Wolf, and C. Ballif, Solar Energy Materials and Solar Cells **115**, 151 (2013).

[19] J. A. Libera, J. N. Hryn, and J. W. Elam, Chemistry of Materials **23**, 2150 (2011).

[20] K. Sharma, M. V. Ponomarev, M. A. Verheijen, O. Kunz, F. D. Tichelaar, M. C. M. van de Sanden, and M. Creatore, Journal of Applied Physics **111**, 103510 (2012).

[21] H. Fujiwara and M. Kondo, Physical Review B **71**, 075109 (2005)

5

Electron Scattering and Doping Mechanisms in Solid-Phase-Crystallized In$_2$O$_3$:H Prepared by Atomic Layer Deposition

Abstract: Hydrogen-doped indium oxide (In$_2$O$_3$:H) has recently emerged as an enabling transparent conductive oxide for solar cells, in particular for silicon heterojunction solar cells because its high electron mobility (>100 cm^2/Vs) allows for a simultaneously high electrical conductivity and optical transparency. Here, we report on high-quality In$_2$O$_3$:H prepared by a low-temperature atomic layer deposition (ALD) process and present insights into the doping mechanism and the electron scattering processes that limit the carrier mobility in such films. The process consists of ALD of amorphous In$_2$O$_3$:H at 100 °C and subsequent solid-phase crystallization at 150–200 °C to obtain large-grained polycrystalline In$_2$O$_3$:H films. The changes in optoelectronic properties upon crystallization have been monitored both electrically by Hall measurements and optically by analysis of the Drude response. After crystallization, an excellent carrier mobility of 128 $\pm$ 4 cm^2/Vs can be obtained at a carrier density of 1.8 × 10^{20} cm^{-3}, irrespective of the annealing temperature. Temperature-dependent Hall measurements

have revealed that electron scattering is dominated by unavoidable phonon and ionized impurity scattering from singly charged H-donors. Extrinsic defect scattering related to material quality such as grain boundary and neutral impurity scattering was found to be negligible in crystallized films indicating that the carrier mobility is maximized. Furthermore, by comparison of the absolute H-concentration and the carrier density in crystallized films, it is deduced that <4% of the incorporated H is an active dopant in crystallized films. Therefore, it can be concluded that inactive H atoms do not (significantly) contribute to defect scattering, which potentially explains why In$_2$O$_3$:H films are capable of achieving a much higher carrier mobility than conventional In$_2$O$_3$:Sn (ITO).

5.1   Introduction

Tin-doped indium oxide (In$_2$O$_3$:Sn or ITO) has become the most widely used transparent conductive oxide (TCO) in a wide range of optoelectronic applications including displays and solar cells. The key advantage of In$_2$O$_3$:Sn is its relatively high electron mobility μ. A high electron mobility allows for a high electrical conductivity at a lower carrier density, thereby mitigating free carrier absorption (FCA) in the infrared. In$_2$O$_3$:Sn films are usually prepared by sputtering, and typical values for the mobility encountered in literature lie in the 20- 40 cm^2/Vs range.[1]

Recently, H doping of In$_2$O$_3$ has gained significant interest over traditional Sn doping. This development was sparked in 2007, when Koida *et al.* demonstrated that H-doped indium oxide (In$_2$O$_3$:H) films can exhibit an extremely high Hall mobility of 130 cm^2/Vs at moderate carrier densities of $1-2 \times 10^{20}$ cm^{-3}.[2,3] Their process consisted of the deposition of amorphous In$_2$O$_3$:H at room temperature by rf magnetron sputtering using an In$_2$O$_3$ ceramic target, with the addition of H$_2$O vapor as a source of H doping. To obtain the excellent film properties, the films were subjected to a postdeposition anneal, which led to solid-phase crystallization (SPC) of the films. Although H doping results in a resistivity similar to that typical for Sn doping, the FCA is strongly reduced because of a lower carrier density and a higher mobility. This makes In$_2$O$_3$:H particularly promising for optoelectronic applications in which FCA is an issue, such as silicon heterojunction (SHJ) solar cells.[4] Indeed, as various authors have shown, the reduced FCA can significantly enhance the short-circuit current density J_{sc} of a SHJ solar cell.[5,6,7,8]

These experimental results were soon followed by further theoretical and experimental work to explore the doping mechanism and scattering processes limiting the mobility in In$_2$O$_3$:H. First, the donor nature of H in In$_2$O$_3$ was confirmed by *ab initio* calculations by Van de Walle and co-workers, who demonstrated that the hydrogen donor state (either interstitial or substitutional) is energetically more favorable than an oxygen vacancy.[9] Second, Preissler *et al.* have performed a detailed experimental and theoretical inves-

tigation of the scattering processes in single-crystal In_2O_3 for a large range of carrier densities (7×10^{16}-1×10^{21} cm^{-3}).[10] Key findings were that optical phonon scattering is dominant for carrier densities <10^{20} cm^{-3}, whereas ionized impurity scattering is dominant for higher carrier densities. At intermediate carrier densities of 1-2 $\times 10^{20}$ cm^{-3}, their model predicts a local maximum in mobility ($\sim$90 cm^2/Vs). This maximum is due to a balance in decreasing phonon scattering by increased screening of optical phonons and increased ionized impurity scattering with increasing carrier density. This predicted local maximum in mobility at carrier densities of 1–2 $\times 10^{20}$ cm^{-3} was also found experimentally, but the experimental values exceeded their predicted local maximum in mobility of $\sim$90 cm^2/Vs. This was tentatively attributed to an underestimated screening of the optical phonons.[10]

In 2011, Libera *et al.* demonstrated a low-temperature ($\geq$100 °C) atomic layer deposition (ALD) process for In_2O_3 using cyclopentadienyl indium (InCp) and a combination of both H_2O and O_2 as reactants.[11] Depending on the growth temperature and reactant exposure sequence, either amorphous or polycrystalline films were obtained. The highest mobility (111 cm^2/Vs) was obtained using a simultaneous exposure of the film to O_2 and H_2O during the reactant step at a deposition temperature of 140 °C, which is just above the transition temperature from amorphous to polycrystalline growth. However, hydrogen incorporation, postannealing, or doping mechanisms were not investigated for this process at that time.

Recently, we demonstrated that In_2O_3:H films of superior quality can be made by an approach combining the work of Koida *et al.* and Libera *et al.*[12] Amorphous In_2O_3:H films of 75 nm were deposited by ALD using InCp and a combination of both H_2O and O_2 at a substrate temperature of 100 °C. H was unintentionally incorporated during the ALD process, leading to a H concentration of 4.2 atomic percent (at. %). By subsequent thermal crystallization at 200 °C, crystal grains that extend over the full film thickness and are a few hundred nanometers in lateral size were obtained. This, together with a high in-grain crystal quality, resulted in films with a very high Hall mobility (138 cm^2/Vs), a moderate carrier density (1.8 $\times 10^{20}$ cm^{-3}), and a low resistivity (0.27 mΩcm).[12] Furthermore, besides excellent material quality, one of the main merits of the preparation process using ALD and SPC is the absence of plasma-induced damage to the underlying layers that is typically found in conventional sputter deposition.[13,14,15] Moreover, this carrier density is in the range of the predicted local maximum by Preissler *et al.*, yet the mobility exceeds their predicted value. This renders these films ideally suited for further study of the electron scattering mechanisms limiting the carrier mobility of In_2O_3:H.

This work aims to extend the understanding of the factors that govern the carrier density and limit the carrier mobility in ALD In_2O_3:H films by analysis of the doping and the

identification of the role of the various scattering processes, respectively. To this end, the optoelectronic properties of the films have been studied as a function of film crystallinity, both optically by spectroscopic ellipsometry focusing on the Drude response and electrically by temperature-dependent Hall measurements. The main results of this study include the finding that in crystallized films only ionized impurity scattering from singly charged donors and optical phonon scattering are of importance and that the experimentally determined contribution of phonon scattering is indeed found to be about half of the value predicted by Preissler *et al.*[10] Furthermore, the analysis rules out the prevalence of doubly charged oxygen vacancies (V_O^{2+}) as dopant in crystallized In$_2$O$_3$:H, and the source of doping is attributed to interstitial (H_i^+) or substitutional (H_O^+) hydrogen. Even though only ∼4% of the H atoms in a crystallized In$_2$O$_3$:H film are observed to be an active dopant, neutral defect scattering from inactive H dopants is found to be negligible or absent. The fact that inactive H does not contribute to scattering could explain why H, besides being a singly charged donor, allows for extremely high carrier mobilities.

5.2   Experimental section

5.2.1   Sample preparation

Si(100) wafers with a 430 nm thermal oxide were used as substrates. A seed layer of 20 cycles of ALD Al$_2$O$_3$ was deposited using trimethylaluminum (TMA) and H$_2$O in an Oxford Instruments OpAL ALD reactor at a substrate temperature of 100 °C. In$_2$O$_3$:H films of 75 nm thickness were subsequently deposited using InCp and a combination of both H$_2$O and O$_2$. All samples used in this study were codeposited in one run. Post-deposition annealing took place in a Jipelec rapid thermal anneal (RTA) in an inert N$_2$ atmosphere. Annealing temperatures were varied between 150 and 200 °C. Note that in order to ensure compatibility with SHJ solar cell processing, the maximum annealing temperature has been limited to 200 °C.[4]

5.2.2   Film analysis

X-ray diffraction (XRD) measurements were used to evaluate the film crystallinity X_c at various stages of crystallization. This was done by comparison of the sum of the integrated peak areas I_{hkl} of the two main diffraction peaks (i.e., (222) and (400)) to the sum of the maximum peak areas $I_{hkl,max}$ of the fully crystallized sample.[12]

$$X_c = \frac{\Sigma_{hkl} I_{hkl}}{\Sigma_{hkl} I_{hkl_{max}}}$$

(5.1)

Example XRD spectra at various stages of crystallization can be found in Supporting Information Figure 5.

Rutherford backscattering (RBS) and elastic recoil detection (ERD) were used to obtain absolute atomic densities of most notably indium, oxygen, and hydrogen. The oxygen and indium binding configurations were assessed from X-ray photoelectron spectroscopy (XPS).

The film optoelectronic properties were evaluated from Hall measurements in the Van der Pauw configuration and by spectroscopic ellipsometry (SE). The Hall mobility μ_{Hall} and carrier density $N_{e,Hall}$ were corrected using the Hall scattering factor R_H to obtain the effective mobility μ and N_e, according to $\mu = \mu_{Hall}/R_H$ and $N_e = N_{e,Hall} \times R_H$.[10] R_H was assumed to be constant at 1.03 for all the samples, as determined by Preissler *et al.* for the carrier densities of interest in this study.[10] SE was used to determine the thicknesses and optical constants of the films. For the SE analysis, the dielectric function in the measured photon energy range of 0.75–5.0 eV was modeled by a combination of a Tauc–Lorentz oscillator to account for absorption across the optical bandgap and a Drude oscillator to account for FCA in the infrared part of the spectrum.[16] From the Drude modeling, the unscreened plasma frequency E_p and optical mobility can be obtained. Note that in principle the optical mobility determined by SE and the electrical mobility obtained from Hall measurements need not be equal because these two techniques are sensitive to scattering phenomena at different length scales. Generally, the microscopic interaction distance of light with free carriers is smaller than the characteristic length scale for grain boundary scattering, and such scattering is thus not optically probed. In macroscopic Hall measurements, all scattering phenomena are probed. Therefore, comparison of the optical and electrical mobility yields information on the contribution of grain boundary scattering.[17]

Additionally, by assuming that the optically probed electron density is equal to the carrier density obtained from Hall measurements (i.e., $N_{opt} = N_e$) the effective electron mass m^* can be calculated from the unscreened plasma frequency E_p and carrier density.[3]

$$m^* = \frac{\hbar^2 e^2 N_e}{m_e \varepsilon_0 E_p^2} \tag{5.2}$$

In this equation, $\hbar$ is the reduced Planck's constant, e is the elementary charge, ε_0 is the vacuum permittivity, and m_e is the electron mass.

Besides being assessed by XRD, the crystallinity X_c has also been assessed by modeling the ellipsometry data using a Bruggeman effective medium approximation (EMA) model, constituted by the optical constants obtained from an as-deposited amorphous, and a fully crystallized In_2O_3:H layer. The optical constants of the amorphous and crys-

tallized layer can be found in Supporting Information Figure 6. The percentage of crystallinity (i.e., crystalline fraction X_c) and the depolarization factor were used as fit parameters.
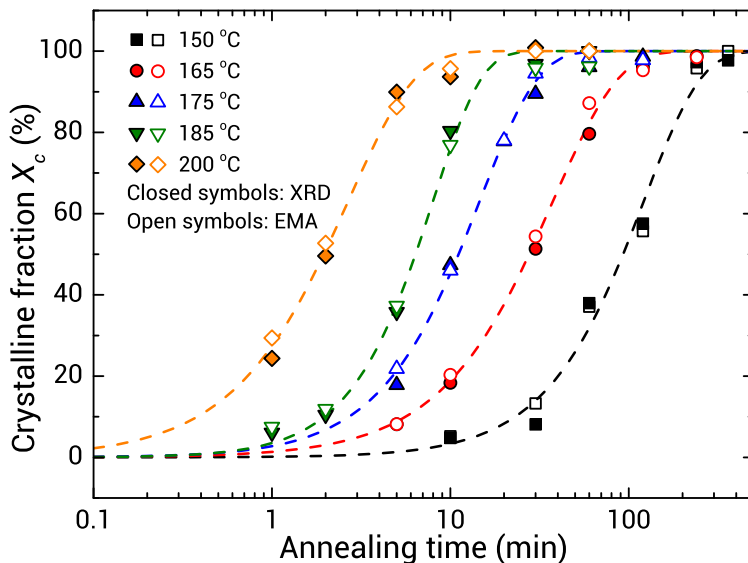

Figure 1: Crystalline fraction of In$_2$O$_3$:H films as a function of annealing time for various annealing temperatures. The crystallinity has been obtained from XRD (closed symbols) and SE modeling using an effective medium approximation (EMA, open symbols). The EMA consisted of the optical constants of fully crystalline and amorphous In$_2$O$_3$:H.

5.3   Results and discussion

5.3.1   Structural changes upon annealing of In$_2$O$_3$:H

To obtain information on the crystallization kinetics, the film crystallinity has been evaluated by both XRD, according to Equation 5.1, and by SE modeling for a range of annealing temperatures. In Figure 1, the evolution of the crystalline fraction during annealing is displayed. It can be seen that there is an overall good agreement between the crystalline fractions determined by XRD and SE.

Crystallization is observed to occur more rapidly at higher annealing temperatures. At an annealing temperature of 200 °C, the film is fully crystallized after only 10 min, whereas it takes over 5 h to fully crystallize a film at 150 °C, indicating that crystallization is a thermally activated process. In Supporting Information Figure 7, cross-sectional TEM images of a fully crystallized sample are shown. In the next sections,

Table 1: Elemental composition of In_2O_3:H films annealed at 200 °C as obtained from RBS and ERD.[*]

Sample	[In] (at. %)	[O] (at. %)	[H] (at. %)	O/In ratio
As-deposited, amorphous	36.8	59.0	4.2	1.6
X_c = 24%	36.5	59.4	4.1	1.6
Crystallized, X_c = 100%	37.1	59.0	3.9	1.6
Stoichiometric In_2O_3	40	60	0	1.5

the determined crystalline fractions X_c have been used to evaluate the evolution of the optoelectronic properties of the film as a function of crystallinity.

Changes in elemental composition during crystallization at 200 °C have been monitored by RBS and ERD, and the results have been summarized in Table 1. As can be seen, the films are slightly oxygen-rich with respect to bulk, single-crystal In_2O_3, and within experimental error, there is no change in the O/In ratio during annealing at 200 °C. A significant amount of hydrogen, 4.2 at. %, is incorporated in the film during deposition. Upon crystallization, a slight reduction in hydrogen content to 3.9 at. % is observed, presumably because of H_2 or H_2O effusion although the relative decrease (10%) is on the same order as the relative error in the determination of the hydrogen content (7%). The presence of OH bonds in amorphous and crystallized In_2O_3:H has also been confirmed by XPS from analysis of the O1s signal (Supporting Information Figure 8).[18,19]

5.3.2 Change in optoelectronic properties upon crystallization

In addition to the change in structural properties, Hall and SE measurements have been performed on films of varying crystalline fraction X_c in order to gain insight into the evolution of the optoelectronic properties during crystallization. In Figure 2 the change upon crystallization in film carrier density N_e, as obtained from Hall measurements, and the plasma frequency E_p, as obtained from the ellipsometry modeling, are shown. As can be seen, the carrier density decreases from $\sim 4.8 \times 10^{20}$ to $\sim 1.8 \times 10^{20}$ cm^{-3} during crystallization. A simultaneous reduction in plasma frequency E_p is observed from ~ 1.5 to ~ 1.0 eV because of a reduction of the carrier density.

The electrical mobility (Figure 3) increases linearly with film crystallinity. This indicates that the measured Hall mobility is basically the average, weighted by X_c, of the electrical mobility values corresponding to the amorphous ($\mu_{e,a}$) and crystalline ($\mu_{e,c}$) phase. From the linear fit in Figure 3, values of $\mu_{e,a}$ = 35 ± 1 cm^2/Vs and $\mu_{e,c}$ = 128 ± 4 cm^2/Vs have been determined. Because the increase in carrier mobility outweighs

---

[*]The relative errors in the atomic percentages of In, O, and H are 2, 2, and 7%, respectively. The error in the O/In ratio is 3%.
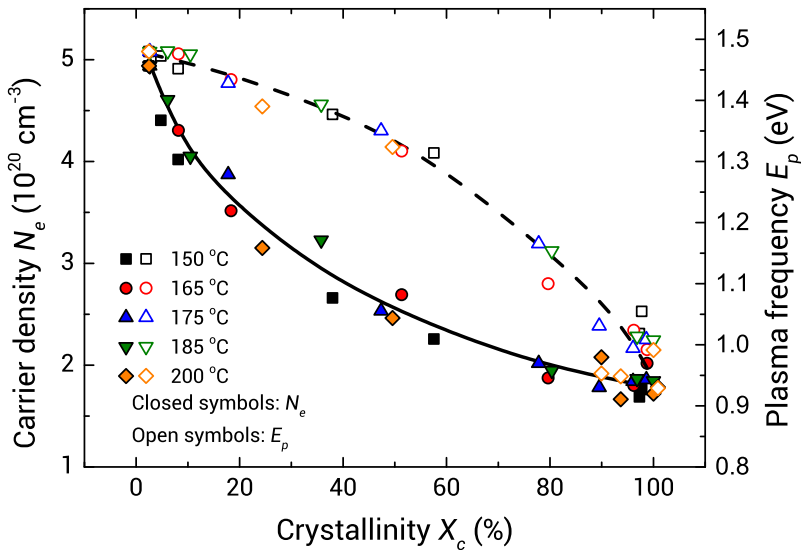
Figure 2: Change in carrier density (closed symbol) as obtained from Hall measurements and plasma frequency (open symbol) as obtained from SE modeling for films of varying crystalline fractions annealed at various temperatures. The solid and dashed lines are guides to the eye.

the decrease in carrier density, the film resistivity decreases from 0.35 mΩcm for the as-deposited sample to as low as 0.26 mΩcm for a fully crystallized sample. Interestingly, all the optoelectronic properties mainly depend on the film crystallinity irrespective of the annealing temperature used. This shows that at lower annealing temperatures In$_2$O$_3$:H can be obtained that is of quality as high as that obtained at higher annealing temperatures. This extends the applicability of the process to substrate materials that have more stringent requirements with respect to the thermal budget. Additionally, it should be noted that the samples showed excellent stability after 1 year of storage at room temperature.

The effective electron mass of amorphous (m_a^*) and crystallized (m_c^*) films has been determined using Equation 5.2, in which the plasma frequency and carrier density were taken from Figure 2. Values have been obtained that are in the range of values previously reported in literature: for the amorphous films, a value of m_a^* = 0.31 ± 0.01, and for the crystallized films, a value of m_c^* = 0.23 ± 0.02. [16,20,21,22] The reduction in effective mass upon crystallization is most likely due to a combination of a reduction in carrier density and an alteration of the band structure.

The optical mobility, obtained from modeling the Drude oscillator in the ellipsometry data, shows very good agreement with the electrical mobility for the as-deposited and fully crystallized samples. Because scattering phenomena at length scales of grain boundary dimensions are not optically probed by ellipsometry, the fact that the optical
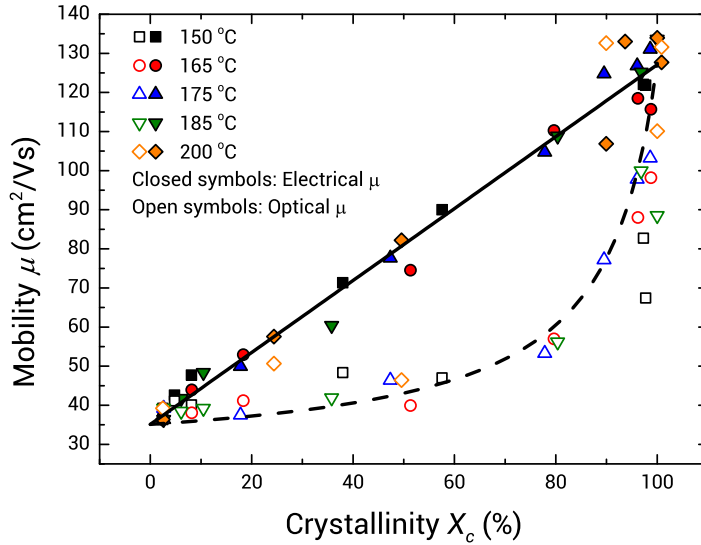
Figure 3: Change in electrical mobility (closed symbol) and optical mobility (open symbol) during crystallization. The solid line is a linear fit of the electrical mobility, whereas the dashed line is generated using Equation 5.3.

and electrical mobility are equal implies that grain boundary scattering plays a negligible role in the crystallized films.[17] This statement can also be corroborated by comparison of the mean free path (MFP) of the charge carrier with the lateral grain size of a few hundred nanometer for crystallized In_2O_3:H films.[12] Using the Fermi velocity $v_F = \hbar(3\pi^2 N_e)^{1/3}/(m^* m_e)$ and the scatter frequency $\omega_\tau = e/(m^* m_e \mu_e)$, MFP $= v_F/\omega_\tau$ has been found to be 15 nm for a fully crystallized sample.[17] Indeed, the length scale for grain boundary scattering greatly exceeds the MFP of the charge carrier. Additionally, the grain boundaries are most likely well passivated by the available hydrogen.[19] Evidently, for the as-deposited samples, the optical and electrical mobility are equal because of the absence of grain boundary scattering in the amorphous material. However, for partly crystallized films the optical mobility is lower than the electrical mobility. This is in contrast to the common observation that depending on the presence of grain boundary scattering the optical mobility should either be equal or exceed the electrical mobility. This discrepancy can be explained by the fact that the film is modeled as a homogeneous medium in which only a single Drude oscillator is used to represent the scattering of electrons in both amorphous and crystalline In_2O_3:H phases. As seen from Figure 3, the electron density belonging to the amorphous phase ($\sim 4.8 \times 10^{20}$ cm^{-3}) is much higher than that belonging to the fully crystalline phase ($\sim 1.8 \times 10^{20}$ cm^{-3}). Because all free electrons contribute equally to the Drude response, the higher electron density of the amorphous phase will weigh more strongly in the fitting of the effective

scatter frequency (and hence to the optical mobility). Under the assumption that the fitted scatter frequency is weighted both by the volume fractions and carrier densities of the respective phases, the weighted optical mobility μ_{opt} for a given crystallinity X_c is represented as

$$\mu_{opt} = \mu_a \mu_c \frac{(1 - X_c)N_{e,a} + X_c N_{e,c}}{(1 - X_c)N_{e,a}\mu_c + X_c N_{e,c}\mu_a} \tag{5.3}$$

In this equation, the subscripts *a* and *c* denote the amorphous and crystalline phase, respectively. When inserting the carrier densities N_e and mobility μ of the amorphous and crystalline phase, as obtained by Hall measurements in Equation 5.3, the dashed curve in Figure 3 is obtained. As can be seen, the trend in fitted optical mobility shows good agreement with Equation 5.3. This confirms the aforementioned hypothesis, and it also demonstrates that for a proper evaluation of the mobility of a multicomponent material by optical means detailed knowledge of the material is prerequisite.

5.3.3   Mobility limit and doping mechanism in In$_2$O$_3$:H

To distinguish between various scattering contributions in In$_2$O$_3$:H films, temperature-dependent Hall measurements have been performed on films of varying crystallinity X_c, as shown in the inset of Figure 4. As can be seen, the temperature dependence of the mobility of In$_2$O$_3$:H greatly varies with the film crystallinity. The carrier densities of the films did however not show a temperature dependence as expected given the degenerate nature of the semiconductor.

Because the various carrier scattering mechanisms have different temperature dependencies, their contributions to the total scattering can be extracted by fitting the temperature-dependent Hall data to an appropriate temperature-dependent mobility model. Defect scattering (including both ionized and neutral impurity scattering) is independent of temperature in a degenerate semiconductor, whereas phonon scattering follows a power law:

$$\mu_{phonon} = \mu_0 \left(\frac{T}{T_0} \right)^{-p} \tag{5.4}$$

In this equation, μ_0 denotes the phonon mobility at a reference temperature T_0. The parameter p is a parameter which should be either 1 if the temperature is above the Debye temperature or in the range of 2-4 if the temperature is below the Debye temperature.[23]

If the mobility is limited by a temperature-independent contribution from defect scattering (either neutral or ionized impurities) and a temperature-dependent contribution
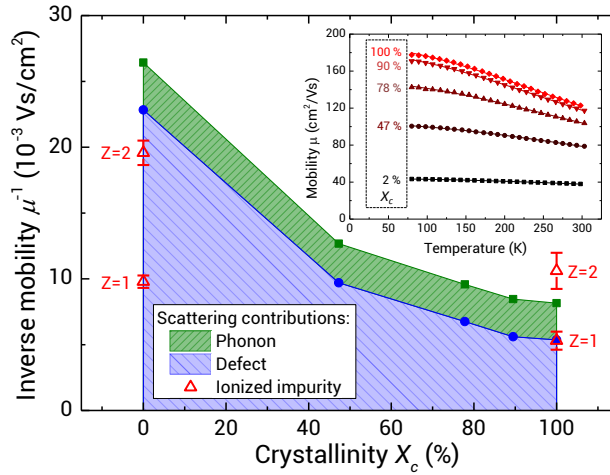
Figure 4: Inverse carrier mobility of In$_2$O$_3$:H films as a function of film crystallinity X_c. The contribution of phonon and defect scattering to the total scattering was obtained from the fits to the data in the inset. The ionized impurity scattering contributions of both singly ($Z = 1$) and doubly charged ($Z = 2$) donors in the amorphous and crystalline phases were calculated using eq Equation 5.6. (Inset) Temperature-dependent carrier mobility of In$_2$O$_3$:H films of varying crystallinity, annealed at 175 °C. Solid lines are fits to the data using Equation 5.5. The percentages denote the crystalline fraction X_c.

from phonon scattering, then the resulting temperature-dependent mobility can be expressed as follows, according to Matthiessen's rule:

$$\frac{1}{\mu(T)} = \frac{1}{\mu_i} + \frac{1}{\mu_0} \left(\frac{T}{T_0} \right)^p \tag{5.5}$$

In this equation, μ_i is the temperature-independent mobility caused by defect scattering. Note that grain boundary scattering is not explicitly taken into account in this expression. Given that the optical and electrical mobility for fully crystallized films are equal, it is expected that grain boundary scattering plays a negligible role. Additionally, at the carrier densities of interest, transport across grain boundaries will be mainly through tunneling instead of thermionic emission.[24] Because tunneling processes are temperature-independent, the grain boundary contribution would be contained in the temperature independent mobility μ_i.

The temperature-dependent Hall data have been fitted using Equation 5.5, which allows for the determination of the room temperature phonon mobility μ_0 and defect scattering mobility μ_i. In all fits, the parameter p converged to values close to 2 and has therefore been fixed at 2. Reported values for the Debye temperature of In$_2$O$_3$ range from 420 to 811 K, and because all measurements were performed at lower temperatures, the value of p is within our expectation.[10,25,26]

In Figure 4, the contribution of phonon and defect scattering to the inverse mobil-

ity at various stages of crystallization has been plotted. By plotting the inverse mobility instead of the mobility, the different scattering contributions can be more readily visualized because they add linearly. As can be seen, the contribution of phonon scattering is rather constant during the crystallization process, whereas defect scattering decreases greatly upon crystallization. For reference, the calculated contribution of ionized impurity scattering to the inverse mobility because of either singly ($Z = 1$) or doubly ($Z = 2$) charged donors in amorphous and crystallized In$_2$O$_3$:H has been added. This has been calculated using Equation 5.6:[27]

$$\mu_{ii} = \frac{3(\varepsilon_r \varepsilon_0)^2 h^3}{Z^2 m^{*2} e^3} \frac{N_e}{N_i} \frac{1}{F_{ii}^{np}(\zeta_0)} \tag{5.6}$$

In this equation, h is Planck's constant, ε_0 and ε_r are the vacuum and relative permittivity, respectively, and $\zeta_0 = (3\pi^2)^{1/3} \varepsilon_r \varepsilon_0 h^2 N_e^{1/3} / m^* e^2$. Z is the charge state of the ionized impurity, and N_i the concentration of ionized impurities (taken to be N_e/Z; i.e., full ionization is assumed). $F_{ii}^{np}(\zeta_0)$ is the carrier-density-dependent screening function for ionized impurity scattering in a degenerate semiconductor.[28] The calculations were performed using the previously determined carrier densities and effective masses (and uncertainties therein) of the amorphous and crystalline phase and a relative permittivity of 8.9 for In$_2$O$_3$.[3]

A few key observations can be made from Figure 4. First, after crystallization the defect scattering contribution to the inverse mobility is much less than the limit for doubly charged donors ($Z = 2$), and within experimental error, ionized impurity scattering from singly charged donors ($Z = 1$) is the sole contributor to the total defect scattering. This proves that doubly charged donors, e.g., V_O^{2+}, cannot be the main electron donors for the crystallized films and that singly charged hydrogen in either an interstitial (H_i^+) or substitutional (H_O^+) site is the main electron donor after crystallization as was also predicted by density functional theory.[9] Interestingly, besides ionized impurity scattering from singly charged donors, the only other contribution to the inverse mobility for a fully crystallized film stems from phonon scattering (34%). This indicates that other defect scattering mechanisms (e.g., grain boundary scattering and neutral impurity scattering) play a negligible role in crystallized films and that the film mobility is limited by the fundamental phonon and ionized impurity scattering processes.

Second, the fitted phonon mobility value of the crystallized sample is around 360 cm^2/Vs, which is higher than the value of $\sim$180 cm^2/Vs predicted by Preissler et al.[10] This is in line with their speculation that their model underestimates optical phonon scattering and explains the fact that experimental mobility values can exceed their predicted values.

Third, the mobility of the as-deposited amorphous samples is very close to the mobil-

ity limit because of ionized impurity scattering from doubly charged donors, calculated using the previously determined effective mass in amorphous In_2O_3:H. A similar observation was made by Koida *et al.*, who suggested that this is due to the fact that ionized impurity scattering from doubly charged oxygen vacancies (V_O^{2+}) is the dominant scattering mechanism in amorphous In_2O_3:H made by sputtering.[3] The results in Figure 4 indicate that the same may apply to amorphous In_2O_3:H made by ALD, although from this data it cannot be concluded whether the mobility is solely limited by ionized impurity scattering from doubly charged donors. It is very well possible that also in amorphous films singly charged donors are prevalent and that other scattering mechanisms such as neutral impurity or defect scattering play an important role as well. Hence, the mobility increase during crystallization can be due to a reduction in other defect scattering mechanisms (e.g., neutral impurity) or due to a change from doubly charged donors to singly charged donors or a combination thereof.

Furthermore, using the concentration of hydrogen as obtained by ERD (4.9×10^{21} cm^{-3}), it has been calculated that only $\sim$3.7% of the incorporated H needs to serve as an active dopant in order to account for the carrier density of crystallized films (1.8×10^{20} cm^{-3}). Because neutral impurity scattering does not appear to play a major role, this suggests that inactive hydrogen ($\sim$96.3%) in the In_2O_3:H matrix does not significantly contribute to scattering. In addition to the possibility of grain boundary passivation by hydrogen, this could very well be the main reason why H-doped films are capable of reaching much higher mobility values than typically obtained with Sn-doping.

5.4 Conclusions

In this work, the role of ionized impurity and optical phonon scattering, along with the doping mechanism in crystallized In_2O_3:H TCOs made by ALD has been established. It has been shown that irrespective of the annealing temperature films with excellent material properties are obtained after crystallization. From a comparison of the electrical and optical mobility of crystallized films, it has been found that grain boundary scattering does not play a significant role in these films. Additionally, the discrepancy between electrical and optical mobility for partly crystallized films has been explained by a difference in Drude response of the amorphous and crystalline parts of the mixed-phase material because of a difference in carrier density therein.

For fully crystallized films, the total scattering is dominated by optical phonon scattering and ionized impurity scattering from singly charged donors. Because these scattering processes are unavoidable, the mobility of the crystallized In_2O_3:H samples is at its upper limit for this specific carrier density. Additionally, the obtained optical phonon mobility exceeds the value predicted by Preissler *et al.*, which confirms their suspicion

of an underestimation of phonon scattering in In$_2$O$_3$.

Ionized impurity scattering of singly ionized dopants was found to be the only relevant defect scattering mechanism in crystallized films, which underlines the role of H as singly charged dopant in these films. The absence of any observable contribution of neutral defect scattering indicates that inactive H dopants do not contribute to a significant extent to defect scattering. This is a strong indication why H, besides being a singly charged donor, allows for extremely high carrier mobilities.

Acknowledgements

References

[1] K. Ellmer and R. Mientus, Thin Solid Films **516**, 4620 (2008).

[2] T. Koida, H. Fujiwara, and M. Kondo, Japanese Journal of Applied Physics **46**, L685 (2007).

[3] T. Koida, M. Kondo, K. Tsutsumi, A. Sakaguchi, M. Suzuki, and H. Fujiwara, Journal of Applied Physics **107**, 033514 (2010).

[4] S. De Wolf, A. Descoeudres, Z. C. Holman, and C. Ballif, Green **2**, 7 (2012).

[5] T. Koida, H. Fujiwara, and M. Kondo, Applied Physics Express **1**, 041501 (2008).

[6] T. Koida, H. Fujiwara, and M. Kondo, Solar Energy Materials and Solar Cells **93**, 851 (2009).

[7] T. Koida, H. Sai, and M. Kondo, Energy Materials: Materials Science and Engineering for Energy Systems **7**, 102 (2012).

[8] L. Barraud, Z. C. Holman, N. Badel, P. Reiss, A. Descoeudres, C. Battaglia, S. De Wolf, and C. Ballif, Solar Energy Materials and Solar Cells **115**, 151 (2013).

[9] S. Limpijumnong, P. Reunchan, A. Janotti, and C. Van de Walle, Physical Review B **80**, 193202 (2009).

[10] N. Preissler, O. Bierwagen, A. T. Ramu, and J. S. Speck, Physical Review B **88**, 085305 (2013).

[11] J. A. Libera, J. N. Hryn, and J. W. Elam, Chemistry of Materials **23**, 2150 (2011).

[12] B. Macco, Y. Wu, D. Vanhemel, and W. M. M. Kessels, physica status solidi (RRL) - Rapid Research Letters **8**, 987 (2014).

[13] B. Macco, D. Deligiannis, S. Smit, R. A. C. M. M. van Swaaij, M. Zeman, and W. M. M. Kessels, Semiconductor Science and Technology **29**, 122001 (2014).

[14] B. Demaurex, J. P. Seif, S. Smit, B. Macco, W. M. M. Kessels, J. Geissbuhler, S. De Wolf, and C. Ballif, IEEE Journal of Photovoltaics **4**, 1387 (2014).

[15] B. Demaurex, S. De Wolf, A. Descoeudres, Z. C. Holman, and C. Ballif, Applied Physics Letters **101**, 171604 (2012).

[16] H. Fujiwara and M. Kondo, Physical Review B **71**, 075109 (2005).

[17] H. C. M. Knoops, B. W. H. van de Loo, S. Smit, M. V. Ponomarev, J.-W. Weber, K. Sharma, W. M. M. Kessels, and M. Creatore, Journal of Vacuum Science & Technology A: Vacuum, Surfaces, and Films **33**, 021509 (2015).

[18] K. K. L. Purvis, G. Lu, J. Schwartz, and S. L. Bernasek, Journal of the American Chemical Society **122**, 1808 (2000).

[19] H. Wardenga, M. Frischbier, M. Morales-Masis, and A. Klein, Materials **8**, 561 (2015).

[20] S. Karazhanov, P. Ravindran, P. Vajeeston, A. Ulyashin, T. Finstad, and H. Fjellvåg, Physical Review B **76**, 075129 (2007).

[21] I. Hamberg, C. G. Granqvist, K. F. Berggren, B. E. Sernelius, and L. Engström, Physical Review B **30**, 3240 (1984).

[22] J. Rosen and O. Warschkow, Physical Review B **80**, 115215 (2009).

[23] A. K. Das, P. Misra, R. S. Ajimsha, A. Bose, S. C. Joshi, D. M. Phase, and L. M. Kukreja, Journal of Applied Physics **112**, 103706 (2012).

[24] D. H. Zhang and H. L. Ma, Applied Physics A Materials Science and Processing **62**, 487 (1996).

[25] H. Sobotta, H. Neumann, G. Kühn, and V. Riede, Cryst. Res. Technol. **25**, 61 (1990).

[26] K. J. Bachmann, F. S. L. Hsu, and J. P. Remeika, Physica Status Solidi (a) **67**, K39 (1981).

[27] K. Ellmer, Nature Photonics **6**, 809 (2012).

[28] T. Pisarkiewicz, K. Zakrzewska, and E. Leja, Thin Solid Films **174**, 217 (1989)

Supplementary information

X-ray diffraction spectra of samples annealed at 175 °C
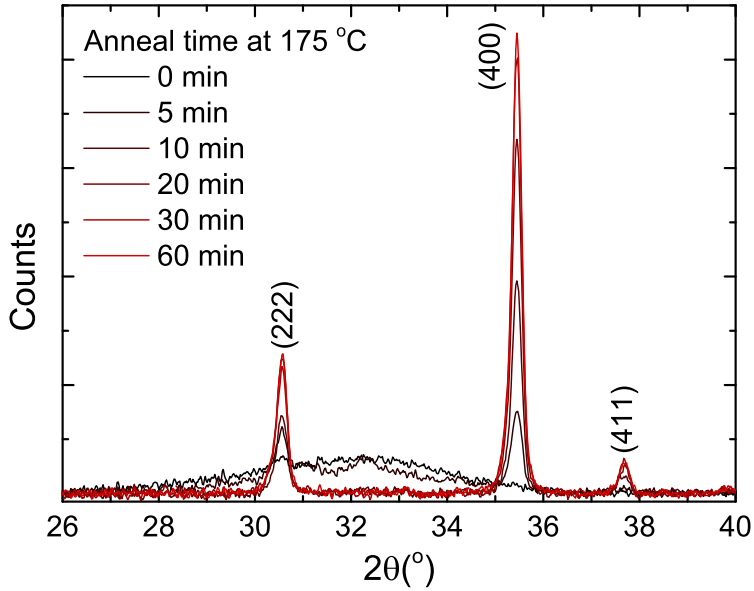
Figure 5: XRD 2θ scans of In$_2$O$_3$:H films for various annealing times at 175 °C. The Miller indices of the diffraction peaks of cubic In$_2$O$_3$ are indicated.

Figure 5 shows XRD 2θ scans of In$_2$O$_3$:H films for various annealing times at 175 °C. As can be seen, the as-deposited film is characterized by a very broad feature around 32° and a very small (222) peak. The small (222) peak indicates the presence of small crystallites in the as-deposited material. After crystallization, the films exhibit a preferential <100> orientation.

Optical constants of amorphous and crystallized In$_2$O$_3$:H
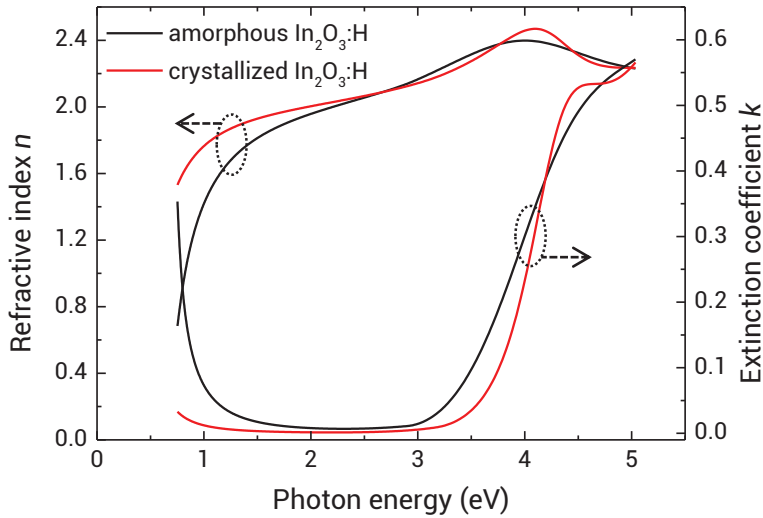
Figure 6: Refractive index *n* and extinction coefficient *k* of amorphous and crystallized In$_2$O$_3$:H. The optical constants were obtained by fitting the SE data using a combination of a Drude and a Tauc-Lorentz oscillator.

Figure 6 shows the optical constants of amorphous and crystallized In$_2$O$_3$:H. After crystallization, the Drude component at low photon energy is greatly reduced. Additionally, the onset of absorption across the bandgap is increased and sharpened after crystallization. This is also reflected by the fitted Tauc-Lorentz parameters: the Tauc-Lorentz optical gap E_{TL} increases from 2.9 to 3.2 eV, whereas increased structural order after crystallization leads to a reduction in the broadening parameter from 2.0 to 1.0 eV.

Cross-sectional TEM images of a fully crystallized In_2O_3:H film
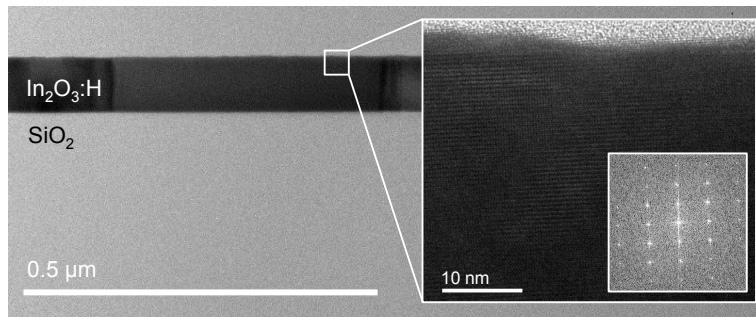
Figure 7: Bright field cross-sectional TEM image of a crystallized In_2O_3:H film. The zoom shows a high-resolution TEM image and its corresponding FFT pattern.

In Figure 7 cross-sectional TEM images of a fully crystallized film are shown. The crystal grains are observed to extend over the full film thickness and are a few hundred nanometer in lateral size. The high resolution TEM image and its corresponding FFT pattern are indicative of the high crystal quality.

XPS spectra of as-deposited and crystallized In$_2$O$_3$:H
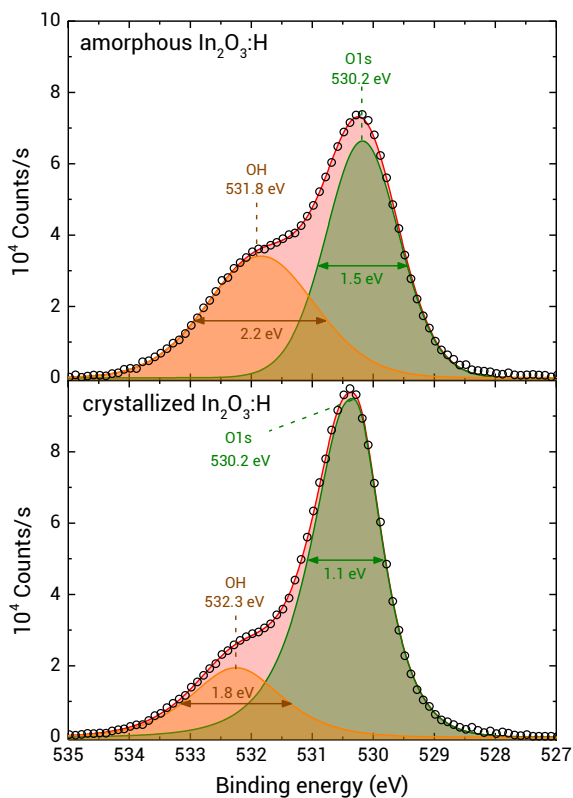
Figure 8: XPS spectra of amorphous (top) and crystallized (bottom) In$_2$O$_3$:H samples. The assignments, position and FWHM of the peaks are indicated in the figure.

XPS measurements of the O1s peak performed on amorphous and crystallized In$_2$O$_3$:H are shown in Figure 8. The O1s peak consists of a contribution of the metal-oxide bond (i.e., In-O) at 530.2 eV and a shoulder at higher binding energy corresponding to OH-bonds. After the crystallization process, both contributions are narrowed, corresponding to increased structural order in the film. Additionally, the OH peak shifts slightly to higher binding energy and the relative area decreases with respect to the O1s peak. This decrease is consistent with the effusion of H upon crystallization as observed by ERD.

6

On the Solid Phase Crystallization of In$_2$O$_3$:H Transparent Conductive Oxide Films Prepared by Atomic Layer Deposition

Abstract:

Hydrogen-doped indium oxide (In$_2$O$_3$:H) has emerged as a highly transparent and conductive oxide, finding its application in a multitude of optoelectronic devices. Recently, we have reported on an atomic layer deposition (ALD) process to prepare high quality In$_2$O$_3$:H. This process consists of ALD of In$_2$O$_3$:H films at 100 $^{\circ}$C, followed by a solid phase crystallization step at 150-200 $^{\circ}$C. In this work, we report on a detailed electron microscopy study of this crystallization process which reveals new insights into the crucial aspects for achieving the large grain size and associated excellent properties of the material. The key finding is that the best optoelectronic properties are obtained by preparing the films at the lowest possible temperature prior to post-deposition annealing. Electron microscopy imaging shows that such films are mostly amorphous, but feature a very low density of embedded crystallites. Upon post-deposition annealing, crystallization proceeds merely from isotropic crystal grain growth of these em-

bedded crystallites rather than by the formation of additional crystallites. The relatively high hydrogen content of 4.2 at. % in these films is thought to cause the absence of additional nucleation, and thereby rendering the final grain size and optoelectronic properties solely dependent on the density of embedded crystallites. The temperature-dependent grain growth rate has been determined, from which an activation energy of (1.39±0.04) eV has been extracted. Finally, on the basis of the observed crystallization mechanism, a simple model to fully describe the crystallization process has been developed. This model has been validated with a numerical implementation thereof, which accurately predicts the observed temperature-dependent crystallization behaviour.

6.1   Introduction

Optoelectronic devices such as displays and solar cells often employ thin films of transparent conductive oxides (TCOs) as conductive window layers. Historically, Sn-doped indium oxide (ITO) made by sputtering has often been the TCO of choice for such purposes. This can mainly be attributed to its relatively high electron mobility μ_e (20-40 cm^2/Vs)[1], which mitigates the need for a high carrier density N_e while still yielding a low resistivity ρ. Due to a lower required N_e, optical losses in the infrared (IR) due to free carrier effects are reduced. In recent years, new In$_2$O$_3$-based TCOs with a higher carrier mobility of >50 cm^2/Vs have gained significant interest, examples include Zn-doped indium oxide (IZO)[2], W-doped indium oxide (IWO)[3], Mo-doped indium oxide (IMO)[4] and H-doped indium oxide (In$_2$O$_3$:H, also referred to as IO:H or IOH)[5,6,7]. Due to the greatly-reduced IR-losses in such TCOs, they have found direct application in various solar cell devices, mainly leading to increased short-circuit current densities J_{sc} when compared to conventional ITO. For example, these high-mobility TCOs have played a key role in achieving the record conversion efficiencies for silicon heterojunction (SHJ) solar cells[8,9], and are also being explored for CIGS[10,11,12] and perovskite tandem cells.[13,14,15]

Among these high-mobility TCOs, In$_2$O$_3$:H is capable of achieving the highest mobility with values even up to 138 cm^2/Vs.[7] This material was originally developed by Koida *et al*., using reactive magnetron sputtering at room temperature from an In$_2$O$_3$ target with the addition of H$_2$O vapour, which resulted in mostly amorphous In$_2$O$_3$:H films. The crucial step for achieving high μ_e values >100 cm^2/Vs is a solid phase crystallization (SPC) step by thermal annealing at 160-400 ^{o}C.[5] Recently we have demonstrated a similar approach to prepare high-mobility In$_2$O$_3$:H using an atomic layer deposition (ALD) process instead of sputtering. After deposition at 100 ^{o}C, the ALD film is almost entirely amorphous. Also here, a crystallization step at 150-200 ^{o}C is key to get μ_e values up to 138 cm^2/Vs.[7,16] Besides achieving such high mobility values, the main advantages of the ALD process are the low temperature processing (post-crystallization

can take place at temperatures as low as 150 ^{o}C), the ability to conformally deposit on non-planar surfaces, and the fact that plasma-induced damage, typically encountered during sputtering ("sputter damage") [17], is absent during ALD. [18,19]

Despite the importance of the crystallization step in realizing high-mobility In_2O_3:H, little is known about the crystallization process itself. Therefore, in this contribution, the crystallization process of ALD In_2O_3:H is studied in detail by electron microscopy to gain a deeper understanding of the physical origin of the very high mobility. The study provides new insights into the crystal growth both during deposition and post-annealing, and explains why films should be prepared at the lowest possible deposition temperature in order to obtain the largest grain size and associated excellent optoelectronic properties after post-annealing. In addition, the temperature-dependent kinetics of the crystallization process is studied. Given the high sensitivity to elevated temperatures of the aforementioned solar cell concepts, knowledge of the temperature-dependent grain growth rate and crystallization kinetics is of direct interest for the optimization of the anneal temperature and time (i.e. thermal budget) when implementing such layers in these cells. As will be shown, the grain growth rate is strongly thermally activated with an activation energy of (1.39 ± 0.04) eV. Based on the observations from electron microscopy, a model to fully describe the crystallization process is proposed. The validity of this model is corroborated by a numerical implementation thereof, which is capable of accurately reproducing the experimentally observed crystallization kinetics. Finally, it is shown that our ALD approach works on silicon nanowires as well, yet subtle differences with respect to the case of planar substrates will be highlighted.

6.2   Experimental Details

6.2.1   Sample preparation

The In_2O_3:H films studied in this contribution were prepared in the same way as in our earlier work. [16] Si(100) wafers with a 430 nm thermal oxide were covered with a seed layer of 20 cycles of ALD aluminum oxide (Al_2O_3) using trimethylaluminum (TMA, $Al(CH_3)_3$) and H_2O. In_2O_3:H films of 75 nm thickness were prepared using an ALD process that is based on the work of Libera *et al*. [6], i.e. using cyclopentadienyl indium (InCp) as the indium source and a combination of O_2 and H_2O as oxidant. All depositions were carried out in an Oxford Instruments OpAL ALD reactor. Depositions were performed at 100, 130 or 200 ^{o}C. Note that 100 ^{o}C is the lowest deposition temperature at which growth was achieved for this ALD process. Subsequently, separate $\sim$1x1 cm^2 samples were cut from the wafers, and the films were annealed separately for various durations and at temperatures ranging from 150 ^{o}C to 200 ^{o}C. Post-deposition annealing was performed in a Jipelec rapid thermal anneal (RTA) furnace in an inert N_2 atmosphere.

Table 1: Electrical properties of In$_2$O$_3$:H films prepared at various deposition temperatures, as determined from Hall measurements. Values for samples both as-deposited (as-dep) and after annealing at 200 ^{o}C for 10 minutes are shown.

Deposition temperature (°C)	Mobility μ_e cm^2/Vs		Carrier density N_e (10^{20} cm^{-3})		Resistivity ρ (mΩcm)	
	As-dep	Annealed	As-dep	Annealed	As-dep	Annealed
100	35	**138**	5.0	1.8	0.35	0.27
130	57	103	1.9	1.3	0.58	0.46
200	48	50	1.8	1.7	0.72	0.73

6.2.2   Film analysis

The films were investigated by TEM (JEOL ARM 200 probe corrected TEM, operated at 200 kV) in cross section using Focused Ion Beam made lamella. An FEI Helios 650 Dualbeam system was used for SEM imaging. Details on the X-ray diffraction and spectroscopic ellipsometry measurements can be found in previous reports.[16] Hall measurements were performed using a Europa HMS-3500 Hall Effect Measurement System in the Van der Pauw configuration. A combination of Rutherford backscattering (RBS) and elastic recoil detection (ERD) was employed to obtain absolute atomic densities of indium, oxygen and hydrogen in the film. Atomic force microscopy (AFM) scans were performed using a NT-MDT Solver P47 microscope in tapping mode using TiN-coated Si tips (NSG10/TiN, NT-MDT).

6.3   Results and Discussion

6.3.1   Influence of the deposition temperature on film crystallinity

In order to first establish the effect of the deposition temperature and post-annealing on the electrical properties of the In$_2$O$_3$:H films, Hall measurements are performed on samples prepared at 100, 130 and 200 ^{o}C, both before and after annealing at 200 ^{o}C for 10 minutes. As can be seen from Table 1, by far the best optoelectronic properties are obtained by annealing the sample prepared at 100 ^{o}C. Under these conditions a very high mobility μ_e of 138 cm^2/Vs and the lowest resistivity ρ of 0.27 mΩcm are achieved. As reported in earlier work, the crystallization process improves the optical properties by leading to a strong reduction in the Drude contribution at low photon energies and to an increase in the optical bandgap.[7] For a sample prepared at 130 ^{o}C the electrical properties improve to a lesser extent after annealing, whereas expectedly annealing a sample at its deposition temperature of 200 ^{o}C does not significantly improve its electrical properties.

In order to explain why the best optoelectronic properties are obtained for films pre-

pared at the lowest deposition temperature, top-view SEM and cross-sectional TEM imaging are employed to study the crystal morphology of both as-deposited and post-crystallized samples. In Figure 1(a-e), top-view SEM images of the samples deposited at 100, 130 and 200 °C are shown, both before and after post-crystallization. As can be seen, the as-deposited film (Figure 1(a)) is not purely amorphous, but contains small embedded crystallites which appear in bright. The presence of such crystallites in as-deposited In_2O_3:H has also previously been observed in In_2O_3:H prepared by sputtering[5] and ALD[20]. Also, the fact that the as-deposited film contains a very small crystalline fraction is in line with our earlier observation that XRD spectra of our as-deposited ALD In_2O_3:H films contain a dim feature of (111)-oriented grains.[7,16] High magnification SEM images (inset of Figure 1 (a)) and AFM images (Figures 11 and 12 in the supplementary material) show that the crystallites protrude from the surface. The higher brightness for the crystallites observed in the SEM images is the result of a higher secondary electron yield due to the presence of this additional surface roughness. After crystallization (Figure 1(b)) the top-view SEM imaging shows a very large grain size of a few hundred nm, in line with our previous results.[7,16]
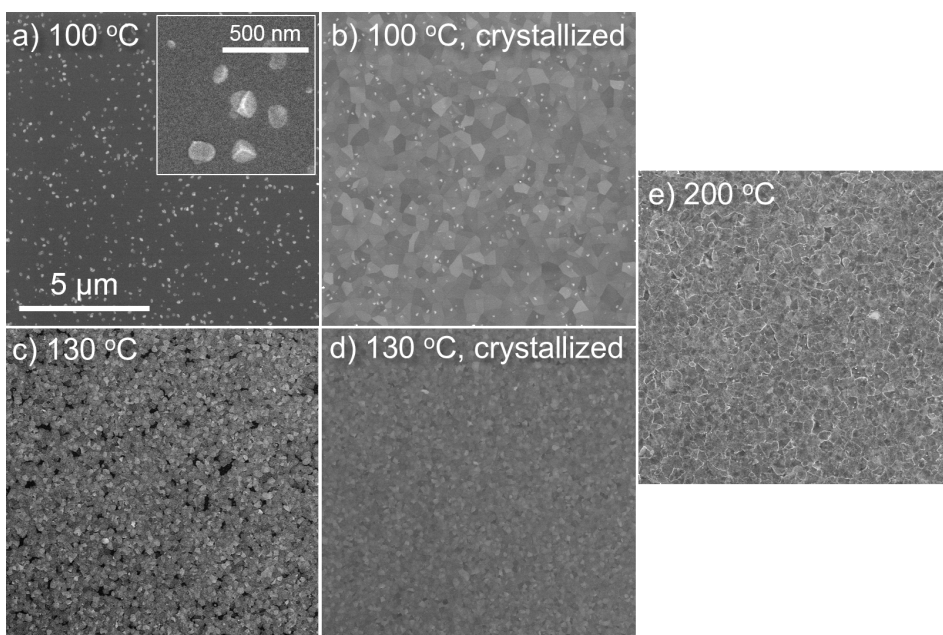

Figure 1: Top-view SEM images of In_2O_3:H films grown at (a) 100, (c) 130 and (e) 200 °C, respectively. (b and d) For the samples prepared at 100 and 130 °C, also images after post-annealing for 10 minutes at 200 °C are shown. The films have a thickness of 75 nm. Image (a) has an inset with an image at higher magnification, showing the morphology of the crystallites protruding from the surface. Except for the inset all images have the same scale.

Figure 1(c) shows that the film prepared at 130 °C is mostly crystalline. Also here the dark areas are thought to be amorphous In$_2$O$_3$:H, since they disappear upon post-annealing (Figure 1(d)). Clearly, the crystallite density for a film prepared at 130 °C is much higher than for a film prepared at 100 °C, which leads to a much smaller grain size after post-annealing. The sample prepared at 200 °C (Figure 1(e)) is observed to be fully crystalline, with a smaller grain size and with a rougher morphology. Therefore, the better electronic properties after crystallization of films prepared at the lowest deposition temperature of 100 °C can be attributed to the fact that that such films have the largest grain size. It should be noted that the protrusion of the crystallites from the surface in Figure 1(a) shows that the growth per cycle (GPC) is enhanced on the crystalline surfaces. This is not uncommon for ALD, and enhanced GPC values on crystalline surfaces have for example also been observed for MoO$_x$ and TiO$_2$.[21,22,23] In fact, from AFM (Figure 11 and 12 in the supplementary material) it is deduced that the crystallites can protrude up to ∼25 nm from the surface. Since the film is 75 nm thick, this suggests an enhancement in GPC of at least 33% on the crystalline surface, if the crystallites were to nucleate directly at the start of the film deposition. As will be shown later, the crystallites are observed to not nucleate directly at the start of the film deposition, and therefore the GPC enhancement on crystalline surfaces should even exceed 33%. Interestingly, in the aforementioned work of Libera *et al*. using the same ALD process, an increase in GPC of almost 50% was observed when going from amorphous growth at a deposition temperature of 100 °C to purely crystalline growth at a deposition temperature 140 °C.[6] Therefore, the increase in GPC at elevated temperatures for this ALD process can be mainly attributed to the change from amorphous to polycrystalline growth.

6.3.2   Electron microscopy imaging of the crystallization process

Since the samples deposited at 100 °C feature the highest mobility and lowest resistivity after crystallization, the crystallization process of these samples is studied in more detail. To this end, top-view SEM imaging is performed on a large set of samples prepared at 100 °C and annealed for various times at 150, 165, 175, 185 or 200 °C. Figure 2 shows two exemplary top-view SEM images of samples annealed at 150 °C for 60 minutes and at 175 °C for 10 minutes, respectively. Interestingly, both images show that upon annealing grain growth occurs from the embedded crystallites (as seen in Figure 1 (a)). Note that this is observed for all the samples studied and a larger set of top-view SEM images can be found in the supplementary material.

The grain growth from the embedded crystallites has been studied by cross-sectional TEM images for films annealed at 175 °C for 5, 10 and 120 minutes, as shown in Figure 3. As can be seen in (a) and (b), the crystals exhibit a hemispherical growth front, imply-
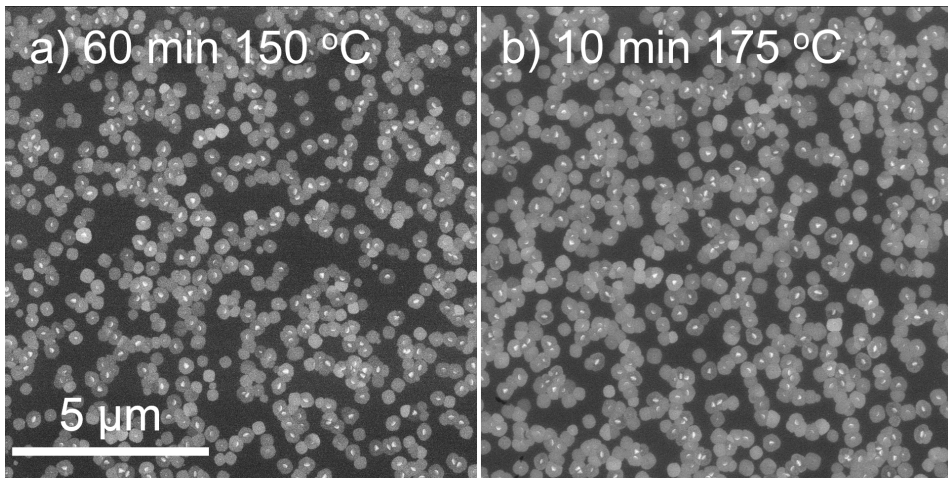
Figure 2: Top-view SEM images of In_2O_3:H films prepared at 100 °C and post-annealed at (a) 150 °C for 60 minutes and at (b) 175 °C for 10 minutes.

ing that grain growth proceeds in an isotropic manner from the embedded crystallites residing at the top surface. This shows that the crystallites in the SEM images of Figure 1(a) are indeed located near and/or at the surface and act as the seeds for further crystallization. Therefore, it is most likely that ALD film growth starts out amorphous, up to a certain thickness where nucleation of crystallites occurs that subsequently grow along with the film.

Upon close inspection of the top-view SEM images, it appears that crystallization occurs solely by grain growth from the embedded crystallites and that additional nucleation is absent or of very minor importance. In order to quantitatively determine whether additional nucleation occurs during annealing, the surface crystallite density n_s has been determined from the SEM images as a function of the film surface crystalline fraction X_c for all the investigated annealing temperatures.[*] The crystalline fraction X_c of the film has been determined from the fraction of the bright parts of the In_2O_3:H surface using image analysis software (ImageJ). The result is shown in Figure 4. Interestingly, there is no clear dependence of n_s on the crystallinity for all annealing temperatures in the range 150-200 °C. This confirms that additional nucleation of crystallites during the annealing process is indeed absent or at least of very minor importance. In other words, the time scale for full crystallization of the film by grain growth from the embedded crystallites is much smaller than the typical timescale for crystallite nucleation for the investigated temperature range of 150-200 °C. This has the important consequence that

---

[*]An overview of SEM images of In_2O_3:H films after various annealing times and temperatures can be found in the Supplementary Information, Figure 13
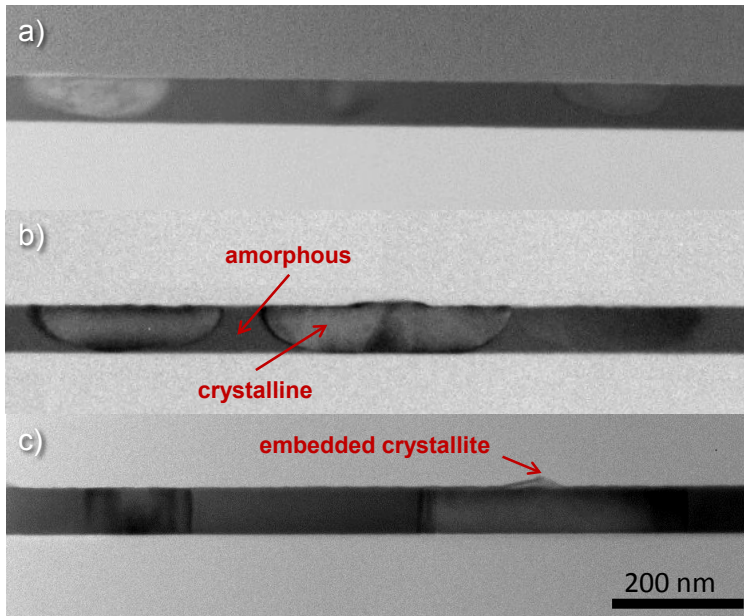
Figure 3: Cross-sectional TEM images of separate In$_2$O$_3$:H films at various stages of crystallization. The samples were annealed for (a) 5, (b) 10 and (c) 120 minutes at 175 °C. Note that only a few of the embedded crystallites protruding from the surface were captured within these images due to the limited thickness of the TEM lamella.

the final grain size is independent of the annealing temperature, in line with our earlier observation that identical properties are obtained for fully crystallized films irrespective of annealing temperature in the range of 150-200 °C.[16] Note that the independence of the electrical quality on the annealing temperature also implies that, besides the grain size, also the intragrain crystal quality is independent of the annealing temperature.

In the absence of additional nucleation, the determined average n_s of 6.3 μm^{-2} predicts an average lateral final grain size of 400 nm, in good agreement with the top-view SEM image of Figure 2(b) and the cross-sectional TEM images of Figure 3. Additionally, since no nucleation from the amorphous phase is observed, it can be concluded that nucleation during post-deposition annealing requires annealing temperatures exceeding the investigated temperature range of 150-200 °C. More importantly, this also implies that the inclusion of a low density of crystallites during the deposition of the film is necessary to enable post-crystallization at low annealing temperatures. Fortunately for our ALD process this inclusion of a small density of crystallites occurs exactly at the lowest end of the ALD temperature window, i.e. 100 °C, although this could be different for other ALD processes or deposition methods.

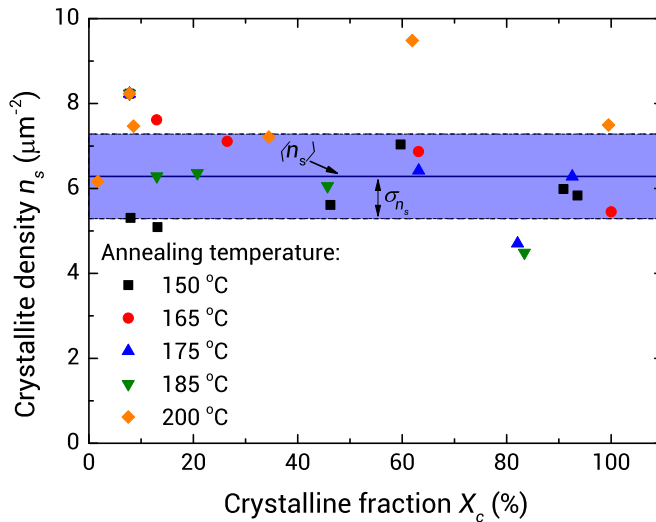On the basis of the presented observations, a model is proposed to describe the crys-

Figure 4: Surface crystallite density n_s as obtained from analysis of top-view SEM images as a function of the film crystalline fraction X_c. No dependence of n_s on X_c can be observed, indicating that additional nucleation during post-annealing is negligible. The average crystallite density $\langle n_s \rangle$ as obtained from SEM analysis and the standard deviation therein σ_{n_s} are shown as well. The annealing times of the samples are the same as reported in Figure 6.

tallization process of the ALD In_2O_3:H films. The model is schematically shown in Figure 5. During the ALD process, initially an amorphous incubation layer develops (A.1) up to a certain thickness. Subsequently, crystallites nucleate at the surface (A.2). During the following ALD cycles these crystallites grow in size and new crystallites nucleate (A.3). Due to the enhanced local growth rate on the crystalline surface, the crystallites protrude from the surface.

During subsequent solid phase crystallization, isotropic growth of the crystallites occurs without the formation of new crystallites, as concluded from cross-sectional TEM and top-view SEM, respectively (B.1). The grain growth proceeds until the crystallites coalesce (B.2.) and finally the film is fully crystallized (B.3). The embedded crystallites can still be distinguished on the surface.

6.3.3 Temperature-dependent crystallization kinetics

In addition to the crystallization mechanism, the temperature-dependent kinetics of the crystallization process is studied. From top-view SEM images, the crystalline fraction X_c of the film is measured as a function of annealing temperature and time. The result is shown in Figure 6 (crossed symbols), in conjunction with the results from previous work based on X-ray diffraction (XRD, closed symbols) and spectroscopic ellipsometry (SE)
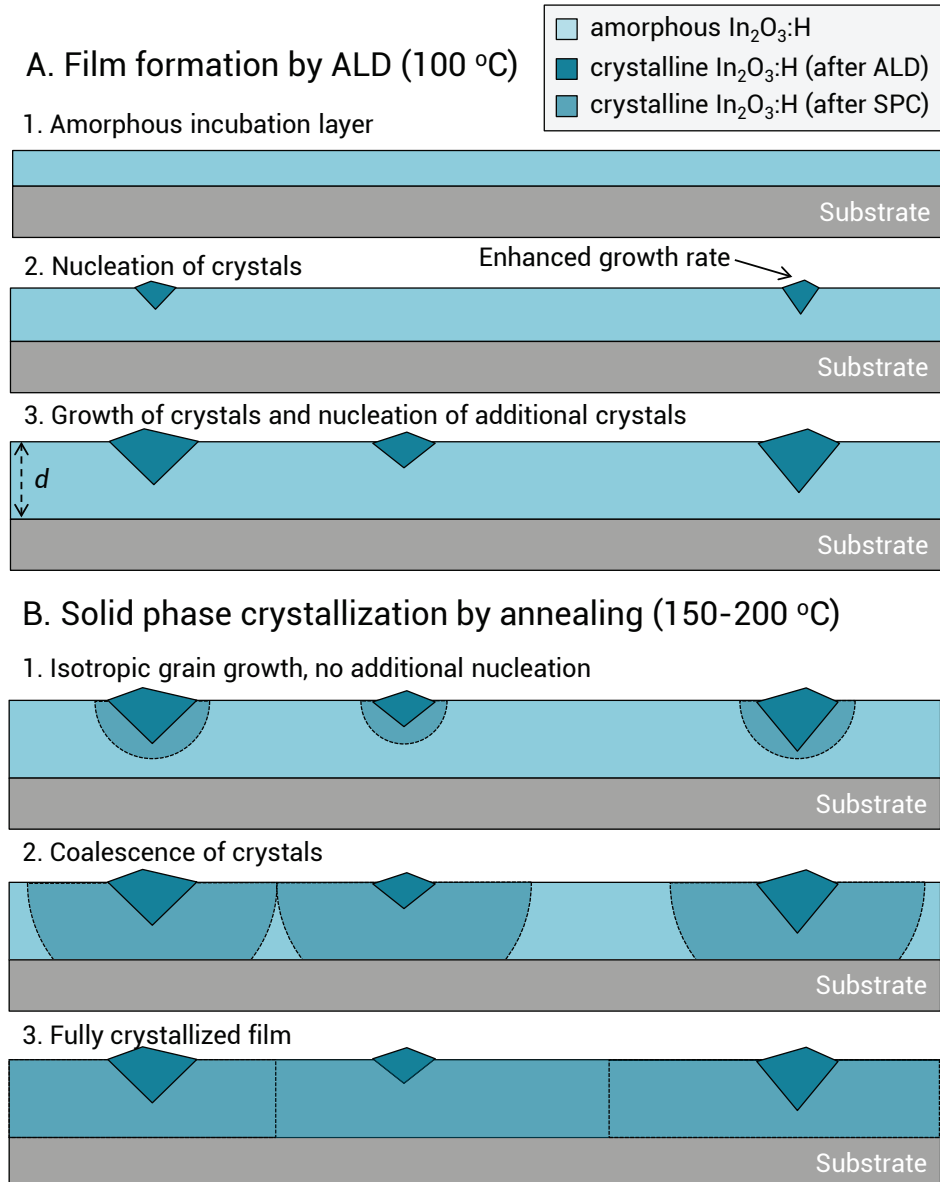
Figure 5: Schematic of the proposed model for the nucleation and growth of crystallites in ALD In$_2$O$_3$:H (A) during the ALD process and (B) during subsequent solid phase crystallization.

modelling using an effective medium approximation (EMA, open symbols).[16] Note that the dashed and dotted lines in Figure 6 are the result of the model that will be addressed later in this paper. As can be seen, the crystallization occurs more rapidly at higher annealing temperatures, clearly indicating thermally activated behaviour, as expected. Also, there is a good agreement between the X_c values obtained from SEM with those obtained from the XRD and SE EMA approaches[16], albeit that the SEM values are slightly higher. This can likely be attributed to the fact that the crystalline fraction determined by SEM is a *surface* projection of the crystallites, whereas the values determined by XRD and SE are *bulk* crystalline fractions. Given the shape of the crystallites during crystallization (as can be seen in Figure 3(b) and in the model of Figure 5), it is evident that the *surface* crystalline fraction exceeds the *bulk* crystalline fraction for partially crystallized films.
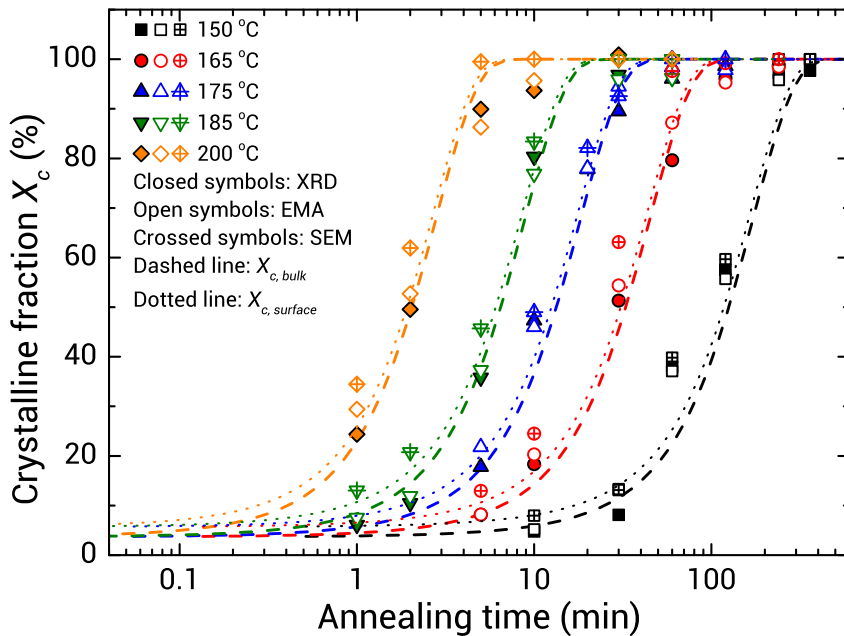

Figure 6: Crystalline fraction of the In_2O_3:H films as a function of annealing time for various annealing temperatures. The crystallinity has been deduced from XRD (closed symbols), SE modelling using an effective medium approximation (EMA, open symbols) of fully crystalline and amorphous In_2O_3:H, and from image analysis of top-view SEM images (crossed symbols). The lines represent the result of a model, where the dashed lines denote the bulk crystallinity, $X_{c,bulk}$, whereas the dotted lines correspond to the surface crystallinity $X_{c,surface}$. The XRD and SE data are replotted from previous work.[16]

From top-view SEM imaging, the grain growth rate v_g as a function of crystallization temperature has also been extracted. This has been done by tracking the crystallite size of non-coalesced crystallites as a function of crystallization time. The result is shown

in Figure 7. A thermally activated behaviour can clearly be observed, with v_g varying from 2 nm/min at 150 °C to 119 nm/min at 200 °C.
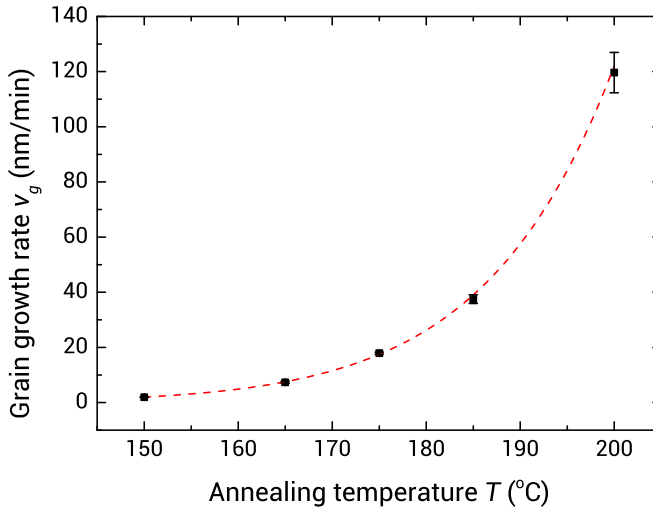

Figure 7: The grain growth rate v_g as a function of annealing temperature as extracted from the SEM images.

From the temperature-dependent grain growth rate the activation energy E_A for grain growth in In$_2$O$_3$:H can be determined through an Arrhenius plot, as has been done in Figure 8. From the fit, an activation energy E_A of (1.39±0.04) eV has been determined. The activation energy for the crystallization process has also been determined by fitting the crystallization curves of Figure 6 with the so-called Avrami equation:

$$X_c = 1 - \exp\left(-(Kt)^n\right) \tag{6.1}$$

with K a temperature-dependent rate constant and n an exponent that reflects the geometry of the transformation.[24] The exponents n of all fitted curves lie in between 1.3-1.6. Being close to 3/2, this suggests site-saturated growth[25] (i.e. all nuclei are present at t=0) with a grain growth dimensionality in between 1D and 2D, in line with the observations obtained from SEM and TEM. From the temperature-dependent Avrami rate constant K an activation energy E_A of (1.31±0.04) eV has been determined as shown in Figure 8, similar to the value obtained from the temperature-dependent growth rate analysis.

It is instructive to compare these results to the work of Wang *et al.*, who reported an activation energy of 0.83 eV for sputtered Sn-doped In$_2$O$_3$, which increased to 1.20 eV
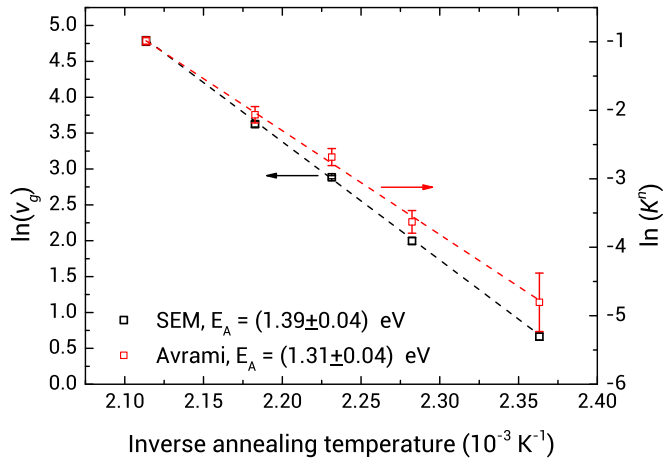
Figure 8: Arrhenius plot of the grain growth rate as obtained from analysis of the SEM images and of the Avrami rate constant. The activation energies have been determined from the slopes.

when adding H-doping. [25] It should be noted that in that work the activation energy was determined from the crystallization rate, and therefore encompasses both nucleation and grain growth, whereas in our case the activation energy purely represents grain growth. Interestingly, they showed that nucleation occurs continuously during the entire annealing process in In_2O_3 without H-doping, whereas the addition of H-doping reduces further nucleation, thereby leading to a larger final grain size (54 to 93 nm). Also, in their work the addition of H-doping led to a decrease of the Avrami exponent from $\sim$5/2 to $\sim$3/2, further evidencing a transition from continuous nucleation to site-saturated growth. Although the hydrogen content in their H-doped films was not reported, it can be speculated that the hydrogen content of 4.2 at. % in our as-deposited ALD films grown at 100 °C [16] is the reason for the observed complete absence of additional nucleation during annealing, for the high activation energy for grain growth and for the large final grain size of $\sim$400 nm. In that respect, the presence of a substantial hydrogen content in the film is highly beneficial for the final film properties. This also favors deposition at the low end of the ALD temperature window, as the hydrogen content in the film is the highest at low deposition temperatures. For example, when increasing the deposition temperature from 100 °C to 130 °C, the hydrogen content decreases from 4.2 to 3.3 at. %. Interestingly, it has previously been observed that almost all the atomic H in the film is retained even after crystallization at 200 °C. [16] The observed reduction in film crystallinity upon the introduction of dopants is not uncommon. For example, the presence of Zn in IZO has been observed to completely hamper crystallization, as an IZO film sputtered from a 90 wt.% In_2O_3 and 10 wt.% ZnO target remains fully amorphous even after a 20 minute anneal at 190 °C. [2]

6.3.4   A numerical simulation of the crystallization process

In the foregoing, a model of the crystallization process has been proposed (Figure 5). Under the assumptions of the model, the crystallization curves of Figure 6 can be calculated, provided the density of embedded crystallites and the temperature-dependent grain growth rate are known. Since these have been determined from the SEM analysis, a numerical implementation of the growth model has been made in an attempt to reproduce the crystallization curves of Figure 6 and thereby to verify its validity.
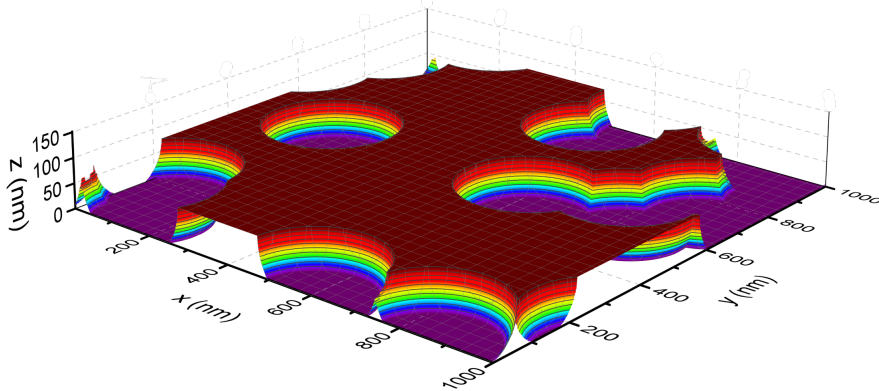

Figure 9: Visualization of the model used to describe the crystallization process. The grid points corresponding to the crystalline state are transparent in this visualization, and the film has a crystalline fraction X_c of 45% For clarity, a smaller grid of 1x1x0.075 μm^3 and fewer nuclei (8) are used in this particular visualization compared to the model used for the calculations. Note that the nuclei are randomly distributed and that the grid has periodic boundaries in the *xy*-directions.

In line with the proposed crystallization mechanism, the basic assumptions of the simulation are that randomly-distributed hemispherical crystallites with surface density n_s are present on the surface, which grow isotropically upon annealing with a certain grain growth rate v_g. A visualization of a grid generated by the implemented model can be seen in Figure 9. Details on the numerical implementation of the model can be found in the supplementary material.

Using the film thickness, crystallite density and temperature-dependent grain growth rate as input parameters, the model can calculate both the bulk crystalline fraction $X_{c,bulk}$ and the surface crystalline fraction $X_{c,surf}$ as a function of time. These input parameters are all known from the SEM analysis and have been used to calculate the evolution of the crystalline fraction for our studied films. The resulting crystallization curves have been plotted in Figure 6 for the various annealing temperatures. As can be seen, despite the simple assumptions and limited number of input parameters, the model accurately predicts the observed crystallization kinetics and thereby corroborates the model proposed in Figure 5.

6.3.5 ALD of In$_2$O$_3$:H on non-planar geometries

The discussion in this paper so far has dealt with depositions on planar surfaces. Nonetheless, one of the strengths of the ALD approach is the ability to conformally deposit on more complex 3-dimensional topologies, which are nowadays becoming ubiquitous in many high-end semiconductor device applications. Therefore, here we would like to briefly highlight that our ALD approach can also be successfully extended to non-planar substrate geometries, i.e. silicon nanowires in this specific case. Although similar results are obtained, subtle differences occur on such a geometry.
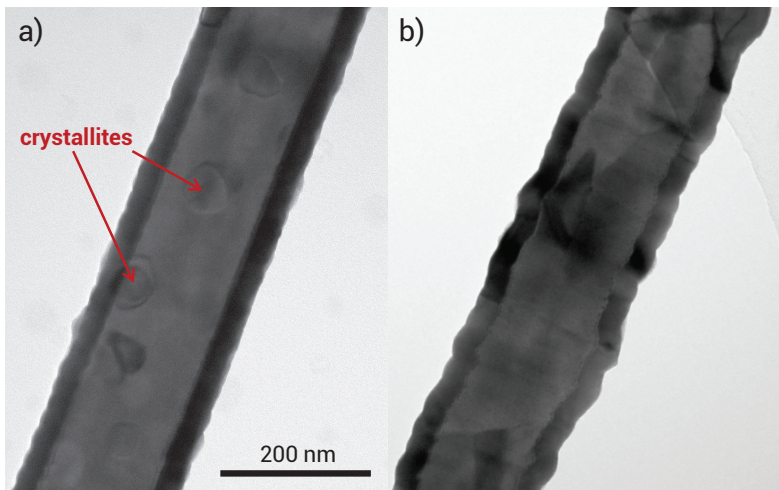

Figure 10: TEM images of silicon nanowires covered with ∼30 nm of ALD In$_2$O$_3$:H prepared at 100 °C, both (a) as-deposited and (b) after annealing for 10 minutes at 200 °C.

Figure 10(a) shows a TEM image of a silicon nanowire which has been covered with a layer of ∼30 nm of In$_2$O$_3$:H, deposited at 100 °C. Note that this film is thinner than the 75 nm used in the study on planar substrates. As can be seen, the silicon nanowire is conformally covered with ALD In$_2$O$_3$:H. Strikingly, already at this lower film thickness the film consists of an amorphous phase with relatively large embedded crystallites. This might point to enhanced nucleation of crystallites during deposition on the nanowire geometry. Nonetheless, a fully crystalline shell with large grains is obtained around the nanowire after post-annealing for 10 minutes at 200 °C, as shown in Figure 10(b).

6.4 Conclusions

In this work, the crystallization mechanism and crystallization kinetics of In$_2$O$_3$:H films have been investigated by a combined structural and optoelectronic characterization

approach involving scanning and transmission electron microscopy, XRD and SE. In order to obtain the best optoelectronic properties it is shown that for the ALD films it is prerequisite to prepare the In$_2$O$_3$:H at the lowest possible temperature prior to post-deposition annealing, since such films reveal the highest grain size after crystallization. This is attributed to their low density of embedded crystallites that act as seeds for further crystallization, and the substantial hydrogen content in those films which likely hampers additional nucleation from the amorphous phase. The temperature-dependent grain growth rate has been determined, from which a thermal activation energy of (1.39±0.04) eV has been found. Based on the observations from SEM and TEM, a growth model for the crystallization of In$_2$O$_3$:H has been proposed. This model has been implemented numerically, and the close match between the experimental and predicted crystallization curves corroborates its validity. Finally, similar results have been observed on non-planar substrates, although subtle differences have been observed which require further research.

6.5   Acknowledgements

References

[1] S. De Wolf, A. Descoeudres, Z. C. Holman, and C. Ballif, Green **2**, 7 (2012).

[2] M. Morales-Masis, S. Martin De Nicolas, J. Holovsky, S. De Wolf, and C. Ballif, IEEE Journal of Photovoltaics **5**, 1340 (2015).

[3] J. Yu, J. Bian, W. Duan, Y. Liu, J. Shi, F. Meng, and Z. Liu, Solar Energy Materials and Solar Cells **144**, 359 (2016).

[4] Y. Yoshida, D. M. Wood, T. A. Gessert, and T. J. Coutts, Applied Physics Letters **84**, 2097 (2004).

[5] T. Koida, M. Kondo, K. Tsutsumi, A. Sakaguchi, M. Suzuki, and H. Fujiwara, Journal of Applied Physics **107**, 033514 (2010).

[6] J. A. Libera, J. N. Hryn, and J. W. Elam, Chemistry of Materials **23**, 2150 (2011).

[7] B. Macco, Y. Wu, D. Vanhemel, and W. M. M. Kessels, physica status solidi (RRL) - Rapid Research Letters **8**, 987 (2014).

[8] M. Taguchi, A. Yano, S. Tohoda, K. Matsuyama, Y. Nakamura, T. Nishiwaki, K. Fujita, and E. Maruyama, IEEE Journal of Photovoltaics **4**, 96 (2014).

[9] L. Barraud, Z. C. Holman, N. Badel, P. Reiss, A. Descoeudres, C. Battaglia, S. De Wolf, and C. Ballif, Solar Energy Materials and Solar Cells **115**, 151 (2013).

[10] T. Jäger, Y. E. Romanyuk, S. Nishiwaki, B. Bissig, F. Pianezzi, P. Fuchs, C. Gretener, M. Döbeli, and A. N. Tiwari, Journal of Applied Physics **117**, 205301 (2015).

[11] A. Steigert, I. Lauermann, T. Niesen, T. Dalibor, J. Palm, S. Körner, H. Scherg-Kurmes, R. Muydinov, B. Szyszka, and R. Klenk, physica status solidi (RRL) - Rapid Research Letters **9**, 627 (2015).

[12] J. Keller, J. Lindahl, M. Edoff, L. Stolt, and T. Törndahl, Progress in Photovoltaics: Research and Applications **24**, 102 (2016).

[13] D. Zhang, W. Soppe, and R. E. Schropp, Energy Procedia **77**, 500 (2015).

[14] F. Fu, T. Feurer, T. Jäger, E. Avancini, B. Bissig, S. Yoon, S. Buecheler, and A. N. Tiwari, Nature Communications **6**, 8932 (2015).

[15] G. Yin, A. Steigert, P. Manley, R. Klenk, and M. Schmid, Applied Physics Letters **107**, 211901 (2015).

[16] B. Macco, H. C. M. Knoops, and W. M. M. Kessels, ACS Applied Materials & Interfaces **7**, 16723 (2015).

[17] B. Demaurex, S. De Wolf, A. Descoeudres, Z. C. Holman, and C. Ballif, Applied Physics Letters **101**, 171604 (2012).

[18] B. Macco, D. Deligiannis, S. Smit, R. A. C. M. M. van Swaaij, M. Zeman, and W. M. M. Kessels, Semiconductor Science and Technology **29**, 122001 (2014).

[19] B. Demaurex, J. P. Seif, S. Smit, B. Macco, W. M. M. Kessels, J. Geissbuhler, S. De Wolf, and C. Ballif, IEEE Journal of Photovoltaics **4**, 1387 (2014).

[20] J. Keller, L. Stolt, M. Edoff, and T. Törndahl, physica status solidi (a) **213**, 1541 (2016).

[21] J. Aarik, A. Aidla, H. Mandar, and V. Sammelselg, Journal of Crystal Growth **220**, 531 (2000).

[22] A. Aarik, J. Karlis, H. Mändar, T. Uustare, and V. Sammelselg, Applied Surface Science **181**, 339 (2001).

[23] M. F. J. Vos, B. Macco, N. F. W. Thissen, A. A. Bol, and W. M. M. Kessels, Journal of Vacuum Science & Technology A: Vacuum, Surfaces, and Films **34**, 01A103 (2016).

[24] M. Avrami, The Journal of Chemical Physics **7**, 1103 (1939).

[25] M. Wang, Y. Sawada, H. Lei, Y. Seki, Y. Hoshi, T. Uchida, T. Konya, and A. Kishi, Thin Solid Films **518**, 2992 (2010)
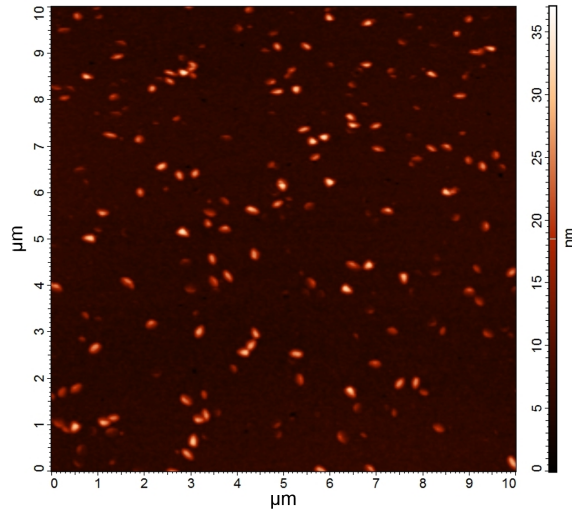
Supplementary information

Figure 11: AFM image of an as-deposited ALD In_2O_3:H film showing the crystals protruding from the surface.

Figure 11 shows an AFM image of an as-deposited ALD In_2O_3:H film. The crystallites on the surface can be clearly distinguished. Figure 12 displays a one-dimensional cross-section of Figure 11, which shows a typical distribution of the height of the crystallites on the surface.
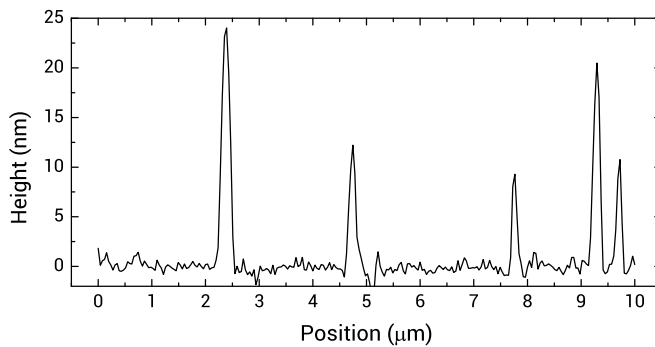

Figure 12: Horizontal cross-section of the AFM image of Figure 11, showing the height distribution of the surface crystallites.

30 min 150 ºC   60 min 150 ºC   240 min 150 ºC

30 min 165 ºC   60 min 165 ºC   240 min 165 ºC

10 min 175 ºC   20 min 175 ºC   60 min 175 ºC

5 min 185 ºC   10 min 185 ºC   30 min 185 ºC
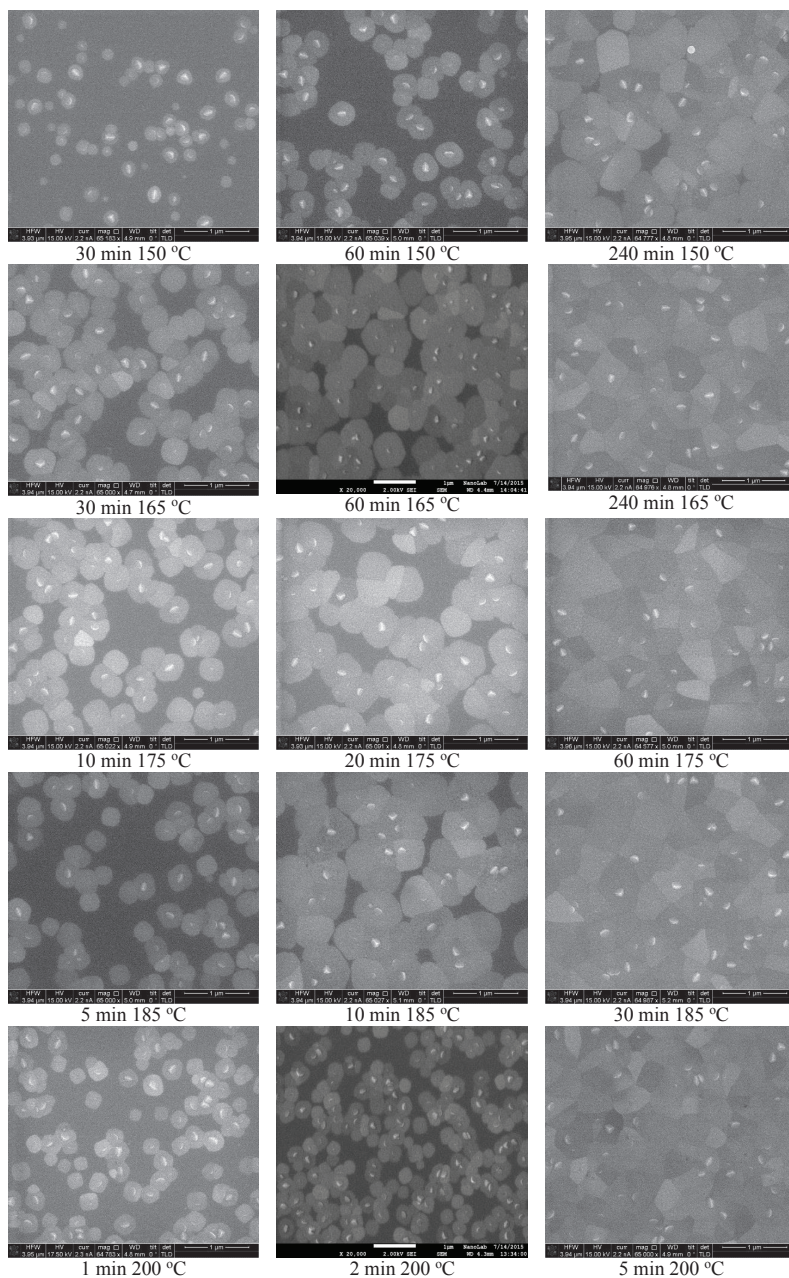
1 min 200 ºC   2 min 200 ºC   5 min 200 ºC

Figure 13: Selection of top-view SEM images of In_2O_3:H films annealed at various temperatures for various times. Note that the images of the samples annealed at 165 ºC for 60 minutes and 200 ºC for 2 minutes have a different scale.

Details of the numerical model

To simulate the crystal growth, a three-dimensional Cartesian grid with a grid spacing of 1 nm was created that can accommodate a number of randomly distributed surface nuclei N_S at a given surface nuclei areal density n_s. Therefore, the size in x- and y-direction (L_x and L_y) of the square grid is given by:

$$L_x = L_y = \frac{N_S}{\sqrt{n_s}} \tag{6.2}$$

In the z-direction, the grid size L_z has been kept constant at 75 nm, corresponding to the film thickness. From SEM imaging, the average areal density of the surface crystallites $\langle n_s \rangle$, is known to be 6.3 μm^{-2}. Since twenty surface crystallites were simulated, i.e. N_S=20, the lateral grid dimensions L_x and L_y are ~8 μm. Also, periodic boundary conditions have been applied to the grid in order to exclude grid size effects.

During initialization of the simulation, N_S crystallites with a size of 1 nm^3 are given random (x, y) positions at the film surface (z=75 nm). The grid points $g(x, y, z)$ corresponding to these nuclei are given a value of 1, corresponding to the crystalline state. All other grid points $g(x, y, z)$ are set to a value of 0, corresponding to the amorphous state. Subsequently, for each iteration number I the crystallites expand radially by a distance of r nm. This means that for each iteration, it is checked for each gridpoint (x, y, z) whether its distance to the closest nucleus is smaller or equal to the product of r and I. If so, the state of the grid point is set to be crystalline.

After each iteration I, the crystalline fraction X_c is determined from the fraction of grid points that are crystalline:

$$X_c(I) = \frac{\sum_{x,y,z} g(x, y, z)}{L_x L_y L_z} \tag{6.3}$$

In order to determine the surface crystalline fraction $X_{c,surf}$, equation 6.3 was evaluated only for the surface grid points (z=75, L_z=1). In our simulations, the number of crystallites N_S has been fixed at 20. Note that these simulations yield a crystalline fraction X_c as a function of the discrete iteration number I and not of the time t. In order to translate the iteration number I to time t, it is important to realize that each iteration step the radius of the crystallites grows by the step size r, i.e. 1 nm in our case, and that the crystallites have an initial radius r_0. Therefore it follows that $t = (Ir - r_0)/v_g(T)$, in which $v_g(T)$ is the temperature-dependent grain growth rate. Both the average initial radius $\langle r_0 \rangle$ of the crystallites (47 nm), and the temperature-dependent grain growth rate

$v_g(T)$ are known from the SEM analysis, and have been used as input parameters.

7

Atomic Layer Deposition of Molybdenum Oxide from (N^{t}Bu)$_2$(NMe$_2$)$_2$Mo and O$_2$ Plasma

Abstract: Molybdenum oxide (MoO$_x$) films have been deposited by atomic layer deposition using bis(*tert*-butylimido)- bis(dimethylamido)molybdenum and oxygen plasma, within a temperature range of 50−350 °C. Amorphous film growth was observed between 50 and 200 °C at a growth per cycle (GPC) around 0.80 Å . For deposition temperatures of 250 °C and higher, a transition to polycrystalline growth was observed, accompanied by an increase in GPC up to 1.88 Å . For all deposition temperatures the O/Mo ratio was found to be just below three, indicating the films were slightly sub-stoichiometric with respect to MoO$_3$ and contained oxygen vacancies. The high purity of the films was demonstrated in the absence of detectable C and N contamination in Rutherford backscattering measurements, and a H content varying between 3 and 11 at. % measured with elastic recoil detection. In addition to the chemical composition, the optical properties are reported as well.

7.1   Introduction

Molybdenum trioxide has received considerable interest due to its optical, electrical, and catalytic properties.[1,2,3,4] Thin films of MoO_3 are being used in gas sensors,[5,6] solid state lithium batteries[7] and in the synthesis of MoS_2 by sulfurization.[8] Moreover, recently, MoO_3 has been used in organic photovoltaics,[9] perovskite solar cells,[10] and silicon solar cells as hole extraction layer.[11,12,13]

A wide range of deposition techniques has been employed for the growth of MoO_3 films, such as thermal evaporation,[14] electron beam evaporation,[15] sputtering,[16,17,18] chemical vapor deposition (CVD),[19] and atomic layer deposition (ALD).[9,20] Of these techniques, ALD offers the advantages of uniform and conformal growth, in conjunction with atomic level thickness control, merits which are highly desirable for some of the above-mentioned applications.

However, only few reports on ALD of MoO_3 can be found in literature. Diskus *et al*. deposited MoO_3 by ALD using molybdenum hexacarbonyl, $Mo(CO)_6$, as precursor and simultaneous doses of ozone and water as reactants.[20] However, the thermal stability of the $Mo(CO)_6$ precursor limited the ALD window to $152-172\,^\circ$C. Another study used MoF_6 and Si_2H_6 for the ALD of molybdenum films, which were subsequently post-treated with UV/ozone to obtain fully oxidized MoO_3.[9] However, the fact that this is a two-step process that involves the use of a halide precursor makes this process less ideal. More recently, Bertuch *et al*. reported an ALD process to deposit MoO_x using bis(tert-butylimido)-bis(dimethylamido)-molybdenum, $(N^tBu)_2(NMe_2)_2Mo$, as the metal-organic precursor and ozone as reactant.[21] This process promisingly shows a high growth per cycle (GPC) of $\sim$1.3 Å at 300 °C, but suffers from a low GPC and from C and N contamination in the films at lower deposition temperatures of $150-200\,^\circ$C. Previously, the $(N^tBu)_2(NMe_2)_2Mo$ precursor has also been used by Miikkulainen *et al*. to grow films of molybdenum nitride using ammonia as reactant.[22]

In this study, we report on an ALD process to deposit high-purity substoichiometric molybdenum trioxide (MoO_{3-x}) films using the $(N^tBu)_2(NMe_2)_2Mo$ precursor and O_2 plasma, for a wide temperature range of $50-350\,^\circ$C. O_2 plasma can offer the advantage of reasonable growth rates at lower deposition temperatures. In recent work, we have already shown the potential of this process for the low-temperature deposition of selective hole contacts for silicon heterojunction solar cells.[23] Here, we extend the temperature range to 350 °C and provide a detailed study of the ALD process and material properties in general.
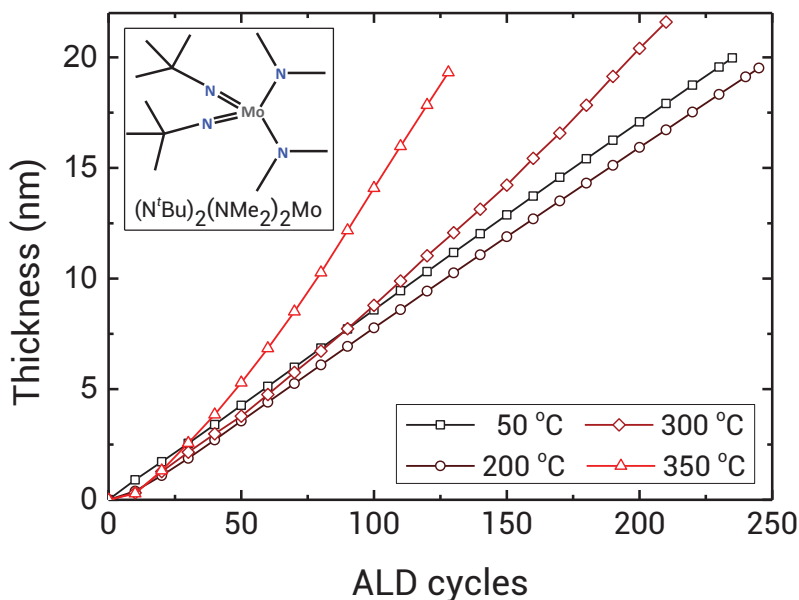
Figure 1: Thickness of the MoO$_x$ films, measured with *in situ* SE, as a function of ALD cycles for deposition temperatures between 50 °C and 350 °C. A precursor dosing time of 6 s and plasma exposure time of 4 s were used. A transition from amorphous to crystalline growth can be observed for 300 °C and 350 °C by a gradual increase in GPC during film growth. The inset shows the chemical structure of the (N^{t}Bu)$_2$(NMe$_2$)$_2$Mo precursor used for the deposition. Some of the data in this figure have been replotted from previous work. [23]

7.2 Experimental details

7.2.1 Film deposition

MoO$_x$ films were deposited in a home-built ALD reactor, consisting of a vacuum chamber connected to an inductively coupled plasma source and a pump unit. The pump unit consists of a rotary and turbomolecular pump reaching a base pressure of $\sim$10^{-6} Torr. An extensive description of the reactor can be found in earlier work from our group. [24] The typical processing conditions and experimental settings are summarized in Table 1. The set temperature of the substrate table was varied between 50 and 350 °C. The temperature of the reactor wall was maintained at 100 °C for all depositions, except for depositions at a table temperature of 50 °C, for which the wall temperature was set to 50 °C. The liquid (N^{t}Bu)$_2$(NMe$_2$)$_2$Mo precursor (98%, Strem Chemicals) was contained in a bubbler at 50 °C, at which it is reported to have a vapor pressure of 0.13 Torr. [21] The chemical structure of the precursor can be seen in the inset of Figure 1. The precursor supply line was heated to 80 °C to prevent condensation of the precursor and Ar was used as a carrier gas. All depositions were done on Si (100) wafers with native oxide.

Table 1: Standard ALD recipe for the deposition of MoO$_x$. The Ar and O$_2$ pressure indicate the chamber pressure during Ar bubbling and plasma exposure, respectively. The reported deposition temperature is the set temperature of the substrate table.

Parameter	Value
Deposition temperature	50 ºC − 350 ºC
Wall temperature	50 ºC − 100 ºC
Bubbler temperature	50 ºC
Line temperature	80 ºC
Base pressure	10^{-6} Torr
Ar pressure	7.5 mTorr
O$_2$ pressure	5.1 mTorr
Precursor dosing time	3.0 s
Precursor pump time	3.0 s
Precursor purge time	6.0 s
Plasma exposure time	4.0 s
Reactant purge	3.0 s

The standard ALD recipe consists of precursor dosing for 6 s in the first half of the ALD cycle. Ar gas is used as a carrier gas during the precursor dose, resulting in a chamber pressure of 7.5 mTorr. Subsequently, the reactor is purged with Ar for 3 s and pumped down for 3 s. The second half-cycle consists of O$_2$ plasma exposure with a plasma power of 100 W at a chamber pressure 5.1 mTorr for 4 s.

7.2.2   Film analysis

The growth of the MoO$_x$ films was monitored *in situ* by spectroscopic ellipsometry (SE) using a J.A. Woollam, Inc., M2000U ellipsometer. The dielectric function of the deposited films was parameterized using a combination of a Tauc-Lorentz and a Gaussian oscillator, as will be addressed later in this paper.

X-ray photoelectron spectroscopy (XPS) was done with a Thermo Scientific KA1066 spectrometer, using monochromatic Al Ka x-rays with an energy of 1486.6 eV. Rutherford backscattering spectroscopy (RBS) and elastic recoil detection (ERD) were performed by AccTec BV, Eindhoven, The Netherlands, using a Singletron with a 2 MeV He$^+$ beam to determine the chemical composition of the films. The mass density was calculated using the areal mass density as obtained from RBS/ERD measurements and the film thickness as obtained from SE. Raman spectroscopy measurements were done using a Renishaw Invia Raman microscope, using a laser wavelength of 514 nm. Grazing incidence x-ray diffraction (XRD) measurements were done with a PANalytical X'Pert Pro MRD system, using Cu Ka x-rays (λ = 1.54 Å). Scanning electron microscopy (SEM) images were obtained using a FEI Nova600i NanoLab.

7.3 Results and discussion

7.3.1 ALD growth

To study the ALD process as a function of the deposition temperature, a set of approximately 20 nm thick samples was deposited at temperatures between 50 and 350 °C, using a standard saturated precursor dosing time of 6 s and a plasma exposure time of 4 s.

In Figure 1, the film thickness is shown as a function of ALD cycles for temperatures between 50 and 350 °C. The thickness of the deposited films proceeds linearly with the number of ALD cycles for deposition temperatures of 50 and 200 °C, corresponding to a GPC of $\sim$0.8 Å. For temperatures of 300 and 350 °C a gradual increase in GPC during film growth can be observed, which is attributed to a transition from amorphous to polycrystalline growth. Such a transition has been observed for other ALD processes before, for instance, for the deposition of TiO_2.[25,26] A transition from amorphous to polycrystalline growth is accompanied by the appearance of grains, very likely leading to an increase in surface area and therefore to an increase in GPC. This will be further corroborated in Section 7.3.2, where the crystallinity and morphology of the films will be discussed.[27] Note that in addition to the increased roughness, an enhanced reactivity of the polycrystalline surface can also contribute to the increase in GPC. To exclude the presence of a thermal CVD component as a possible explanation for the enhanced growth rate at higher deposition temperatures, it was verified that no growth occurs when using O_2 gas instead of O_2 plasma as reactant.

In Figure 2, the saturation curves for the precursor dose step (Figure 2(a)) and plasma exposure time (Figure 2(b)) are shown for various temperatures. The GPC as a function of precursor dosing time [Figure 2(a)] shows a relatively soft saturation and a precursor dosing time of 6 s was chosen as standard for all deposition temperatures. The plasma saturation curve [Figure 2(b)] shows a slightly higher GPC for low plasma exposure times, likely corresponding to incomplete combustion of precursor ligands or redeposition.[28] To assure complete combustion of ligands and to prevent impurity incorporation in the films a plasma exposure time of 4 s was chosen as standard.

In Figure 3, the GPC as a function of deposition temperature is shown, both in terms of thickness, determined from SE, and in terms of deposited Mo atoms/nm^2, determined from RBS. Note that the samples used for determination of the GPC data in Figure 3 correspond to the samples used in Figure 1 and had a thickness of $\sim$20 nm. As can be seen in Figure 3, the GPC determined by SE (closed squares) varies only slightly for temperatures between 50 and 200 °C. At these deposition temperatures, the films are completely amorphous (see Section 7.3.2). For higher temperatures, the GPC increases, which is due to a transition to polycrystalline growth. For a deposition temperature of 300 °C, a
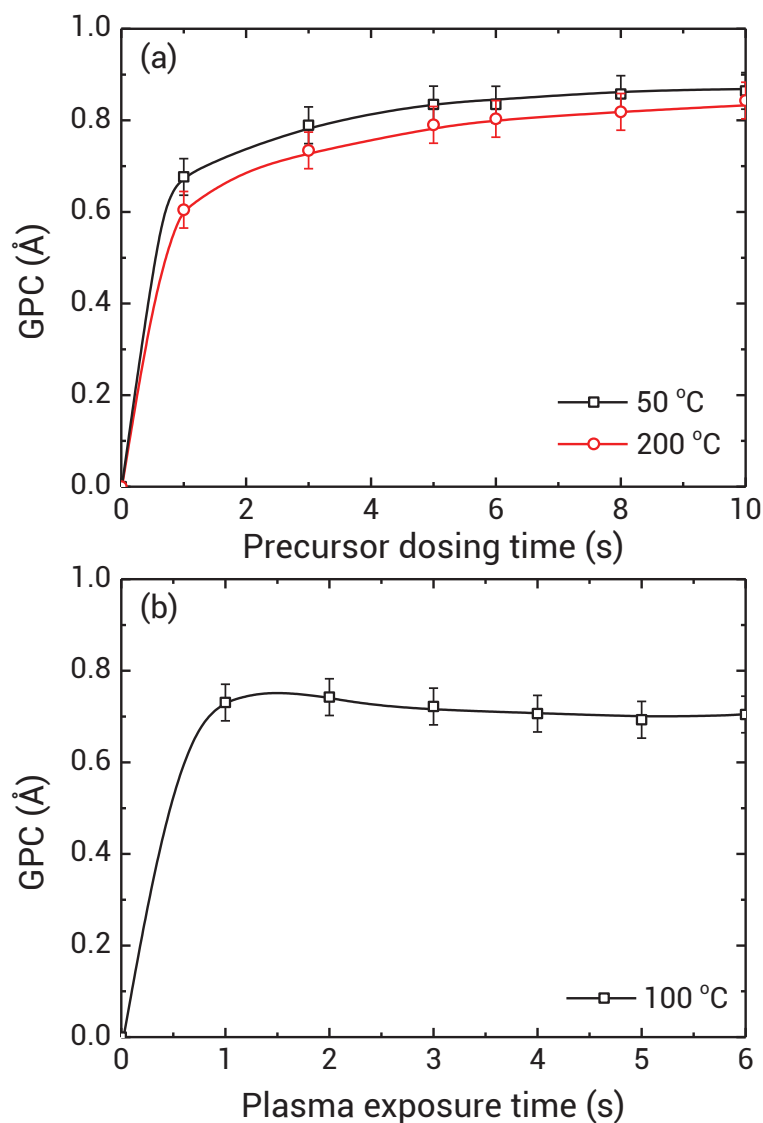
Figure 2: (a) Precursor saturation curve showing the GPC as a function of precursor dosing time for a constant plasma exposure time of 4 s. (b) Plasma exposure saturation curve for a deposition temperature of 100 °C depicting the GPC as a function of plasma exposure time. The precursor dosing time was kept constant at 6 s. The lines serve as guides to the eye. Some of the data in this figure have been replotted from previous work.[23]

distinction can be made between amorphous growth at the start of the deposition, and polycrystalline growth at a larger film thickness, as is also shown in Figure 3. The GPC determined from the first 20−100 cycles was found to be 0.93 Å , while calculating the GPC from the last 50 cycles of the deposition at 300 °C yields a GPC of 1.25 Å . Note that these values for the GPC were calculated by determining the slope at different positions on the curves in Figure 1. Since at 350 °C the amorphous-polycrystalline transition occurs already at a very early stage, only the GPC for polycrystalline growth is reported for this temperature.
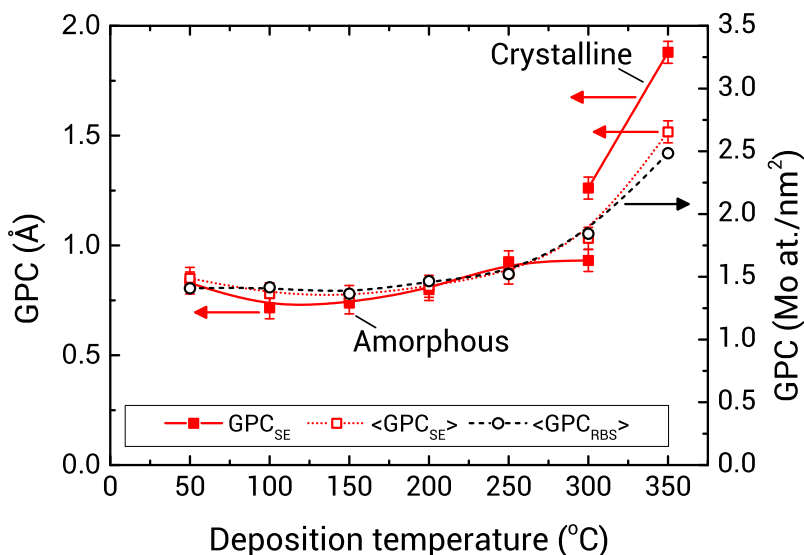

Figure 3: GPC in terms of thickness from *in situ* SE (left axis) and GPC in terms of deposited Mo atoms/nm^2 (right axis) from *ex situ* RBS, as a function of deposition temperature. The open circles show the average GPC in terms of deposited Mo atoms/nm^2, determined by division of the total Mo atoms/nm^2 by the number of ALD cycles. The open squares depict the average GPC ($\langle GPC_{SE} \rangle$), determined from the final thickness and the number of cycles, while the solid squares show the final GPC (GPC_{SE}), determined using the *in situ* data of the last 50 cycles of the deposition. In addition, a GPC determined before the onset of polycrystalline growth (<100 cycles) is displayer for a deposition temperature of 300 °C. The lines are a guide to the eye. The relative error in the measured number of Mo atoms is 2%.

Figure 3 also shows the GPC in terms of the number of deposited Mo atoms/nm^2 (open circles), as determined from RBS, which shows an increase with temperature. Note that this value was determined ex situ by dividing the total number of Mo atoms/nm^2 by the number of ALD cycles. The value is therefore an average over all the ALD cycles used to deposit the film. For this reason this quantity is denoted as $\langle GPC_{RBS} \rangle$. For a direct comparison of the RBS and SE data, also the average GPC as determined from SE ($\langle GPC_{SE} \rangle$), which is the final film thickness divided by the total number of cycles, is shown in Figure 3 (open squares). As can be seen, there is a very strong correlation between

$\langle GPC_{RBS} \rangle$ and $\langle GPC_{SE} \rangle$, which demonstrates that the increased GPC at high tempera-tures is mainly caused by an actual increase in the number of deposited Mo atoms per cycle and not by a decrease in film density. This increase in GPC at high temperatures is thought to be caused by an increase in surface area due to increased roughness, an increased reactivity of the surface, or a combination of both.[27]

7.3.2   Film characterization

In this section, the chemical composition, morphology, and optical properties of the $\sim$20 nm films deposited at temperatures between 50 and 350 °C will be discussed. The most important film properties have been summarized in Table 2.

Chemical composition

From RBS/ERD measurements, both the stoichiometry and the elemental composition were determined. The O/Mo ratio and the atomic percentage of H as a function of de-position temperature can be found in Table 2. The O/Mo ratio was found to be below 3 for all investigated deposition temperatures (2.9 on average), indicating the films were slightly substoichiometric with respect to molybdenum trioxide (O/Mo ratio=3). Note that the samples were transferred in ambient and therefore an effect of ambient on the film stoichiometry cannot be excluded. For all deposition temperatures the contents of C and N impurities were below the detection limit of 3 and 2 at. %, respectively, showing the high quality of the films. No substantial C or N contamination is present in the bulk of the films, which is in line with the fact that there is no indication of thermal decompo-sition of the precursor molecule for high decomposition temperatures. The H content of the films deposited at 50 and 100 °C was found to be around 10 at. %, which de-creased to $\sim$5 at.% for higher temperatures. This H can originate from the ligands of the precursor molecule, which contains 30 H atoms, as well as from residual water in the reactor.

The mass density of the films was calculated using the RBS/ERD measurements and the layer thicknesses from SE. For deposition temperatures from 100 to 300 °C the den-sity was found to be around 4.2 g cm^{-3}, which is slightly lower than the bulk density of crystalline MoO$_3$ of 4.69 g cm^{-3}. The density is somewhat lower (3.9 g cm^{-3}) for 50 and 350 °C. XPS was used to further study the chemical composition of the deposited films. In Figure 4(a), the Mo3d peak is depicted for a deposition temperature of 50 and 350 °C. It was found that sputtering of MoO$_x$ with Ar ions causes a change in stoichiometry of the material due to preferential O sputtering, which is known from literature.[29] For this reason, the XPS data in Figure 4 were collected prior to any sputtering, and thus, the presence of surface contamination cannot be excluded.

Table 2: Properties of MoO$_x$ films for deposition temperatures 50-350 °C, as determined from RBS, SE and XPS. The thickness of the films was approximately 20 nm and the GPC was determined from the last 50 cycles of the deposition. The number of deposited Mo at. nm^{-2}cycle^{-1} and the chemical composition were determined from RBS, the refractive index and the Tauc band gap (E$_g$) from SE and the density from combining the RBS and SE results. C and N contamination in the bulk were below the RBS detection limit of 3 and 2 at. %, respectively. Typical errors are indicated in the top row and in the third row for the H content.

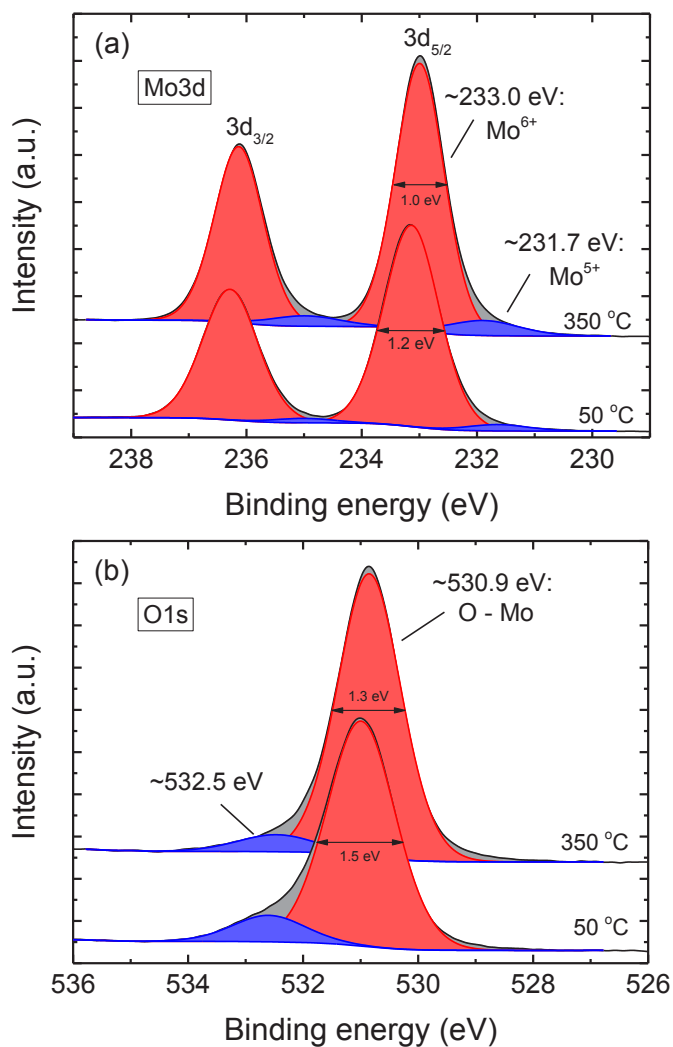| Deposition temperature (°C)	GPC (Å)	Mo (at. nm^{-2}cycle^{-1})	O/Mo ratio	[H] (at. %)	Mass density (g cm^{-3})	Refractive index (at 1.96 eV)	E$_g$ (eV)
50	0.83±0.03	1.41±0.05	2.9±0.1	11±1	3.9±0.2	2.11±0.03	2.87±0.03
100	0.72	1.42	2.8	10	4.3	2.20	2.80
150	0.74	1.37	2.9	3.3±0.4	4.2	2.19	2.81
200	0.80	1.47	2.9	3.3	4.2	2.18	2.80
250	0.93	1.52	3.0	3.6	4.2	2.13	2.77
300	1.25	1.84	2.9	4.3	4.2	2.12	2.92
350	1.88	2.48	2.9	4.1	3.9	1.98	2.92

Figure 4: XPS core level spectra for Mo3d (a) and O1s (b) for MoO$_x$ deposited at 50 $^\circ$C and 350 $^\circ$C. The data was obtained prior to Ar sputtering to avoid reduction to lower oxidation states.

The Mo3d XPS spectrum in Figure 4(a) shows a dominant doublet with the Mo3d$_{5/2}$ peak at ∼233.0 eV and the Mo3d$_{3/2}$ peak at 236.2 eV, corresponding to the fully oxidized Mo^{6+} state, i.e., MoO$_3$.[29,30] The binding energy of the Mo3d$_{5/2}$ peak is slightly higher than other literature reports, which is likely an effect of surface charging.[17] A second doublet at 231.7 and 235.0 eV is required to obtain a good fit to the experimental data. This doublet has previously been attributed to the Mo^{5+} state, corresponding to oxygen vacancies.[11,31] For instance, Battaglia *et al.*demonstrated an increase in the Mo^{5+} peak upon annealing the samples in N$_2$ environment, whereas no change was observed when annealing in O$_2$ environment.[11] Similar experiments were carried out in this study and yielded similar results, showing an increase in the Mo^{5+} state and even the appearance of the Mo^{4+} state upon annealing at 500 °C in N$_2$ environment (not shown here).

The presence of oxygen vacancies is also consistent with the substoichiometric O/Mo ratio as was found with RBS. The O1s peak in Fig. 4(b) consists of a dominant peak at approximately 530.9 eV, corresponding to O bound to Mo atoms[29] and a small shoulder around 532.5 eV, which could possibly be explained by O−H bonds[31] or by absorbed surface species.[17] Although the presence of C and N was observed in the XPS spectrum, their signals were almost completely absent after shortly sputtering with Ar$^+$ ions. This indicates that C and N were mainly present on the surface, which is consistent with the RBS results.

Crystallinity and surface morphology

Raman spectroscopy and XRD were used to assess the crystallinity of the films as a function of the deposition temperature. From Figure 5(a) it can be seen that the film deposited at 250 °C shows two peaks, at 777 and 849 cm^{-1}, corresponding to the metastable monoclinic *β*-crystal phase.[32,33] For 300 and 350 °C a clear peak is visible at 818 cm^{-1}, indicating the films are in the stable orthorhombic *α*-phase. The absence of these peaks for temperatures of 200 °C and lower confirms their amorphous nature.

The x-ray diffractograms in Figure 5(b) show similar results of crystalline films at higher deposition temperatures. The (110) peak in Figure 5(b) corresponds to the *β*-phase, while the (020), (040), and (060) peaks originate from the *α*-phase.[34] For 300 °C the Raman spectrum in Figure 5(a) only shows the presence of the *α*-phase, while the x-ray diffractogram in Figure 5(b) shows mainly the *α*-phase, with a small additional contribution originating from the *β* crystal-phase. For 200 and 250 °C no peaks are visible, corresponding to amorphous material.

Although Raman spectroscopy shows crystallinity for a deposition temperature of 250 °C it is thought that the bulk material is amorphous and some small crystallites are present at the surface of the film.
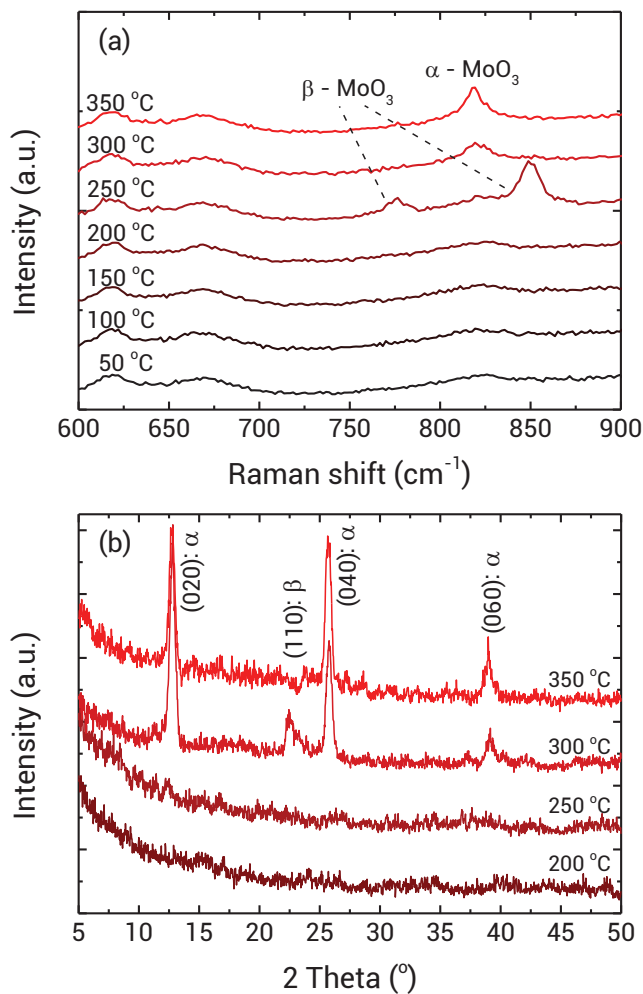
Figure 5: (a) Raman spectra of the MoO$_x$ films deposited at temperatures between 50 °C and 350 °C, for films of approximately 20 nm thick. At 250 °C the monoclinic β-phase of MoO$_3$ is visible, while films deposited at 300 °C and 350 °C show features of the orthorhombic α-phase. (b) X-ray diffractograms spectra of the ∼20 nm thick MoO$_x$ films deposited at temperatures between 200 °C and 350 °C. For 300 and 350 °C distinct peaks are visible, corresponding to crystalline material, while the spectra for lower temperatures indicate the films are amorphous. The spectra are offset vertically for clarity.

This can also be seen in the SEM images in Figure 6. The film morphology as a function of deposition temperature was studied by top-view SEM (Figure 6). For a deposition temperature of 50 °C, a relatively smooth surface is observed, corresponding to amorphous film growth. At 250 °C, some small nuclei are visible, surrounded by amorphous material. The film deposited at 300 °C contains many, larger crystallites, but amorphous material is still visible in the background. For 350 °C, the surface of the film appears fully crystalline. The appearance of crystallites and increasing crystallinity at higher temperatures is in agreement with the Raman data as presented in Figure 5, as well as the observations made based on Figure 1. Moreover, the increased roughness at higher deposition temperatures was also confirmed with atomic force microscopy (not shown), which showed a RMS roughness of 0.2 nm for 50 °C vs 1.9 nm for 350 °C.
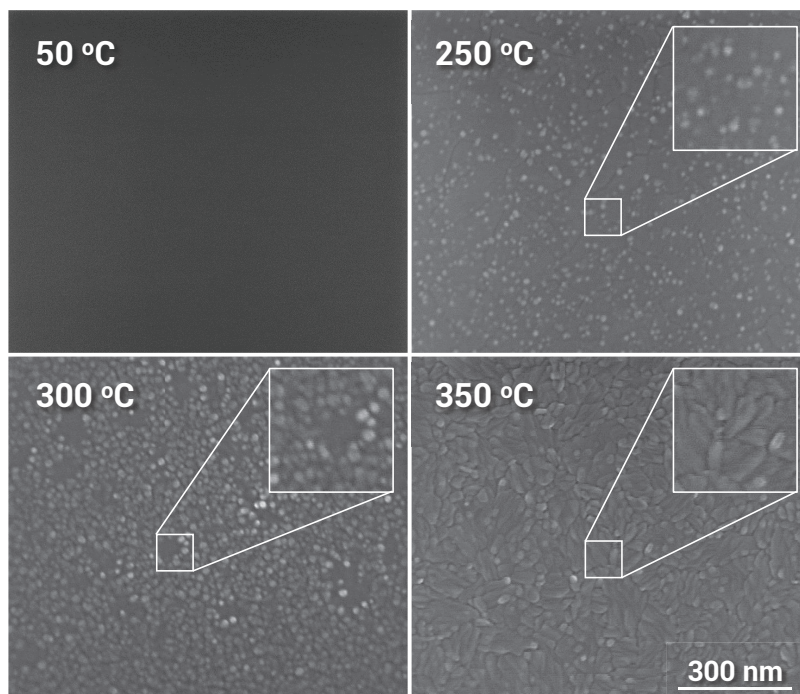

Figure 6: Top-view SEM images of samples deposited at 50, 200, 300 and 350 °C. The thickness of the films was approximately 20 nm. For the three higher temperatures an area is shown at higher magnification for clarity.

Optical properties

The optical properties of the MoO_x films have been analyzed using SE. A Tauc-Lorentz oscillator was used to account for interband absorption. Additionally, a Gaussian oscil-

lator at low photon energy (∼1 eV) was used for absorption inside the band gap, likely caused by defects. This absorption at low photon energy has been reported earlier for MoO$_x$ and has been attributed to oxygen defects. [4,11,16,35] The refractive index (*n*) and the extinction coefficient (*k*) obtained from the modeling are shown in Figure 7.

The refractive index in Figure 7 lies in the 1.8−2.2 range, which is consistent with other literature on MoO$_x$. [16,36] Although the extinction coefficient *k* varies only slightly with deposition temperature, the refractive index *n* is strongly dependent on the deposition temperature, likely caused by differences in film density. From the absorption coefficient a obtained from the SE measurements the Tauc band gap was determined by plotting (*ahv*)$^{1/2}$ as a function of photon energy (considering MoO$_x$ is an indirect band gap material) and extrapolating the linear part to zero absorption. [37] The results of this procedure are listed in Table 2. The obtained band gap values of 2.7−2.9 eV are in the range of the values of 2.5−3.0 eV previously reported in the literature. [1,2,38,36] For deposition temperatures of 300 and 350 °C, a slightly higher band gap of 2.9 eV than for lower deposition temperatures was found, which is in line with the polycrystalline nature of the material.
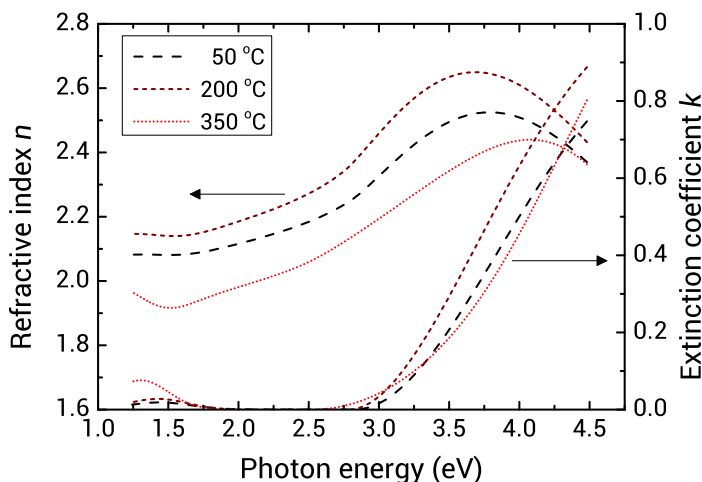

Figure 7: Refractive index (*n*) and extinction coefficient (*k*) for samples deposited at temperatures of 50, 200 and 350 °C. The data was obtained from *in situ* SE measurements. A Tauc-Lorentz oscillator was used to account for interband absorption, while an additional Gaussian oscillator at ∼1.3 eV was used for subgap absorption. The Gaussian oscillator been attributed to oxygen-vacancy-derived defects. [4,11,16,35]

7.4   Summary and conclusions

An ALD process to deposit high-purity MoO$_x$ films has been presented, which is based on (N^{t}Bu)$_2$(NMe$_2$)$_2$Mo dosing and O$_2$ plasma exposure and which yields a high GPC over

a temperature range of 50−350 °C. For amorphous growth at low temperature (<250 °C), GPC values of 0.72−0.93 Å were obtained. For higher deposition temperatures, a transition to polycrystalline growth occurs, which is accompanied by an increase in GPC up to 1.88 Å for 350 °C. It was shown that this increase in GPC is consistent with an increase in the amount of deposited Mo at. nm^{-2} $cycle^{-1}$. For all deposition temperatures the MoO_x films were found to be slightly substoichiometric with respect to MoO_3. Contamination by C and N was determined to be below the RBS detection limit of 3 and 2 at. %, respectively, which shows the high quality of the material. In addition, the MoO_x films contain 3−11 at. % hydrogen. The Tauc band gap was found to vary between 2.77 and 2.87 eV for amorphous films and was 2.92 eV for polycrystalline films deposited at 300 and 350 °C.

Due to the high purity of the films and the relatively high GPC, the presented process is likely suitable for many applications, such as photovoltaics and other optoelectronic devices.

Acknowledgements

References

[1] T. He and J. Yao, Journal of Photochemistry and Photobiology C: Photochemistry Reviews **4**, 125 (2003).

[2] T. Ivanova, K. Gesheva, G. Popkirov, M. Ganchev, and E. Tzvetkova, Materials Science and Engineering: B **119**, 232 (2005).

[3] J. Scarminio, A. Lourenço, and A. Gorenstein, Thin Solid Films **302**, 66 (1997).

[4] T. S. Sian and G. B. Reddy, Solar Energy Materials and Solar Cells **82**, 375 (2004).

[5] M. Ferroni, V. Guidi, G. Martinelli, P. Nelli, M. Sacerdoti, and G. Sberveglieri, Thin Solid Films **307**, 148 (1997).

[6] O. M. Hussain and K. S. Rao, Materials Chemistry and Physics **80**, 638 (2003).

[7] H. Ohtsuka, Solid State Ionics **144**, 59 (2001).

[8] Y.-C. Lin, W. Zhang, J.-K. Huang, K.-K. Liu, Y.-H. Lee, C.-T. Liang, C.-W. Chu, and L.-J. Li, Nanoscale **4**, 6637 (2012).

[9] Y.-C. Tseng, A. U. Mane, J. W. Elam, and S. B. Darling, Solar Energy Materials and Solar Cells **99**, 235 (2012).

[10] Y. Zhao, A. M. Nardes, and K. Zhu, Applied Physics Letters **104** (2014), 10.1063/1.4880899.

[11] C. Battaglia, X. Yin, M. Zheng, I. D. Sharp, T. Chen, S. McDonnell, A. Azcatl, C. Carraro, B. Ma, R. Maboudian, R. M. Wallace, and A. Javey, Nano letters **14**, 967 (2014).

[12] C. Battaglia, S. M. de Nicolás, S. De Wolf, X. Yin, M. Zheng, C. Ballif, and A. Javey, Applied Physics Letters **104**, 113902 (2014).

[13] J. Bullock, A. Cuevas, T. Allen, and C. Battaglia, Applied Physics Letters **105**, (2014).

[14] T. Siciliano, A. Tepore, E. Filippo, G. Micocci, and M. Tepore, Materials Chemistry and Physics **114**, 687 (2009).

[15] R. Sivakumar, R. Gopalakrishnan, M. Jayachandran, and C. Sanjeeviraja, Current Applied Physics **7**, 51 (2007).

[16] S. Mohamed and S. Venkataraj, Vacuum **81**, 636 (2007).

[17] C. Ramana, V. Atuchin, V. Kesler, V. Kochubey, L. Pokrovsky, V. Shutthanandan, U. Becker, and R. Ewing, Applied Surface Science **253**, 5368 (2007).

[18] S. Uthanna, V. Nirupama, and J. Pierson, Applied Surface Science **256**, 3133 (2010).

[19] K. A. Gesheva, A. Cziraki, T. Ivanova, and A. Szekeres, Thin Solid Films **515**, 4609 (2007).

[20] M. Diskus, O. Nilsen, and H. Fjellvåg, Journal of Materials Chemistry **21**, 705 (2011).

[21] A. Bertuch, G. Sundaram, M. Saly, D. Moser, and R. Kanjolia, Journal of Vacuum Science & Technology A: Vacuum, Surfaces, and Films **32**, 01A119 (2014).

[22] V. Miikkulainen, M. Suvanto, and T. A. Pakkanen, Chemistry of Materials **19**, 263 (2007).

[23] B. Macco, M. F. J. Vos, N. F. W. Thissen, A. A. Bol, and W. M. M. Kessels, physica status solidi (RRL) – Rapid Research Letters **9**, 393 (2015).

[24] S. B. S. Heil, E. Langereis, F. Roozeboom, M. C. M. van de Sanden, and W. M. M. Kessels, Journal of The Electrochemical Society **153**, G956 (2006).

[25] J. Aarik, A. Aidla, H. Mandar, and V. Sammelselg, Journal of Crystal Growth **220**, 531 (2000).

[26] A. Aarik, J. Karlis, H. Mändar, T. Uustare, and V. Sammelselg, Applied Surface Science **181**, 339 (2001).

[27] O. Nilsen, O. B. Karlsen, A. Kjekshus, and H. Fjellvåg, Thin Solid Films **515**, 4538 (2007).

[28] H. C. M. Knoops, K. de Peuter, and W. M. M. Kessels, Applied Physics Letters **107**, 014102 (2015).

[29] F. Werfel and E. Minni, Journal of Physics C: Solid State Physics **16**, 6091 (1983).

[30] J. G. Choi and L. T. Thompson, Applied Surface Science **93**, 143 (1996).

[31] M. Vasilopoulou, A. M. Douvas, D. G. Georgiadou, L. C. Palilis, S. Kennou, L. Sygellou, A. Soultati, I. Kostis, G. Papadimitropoulos, D. Davazoglou, and P. Argitis, Journal of the American Chemical Society **134**, 16178 (2012).

[32] E. Haro-Poniatowski, M. Jouanne, J. F. Morhange, C. Julien, R. Diamant, M. Fernández-Guasti, G. A. Fuentes, and J. C. Alonso, Applied Surface Science **127-129**, 674 (1998).

[33] L. Seguin, M. Figlarz, R. Cavagnat, and J. C. Lassègues, Spectrochimica Acta Part A: Molecular and Biomolecular Spectroscopy **51**, 1323 (1995).

[34] S.-Y. Lin, Y.-C. Chen, C.-M. Wang, P.-T. Hsieh, and S.-C. Shih, Applied Surface Science **255**, 3868 (2009).

[35] S. H. Mohamed, O. Kappertz, J. M. Ngaruiya, T. P. Leervad Pedersen, R. Drese, and M. Wuttig, Thin Solid Films **429**, 135 (2003).

[36] A. Szekeres, T. Ivanova, and K. Gesheva, Journal of Solid State Electrochemistry **7**, 17 (2002).

[37] J. Tauc, R. Grigorovic, and A. Vancu, Physica Status Solidi (B) **15**, 627 (1966).

[38] Z. Hussain, Journal of Materials Research **16**, 2695 (2001)

8

Low-Temperature Atomic Layer Deposition of MoO$_x$ for Silicon Heterojunction Solar Cells

Abstract: The preparation of high-quality molybdenum oxide (MoO$_x$) is demonstrated by plasma-enhanced atomic layer deposition (ALD) at substrate temperatures down to 50 °C. The films are amorphous, slightly substoichiometric with respect to MoO$_3$, and free of other elements apart from hydrogen (< 11 at.%). The films have a high transparency in the visible region and their compatibility with a-Si:H passivation schemes is demonstrated. It is discussed that these aspects, in conjunction with the low processing temperature and the ability to deposit very thin conformal films, make this ALD process promising for the future application of MoO$_x$ in hole-selective contacts for silicon heterojunction solar cells.

8.1   Introduction

In conventional silicon heterojunction (SHJ) solar cells, charge carrier selectivity towards either electrons or holes is achieved by applying *n*- and *p*-type doped *a*-Si:H layers, respectively, on top of very thin intrinsic *a*-Si:H passivation layers.[1] However, parasitic absorption of light in the *a*-Si:H layers severely limits the short circuit current density J_{sc} of such a cell.[2] A highly promising route to reduce this parasitic absorption is to replace doped *a*-Si:H by highly transparent metal oxides that provide charge carrier selectivity through band alignment and band offsets instead of doping.[3,4,5,6,7]

Most notably, evaporated substoichiometric molybdenum trioxide (MoO$_x$) has recently attracted much attention. This material is highly transparent and selective towards holes due to its high workfunction.[3,4,5] Battaglia *et al*. have shown an increase in J_{sc} of 1.9 mA/cm^2 when replacing a-Si:H(*p*) by evaporated MoO$_x$ which is due to reduced parasitic absorption. The MoO$_x$ still has to be combined with a thin layer of intrinsic *a*-Si:H in order to obtain a high open circuit voltage V_{oc}, since MoO$_x$ does not provide surface passivation.[4,5] However, the deposition of conformal, non-porous ultrathin (<10 nm) films on textured surfaces by evaporation is very challenging.

The stringent requirements on thickness, conformality and density make atomic layer deposition (ALD) an ideal candidate for the deposition of such films as already suggested in the initial report on MoO$_x$ by Battaglia *et al*.[3] In addition, ALD has recently gained a strong foothold in the photovoltaics industry with the introduction of high volume manufacturing ALD tools for Al$_2$O$_3$ passivation layers.[8,9] Even though ALD recipes for MoO$_x$ have been reported in the last years, none of these recipes focus on low processing temperatures required for compatibility with the commonly used *a*-Si:H passivation layers.[10,11,12]

In this work we report on a plasma-enhanced ALD (PE-ALD) process to deposit high-quality MoO$_x$ at low temperatures down to 50 °C. Firstly, the deposition process is described and the film composition, morphology and optical properties are discussed. Next, the potential of the process for depositing ultrathin MoO$_x$ in passivating contacts is explored by performing lifetime measurements on a stack consisting of an *a*-Si:H passivation layer, an ALD MoO$_x$ layer as hole-selective layer and an ALD In$_2$O$_3$:H film as transparent conductive oxide. As will be shown, such stack combines a high level of surface passivation with an excellent optical light incoupling into the silicon absorber material thanks to the high transparency of both ALD-prepared metal oxides.
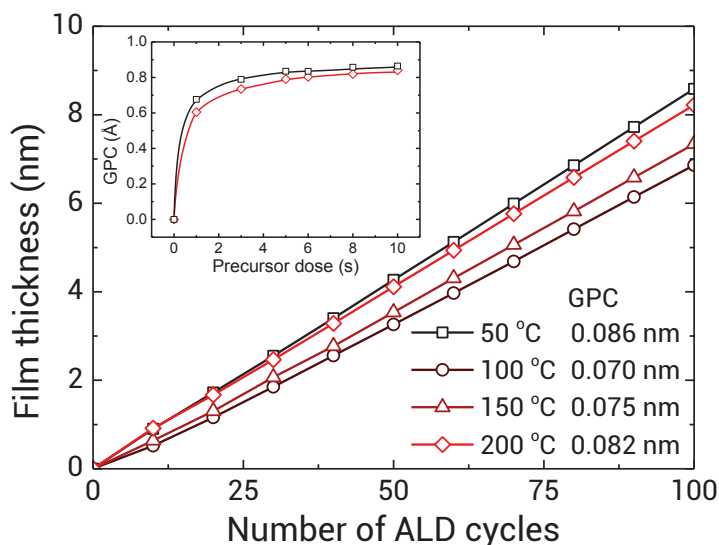
Figure 1: MoO$_x$ film thickness as a function of the number of ALD cycles for deposition temperatures between 50 and 200 °C. The GPC for each temperature is indicated. (Inset) Precursor dose saturation curves for 50 and 200 °C.

8.2   Experimental details

Slightly substoichiometric molybdenum trioxide (MoO$_x$) was deposited by a plasma-assisted ALD process using (N^{t}Bu)$_2$(NMe$_2$)$_2$Mo as Mo precursor and O$_2$ plasma as oxidant in a home-built ALD reactor.[13] The reactor has an inductively-coupled plasma source and is pumped to a base pressure of <7.5×10^{-3} mTorr by a turbomolecular and rotary pump. The precursor is delivered to the chamber by Ar bubbling from a precursor pot heated to 50 °C through gas delivery lines that are heated to 80 °C. The substrate temperature has been varied between 50 and 200 °C. The chamber walls are heated to 50 °C for depositions at a substrate temperature of 50 °C, or to 100 °C for higher deposition temperatures. The saturated precursor dosing time is 6 s at 7.5 mTorr (Inset of Figure 1), whereas saturation for the O$_2$ plasma step was reached within 4 s at 5.3 mTorr and 100 W plasma power. Purge times using Ar were 6 and 3 s after the precursor dose and plasma exposure steps, respectively.

The film thickness, growth per cycle (GPC) and optical constants of the MoO$_x$ films have been determined from spectroscopic ellipsometry using a Tauc-Lorentz oscillator to model the band-to-band absorption, and an additional Gaussian oscillator to account for weak subgap absorption, which is attributed to oxygen-vacancy-derived defects.[4] Lifetime measurements were performed using a Sinton WCT-120TS lifetime tester. Films were deposited on c-Si(p) wafers with native oxide. For the lifetime sam-

Table 1: Summary of the properties of a 20 nm MoO$_x$ film deposited at 50 °C.

Parameter	Value
Refractive index n @ 2eV	1.97
Extinction coefficient k @ 2 eV	1.94×10^{-4}
Tauc bandgap	2.9 eV
O/Mo ratio	2.95
H content	10.6 at. %
Mass density	3.95 g/cm^3
Phase	Amorphous

ples, floatzone c-Si(100) wafers (*n*-type, 285 μm, 3 Ωcm) were used as substrates, from which the oxide was removed by a one minute dip in 1%-dilute HF.

Intrinsic *a*-Si:H passivation layers were deposited by inductively-coupled plasma chemical vapor deposition (ICP-CVD) in an Oxford Instruments PlasmalabSystem100 ICP 180 at 50 °C from pure SiH$_4$. Amorphous In$_2$O$_3$:H (*a*-In$_2$O$_3$:H) was made by thermal ALD in an Oxford Instruments OpAL^{TM} tool at 100 °C using InCp, H$_2$O and O$_2$.[14] The *a*-In$_2$O$_3$:H films were subsequently crystallized (*c*-In$_2$O$_3$:H) by a 10 minute anneal at 200 °C in N$_2$, which yields a very high Hall mobility of 138 cm^2/Vs at a device-relevant carrier density of 1.8×10^{20} cm^{-3}. Due to the extremely high electron mobility, *c*-In$_2$O$_3$:H combines a very low resistivity (0.27 mΩcm) with negligible free carrier absorption, as reported recently.[14]

8.3   Results and discussion

In Figure 1, the MoO$_x$ film thickness is shown as a function of the number of ALD cycles for temperatures between 50 and 200 °C. As can be seen, for all temperatures linear growth is achieved with relatively high growth per cycle (GPC) values of around 0.08 nm. The slight variation of the GPC with temperature is consistent with Rutherford backscattering (RBS) analysis of the amount of Mo atoms deposited per cycle ($\sim$1.5$\times$10^{14} Mo atoms nm^{-2} cycle^{-1}). Figure 1 also shows that there is no nucleation delay, which facilitates an accurate control over the MoO$_x$ layer thickness even for very thin films.

For all deposition temperatures, the incorporation of N and C contaminants was found to be below the detection limit of RBS measurements (3 and 2 at.% respectively), which demonstrates the high purity of the films. All films deposited in this temperature range are amorphous, as confirmed by X-ray diffraction and Raman spectroscopy measurements (not shown). Additionally, all films have an O/Mo ratio of $\sim$2.9 as determined by RBS and are thus slightly substoichiometric with respect to MoO$_3$. The presence
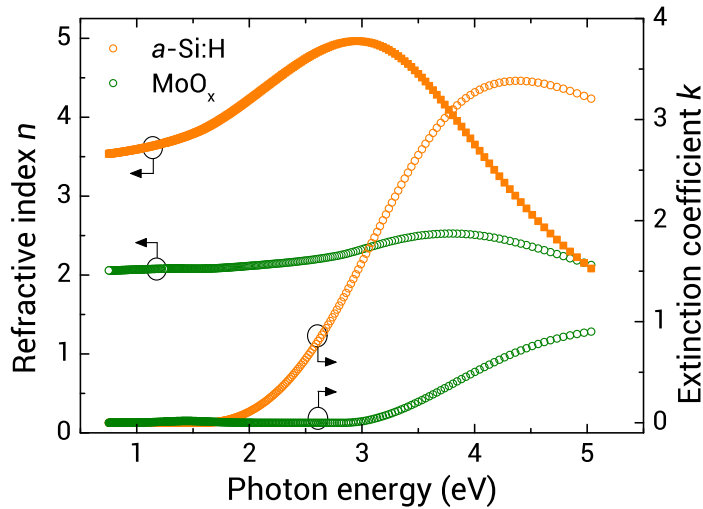
Figure 2: The refractive index *n* and extinction coefficient *k* of ALD MoO$_x$ as determined from *in-situ* spectroscopic ellipsometry. The optical constants of a-Si:H are shown for comparison.

of oxygen vacancies in the substoichiometric matrix was confirmed by an observable shoulder in the Mo 3d$_{5/2}$ peak in the XPS spectra (not shown).[3] Note that an influence of ambient on the stoichiometry cannot be excluded as samples were not transferred *in vacuo*. Moreover, elastic recoil detection analysis has revealed a H content around 11 at. % for the sample deposited at 50 °C, which decreased to 3 at. % when going to 200 °C.

The potential for this process for the implementation of MoO$_x$ in passivated hole contacts for SHJ solar cells has been evaluated by determining the passivation performance and light incoupling for a stack similar to the stack of Battaglia *et al.*[4] The stack consists of an *a*-Si:H passivation layer, an ALD MoO$_x$ film to serve as hole selective layer and an ALD *c*-In$_2$O$_3$:H film as transparent conductive oxide. The as-deposited, amorphous In$_2$O$_3$:H film, which was 75 nm thick, has been crystallized by annealing at 200 °C for ten minutes in order to obtain excellent optoelectronic properties.[14] A high resolution cross-sectional TEM image of the stack after the full process is shown in Figure 3.

For the remainder of this article, we focus on MoO$_x$ films prepared at the lowest temperature of 50 °C, as the low temperature is the main merit of this ALD process and as this temperature also yields the highest GPC. The properties of the films prepared at 50 °C are summarized in Table 1.

Figure 2 shows a comparison of the optical constants of MoO$_x$ and *a*-Si:H as obtained from spectroscopic ellipsometry. As can be seen, the refractive index *n* of MoO$_x$
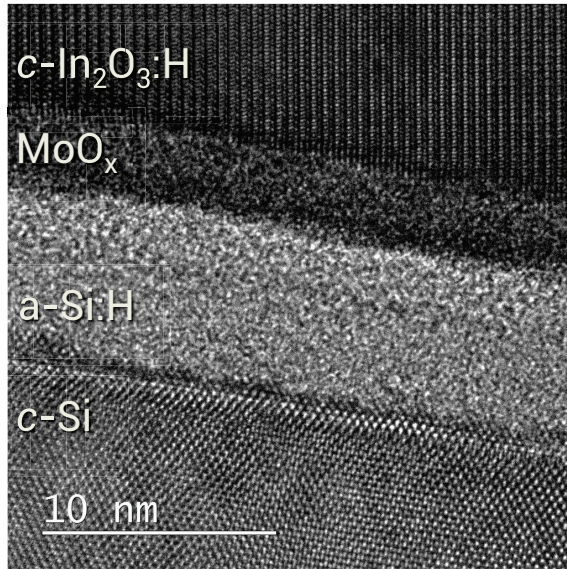
Figure 3: High resolution cross-sectional TEM image showing the passivating *a*-Si:H/MoO$_x$/*c*-In$_2$O3:H stack on *c*-Si. As can be seen, the ALD process allows for the deposition of a very thin uniform MoO$_x$ layer.

is close to 2, which is ideal for efficient light incoupling into the high-index c-Si substrate. Additionally, the extinction coefficient k is much lower for MoO$_x$ than for *a*-Si:H and the bandgap is significantly higher. Therefore, strongly reduced optical losses due to both less light absorption and reflection are expected for MoO$_x$ in comparison to *a*-Si:H.

As can be seen, the *a*-Si:H layer forms a sharp interface with c-Si, which is prerequisite for good surface passivation after post-annealing.[15] The MoO$_x$ layer is uniformly deposited on top of the *a*-Si:H layer and has remained amorphous during the post-annealing step for the whole stack. At the *a*-Si:H/MoO$_x$ interface an increased contrast can be observed, which could suggest that some layer intermixing has taken place, either during deposition of the MoO$_x$, during post-annealing or during focused ion beam preparation of the TEM sample. The crystallized In$_2$O$_3$:H film shows a very defect-free crystal structure, in line with our previous results.[14]

In order to evaluate the passivation quality of the stack in Figure 3, the injection-dependent minority carrier lifetime has been tracked after each processing step, as shown in Figure 4. As evidenced by a high implied V_{oc} of 722 mV, the *a*-Si:H layer offers an excellent level of surface passivation. After the deposition of MoO$_x$ a significant decrease in passivation is observed. This is attributed to plasma-induced damage during the O$_2$ plasma step in the PE-ALD process.[16,17] Note that for this lifetime sample, milder plasma conditions (7.5 mTorr pressure, 48 W power, 2 s exposure) were used to mitigate
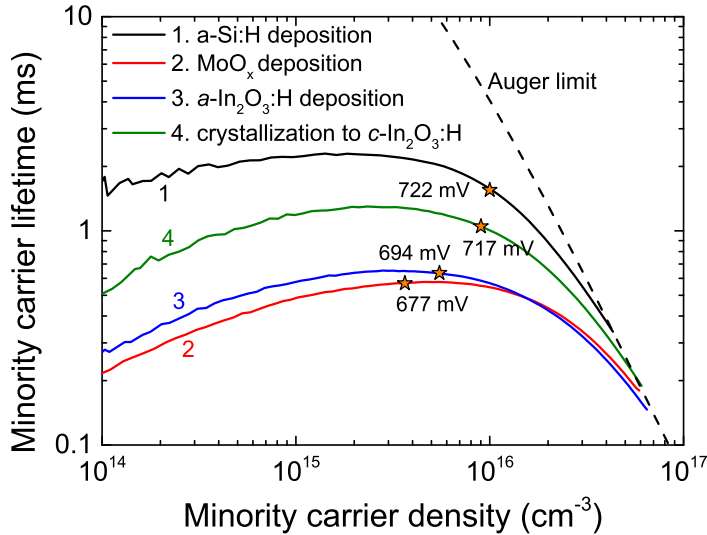
Figure 4: Injection-dependent minority carrier lifetime after subsequent processing steps during the preparation of the a-Si:H/MoO$_x$/c-In$_2$O3:H stack. The star symbols indicate the implied V_{oc} under 1 sun illumination.

plasma-induced damage to the *a*-Si:H layer, which did not result in an observable effect on the GPC or film properties studied.

Although the damage by the plasma process is a disadvantage with respect to thermal ALD (without plasma), the plasma-induced damage to the *a*-Si:H passivation layer can fortunately largely be recovered after the deposition of In$_2$O$_3$:H by the subsequent thermal crystallization step.[17,18,19] After the final step, a promising high implied V_{oc} of 717 mV is achieved, which demonstrates the high level of surface passivation that can be achieved for such a stack.

The expected improvement in J_{sc} when replacing *a*-Si:H(*p*) by ALD MoO$_x$ has been assessed by optical simulations on the light incoupling into a solar cell using the PV-Lighthouse OPAL 2 calculator.[20] For the simulations, a surface consisting of random upright pyramids was chosen, along with a normally incident AM1.5g spectrum. For the stack in this work, a promising active-area J_{sc} of 41.7 mA/cm^2 is predicted, very close to the maximum absorbable photon current of 44.0 mA/cm^2 present in the AM1.5g spectrum. In addition, this is significantly higher than the 41.2 mA/cm^2 and 40.7 mA/cm^2 calculated for a very thin 5 nm or more commonly-used 10 nm *a*-Si:H(*p*) layer, respectively.

8.4   Conclusions

A new PE-ALD process for the deposition of MoO$_x$ at low temperatures has been presented. The deposited films are free of C and N contaminants and slightly substoichiometric with respect to MoO$_3$. Films deposited at 50 °C contain 11 at. % of H. A promising high implied V_{oc} of 717 mV was achieved with a stack of *a*-Si:H/MoO$_x$/*c*-In$_2$O$_3$:H, in which the MoO$_x$ was deposited using the newly developed ALD process. Optical simulations have predicted an exceptional active-area J_{sc} of 41.7 mA/cm^2 due to the good optical properties of both MoO$_x$ and *c*-In$_2$O$_3$:H. This shows the high potential of this new ALD process for the implementation of MoO$_x$ in solar cells with passivated hole contacts. Future work will focus on the verification of hole-selectivity of the ALD MoO$_x$ films and on the implementation of stacks with ALD MoO$_x$ in SHJ solar cells.

Acknowledgements

References

[1] S. De Wolf, A. Descoeudres, Z. C. Holman, and C. Ballif, Green **2**, 7 (2012).

[2] Z. C. Holman, A. Descoeudres, L. Barraud, F. Z. Fernandez, J. P. Seif, S. De Wolf, and C. Ballif, IEEE Journal of Photovoltaics **2**, 7 (2012).

[3] C. Battaglia, X. Yin, M. Zheng, I. D. Sharp, T. Chen, S. McDonnell, A. Azcatl, C. Carraro, B. Ma, R. Maboudian, R. M. Wallace, and A. Javey, Nano letters **14**, 967 (2014).

[4] C. Battaglia, S. M. de Nicolás, S. De Wolf, X. Yin, M. Zheng, C. Ballif, and A. Javey, Applied Physics Letters **104**, 113902 (2014).

[5] J. Bullock, A. Cuevas, T. Allen, and C. Battaglia, Applied Physics Letters **105**, (2014).

[6] D. L. Young, W. Nemeth, S. Grover, A. Norman, B. G. Lee, and P. Stradins, in *2014 IEEE 40th Photovoltaic Specialist Conference (PVSC)* (IEEE, 2014) pp. 1–5.

[7] S. Avasthi, W. E. McClain, G. Man, A. Kahn, J. Schwartz, and J. C. Sturm, Applied Physics Letters **102**, 203901 (2013).

[8] J. A. van Delft, D. Garcia-Alonso, and W. M. M. Kessels, Semiconductor Science and Technology **27**, 074002 (2012).

[9] G. Dingemans and W. M. M. Kessels, Journal of Vacuum Science & Technology A: Vacuum, Surfaces, and Films **30**, 040802 (2012).

[10] A. Bertuch, G. Sundaram, M. Saly, D. Moser, and R. Kanjolia, Journal of Vacuum Science & Technology A: Vacuum, Surfaces, and Films **32**, 01A119 (2014).

[11] Y.-C. Tseng, A. U. Mane, J. W. Elam, and S. B. Darling, Solar Energy Materials and Solar Cells **99**, 235 (2012).

[12] M. Diskus, O. Nilsen, and H. Fjellvåg, Journal of Materials Chemistry **21**, 705 (2011).

[13] S. B. S. Heil, E. Langereis, F. Roozeboom, M. C. M. van de Sanden, and W. M. M. Kessels, Journal of The Electrochemical Society **153**, G956 (2006).

[14] B. Macco, Y. Wu, D. Vanhemel, and W. M. M. Kessels, physica status solidi (RRL) - Rapid Research Letters **8**, 987 (2014).

[15] S. De Wolf and M. Kondo, Applied Physics Letters **90**, 042111 (2007).

[16] H. B. Profijt, P. Kudlacek, M. C. M. van de Sanden, and W. M. M. Kessels, Journal of The Electrochemical Society **158**, G88 (2011).

[17] B. Demaurex, S. De Wolf, A. Descoeudres, Z. C. Holman, and C. Ballif, Applied Physics Letters **101**, 171604 (2012).

[18] B. Macco, D. Deligiannis, S. Smit, R. A. C. M. M. van Swaaij, M. Zeman, and W. M. M. Kessels, Semiconductor Science and Technology **29**, 122001 (2014).

[19] B. Demaurex, J. P. Seif, S. Smit, B. Macco, W. M. M. Kessels, J. Geissbuhler, S. De Wolf, and C. Ballif, IEEE Journal of Photovoltaics **4**, 1387 (2014).

[20] K. R. McIntosh and S. C. Baker-Finch, in *2012 38th IEEE Photovoltaic Specialists Conference* (IEEE, 2012) pp. 265–271

<div style="text-align: right; font-size: 3em; color: orange;">**9**</div>

First steps towards solar cell implementation of developed metal oxides

In this chapter the current status of the implementation of the developed ALD In$_2$O$_3$:H and MoO$_x$ films in solar cell devices is discussed. ALD In$_2$O$_3$:H has been tested as front side TCO in SHJ cells, in a collaboration with Y. Kuang of Eindhoven University of Technology and Energieonderzoek Centrum Nederland (ECN). A manuscript on the basis of this work is currently under preparation, and the most important aspects regarding the implementation and initial results will be discussed here. The suitability of ALD MoO$_x$ as a hole selective contact has been investigated in a collaboration with Fraunhofer ISE. The resulting manuscript has been accepted for publication in Energy Procedia, and the most important findings regarding the selectivity of the ALD MoO$_x$ layer will be discussed here as well.

9.1 ALD In$_2$O$_3$:H

In order to evaluate the performance of the developed ALD In$_2$O$_3$:H TCO in actual solar cells, Si heterojunction cells on 6″ pseudo-square wafers with a HIT-type configuration were acquired from ECN. More specifically, the cell precursors feature Ag/*a*-Si:H(*n*)/*a*-Si:H(*i*) at the rear side and *a*-Si:H(*i*)/*a*-Si:H(*p*) at the front side.

The cells received a 1 minute dip in 1% dilute HF prior to the ALD process to remove
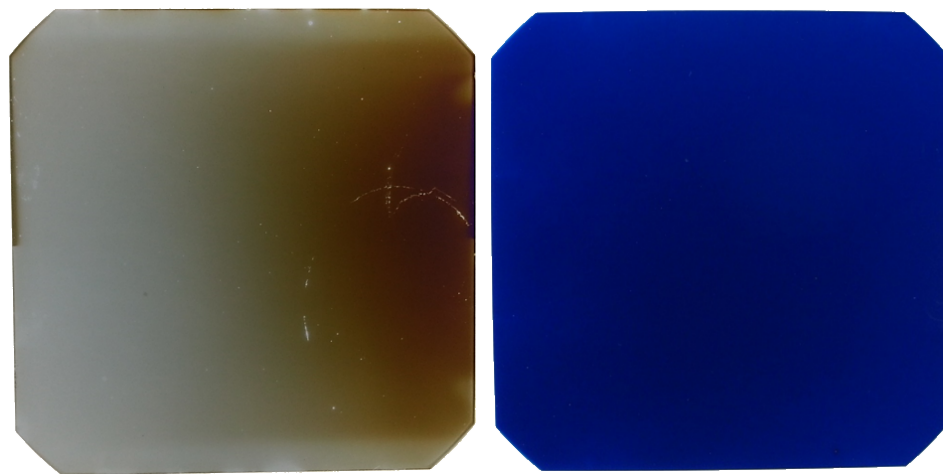
Figure 1: (Left) Picture of a Si wafer coated with PECVD *a*-Si:H (i/p) and 770 cycles of ALD In_2O_3:H. The wafer did not receive an HF dip prior to the ALD process. (Right) Same experiment, but using a 120 sec H_2 plasma treatment at 17 mTorr and 100 W input power before the ALD In_2O_3:H process. The inlet of the InCp is positioned to the right of the wafers.

any possible oxide formed on the *a*-Si:H(p) layer. Remarkably, it was however observed that no (or limited) growth of the ALD In_2O_3:H occurs on such a HF-dipped surface after 770 ALD cycles. Therefore, it was attempted to deposit the ALD layer on the as-received solar cell precursors, with the possibility of having a thin oxide on the *a*-Si:H(p) layer that could potentially act as an electrical barrier. However, also in this case the ALD process suffered from a strong nucleation delay and non-uniformity, as can be seen in Figure 1 (left). At the right side of the wafer, which is closest to the inlet of the InCp into the chamber, the layer thickness is $\sim$40 nm instead of the expected 75 nm, and at the left side of the wafer there is barely any deposition. Therefore, even without an HF-dip a significant nucleation delay is observed, which seems to be dependent on the exposure of the surface to the InCp precursor.

The inhibition of nucleation of the ALD In_2O_3:H layer on pristine *a*-Si:H likely originates from an insufficient reactivity of the precursor with the H-terminated surface. Density functional theory (DFT) calculations[*] suggest that the InCp has a very low adsorption energy on such an *a*-Si:H surface, in contrast to for example an OH-terminated surface.

In order to enable In_2O_3:H film growth on *a*-Si:H, plasma pretreatments have been developed that enhance the adsorption of the InCp precursor. More specifically, Ar, O_2 and H_2 plasma pretreatments have been investigated. In Figure 2 the In_2O_3:H film thickness as a function of the number of ALD cycles is shown for both pristine *a*-Si:H and
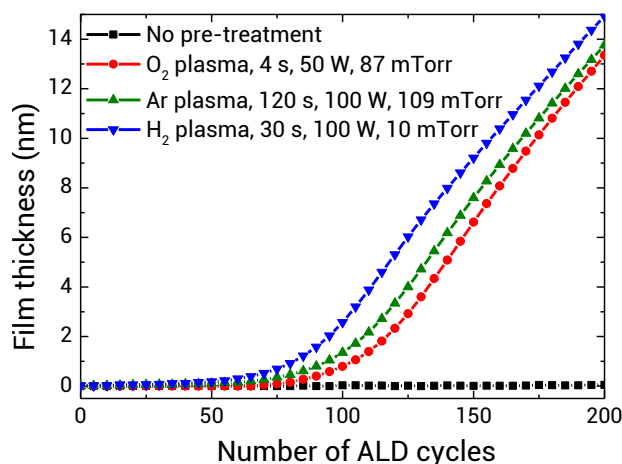
Figure 2: Nucleation delay of the ALD In$_2$O$_3$:H process on *a*-Si:H surfaces with various plasma pre-treatments.

plasma-treated *a*-Si:H layers. As can be seen, no growth is obtained on the pristine *a*-Si:H layer for at least 200 cycles, whereas growth is observed after the various plasma pretreatments. The plasma pretreatments enable the deposition of a uniform In$_2$O$_3$:H layer on a 6" pseudo-square wafer, as shown for example in Figure 1 for the case of wafer pretreated for 120 seconds by H$_2$ plasma.

The successful activation of the *a*-Si:H surface in the case of the O$_2$ plasma is most likely due to the oxidation of the (sub)surface of the *a*-Si:H layer. However, excessive oxidation of the *a*-Si:H (sub)surface by O$_2$ plasma potentially leads to an electrical barrier. Therefore, although not experimentally confirmed, it is thought that the Ar and H$_2$ plasma pretreatments are a safer option. Although Figure 2 convincingly shows that such pretreatments also work, the mechanism is not as evident as for the case of the O$_2$ plasma. Potentially residual H$_2$O and O$_2$ in the chamber background lead to oxidation of the surface during the Ar or H$_2$ plasma treatment, i.e. unintentional oxidation occurs. Another possibility is that the plasma pretreatments create reactive sites through the formation of non-coordinated bonds such as dangling bonds.

Although Figure 2 shows that plasma pre-treatments are effective in enabling In$_2$O$_3$:H film growth, one of the other concerns with the use of a plasma is degradation of the surface passivation. Therefore, the effect of the plasma pretreatment and a post-anneal step on the surface passivation has been studied, as shown in Figure 3. As can be seen, a strong degradation of the passivation quality occurs during the H$_2$ plasma pretreatment, Nonetheless, full recovery is observed upon a short post-anneal at modest temperatures. A similar degradation and recovery behaviour was observed for the O$_2$ and Ar plasma treatments.
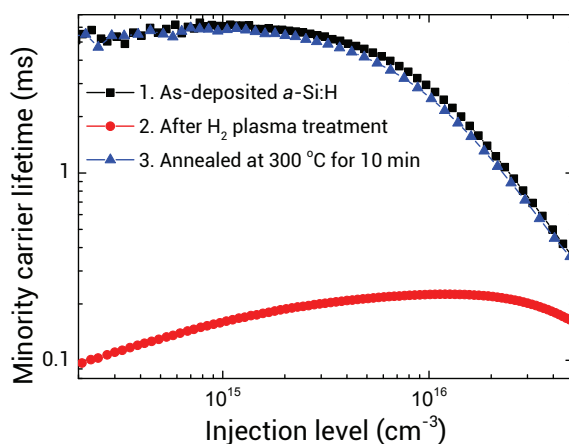
Figure 3: Demonstration of the plasma-induced damage during the H_2 plasma pre-treatment on the a-Si:H-based surface passivation, and the complete recovery upon post-annealing.

In a dedicated experiment using various optical filters, it has been shown that VUV photons rather than ion bombardment lead to degradation the surface passivation.[†] This is similar to the case of plasma-induced depassivation of Al_2O_3 in the same ALD reactor (Oxford Instruments OpAL), and the absence of considerable damage induced by ion bombardment is most likely related to the low ion energy in this remote ICP plasma system.[1] Fortunately, the defects induced by the plasma radiation are metastable, as evidenced by the full recovery of the initial passivation quality upon post-annealing, and should therefore in principle not deteriorate the final device efficiency.

The implementation of ALD In_2O_3:H in SHJ solar cells has been tested using the developed plasma pretreatment, and a comparison with conventional sputtered ITO has been made. The front ITO was omitted for the cells acquired from ECN. After travel, either PVD ITO or ALD In_2O_3:H was deposited on top of the a-Si:H(p).The measured EQE and illuminated $J - V$-curves of both the cell with ALD In_2O_3:H and the reference with sputtered ITO are shown in Figures 4 and 5, respectively.

As can be seen, the cell with ALD In_2O_3:H has a 1.6 mA/cm^2 higher integrated photocurrent, clearly demonstrating reduced optical losses for the ALD layer. Interestingly, gains in the EQE are observed both at short wavelengths ($\sim$400-600 nm) and long wavelengths (>900 nm). The gain at the long wavelength range can be easily understood from the reduced Drude response in the high-mobility In_2O_3:H TCO. The increased blue-response of the cell potentially stems from a somewhat higher bandgap of the In_2O_3:H layer, similar to what has been observed by EPFL in a comparison between sputtered

---

[†]These experiments were performed by dr. Y. Kuang and are not shown here. A full manuscript describing the implementation of ALD In_2O_3:H in SHJ solar cells is currently under preparation by dr. Y. Kuang.
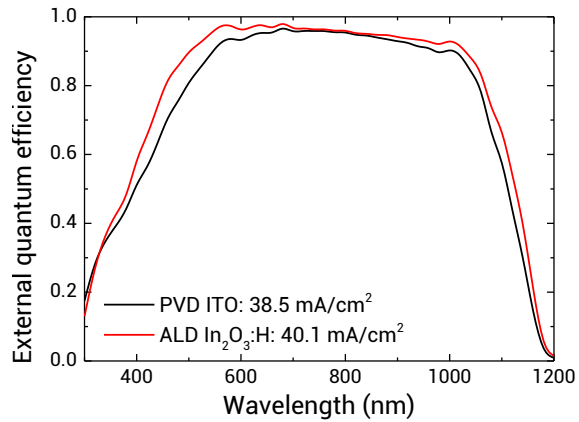
Figure 4: External quantum efficiency of SHJ solar cells featuring either sputtered (PVD) ITO or ALD In$_2$O$_3$:H as TCO. The integrated photocurrent values are shown.

ITO and sputtered In$_2$O$_3$:H.[2] Nonetheless, further investigations regarding the optical properties of the employed ITO layer would be needed to confirm this.

The illuminated *JV*-curves corresponding to the two cells are shown in Figure 5. The cell featuring In$_2$O$_3$:H has a convincing J_{sc} above 40 mA/cm^2, although both cells with a conversion efficiency around 16% are by no means record cells. Both cells seem to be mostly limited by a low *FF* around 60% and low V_{oc} values of $\sim$ 680 mV. The ECN baseline usually delivers cells with conversion efficiencies above 20%, proper *FF* and V_{oc} values above 700 mV. Therefore, it is thought that both cells are limited by a barrier somewhere in the cell or potentially have degraded during transport due to the absence of a front TCO. Although the J_{sc} displayed by the ALD In$_2$O$_3$:H is already promising, the losses in *FF* and V_{oc} are currently under investigation.

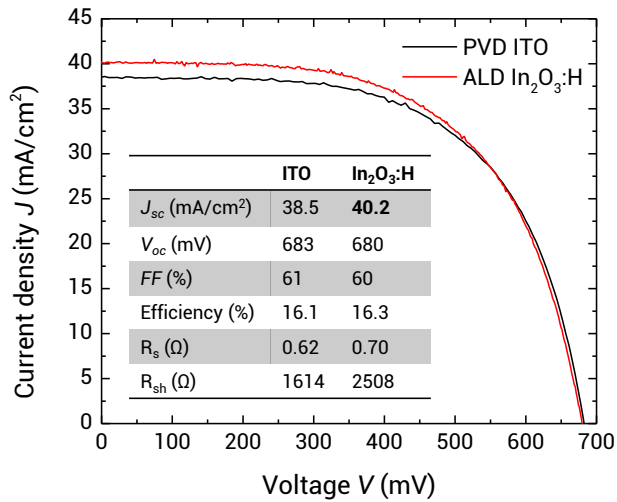**Figure 5:** $J - V$ curves of SHJ solar cells featuring either sputtered ITO or ALD In$_2$O$_3$:H as TCO under standard test conditions. The inset table shows the most important derived solar cell parameters.

9.2 ALD MoO$_x$

For the evaluation of ALD MoO$_x$ as a hole-selective contact on Si, the ALD process developed on the ALD-II reactor as described in **Chapter 7** has first been transferred to the Oxford Instruments OpAL reactor. The motivation for this was two-fold: Firstly, the OpAL reactor allows for the deposition on 8" wafers (including 156x156 mm^2 square solar cell wafers), thereby enabling the ALD MoO$_x$ layers to be tested on an industrially-relevant substrate size. Secondly, since also the ALD In$_2$O$_3$:H process has been developed on the OpAL reactor, the availability of both processes on the same reactor allows for the deposition of the TCO on top of the MoO$_x$ without breaking the vacuum.[‡]
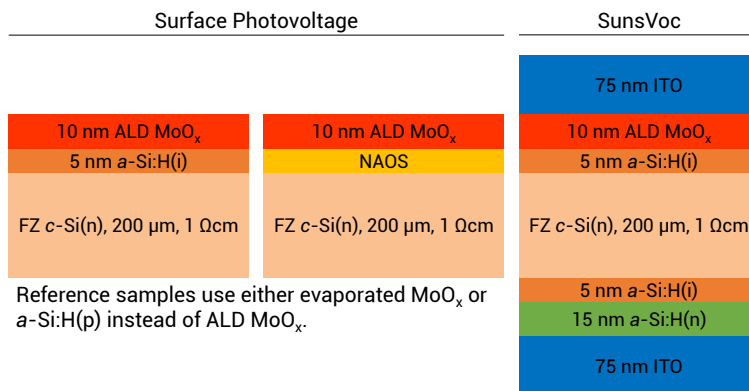

Surface Photovoltage		SunsVoc

Figure 6: Sample layout for the SPV and SunsVoc measurements. For the SPV sample, either *a*-Si:H(i) or NAOS SiO$_2$ is used as buffer layer. The sample layout for the SunsVoc measurement resembles the standard HIT-layout, with *a*-Si:H(p) replaced by ALD MoO$_x$.

As was shown in Figure 18(d) in Chapter 2, MoO$_x$ relies on the upward band bending it induces by its high work function for achieving hole-selectivity. Therefore, in order to evaluate the selectivity of the ALD MoO$_x$ the band-bending induced by the MoO$_x$ has been investigated by surface photovoltage (SPV) measurements. In addition, a comparison between the $_iV_{oc}$ (i.e. internal voltage or quasi-Fermi level splitting) and the external voltage (i.e. SunsVoc) has been made.[§]

The induced band bending has been measured by SPV on sample structures as indicated in Figure 6 (left). The structure shown in Figure 6 (right) has been used to measure

---

[‡]It should be noted that slight differences between the films prepared on the OPAL and ALD-II systems were observed. Most notably, the OPAL films contain traces of carbon. Potentially, this stems from redeposition effects during the O$_2$ plasma stap due to a higher residence time in the OPAL system. [3] Also, differences in the O$_2$ plasma during the oxidation step can potentially explain the difference in impurity content. However, the hole-selectivity of some ALD MoO$_x$ layers prepared by the ALD-II reactor has also been evaluated and was found to give very similar results as for the films prepared on the OPAL system.

[§]This has been done in collaboration with Martin Bivour and Jan Temmler of Fraunhofer ISE, who provided both the *a*-Si:H and NAOS passivation and ITO layers, and performed the SPV measurements. A manuscript describing these results has been accepted for publication in Energy Procedia.

both the internal voltage (i.e. the quasi-Fermi level splitting) and the external voltage by QSSPC and sunsVoc measurements, respectively. Both PECVD *a*-Si:H and SiO$_2$ prepared by a nitric acid oxidation step (NAOS) have been used as passivation layer. The thickness of the ALD MoO$_x$ layer has been kept constant at 10 nm, whereas the deposition temperature has been varied between 100 and 350 °C. Both evaporated MoO$_x$ and PECVD *a*-Si:H(*p*) have been used as references.
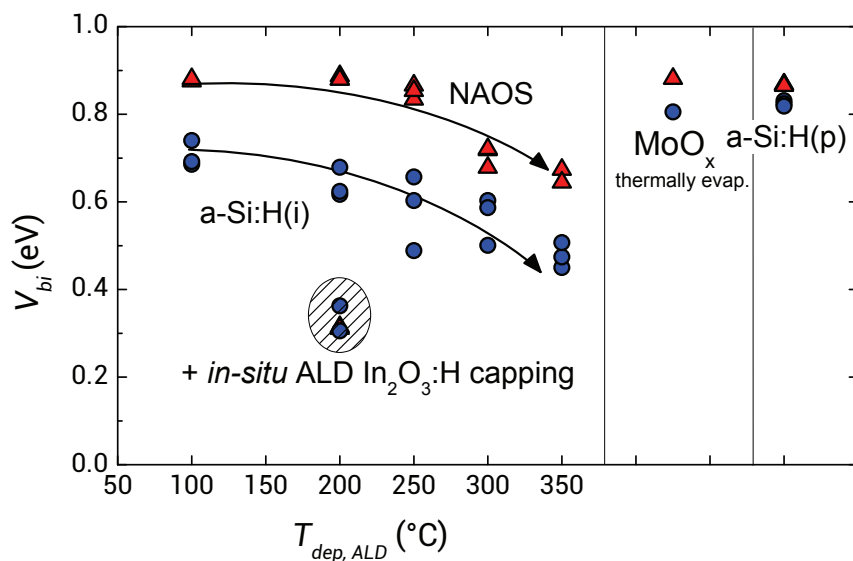

Figure 7: Induced band bending V_{bi} for ALD MoO$_x$ layers prepared at various substrate temperatures on both *a*-Si:H(*i*) and NAOS SiO$_2$. Thermally evaporated MoO$_x$ and PECVD *a*-Si:H(*p*) have been added as reference hole-selective layers. The V_{bi} of one ALD MoO$_x$ layer capped by ALD In$_2$O$_3$:H without breaking the vacuum is shown as well.

In Figure 7 the upward band-bending in the *c*-Si, V_{bi}, induced by the ALD MoO$_x$ layers and the two reference samples prepared on both *a*-Si:H(*i*) and NAOS SiO$_2$ is shown. As can be seen, both reference layers induce a strong upward band bending of ∼0.8-0.9 eV. For the ALD layers the induced band bending decreases with the deposition temperature. At a low deposition temperature, the V_{bi} on NAOS is very similar to the values obtained by evaporated MoO$_x$ and *a*-Si:H(*p*). Although this high V_{bi} points to a high level of selectivity, the absence of reasonable passivation observed for MoO$_x$ on NAOS renders them unsuited for photovoltaic application. The V_{bi} on *a*-Si:H(*i*) is found to be consistently lower, hinting to either loss of band bending over the *a*-Si:H(*i*) layer or the presence of Fermi level pinning. For some ALD MoO$_x$ samples prepared at 200 °C, the layer was capped by 75 nm ALD In$_2$O$_3$:H at 100 °C without breaking the vacuum. As can be seen, the induced band-bending is strongly reduced. Note that this is not due to wrap-around of the ALD In$_2$O$_3$:H layer, as the edges were isolated by laser cutting prior
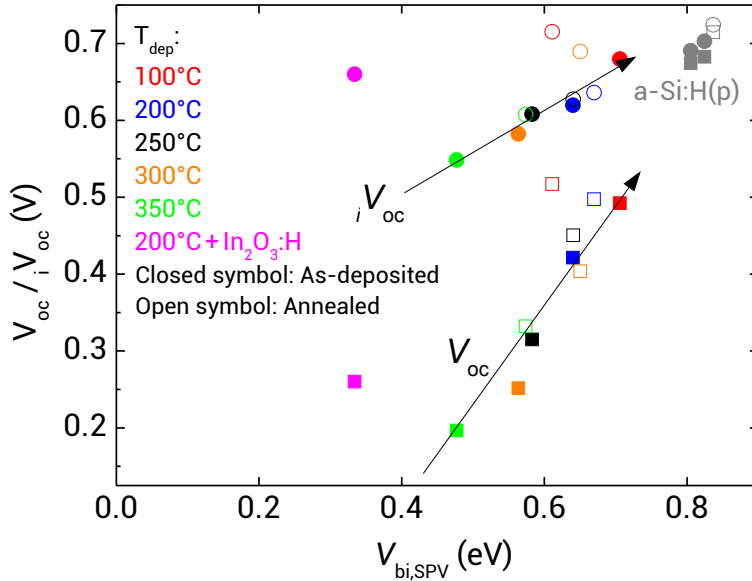
to the SPV measurement.

Figure 8: The internal voltage $_iV_{oc}$ and the external voltage V_{oc} as a function of the c-Si band bending $V_{bi,SPV}$ as measured by SPV. The values for a reference a-Si:H(p) layer have been added. The arrows are guides to the eye. Closed symbols are as-deposited samples, open symbols are values for samples annealed at 180 ºC for 15 minutes.

The lower level of induced band-bending for the ALD layers hints at a reduced selectivity of such layers. To investigate this, both the internal (i.e. the $_iV_{oc}$) and external voltage (i.e. the sunsVoc) have been determined for these samples, as shown in Figure 8. For perfectly selective passivating contacts, the external voltage almost equals the internal voltage[4], i.e. the quasi-Fermi level of the carrier that is to be collected is virtually flat up to the metal contact. For a reference a-Si:H(p) layer both voltages are equal, indicating good selectivity. For the ALD MoO$_x$ layers, both the $_iV_{oc}$ and sunsVoc increase with the built-in voltage, which varies with deposition temperature. The increase in $_iV_{oc}$ at lower deposition temperatures can most likely be attributed to both a higher level of *chemical* passivation due to less degradation of the a-Si:H(i) layer as well as improved *field-effect* passivation due to a stronger inversion layer induced in the c-Si(n) by the MoO$_x$. At low deposition temperatures values around 700 mV are obtained, indicative of good interface passivation.

Nonetheless, the obtained external voltage values are well below the $_iV_{oc}$ values, even for the samples prepared at the lowest deposition temperature. This demonstrates that the ALD layers do not provide sufficient selectivity for holes. Since the hole-selectivity of MoO$_x$ is based on the band-bending induced by a high work function, it is likely that

the work function of the ALD MoO_x layer is lower than that of its evaporated counterpart, for which a work function of 6.6 eV has been reported.[5]

Significant effort has been put in determining the work function of the ALD MoO_x layers by biased XPS measurements. However, these attempts were mostly unsuccessful for a few reasons. First, the samples were exposed to ambient during transport to the XPS setup and the work function of MoO_x is known to be highly sensitive to surface contamination. Attempting to remove surface contamination with the ion gun in the XPS setup leads to preferential sputtering of oxygen, thereby strongly influencing the measurement. Secondly, it was found that the measured work function reduces upon X-ray exposure, showing that the measurement itself influences the material properties. All these effects led to a relatively low work function of $\sim$4-5 eV being measured for all the samples, and it is doubted whether these values are trustworthy.

In literature some reasons for a lower WF of MoO_x can be found. Greiner *et al.* have shown through a well-controlled experiment that the presence of oxygen vacancies strongly reduces the work function of MoO_x.[6] For stoichiometric MoO_3 they reported a work function of 6.9, which decreased to $\sim$6.6 and $\sim$6.4 for O/Mo ratios of 2.9 and 2.8, respectively. Also in the case of WO_x, the presence of oxygen vacancies has been shown to reduce the work function and thereby the hole-selectivity of this high work function metal oxide.[7] In Chapter 7, it has been shown by RBS that for the ALD MoO_x layers prepared on the ALDii system the O/Mo ratio scatters around 2.9, indicating the ALD layers are substoichiometric. It should also be noted that the samples have been exposed to ambient prior to the RBS measurements, and that it is thus quite well possible that the samples have been oxidized further upon taking them out of the reactor. This does not hold for the MoO_x layer that was capped *in-situ* with ALD In_2O_3:H, and the strongly reduced selectivity for that sample also hints at an influence of post-deposition oxidation of the MoO_x layer on its selectivity. In view of these considerations, future research on the implementation of MoO_x as hole-selective contact should focus on bringing the oxygen content of the ALD layers closer to stoichiometric MoO_3, *e.g.* by alteration of the oxidant step of the ALD cycle or by post-deposition treatments of the deposited layers.

References

[1] H. B. Profijt, P. Kudlacek, M. C. M. van de Sanden, and W. M. M. Kessels, Journal of The Electrochemical Society **158**, G88 (2011).

[2] L. Barraud, Z. C. Holman, N. Badel, P. Reiss, A. Descoeudres, C. Battaglia, S. De Wolf, and C. Ballif, Solar Energy Materials and Solar Cells **115**, 151 (2013).

[3] H. C. M. Knoops, K. de Peuter, and W. M. M. Kessels, Applied Physics Letters **107**, 014102 (2015).

[4] M. Bivour, M. Reusch, S. Schroer, F. Feldmann, J. Temmler, H. Steinkemper, and M. Hermle, IEEE Journal of Photovoltaics **4**, 566 (2014).

[5] C. Battaglia, X. Yin, M. Zheng, I. D. Sharp, T. Chen, S. McDonnell, A. Azcatl, C. Carraro, B. Ma, R. Maboudian, R. M. Wallace, and A. Javey, Nano letters **14**, 967 (2014).

[6] M. T. Greiner, L. Chai, M. G. Helander, W. M. Tang, and Z. H. Lu, Advanced Functional Materials **22**, 4557 (2012), arXiv:0706.1062v1 .

[7] M. Mews, L. Korte, and B. Rech, Solar Energy Materials and Solar Cells , 1 (2016)

10

Conclusions and Future Research

This final chapter serves to summarize the main outcomes and conclusions from this PhD project. In addition, future lines of research related to the work presented in this dissertation are discussed.

10.1   Conclusions

On the basis of the research presented within this dissertation, the following main conclusions and new insights can be discerned:

- In **Chapter 3** it has been shown that thermal ALD is a "soft deposition technique". The absence of plasma damage during ALD allows for the formation of much better defined interfaces than achievable by *e.g.* sputtering. The idea of using ALD as a "soft deposition technique" has found follow-up in literature besides in our own work[1] and collaboration with EPFL[2]: At Fraunhofer ISE, ALD ZnO:Al has been used as protective interlayer before sputtering the ITO TCO in a TOPCon-type heterojunction cell.[3] An increase in V_{oc} of 20 mV and an absolute gain of 0.8% in efficiency were observed. More importantly, whereas sputter damage is (mostly) reversible in *a*-Si:H-based HIT-type heterojunctions, this is not the case for polysilicon-based TOPCon-type heterojunctions.[3] Therefore, avoidance of sputter damage is even more important in this or other upcoming solar cell concepts.

- Since the doping level of the TCO affects its work function, the doping level of the TCO layer is of importance in determining the band structure of the solar cell. This has been demonstrated in **Chapter 3** using the excellent control over the doping level offered by ALD. Interestingly, Kirner *et al.* further investigated the influence of the dopant density in a thin ITO TCO interlayer on the working of a HIT-type SHJ cell.[4] They observed a similar reduction in *FF* at high ITO dopant densities, but also observed that the interlayer should at least have a carrier density of a few times 10^{19} cm^{-3} in order to make a good tunnel contact at the *a*-Si:H(*p*)-TCO interface.

- In_2O_3:H is both very transparent and conductive, which is enabled by its extremely high carrier mobility well above 100 cm^2/Vs. In conjunction with the relatively high work function of In_2O_3:H, this makes In_2O_3:H highly suited for contacting the hole-collecting front side of heterojunction solar cells. The limited electron mobility of ZnO makes it less transparent than indium-based TCOs. In addition to the less ideal work function of ZnO for contacting the hole-collecting side, this makes it challenging to successfully apply this TCO at the front side of high efficiency heterojunction cells. Doped ZnO is however perfectly capable of replacing the rear indium-based TCO without efficiency losses.[5]

- Atomic hydrogen is an excellent dopant in TCOs. In **Chapter 5** it has been shown that even though for ALD In_2O_3:H only $\sim$3 % of the incorporated H acts as an active dopant, the remaining inactive H atoms do not contribute to the electron scattering. Besides the possibility of grain boundary passivation by atomic H, this is thought to be main reason why H works so much better as a dopant than the conventionally used Sn in In_2O_3:Sn.

- The key to obtaining the highest quality In_2O_3:H is to deposit an amorphous layer which is crystallized after the deposition, since this leads to a material with very large grains. Preferably, a small density of crystallites is already embedded during the deposition, so that crystallization can start at the crystallites and take place at low temperatures of 150 - 200 °C. The fact that ZnO tends to always grow in a polycrystalline structure is a strong downside in this respect. Moreover, together with the higher scattering activity of grain boundaries in ZnO, this is probably the main reason why deposited ZnO films do not reach the mobility limit as is the case for In_2O_3.

- In_2O_3:H prepared by sputtering has already proven itself in SHJ solar cells. However, ALD seems to have some unique advantages over sputtering. Besides the aforementioned "soft deposition" nature and the fact that the optoelectronic prop-

erties of the ALD material are somewhat better, the optoelectronic properties of the ALD material are also highly uniform and reproducible, which is not always the case for sputtered In_2O_3:H. [6,7] Nonetheless, it is currently an open question whether ALD will be able to compete with sputtering on an industrial level. The InCp precursor is currently rather expensive, although this is most likely caused by the fact that only very small quantities are produced for research institutes. Additionally, potentially cheaper precursors can be found that yield amorphous, H-doped In_2O_3. Finally, it is imagineable that ALD In_2O_3:H will also find its application in areas other than Si PV that are less demanding in terms of cost.

- Film deposition during ALD is driven by surface chemistry, through self-limiting half-cycles. This contrasts to CVD and sputtering processes, in which the fluxes of the reactive species control the deposition process. This fundamental difference yields unique opportunities for ALD as well as challenges. The self-limited reactions enable the well-known strong points of a high uniformity and conformality of ALD. Moreover, the surface chemistry can also provide additional control over the film composition, e.g. by the smart choice of dopant precursor when doping ALD ZnO in a supercycle approach. Because of the role of the surface chemistry, the chemical nature of the initial growth surface is of great influence in determining the initial growth. This can make it challenging to achieve film growth on certain surfaces, as was observed for example by the absence of growth for the ALD In_2O_3:H process on *a*-Si:H. This selectivity of an ALD process for different surfaces can however also be exploited to grow *selectively* on substrates or even certain well-defined parts of the substrate. This has been done for the ALD In_2O_3:H process and has become an active field of follow-up research, as will be briefly shown in the next section.

- It has been shown that molybdenum oxide films can be grown by plasma-assisted ALD at deposition temperatures as low as 50 °C. Nonetheless, the hole-selectivity of ALD MoO_x has been found to be lower than that of evaporated MoO_x. Conceivably, the work function of the ALD material is lower due to a higher concentration of oxygen vacancies. Therefore, future research should focus on a structural comparison between both materials, and the oxygen content of the ALD MoO_x layer should be increased so that the deposited material is closer to stoichiometric MoO_3.
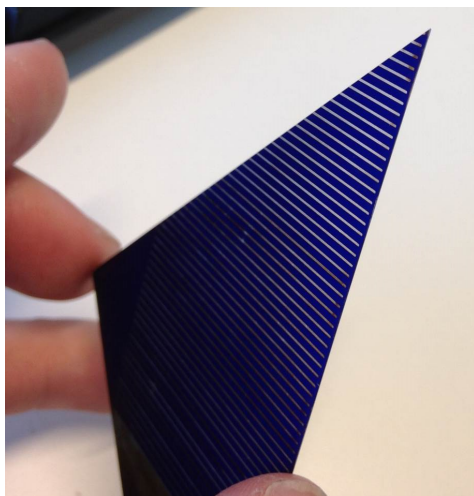
Figure 1: Picture of a random pyramid-textured Si wafer with interdigitated n^+ and p^+ regions. ALD In$_2$O$_3$:H is selectively deposited on the p^+ regions, which remain hydrophilic after an HF dip. Courtesy B.W.H. van de Loo, A. Mameli and Y. Kuang.

10.2   Prospects: Beyond the FLASH project

As discussed in chapter 9, the implementation of the metal oxides developed within the FLASH project in Si solar cells is currently still under development. These activities will continue within a recently-granted follow-up project, the COMPASS (competitive passivating contact technology for PV) project*, and the use of ALD In$_2$O$_3$:H and MoO$_x$ as TCO and hole-selective layer, respectively, will be investigated further.

In addition, the metal oxides developed within this project have also found their way into other research projects. For example, ALD In$_2$O$_3$:H is being explored as TCO in both CIGS solar cells (in collaboration within Solliance) and perovskite solar cells (by D. Koushik and Y. Kuang) which are to be applied in c-Si/perovksite tandem cells. Also, very thin ALD MoO$_x$ is being used by A. Sharma for the sulphurization of MoO$_x$ into molybdenum disulfide (MoS$_2$), a two-dimensional transition metal dichalcogenide which has lately attracted great attention.

Finally, one possible future application of ALD of metal oxides for Si solar cells should be mentioned: The fact that for some ALD processes the nucleation is heavily dependent on the chemical nature of the surface can be used to deposit an ALD layer selectively on certain well-defined parts of the wafer, i.e. *area-selective ALD*. As an example of this, a

---

*The COMPASS project is a TKI (Topconsortia for Knowledge and Innovation) project and aims to produce passivating contact solar cells through a consortium of Dutch research institutes and equipment manufacturers, including ECN, Solmates, Levitech, AMOLF, Delft University of Technology and Eindhoven University of Technology.

picture of an interdigitated back contact cell with ALD In_2O_3:H is shown in Figure 1 . The ALD layer has been deposited *selectively* on the p^+ regions and not on the n^+ regions. This is thought to be caused by the fact that p^+ regions remain hydrophilic after an HF dip, whereas the n^+ regions become hydrophobic. Although the current structure does not work as a solar cell, it does serve as an initial demonstrator to show how a concept such as area-selective ALD, which is probably currently not well-known in the PV community, can potentially be used to prepare interdigitated contacts with less or easier masking.

References

[1] B. Macco, D. Deligiannis, S. Smit, R. A. C. M. M. van Swaaij, M. Zeman, and W. M. M. Kessels, Semiconductor Science and Technology **29**, 122001 (2014).

[2] B. Demaurex, J. P. Seif, S. Smit, B. Macco, W. M. M. Kessels, J. Geissbuhler, S. De Wolf, and C. Ballif, IEEE Journal of Photovoltaics **4**, 1387 (2014).

[3] F. Feldmann, K. U. Ritzau, M. Bivour, A. Moldovan, J. Temmler, M. Hermle, and S. W. Glunz, Energy Procedia **00**, 263 (2015).

[4] S. Kirner, M. Hartig, L. Mazzarella, L. Korte, T. Frijnts, H. Scherg-Kurmes, S. Ring, B. Stannowski, B. Rech, and R. Schlatmann, Energy Procedia **77**, 725 (2015).

[5] G. R. P. Carroy, D. Muñoz, F. Ozanne, A. Valla, P. Mur, in *30th EU PVSEC* (2015) pp. 359 – 364.

[6] H. Scherg-Kurmes, A. Hafez, M. Siemers, A. Pflug, R. Schlatmann, B. Rech, and B. Szyszka, Physica Status Solidi (a) **7**, 1 (2016).

[7] G. C. E. Jost, A. N. Hamri, F. Köhler, and J. Hüpkes, physica status solidi (a) **213**, 1751 (2016)

Summary

Atomic Layer Deposition of Metal Oxide Thin Films for Si Heterojunction Solar Cells

Within the field of crystalline silicon photovoltaics, the deposition technique of atomic layer deposition (ALD) is mostly known for the preparation of high-quality Al_2O_3-based surface passivation layers for homojunction solar cells. High-throughput ALD tools specially designed for this application are commercially available, enabling substantial gains in solar cell efficiency. Currently silicon heterojunction (SHJ) or *passivating contact* solar cells are receiving a lot of attention, mainly because such cells can yield even higher efficiencies and can potentially be made by straight-forward, low-temperature processing. Whereas for the more conventional homojunction concepts thin films are only used for surface passivation and anti-reflection, heterojunction cells are truly thin-film powered devices: Thin films deposited on the silicon wafer provide all of the functionalities, such as surface passivation, selective extraction of carriers and lateral electrical conduction in the form of transparent conductive oxides (TCOs). In this dissertation, the use of ALD to prepare these functional thin films for these upcoming classes of solar cells has been explored.

As described in chapter 3, ALD has been employed for the preparation of the TCO films for SHJ cells, which is conventionally done by sputter deposition. Using atomic layer deposited Al-doped zinc oxide (ZnO:Al), two key merits of ALD over conventional sputtering have been demonstrated. Firstly, whereas it is well-known that the harsh plasma conditions during sputter deposition lead to substrate damage, the absence of a plasma during thermal ALD ensures a high compatibility with the underlying sensitive thin films. Secondly, the use of so-called ALD supercycles has been shown to give an unprecedented level of control over the doping level and doping profile of the TCO. The ability to turn this "knob" is of great interest: The doping level determines the fundamental trade-off between transparency and conductivity of the TCO. In addition, it has been experimentally shown that the interfacial doping level, which determines the work function of the TCO, is of strong influence on the junction properties.

During the course of the project, it became clear that *high-mobility* hydrogen-doped indium oxide (In_2O_3:H), a TCO originally developed by sputtering, has enormous potential for heterojunction cells. In such high-mobility TCOs, electrons are able to move much more freely than in conventional Sn-doped In_2O_3 and doped ZnO. Therefore, the doping level required to achieve the desired level of conductivity is strongly reduced,

which mitigates optical losses in the infrared due to free carrier effects as found in the conventional TCOs. As such, high-mobility TCOs have proven to be crucial to obtain high short circuit density J_{sc} values exceeding 40 mA/cm^2 for this class of solar cells. Within this thesis work, an ALD approach to prepare *high-mobility* hydrogen-doped indium oxide (In_2O_3:H) has been developed, as described in chapter 4. The process consists of the preparation of mostly amorphous In_2O_3:H, followed by crystallization at 150-200 ^{o}C, which results in polycrystalline In_2O_3:H with grains a few hundred nm in lateral size. Besides the low-temperature processing and the aforementioned merits of ALD over sputtering, the salient features of the developed ALD process are the record-high carrier mobility and low resistivity of 138 cm^2/Vs and 0.27 mΩcm, respectively.

In order to gain fundamental understanding for the reasons why this hydrogen-doped TCO works so well, the optoelectronic and structural properties of ALD In_2O_3:H and the change thereof upon crystallization have been scrutinized. As described in chapter 6, it has been found crucial to prepare the In_2O_3:H film at 100 ^{o}C, since at this temperature a very low density of crystallites is embedded in the otherwise amorphous film. Upon post-annealing grain growth proceeds isotropically from these crystallites without nucleation of additional crystallites. The absence of additional nucleation leads to a large final grain size and is attributed to the high hydrogen content in the films deposited at low temperatures. In addition, the doping mechanism and electron scattering in ALD In_2O_3:H have been studied, as reported on in chapter 5. Atomic hydrogen has been found to be an excellent dopant in this post-crystallized material: Although only ∼4 at.% of the embedded H acts as an active dopant, the inactive H has been found to not contribute to electron scattering, which is a strong advantage over the traditional Sn dopant. Ionized impurity from the H dopants and phonon scattering were found to be the only scattering mechanisms of relevance in the crystallized film, with a contribution of ∼66 % and ∼34 %, respectively. Since these scattering processes are unavoidable, the carrier mobility in the ALD In_2O_3:H is at its fundamental limit for its carrier density.

The developed ALD In_2O_3:H has been implemented as the front TCO in a silicon heterojunction solar cell. A convincingly high short-circuit current density J_{sc} of 40.2 mA/cm^2 was obtained, exceeding that of the ITO reference by 1.7 mA/cm^2.

In addition, evaporated molydenum oxide (MoO$_x$) emerged during the project as a promising, highly transparent hole-selective contact. Initial reports showed that the performance of MoO$_x$ was highly thickness-dependent, which made ALD a very interesting candidate to prepare these MoO$_x$ films. Therefore, an ALD process for MoO$_x$ has been developed within this project, described in chapter 7. The ALD process allows for the preparation of MoO$_x$ over a wide temperature range of 50 - 350 ^{o}C. At deposition temperatures below 250°C amorphous material is obtained, whereas at higher temperatures a transition to polycrystalline growth has been observed which is accompanied

by a strong increase in the growth per cycle. Apart from a reasonable amount of embedded atomic H of 3-11 at. %, the films are of high purity and are slightly substoichiometric with an O/Mo ratio of $\sim$2.9.

In chapter 8, the developed ALD MoO$_x$ has been implemented in a solar cell precursor together with a-Si:H and ALD In$_2$O$_3$:H. A very high level of passivation and optical incoupling have been obtained, as witnessed by excellent implied open-circuit voltage and simulated short-circuit current values of 717 mV and 41.7 mA/cm^2, respectively. However, the carrier-selectivity of the ALD material was found to be not yet on par with its evaporated counterpart. This has been found to be due to a lower induced band bending by the ALD MoO$_x$ in comparison to the evaporated material, pointing to a lower work function for the ALD material. This lower work function is thought to originate from oxygen vacancies in the substoichiometric ALD MoO$_x$. Therefore, future research focuses on the reduction of the oxygen vacancies in this ALD material.

The experience gained within this project on the use of ALD for the preparation of passivation, carrier-selective and transparent conductive oxide layers for silicon solar cells has been culminated in a book chapter, which forms chapter 2 of this thesis. Finally, much of the work presented within this dissertation will be used and developed further within the recently started COMPASS project on passivating contacts for silicon solar cells.

Samenvatting

Atoomlaagdepositie van Dunne Metaaloxide Films voor Si Heterojunctie Zonnecellen

Atoomlaagdepositie (ALD) is binnen het veld van silicium zonnecellen vooral bekend van de bereiding van hoge kwaliteit Al_2O_3 oppervlaktepassivatielagen voor homojunctie zonnecellen. Industriële ALD machines, speciaal geënt op deze applicatie, zijn commercieel verkrijgbaar en bewerkstelligen substantiële toenames in het rendement van zulke zonnecellen. Momenteel staan silicium heterojunctie (SHJ) ofwel *passiverende contact* zonnecellen volop in de belangstelling, vooral omdat met zulke cellen nog hogere rendementen behaald kunnen worden en mogelijk volledig op lage temperatuur en met simpele processtappen geproduceerd kunnen worden. In de conventionele homojunctie cellen worden functionele dunne films louter gebruikt voor oppervlaktepassivatie en antireflectie. Heterojunctie cellen daarentegen leunen volop op functionele dunne films: dunne films die op de silicium wafer gedeponeerd zijn voorzien de cel van alle functionaliteiten, zoals oppervlaktepassivatie, selectieve extractie van ladingsdragers en laterale elektrische geleiding door transparante geleidende oxides (TCOs). In dit proefschrift is het gebruik van ALD voor de depositie van functionele dunne films voor deze opkomende zonnecelconcepten verkend.

Zoals beschreven in hoofdstuk 3 is ALD gebruikt voor de depositie van TCOs voor SHJ cellen, hetgeen conventioneel gedaan wordt met sputterdepositie. Er zijn twee belangrijke voordelen van ALD ten opzichte van de gangbare sputterdepositie methode gedemonstreerd. Dit is gedaan aan de hand van aluminium-gedoteerd zink oxide (ZnO:Al) bereid met ALD. Ten eerste, waar sputterdepositie notoir is om de schade die het plasma aanbrengt aan het substraat tijdens de depositie, wordt er geen plasma gebruikt bij thermische ALD. Dit garandeert een hoge compatibiliteit met de gevoelige dunne films van een SHJ zonnecel. Ten tweede is aangetoond dat het gebruik van zogeheten ALD supercycli een ongekende controle geeft over zowel het doteringsniveau als het doteringsprofiel van het TCO. De controle hierover is van groot belang: Het doteringsniveau bepaalt het fundamentele compromis tussen optische transparantie en elektrische geleiding van het TCO. Bovendien is experimenteel aangetoond dat het doteringsniveau, dat de werkfunctie van het TCO bepaalt, van grote invloed is op de eigenschappen van de junctie.

Tijdens het project werd duidelijk dat *hoge-mobiliteit* waterstof-gedoteerd indium oxide (In_2O_3:H), een TCO dat oorspronkelijk ontwikkeld is met sputterdepositie, een enorme

211

potentie heeft voor heterojunctie zonnecellen. In zulke hoge-mobiliteit TCOs is de bewegingsvrijheid van elektronen veel groter dan in het gangbare tin-gedoteerd In_2O_3 en gedoteerd ZnO. Dit heeft tot gevolg dat het doteringsniveau dat benodigd is om de gewenste elektrische geleiding te bereiken sterk gereduceerd wordt. Hierdoor zijn optische verliezen in het infrarood door vrijeladingsdragereffecten verwaarloosbaar in vergelijking met de gebruikelijke TCOs. Om deze reden zijn hoge-mobiliteit TCOs cruciaal gebleken voor het behalen van een korstsluitstroomdichtheid J_{sc} boven de 40 mA/cm^2 voor dit type zonnecel. Er is een ALD proces voor de bereiding van hoge-mobiliteit In_2O_3:H ontwikkeld, zoals beschreven in hoofdstuk 4. Het proces bestaat uit de groei van bijna geheel amorf In_2O_3:H, gevolgd door een kristallisatiestap op 150-200 ^{o}C, wat resulteert in polykristallijn In_2O_3:H met korrels met een laterale grootte van enkele honderden nanometers. Naast de lage temperatuur van het proces en de eerder genoemde voordelen van ALD ten opzichte van sputterdepositie, zijn de record-hoge mobiliteit en de lage resistiviteit van respectievelijk 138 cm^2/Vs en 0.27 mΩcm de sterke punten van de ALD aanpak.

Om fundamenteel begrip te verkrijgen van de reden waarom deze waterstof-gedoteerde TCO zo goed werkt, zijn de optoelektronische en structurele eigenschappen van ALD In_2O_3:H en hun veranderingen tijdens kristallisatie onder de loep genomen. Zoals beschreven in hoofdstuk 6 is het cruciaal gebleken om de In_2O_3:H lagen op 100 ^{o}C te deponeren, aangezien bij deze temperatuur een zeer lage dichtheid aan kristallieten wordt ingesloten in de voor het overige amorfe film. Bij verhitting vindt isotrope aangroei van deze kristallieten plaats zonder enige additionele nucleatie van nieuwe kristallieten in de amorfe fase. Deze afwezigheid van additionele nucleatie leidt tot een grote uiteindelijke korrelgrootte en wordt toegeschreven aan de hoge concentratie van atomair waterstof in de lagen die bij lage temperaturen worden gedeponeerd. Daarnaast zijn zowel het mechanisme van dotering en de verstrooiing van elektronen in ALD In_2O_3:H bestudeerd, zoals beschreven in hoofdstuk 5. Atomair waterstof blijkt een zeer geschikt atoom te zijn voor de dotering van dit gekristalliseerde materiaal: hoewel slechts ∼4 at. % van alle ingesloten waterstof fungeert als actieve dotering is vastgesteld dat de inactieve waterstofatomen niet bijdragen aan additionele verstrooiing van elektronen, hetgeen een sterk voordeel is ten opzichte van traditionele dotering met tin. Het is verder vastgesteld dat elektronen in dit materiaal alleen verstrooien aan geïoniseerde doteeratomen en aan fononen. Deze verstrooiingsprocessen zijn onontkoombaar, wat betekent dat de microstructuur van het gekristalliseerde ALD In_2O_3:H van dusdanige kwaliteit is dat de mobiliteit aan zijn fundamentele limiet zit voor de gegeven ladingsdragersdichtheid.

Het ontwikkelde ALD In_2O_3:H is toegepast als TCO aan de voorkant van een silicium heterojunctie zonnecel. Een overtuigend hoge kortsluitstroomdichtheid J_{sc} van 40.2 mA/cm^2 is behaald, wat 1.7 mA/cm^2 hoger is dan de referentiecel met conventioneel

ITO.

Recentelijk is opgedampt molybdeen oxide (MoO_x) verschenen als een veelbelovend, zeer transparant gatenselectief contact. De eerste rapporten over deze toepassing toonden aan dat MoO_x als gatenselectief contact zeer dun moet zijn, wat ALD een zeer geschikte techniek maakt om deze MoO_x lagen te deponeren. Daarom is een ALD proces voor MoO_x ontwikkeld, wat beschreven is in hoofdstuk 7. Het ALD proces biedt de mogelijkheid om de MoO_x lagen over een groot temperatuurbereik van 50 - 350 °C te deponeren. Bij depositietemperaturen lager dan 250 °C zijn de lagen amorf. Bij hogere temperaturen is een transitie van amorf naar polykristallijn materiaal vastgesteld, die vergezeld wordt van een sterke toename in de groei-per-cyclus. Buiten een redelijke hoeveelheid ingesloten waterstof van 3-11 at. % zijn de lagen vrij van onzuiverheden en zijn ze licht substoichiometrisch met een O/Mo verhouding van $\sim$2.9.

In hoofdstuk 8 is beschreven hoe het ontwikkelde ALD MoO_x geïmplementeerd is in een zonnecelstructuur in combinatie met gehydrogeneerd amorf silicium (a-Si:H) en ALD In_2O_3:H. Deze stapeling van lagen geeft een zeer goede oppervlaktepassivatie en optische lichtinkoppeling, zoals blijkt uit de uitstekende geïmpliceerde openklemspanning en gesimuleerde korstsluitstroomdichtheid van respectievelijk 717 mV en 41.7 mA/cm^2. Desalniettemin is gebleken dat de mate van ladingsdragerselectiviteit die behaald wordt met het ALD MoO_x nog lager is dan die van het opgedampte MoO_x. Dit wordt toegeschreven aan een lagere geïnduceerde bandbuiging door het ALD MoO_x in vergelijking met het opgedampte MoO_x, wat duidt op een lagere werkfunctie voor het ALD materiaal. Deze lagere werkfunctie vindt naar alle waarschijnlijkheid zijn oorsprong in het feit dat het ALD materiaal substoichiometrisch is en dus gekenmerkt wordt door een tekort aan zuurstofatomen in het rooster. Om deze reden is het huidige vervolgonderzoek toegespitst op het manipuleren van het zuurstofgehalte in het ALD MoO_x met als doel om meer stoichiometrisch materiaal met een hogere werkfunctie te maken.

De ervaring en kennis met betrekking tot het gebruik van ALD voor de bereiding van passiverende, ladingsdragerselectieve en TCO lagen voor silicium zonnecellen die is opgedaan binnen dit project is samengebracht in een bijdrage aan een boek, dat hoofdstuk 2 vormt van dit proefschrift. Tot slot vindt een groot deel van het werk dat gepresenteerd is in dit proefschrift opvolging in het recent gestarte COMPASS project, waarbinnen de focus ligt op de ontwikkeling van passiverende contacten voor silicium zonnecellen.

List of publications related to this work

Peer-reviewed publications

1. **Metal-Insulator-Semiconductor Nanowire Network Solar Cells**
   S.Z. Oener, J. van de Groep, <u>B. Macco</u>, P.C.P. Bronsveld, W.M.M. Kessels, A. Polman, E.C. Garnett, Nano Letters (2016).

2. **Atomic Layer Deposited Molybdenum Oxide for the Hole-Selective Contact of Silicon Solar Cells**
   M. Bivour, <u>B. Macco</u>, J. Temmler, W.M.M. Kessels, M. Hermle, Energy Procedia (2016).

3. **Atomic Layer Deposition of Molybdenum Oxide from (N^{t}Bu)$_2$(NMe$_2$)$_2$Mo and O$_2$ Plasma**
   M.F.J. Vos, <u>B. Macco</u>, N.F.W. Thissen, A. A. Bol, and W.M.M. Kessels, Journal of Vacuum Science & Technology A: Vacuum, Surfaces, and Films 34(1), 01A103 (2016). *Chapter 7 of this thesis*

4. **Low-Temperature Atomic Layer Deposition of MoO$_x$ for Silicon Heterojunction Solar Cells**
   <u>B. Macco</u>, M.F.J. Vos, N.F.W. Thissen, A.A. Bol, and W.M.M. Kessels, Phys. Status Solidi − Rapid Res. Lett. 9, 393 (2015). *Chapter 8 of this thesis*

5. **Electron Scattering and Doping Mechanisms in Solid-Phase-Crystallized In$_2$O$_3$:H Prepared by Atomic Layer Deposition**
   <u>B. Macco</u>, H.C.M. Knoops, and W.M.M. Kessels, ACS Appl. Mater. Interfaces 7(30), 16723−16729 (2015). *Chapter 5 of this thesis*

6. **High Mobility In$_2$O$_3$:H Transparent Conductive Oxides Prepared by Atomic Layer Deposition and Solid Phase Crystallization**
   <u>B. Macco</u>, Y. Wu, D. Vanhemel, and W.M.M. Kessels, Phys. Status Solidi - Rapid Res. Lett. 8, 987 (2014). *Chapter 4 of this thesis*

7. **Influence of Transparent Conductive Oxides on Passivation of *a*-Si:H/*c*-Si Heterojunctions as Studied by Atomic Layer Deposited Al-doped ZnO**
   <u>B. Macco</u>, D. Deligiannis, S. Smit, R.A.C.M.M. van Swaaij, M. Zeman, and W.M.M. Kessels, Semicond. Sci. Technol. 29, 122001 (2014). *Chapter 3 of this thesis*

8. **Atomic-Layer-Deposited Transparent Electrodes for Silicon Heterojunction Solar Cells**
B. Demaurex, J.P. Seif, S. Smit, <u>B. Macco</u>, W.M.M. Kessels, J. Geissbuhler, S. De Wolf, and C. Ballif, IEEE J. Photovoltaics 4, 1387 (2014).

9. **Al_2O_3/TiO_2 Nano-pattern Antireflection Coating with Ultralow Surface Recombination**
P. Spinelli, <u>B. Macco</u>, M. A. Verschuuren, W.M.M. Kessels, and A. Polman, Appl. Phys. Lett. 102, 233902 (2013).

10. **Passivating Contacts for Crystalline Silicon Solar Cells: from Concepts, Classifications, and Materials to Prospects**
J. Melskens, B.W.H. van de Loo, <u>B. Macco</u>, M.F.J. Vos, J. Palmans, W.M.M. Kessels, *submitted to Journal of Photovoltaics*.

11. **On the Solid Phase Crystallization of In_2O_3:H Transparent Conductive Oxide Films Prepared by Atomic Layer Deposition**
<u>B. Macco</u>, M.A. Verheijen, L.E. Black, B. Barcones, J. Melskens, W.M.M. Kessels, accepted for publication in *Journal of Applied Physics*. *Chapter 6 of this thesis*

12. **Correlating the Crystalline Silicon Surface Passivation to the Nanostructure of Low-Temperature *a*-Si:H Upon Rapid Thermal Annealing**
<u>B. Macco</u>, J. Melskens, N. Podraza, K. Arts, W.M.M. Kessels, *under preparation*.

13. **Compositional, Structural and Optoelectronic Properties of In_2O_3:H Thin Films Prepared by Atomic Layer Deposition from InCp and O_2/H_2O**
<u>B. Macco</u>, Y. Wu, D. Vanhemel, S. Koelling, M.A. Verheijen, P.M. Koenraad, F. Roozeboom, W.M.M. Kessels, *under preparation*.

14. **The Mobility of Open Volume Deficiencies in Hydrogenated Amorphous Silicon During Annealing**
J. Melskens, S.W.H. Eijt, M. Schouten, A.S. Vullers, A. Mannheim, H. Schut, <u>B. Macco</u>, M. Zeman, A.H.M. Smets, *under review at Journal of Photovoltaics*.

15. **Towards the Implementation of Atomic Layer Deposited In_2O_3:H in Silicon Heterojunction Solar Cells**
Y. Kuang, <u>B. Macco</u>, C.K. Ande, P.C.P. Bronsveld, M.A. Verheijen, Y. Wu, W.M.M. Kessels, R.E.I. Schropp, *under preparation*.

Book chapters

1. **Atomic Layer Deposition for High Efficiency Crystalline Silicon Solar Cells**
<u>B. Macco</u>, B.W.H. van de Loo, and W.M.M. Kessels, in J. Bachmann, "Atomic Layer

Deposition in Energy Conversion Applications", Wiley (2016). *Chapter 2 of this thesis*

Conference proceedings

1. **Status and Prospects for Atomic Layer Deposited Metal Oxide Thin Films in Passivating Contacts for c-Si Photovoltaics**
   B. Macco, J. Melskens, B.W.H. van de Loo, S. Smit, W.M.M. Kessels, IEEE PVSC proceedings (2016).

2. **Atomic-Layer Deposited Passivation Schemes for c-Si Solar Cells**
   B.W.H. van de Loo, B. Macco, J. Melskens, M.A. Verheijen, W.M.M. Kessels, IEEE PVSC proceedings (2016).

3. **Concepts and Prospects of Passivating Contacts for Crystalline Silicon Solar Cells**
   J. Melskens, B.W.H. van de Loo, B. Macco, M.F.J. Vos, J. Palmans, W.M.M. Kessels, IEEE PVSC proceedings (2015).

Popular publications

1. **Een Nieuw Atoomlaagdepositieproces voor Efficiëntere Zonnecellen**
   M.F.J. Vos, B. Macco, and W.M.M. Kessels, Nevac Blad 5(1),8 (2016).

2. **Depositie van polykristallijn silicium voor dunne-film zonnecellen**
   B. Macco, K. Sharma, W.M.M. Kessels and M. Creatore, Nevac Blad 51(1), 6-11 (2013).

Contributions of the author

The work presented in this dissertation is original work of the author. Nonetheless, some parts of this dissertation deserve extra clarification:

The book chapter presented in **Chapter 2** of this disseration was written in collaboration with B.W.H. van de Loo. The book chapter is a joint effort of both authors, although B.W.H. van de Loo focused on the section on surface passivation, whereas the author's main contribution lies in the sections on transparent conductive oxides and passivating contacts.

The publication in **Chapter 7** resulted from a collaboration between the author and M.F.J. Vos, who did his MSc. project under supervision of the author on atomic layer deposition of molybdenum oxide. Since the experimental work, the analysis thereof and the writing of the paper were joint work, it was chosen to submit this work with two equally contributing first authors.

The ongoing experiments on the implementation of ALD In_2O_3:H in solar cells are done in collaboration with dr. Y. Kuang. The plasma pretreatment was developed by the author, whereas dr. Y. Kuang has taken care of the careful analysis and optimization of the plasma pretreatment and the preparation of the solar cells.

Curriculum Vitae

Bart Macco was born in Sittard, the Netherlands, on 9 December 1988. After obtaining his gymnasium diploma *cum laude* in 2007 at Trevianum Scholengroep in Sittard, he studied Applied Physics at the Eindhoven University of Technology. He received both his BSc and MSc degree in Applied Physics *cum laude* in September 2010 and 2012, respectively. During his master, Bart spent four months at the Colorado School of Mines, Golden, Colorado, researching surface passivation of plasma-synthesized Si nanocrystals by hydrosilylation. Bart's MSc research project was on the growth and characterization of polycrystalline silicon for thin-film photovoltaics. On the basis of this work, Bart became a finalist for the Shell Master prize and received the NEVAC award for best scientific article. In September 2012 Bart started to pursue a PhD degree in the Plasma & Materials Processing group. Bart pioneered and advocated the use of atomic layer deposition (ALD) for the preparation of metal oxide thin films for application in silicon heterojunction photovoltaics. Firstly, Bart focused on ALD of transparent conductive oxides (TCOs) and demonstrated the main merits of using ALD in this field. The resulting manuscript in Semiconductor Science & Technology was selected as Highlight of 2014 by the editorial board. Subsequently, Bart developed a novel ALD approach to make hydrogen-doped indium oxide TCOs of record electronic quality, which was featured on the cover of Rapid Research Letters. Later, Bart expanded his interest into the upcoming field of passivating contacts, and developed a novel ALD process for molybdenum oxide as a hole-selective contact. His PhD research has led to 6 first-author publications in peer-reviewed journals, a conference proceeding, two manuscripts which are under preparation, and a Wiley book chapter on ALD for high efficiency c-Si photovoltaics. In addition, Bart is recipient of the MRS Spring Meeting 2015 Symposium A Award for best student presentation, and both the Thin Film Graduate Student Award and James Harper Award of the 62nd AVS International Symposium. Finally, Bart is co-owner of Macco VOF, a software company for which he develops language-learning software packages that are used by students throughout the Netherlands and Belgium.

Acknowledgments

After a great four years, I find myself with a long list of people that I would like to thank for their contributions to the content of this thesis as well as for making PMP a great place to work.

I would like to start with my promotor, **Erwin**. I mostly value the freedom you have given me within the project to explore the research topics I found interesting. Additionally, after our usually short and effective meetings I almost always found myself extremely motivated, with clear objectives in my mind. Also, I think I learnt a lot from you in terms of presenting and the importance of building a good story, which will certainly prove to be of use in the future. Secondly, I want to thank **Richard**. Although we have not really been in touch during the project, you were to one to write my project within the FLASH programme and thus stood at the cradle of this PhD thesis. This brings me to thank **Ruud**. I think you have led a very fruitful FLASH project, which has not only lead to great scientific outcomes, but has also strengthened collaborations in the field of silicon heterojunctions in the Netherlands. This is also evidenced by the new projects that have been granted which could be seen as successors of FLASH. **Adriana**, I think I should thank you most for the period just prior to this PhD project: You introduced me to PMP, and a great MSc project supervised by you led to my decision to also pursue a PhD in this group. Also, you arranged my internship at Colorado School of Mines, which I can safely say was pretty much the best time of my life. At this point I should also thank **Kashish**, my supervisor during my MSc. project in PMP. Next to being a great friend, you gave me all the freedom but also advice to conduct the experiments as I deemed necessary. I'm sure we'll meet again! **Marcel**, I think our discussions on crystallization processes were not only very fruitful, and have contributed greatly to the chapter on crystallization, but our shared passion for the subject even made them highly enjoyable. **Fred**, I would like to thank you for the involvement in the indium oxide work: I don't think I can think of anyone that can speak as enthusiastic about research as you do! **Ageeth**, I would like to thank you for your contribution on the MoO_x work. I think that finding a mutual benefits for developing an ALD process for MoO_x and WO_x (PV for me, 2D TMDs for you) is a textbook example of good collaboration within our research group. **Jeanne** and **Lianne**, I would like to thank you for your perpetual willingness to assist in every imagineable situation. Of course I should also thank the technicians, **Cristian**, **Wytze**, **Jeroen**, **Janneke**, **Caspar**, **Joris** and **Bernadette**. I think that many research groups should be jealous of such a large group of skilled supportive staff.

Next on the list are the **Colorado 4**: **Bas**, **Nick**, **René** (excluding myself here). We used our days off to the maximum extent to make roadtrips of epic proportions and I think that together we have seen more of the world than most people see in their lifetime. **René** thanks for extending my Limburgian vocabulary ("sjerre"), **Nick** thanks for reminding us about the whereabouts of the Pepsi center in Denver and the many SEM images. En **Bas**, bedankt. I should of course not forget our aspiring member **Roger, the +1**. I think I learnt a great deal from you, especially the "fotografeer je biertje" move. I should also thank our WhatsApp group **Jeep 3.0**, whose name stems from the greatest car ever made. Over the years this has been a great source of entertainment and by now contains a big database of pictures of the last years, although I fear that these will be used against me at my defense party...

Sjoerd, I think you had the largest influence on my PhD of all people. Without your theoretical approach (a great choice of Erwin to bring in a more theoretical guy!) I probably would not have drawn quasi-Fermi levels in this thesis, but rather electrons rolling off a hill. Also your great sense of humor and claim about the level of pittoresqueness of Hamelin will be great memories. Best of luck in England! **The Harm(inator)**, de rots in de branding bij PMP, the one we turn to in times we do not understand our data. Thank you for your contribution to this thesis, especially in Chapter 5. We had a great holiday in Costa Rica, and I look forward to our holiday in Ireland. This brings me to **Martinus**. Also thanks for making our Costa Rica trip a great experience, our midnight hotel cart race through the hotel in San Jose and I look forward to Ireland. Although you were "my" master student, it felt more as if you were a direct colleague, many thanks for the great contribution to this thesis! The same goes for **Karsten**. You did your bachelor project under my supervision, although also for you the word supervision did not really apply. The a-Si:H layers we worked on played a large role in the last four years, and I'm sorry the a-Si:H paper is still not published :) **Vincent**, we have a lot of nerdy interests in common, and you were always prepared to help when it came to Linux or programming. Also, I think no-one in the group deserved a great dataset more than you after your perseverance has been tested for such a long time by the SFG setup. **Jimmy**, thank you for convincing me that I am not a caffeine-addict, since your consumption level of coffee is at least a few orders of magnitude higher. Also, thanks for improving my reading level by sending emails that are typically longer than the average letter-publication. On a more serious note, your input in my work in the last $\sim$1 year is highly appreciated, and I foresee all the best for COMPASS! **Yizhi**, thanks for your big part in my thesis work: Both the ZnO and In_2O_3 work. I'm also highly impressed with the pace at which you went from the Chinese guy to a true Dutchman. You traded in rice for boterhammen and went from gaming to swimming. I'm sure you will find a nice position soon! **Jan-Willem** (or should I say Uli?), I think you are the most sincere person I have ever met. Thanks for proofread-

ing my ACS manuscript with spectroscopic eyes, and I hope we will talk German to one another at many a Borrel in the near future. Speaking of the **Borrel**, I think I should also thank the bartenders that make the Borrel possible every Thursday, providing a great place to socialize with colleagues (which is very important!) while enjoying low-cost special beers. **Bart K.**, fellow Barbār-lover, thanks for making your attendance to the Borrel a universal constant.

I also have great memories (or do I?) of the Oktoberfest weekend in Münich. **Florian**, thanks for organizing and hosting it, and thanks to the people who were there to make it a great time. **René**, **Roger**, **Adrie**, **Chai**, **Harm**, **Vincent**: Ein prosit! Also the PEST soccer team is thanked for making the breaks highly enjoyable: **Valerio & Valerio DP**, **Ben**, **Maarten & Maarten**, **Simone**, **Ugur**, **Rafael**, **Karsten** and **Remco**: Keep us in the first league!

Noémi, thanks for recording thousands of French sentences for our company, you have been vital for our new software package! I'm sure you're doing well in Colorado with Sumit! **Sumit**, I think I should also devote a few words to you. Not only were you and **Marina** extremely hospitable when we did our internship in Colorado, you also taught me to really scrutinize a data set. I think that without this wisdom, I wouldn't have been able to write three publications out of a week's worth of In_2O_3:H experiments.

Also the collaboration with ECN, and especially the contribution of **Paula**, is highly appreciated. Without your contribution this thesis would be much less PV-ish. Fortunately the collaboration continues within COMPASS! This also brings me to **Yinghuan**, my In_2O_3:H-partner-in-crime. Thanks for so carefully exploring the integration of ALD In_2O_3:H in SHJ solar cells, something for which I wouldn't have had the time.

Ravi and **Dimitris**, my fellow FLASH-PhDs from Delft, I had the best time with you at Quantsol: The étendue! Ravi, you were a great host for Weerwolven, and Dimitris, many, many, many thanks for the experiments in Chapter 3. I think that was a very efficient and fruitful collaboration!

Last but certainly not least of course my **family**. Mom and dad, you have raised three children that all live a successful life. That's something to be proud of. In the last two-three years we have seen each other a lot because of our activities in the software company. This also provided me with an intellectual challenge other than my PhD, which I think was beneficial for both my PhD and the company.

If after this long list of people you find your name is missing, please don't be sad. In Dutch we say: "Het beste paard van stal vergeten".

Bart Macco - 19th of May, 2016